Geology of the North Fiji Basin Triple Junction and an Investigation into Triple Junction Formation

MARY BESAW

Thesis submitted to the University of Ottawa
in partial fulfillment of the requirements
for the Master's degree in Earth Science

Department of Earth and Environmental Sciences
Faculty of Science
University of Ottawa

© Mary Besaw, Ottawa, Canada, 2022

Abstract

Triple junctions form at the intersection of three tectonic plates and are a necessary consequence of new microplate formation. The splitting of a plate into two smaller plates always results in the formation of two triple junctions. As a result, they are fundamental structural elements of ocean floor geodynamics. Their evolution is influenced by the complex interplay of near- and far-field plate dynamics, crustal types, and mantle processes, and they include a wide range of boundary types. The long-term stability and evolution of triple junctions are influenced by continuous plate reorganization, such as in the complex microplate mosaics of the Western Pacific margin.

To better understand how triple junctions form and respond to near- and far-field stresses, this study presents a detailed examination of the North Fiji Basin Triple Junction (NFBTJ), which is located within one of the largest and most mature back-arc basins of the Pacific margin. A new geological map of the NFBTJ at a 1:500,000 scale is presented. The mapping provides insight into the factors controlling plate fragmentation and crustal growth during triple junction formation. The map is based on a compilation of more than 50 years of ship-based bathymetry, backscatter data, gravity and magnetics used to reconstruct the spreading history, magmatic productivity, tectonic fabric and origin of geological formations of the basin. These aspects also have important implications for understanding the origins and evolution of large-scale back-arc basin hydrothermal systems.

Crustal growth in the NFB is recorded by the area-age relationships of different geological formations identified in the new geological map. The triple junction is the site of volume addition related to enhanced magmatic productivity, with a large Central Volcanic Complex (CVC) (shield volcano and inflated ridge) at its centre and a well-developed spreading ridge along the SW limb. Extensive lava flows emanating from the CVC covers early spreading-related fabric in the NE and NW limbs. The large shield volcano, which is 0.5 km high and occupies an area of at least 62.3 km^2, has a distinctive 2.5-km diameter summit caldera with extensive hydrothermal activity in the south. The CVC and surrounding lava flows are estimated to have grown in place at a rate of 3,000 m^2/yr, thus dominating the recent history of the NFBTJ. By contrast, earlier crustal growth along the SW and NW spreading segments, prior to the emergence of CVC, is estimated to have been

~1,650 m^2/yr and 200 m^2/yr respectively. The quantitative analysis of rifting and the eruptive history highlight previously unrecognized near and far-field geodynamic influences on the triple junction formation. In particular, the pulse of crustal growth at the NFB beginning at 3 Ma was related to rift propagation from the south in response to rotation of the NFB that produced some of the fastest growing crust in the oceans.

Comparisons with a global database of triple junctions show that the evolution of the NFBTJ shares many features with other microplate mosaics and that processes related to triple junction formation is associated with crustal growth wherever triple junctions occur. The high heat flow and voluminous mafic magmatism has been compared to rapid crustal growth in some ancient greenstone belts, such as the Archean Abitibi Greenstone Belt in the Superior Province of Canada. In particular, the NFBTJ is a possible modern analog of large central volcanic complexes that characterize ancient greenstone-belt development.

Acknowledgments

This research is a product of the Metal Earth Project funded by the Canada First Research Excellence Fund (CFREF), the Natural Sciences and Engineering Research Council of Canada (NSERC), and the Marine Mineral Resources Group at the GEOMAR-Helmholtz centre for Ocean Research Kiel. The Helmholtz Association, NSERC, and CFREF are acknowledged for supporting this work through research grants and project funding. The project is also supported by the NSERC Collaborative Research and Training Experience program (iMAGE-CREATE) on Marine Geodynamics and Georesources. This is contribution MERC-ME-2022-27 to the modern-ancient crust project of the Canadian Metal Earth program.

I want to thank the following, without whom I would not have been able to complete this project. First and foremost, I thank my supervisor, Dr. Mark Hannington, for providing his expertise and guidance throughout this project. As well as Dr. Alan Baxter of the Metal Oceans research group who has constantly been available to provide feedback, advice, and support throughout this project. I must also thank Alex Grey, another master's student with the Metals Oceans group, with whom I have had countless troubleshooting discussions while also providing praise, encouragement and advice to each other; I could not imagine completing this project without her. Other members of the Metal Oceans group, including Anna Krätschell, Dr. David Diekrup, Dr. Meg Stewart, and Kaitlyn Breker, have also been crucial in providing thein expertise at various stages of this project., I, of course would also like to thank my family for housing me during the pandemic and my friends, in particular Rachael and Ruby, for all their constant support and encouragement. As well as my past foster dogs, Sophie, Ruben and Ruth for providing me with a sense of pride, an outlet for fun and helping keep my sanity while meeting deadlines.

Table of Contents

Abstract ..... **ii**

Acknowledgments ..... **iv**

Table of Contents ..... **v**

List of Figures ..... **vii**

List of Tables ..... **x**

Chapter 1: Introduction **1**

1.2 Thesis Objectives 3

1.3 Approach and Methods 4

1.4 Published Results 5

Chapter 2: A New Geological Map of the North Fiji Basin Triple Junction and Implications for Regional Volcanism and Kinematics **6**

2.1 Introduction 6

2.2 Regional Geology 7

2.3 Previous Interpretations of the North Fiji Basin Triple Junction 9

2.4 Methods and Data 11

2.5 Geological Map of the North Fiji Basin Triple Junction 15

2.6. Discussion 22

2.7 Summary and Conclusions 35

Figures 38

Tables 64

Chapter 3: A Global Database of Triple Junctions in the Oceans: Lessons for the North Fiji Basin **71**

3.1 Introduction 71

3.2 Previous Work 73

3.3 Methods and Data 75

3.4 Summary Statistics 78

3.5 Results 80
3.6 Comparisons with the North Fiji Basin Triple Junction 86
3.7 Conclusions 91
Figures 92
Tables 105
Chapter 4: Summary and Conclusions 110
References 113
Appendices Contents 127
Appendix A - Supplementary Figures 128
Appendix B - Geological Map Sheet of the North Fiji Basin Triple Junction 139
Appendix C - Supplementary Tables 140
Appendix D Global Triple Junction Database of 117 Triple Junctions 146
Appendix E Oceanic Triple Junction Database 147
Triple Junction Database References (Global and Oceanic) 148

List of Figures

Figure 2.1 Multibeam bathymetry compilation and regional tectonic map of the North Fiji Basin

Figure 2.2 Schematic illustration of the opening of the North Fiji Basin and the emergence of the North Fiji Basin Triple Junction (NFBTJ)

Figure 2.3 Regional Bathymetric data, local integrated Digital Elevation Model (DEM) and ship-based acoustic backscatter of the NFBTJ

Figure 2.4 Free-air gravity, Bouguer gravity anomaly and vertical gravity gradient (VGG) of the NFBTJ.

Figure 2.5 Global magnetic anomalies and magnetic signatures modified from Huchon et al. (1994).

Figure 2.6 Harvard Centroid Moment Tensors (CMTs) for earthquakes in the vicinity of the NFBTJ

Figure 2.7 Reduced version of the 1:500,000 geological map of the North Fiji Basin Triple Junction

Figure 2.8 Schematic illustration of stratigraphic relationships depicted in the 1:500,000 scale geological map (not to scale)

Figure 2.9 Detailed view of used methods, geological map and hydrothermal vent data at the Central Volcanic centre.

Figure 2.10 Lineament map of the NFBTJ

Figure 2.11 Orientations of faults within the back-arc rifts and spreading centre formations of the three limbs of the NFBTJ

Figure 2.12 Step-wise reconstruction of the NFBTJ through time based on the mapped formations

Figure 2.13 3-D cross sections of the NW, NE and SW limbs of the NFBTJ (6x vertical exaggeration)

Figure 2.14 NFBTJ growth curve (area-age) from calculated ages of the formations and their mapped areas

Figure 2.15 Stability diagrams based on the spreading rates for the three limbs of the NFBTJ

Figure 3.1 Global distribution of all 117 triple junctions included in the Database of Global Triple Junctions (Appendix D)

Figure 3.2 Global distribution of 46 oceanic triple junctions analyzed in this study (Table 3.1)

Figure 3.3 Illustration of segment labelling used in the Database of Global Triple Junctions

Figure 3.4 Ternary diagram illustrating relative importance of different geodynamic settings of oceanic triple junctions from the Database of Oceanic Triple Junctions (Table 3.1)

Figure 3.5 Distribution of inter-limb angles of different triple junctions according to their geodynamic settings from the Database of Oceanic Triple Junction (Appendix E)

Figure 3.6 Schematic illustration of crustal inflation and volume addition at triple junctions through accretion and rifting

Figure 3.7 Variability of volume addition associated with triple junctions in different geodynamic settings and among different triple junction types

Figure 3.8 Comparison of average spreading rates and volume addition of oceanic triple junctions according to geodynamic settings and triple junction type

Figure 3.9 Spatial relationship of hotspots with oceanic triple junctions, illustrating different potential areas of influence on triple junction formation

List of Tables

Table 2.1 Description of formation types in the North Fiji Basin Triple Junction

Table 2.2 Summary statistics of volcano types of the North Fiji Basin Triple Junction (including surface area and volumes)

Table 2.3 Summary statistics of the principal formation types of the North Fiji Basin Triple Junction (including total areas and estimated volumes)

Table 2.4 List of active hydrothermal vent sites of the SW limb of the North Fiji Basin Triple Junction

Table 2.5 Summary statistics of each limb of the triple junction and the Central Volcanic Complex (including surface area and volumes)

Table 2.6 Area-age calculations of each limb of the triple junction and the Central Volcanic Complex

Table 3.1 Summarized attributes of the 46 oceanic triple junctions included in the Database of Oceanic Triple Junctions (Appendix E)

Table 3.2 Cumulative spreading rates of oceanic triple junctions, averaged across 100 km radius

Table 3.3 Comparisons spreading rates and volume addition between mid-ocean ridge spreading centres and representative triple junctions

Chapter 1: Introduction

The mosaic of tectonic plates that overlay the mantle is in constant motion. Microplate formation occurs continuously in response to plate reorganization, which accommodates regional stresses applied to the larger plates. Each plate has its own boundaries, and where three plate boundaries meet at a single point a triple junction is created. There is also a clear connection between triple junction formation and crustal growth, which occurs at the plate boundaries, making triple junctions a fundamental element of plate tectonic theory (Bird, 2003). This study examines a type locality of triple junction formation and evolution in the North Fiji Basin, the largest intraoceanic back-arc basin in the world, to better understand how triple junctions evolve and contribute to crustal growth in the oceans.

1.1 The Origin of Triple Junctions

Bird's (2003) model of the global plate boundaries identifies 14 major plates and 38 microplates, for a total of 52 plates. However, the total number of plates has varied over time, with plate fragmentation occurring in response to continuous plate reorganization. Splitting a plate in two always creates two triple junctions (Rey and Mueller, 2010; Smith et al., 2011). The type of triple junction depends on the types of plate boundaries involved (e.g., spreading ridges/rifts, transform faults or a trench in the simplest configurations: McKenzie and Morgan, 1969; Cronin, 1992; Mitchell et al., 2011). New crust is formed at the spreading ridges, whereas crust is preserved at transform boundaries and destroyed at trenches. Changes in plate motion, rift propagation, transfer of lithosphere from one plate to another, and abandonment of ridges are all fundamental processes in the formation and evolution of triple junctions (e.g., Bird, 2003; Rey and Mueller, 2010; Li et al., 2018). Intense deformation at plate boundaries and triple junctions is common, as is the attachment or amalgamation of the microplates to one of the larger plates (Bird et al., 1999; see also a review by Li et al., 2018). Among the major changes observed are the thickening of the lithosphere in some places, e.g., where crust is accreted, and thinning in others, e.g., where rifting occurs. The most stable triple junctions sometimes become centres of voluminous mafic magmatism and crustal growth, as they are commonly associated with anomalous mantle melting and mantle plumes (Gerya and Burov, 2018). Georgen and Lin (2002) showed that triple junctions

provide a unique window into the mantle. However, questions remain about how the most stable triple junctions are established and how their evolution is linked to near- and far-field tectonic influences. Little work has been done to characterize the geological formations and structures associated with each type of boundary at different triple junction locations and how they might be recognized in the geological record.

1.2 Thesis Objectives

This study aims to establish a detailed history of the North Fiji Basin Triple Junction (NFBTJ) by combining regional geodynamic models of the NFB with detailed geological mapping of the triple junction. The hypothesis is that mappable features of different parts of the triple junction, including geological formations and structures, can be used to reconstruct its origin and evolution over the last 3 to 5 Myr. The mapping aims to clarify the role of different crustal types, highly variable near-field stresses, such as spreading or transpression, and the link to crustal growth. The study suggests that the structure and composition of the crust affect how stresses are accommodated at the triple junction, including which limbs propagate or go extinct and how this influences the degree of magmatic versus tectonic opening of the basin. In particular, the study examines whether geological mapping of different formations manifested as volcanic geomorphology (ridges, depressions, slopes, texture, seafloor fabric) and their geophysical attributes (magnetic signature, gravity) can shed light on the local magmatic and tectonic history. To test this, the first geological map of its type in the North Fiji Basin has been created at a scale of 1:500,000 and is analyzed in the context of crustal growth and regional kinematics.

The NFBTJ is also compared to other triple junctions assembled in a comprehensive new global database of 117 known triple junctions. A subset of 46 oceanic triple junctions are directly compared to the NFBTJ, examining different attributes including crustal type, geodynamic setting, triple junction geometry, boundary types for each of the limbs, initiation age of the triple junction, spreading rate, gravity, the amount of volume addition and the relationship to known hydrothermal vent fields and any associated volcanoes, overlapping hotspots large igneous provinces (LIPs), sedimentary basins, seabed lithology, and geomorphological features. These datasets provide a detailed understanding of the evolution of the NFBTJ in comparison to other known oceanic triple junctions, including differences in crustal makeup, magmatic productivity, and potential for magmatic-hydrothermal activity

1.3 Approach and Methods

A review of more than 50 years of ship-based bathymetry, backscatter data, gravity and magnetics was carried out to map the structure and crustal elements of the NFBTJ, focusing on the geological make-up and age of the crust, tectonic fabric development, and magmatism. These data and comparisons with well-mapped locations as training areas were used to identify 10 different geological formations plus various structures and different volcano types that are represented mappable at 1:500,000 scale. Crustal types with similar properties, age, and origin were identified as distinct geological formations and then assembled into a map legend that considers the sequence of depositional events (inferred stratigraphic relationships between units), the composition of different units, tectonic fabric and structure. When coupled with available geophysical data and seafloor observations, the map data provide a framework for describing the evolution of the triple junction and enable a quantitative analysis of crustal growth related to triple junction formation. The magmatic and tectonic history of each limb of the triple junction is examined independently and as a system, including age relationships, overprinting fabrics, and the movement and rotation of the plate boundaries.

A comprehensive review and comparison of the geology of the NFBTJ with 46 similar oceanic triple junctions worldwide reveals common near and far-field geodynamic influences on triple junction formation. The comparison identifies key drivers of kinematics and magmatic productivity related to triple junction formation. In particular, a method to quantify volume addition was developed comparing oceanic triple junctions. The study also examines differences in triple junction type in different geodynamic settings.

1.4 Published Results

The results of this study have been presented at three scientific conferences:

Besaw, M., 2021, Geology of the North Fiji Basin Triple Junction: A possible modern analog of late Archean mafic magmatism and VMS formation. Annual Ottawa-Carleton Geoscience centre Graduate Seminar, Ottawa, ON, April 2021.

Besaw, M., Hannington, M.D., Baxter, A.T., Stewart, M.S., Petersen, S., Krätschell, A., Emberley, J., 2021, Geology of the North Fiji Basin Triple Junction: A possible modern analog of late Archean mafic magmatism and VMS formation. Annual Student Minerals Colloquium at the Prospectors & Developers Association of Canada Convention, Toronto, ON, March 2021.

Besaw, M., Hannington, M.D., Baxter, A.T., Stewart, M.S., Petersen, S., Krätschell, A., Emberley, J., 2020, Geology of the North Fiji Basin Triple Junction: A possible analog for voluminous late Archean mafic volcanism. Annual Student Minerals Colloquium at the Prospectors & Developers Association of Canada Convention, Toronto, ON, March 2020.

Chapters 2 and 3 of the thesis are currently being combined for submission to a peer-reviewed journal, focusing on the geology of the North Fiji Basin and a geodynamic investigation of triple junction formation with implications for microplate evolution in back-arc basins.

Chapter 2: A New Geological Map of the North Fiji Basin Triple Junction and Implications for Regional Volcanism and Kinematics

2.1 Introduction

Triple junctions are classified by their plate boundaries (McKenzie and Morgan, 1969; Cronin, 1992; Mitchell et al., 2011). Common configurations include spreading ridges or rifts, transform faults and trenches. Their evolution is influenced by the complex interplay of near- and far-field plate dynamics and by continuous plate reorganization. However, some types are considered kinematically more stable than others, retaining their geometry (Cronin, 1992) and, where spreading dominates, becoming important centres of magmatism and crustal growth. Important geological controls on the formation of stable triple junctions are revealed in a new geological map at 1:500,000 scale of the North Fiji Basin Triple Junction (NFBTJ), one of the longest-lived triple junctions in a mature back-arc basin. The spreading history, tectonic fabric and geological formations that characterize the triple junction evolution have been identified in a review of more than 50 years of ship-based bathymetry and backscatter data, as well as gravity measurements and magnetics. This study identifies the key geological features of the triple junction and reconstructs its complex structural evolution and magmatic history. Quantitative analysis of the kinematics of rift propagation, plate boundary rotations, and the eruptive history are presented that highlight previously unrecognized geodynamic influences on plate fragmentation and crustal growth during the formation of the triple junction. The study also considers the possible role of enhanced mafic magmatism at triple junctions as a favourable setting for volcanic-hosted massive sulfide deposits in ancient greenstone belts.

2.2 Regional Geology

The North Fiji Basin (NFB) is a large (1,000 km x 1,000 km) back-arc basin situated between the Pacific Plate and the Australian Plate (Figure 2.1). It is bordered by the Vitiaz Lineament to the north, the Matthew-Hunter Fracture Zone to the south, the Fiji Platform to the east, and the New Hebrides Arc to the west. The basin contains three large microplates: the New Hebrides (NH), Conway Reef (CR) and Balmoral Reef (BR) microplates. Bird (2003) initially concluded that the microplates and their boundaries are not definitive, owing to the lack of clear magnetic anomalies and the complicated tectonic history of the basin. However, he identified the triple junction as a Ridge-Ridge-Fault (RRF-type) intersection.

The NFB opened in the Miocene in response to rifting of the former Vitiaz arc and back-arc extension behind the newly formed New Hebrides subduction zone (Falvey, 1978; Martin, 2013). The history of basin opening is summarized in Figure 2.2, modified after Auzende et al. (1995), Taylor (2000), Ruellan and Lagabrielle (2005), Schellart et al. (2006), and Martin (2013). Until 12 Ma, the Pacific Plate was subducting to the southwest under the Vitiaz arc when subduction was interrupted by the collision of the Melanesian Border Plateau. The collision stopped subduction of the Pacific Plate along the Vitiaz Trench and induced a polarity reversal that initiated subduction of the Australian Plate along the New Hebrides Trench (Martin, 2013). Early back-arc basin spreading was driven by rollback of the Indo-Australian slab, with new crust forming along a now extinct spreading centre that was oriented parallel to the rotating New Hebrides arc (Auzende et al., 1995; Martin, 2013). The initial spreading centres parallel to the New Hebrides Arc were abandoned early in the history of opening, and a new configuration emerged with two main spreading centres, the South Pandora and Tripartite ridges (Figure 2.1 and 2.2), oriented E-W in the north of the NFB, and the Central Spreading Ridge (CSR) oriented N-S, in the centre of the NFB. Lagabrielle et al. (1996) suggested that the South Pandora-Tripartite ridge was active since 7.2 Ma, although it remains unclear if a triple junction formed in the north. Lagabrielle et al. (1996) and Martin (2013) show a triple junction in the north already at 7 Ma. However, this older structure was eventually captured by the Hazel Holme Fracture Zone and now defines the northern termination of back-arc spreading in the NFB.

Due to the location of the Euler pole at the northern end of the New Hebrides Arc (Figure 2.2), spreading rates and crustal accretion were greatest in the southern half of the NFB. Clockwise rotation of the New Hebrides Arc and counter-clockwise rotation of the Fiji Platform resulted in back-arc spreading in a 'double saloon door' fashion, as described by Martin (2013). Between 7 and ~3 Ma, the opposing rotation of the Fiji Platform and the New Hebrides arc resulted in a reorganization of the back-arc spreading axes, from dominantly NW-oriented, to the present N-S orientation along the CSR. Reorganization of the spreading centres was accompanied by rift propagation. deAlteriis et al. (1993) used magnetic and morphostructural mapping to suggest that the CSR actively propagated both north and south. In this case, the formation of the CSR may have been more closely linked to the extension caused by the 'double saloon door' opening rather than extension caused by sinking of the subducting slab. A double saloon door model (Martin, 2007, 2013) two poles of rotation result in two propagating rifts. Collisions of two ridges with the New Hebrides Trench in the west (D'Entrecastaux Ridge and Loyalty Ridge: Figure 2.1) also influenced the development of the arc and back-arc (Meffre and Crawford, 2001; Patriat et al., 2015; Schellart et al., 2002; Collot et al., 2020), while in the east, the Fiji Fracture Zone (FFZ) emerged as the rotation of the Fiji Platform ended. The FFZ propagated westward toward the CSR between 3 Ma and 1 Ma, eventually reaching the present location of the triple junction.

The make-up of the NFBTJ crust has been constrained by regional geophysical measurements, including bathymetry, gravity, magnetics and seismic activity (Figure 2.3 to Figure 2.6). Figure 2.3A shows the regional structure represented by lineaments (ridges, faults and spreading centres) overlain on topography from the Global Bathymetric Chart of the Oceans (GEBCO Compilation Group, 2021). Three dominant spreading axes forming the three limbs of the triple junction are shown in red; the longest has a SW orientation, another has a NW orientation, and the third and shortest spreading centre has a NE orientation. Each spreading axis is characterized by major faulting, with throws over 100 m (shown in black). The largest faults are associated with the NW-oriented spreading axis, followed by the NE limb, and less faulting is associated with the SW limb. The NW-trending faults to the east of the triple junction are a part of the Fiji Fracture Zone. Volcanic ridges typical of back-arc spreading fabric away from the triple junction (shown in gray) are sub-parallel to the three limbs of the triple junction, except south of 19°S and east of the termination of the NE limb at ~174.6 E.

2.3 Previous Interpretations of the North Fiji Basin Triple Junction

Jarvis et al. (1987) first reported the presence of a triple junction at 17°S, 174°E, identified from SeaMARC II imagery and bathymetry. They observed fresh basalt and pillow structures and recorded methane anomalies along the SW limb. They also inferred recent volcanic activity in the NE limb from side-scan imagery and dredge samples. Although the NFB began opening at 12 Ma, the NFBTJ appeared much later, first in the north of the basin around 7 Ma and then migrating southward to its present position (Lagabrielle et al., 1996). Some of the major structures were interpreted as part of an earlier triple junction once active between the Hazel Holme Fracture Zone and the earliest back-arc spreading centres (Auzende et al., 1994). However, the present-day NFBTJ was created by the westward propagation of the Fiji Fracture Zone (FFZ) between ~3 Ma and 1.5 Ma when it intercepted the already established SW spreading centre. Martin (1994) proposed that the NFBTJ was created as early as 1.9 Ma. The original configuration was a ridge-ridge-fault (RRF-type) triple junction, which comprised the actively spreading NW and SW limbs with the NE limb connected to the FFZ along a short, seismically active NW-SE trending structure (outside the red box in Figure 2.1: Huchon et al., 1994). Although there is no available high-resolution multibeam bathymetry of this structure, earthquake motions suggest that it is an active strike-slip fault (Figure 2.4: Heidbach et al., 2016).

Measured from the centre of the triple junction to the first axial discontinuity, the NE, SW and NW limbs of the triple junction are 50 km, 150 km and 100 km in length, respectively. The NE limb is oriented at azimuth 055° and defines a plate boundary segment between the Balmoral Reef and Conway Reef microplates. Magnetic anomalies suggest that the NE limb has been spreading at 18 mm/yr (full rate) since 1.1 Ma (Huchon et al. 1994). The NE graben is about 30 km wide at the triple junction intersection, but it narrows to the NNE where it intersects the NNW-SSE-trending structure connecting to the FFZ, a distance of about 57 km from the centre of the triple junction. The beginning of spreading at the NE limb at ~1 Ma isolated the NFBTJ from the FFZ and created the currently stable RRR (ridge-ridge-ridge) configuration. The rift-bounding faults on the NE limb are ~1 km high and expose back-arc crust older than 1 Ma, based on the spreading fabric and magnetic chrons (Martin, 2013). Huchon et al. (1994) concluded that NE limb is the slowest of the three limbs, with a narrow neovolcanic zone, 1 km wide and disappearing 43 km

from the centre of the triple junction. At its widest, the NE limb has produced about 23 km of back-arc crust, consistent with the initiation of spreading at 1 Ma and the full spreading rate of 18 mm/yr determined by Huchon et al. (1994).

The SW limb is at azimuth 195° and forms part of the boundary between the Conway Reef and New Hebrides microplates. The southern end is interpreted as an extension of a northward propagating spreading segment (deAlteriis et al., 1993). The propagator was initiated after magnetic anomaly 2 and before anomaly J, indicating an origin between 1.6 and 1 Ma (Ruellan et al., 1994 in Huchon et al., 1994). The southern termination is characterized by eastward-stepping ridge jumps that were initially considered to be spreading at 70-78 mm/yr (Chase, 1971; Malahoff et al., 1982). However, magnetic data suggest a full-spreading rate for the SW limb of 52 mm/yr (Huchon et al., 1994).

The NW limb of the triple junction, at azimuth of 330°, is a plate boundary segment between the New Hebrides and Balmoral Reef microplates. Rifting has been occurring at ~47 mm/yr (full-spreading rate) since at least 1.1 Ma (Huchon et al., 1994). However, we interpret that the current extension is mainly tectonic, dominated by faulting with only minor volcanism and seismicity (Figure 2.4; see below). The lack of seismicity is consistent with spreading in the northwest of the NFB being disabled when the connection was made between the triple junction and the FFZ (Ruellan and Lagabrielle, 2005).

2.4 Methods and Data

For this study, we compiled 10,000 km² of ship-based acoustic data over the NFBTJ, including Multibeam echosounder (MBES) and backscatter (reflectivity/adsorption), and compared these data with available magnetics and gravity, together with descriptions of geological samples and seabed observations from cruise reports and published sources. The data available for this study was acquired at global, regional and local scales and converted to common layers at 1:500,000 and overlain on an integrated digital elevation model (DEM) (Figure 2.3). Figure 2.3A is a regional-scale lineament map of large-scale ridges, faults and spreading axes underlain by bathymetric data from the Global Bathymetric Chart of the Oceans (GEBCO Compilation Group, 2021). Spreading fabrics (mostly ridge lineaments) are shown in grey, major faults, defined as faults with throws of >100 m, are in black, and spreading axes are in red. The three longest segments correspond to the limbs of the NFBTJ. Most of the spreading fabric (gray lines) mimics the three active spreading axes, except south of 19ºS and in the northeast of the map area, east of ~174.6 E.

The mapped region for this study and displayed at a local scale (1:500,000) in Figure 2.3B. The base map is from version 3.7 of the Global Multi-Resolution Topography Data Synthesis (GMRT) bathymetric grid (Ryan et al., 2009), providing coverage for areas without MBES. MBES data were collected during the RV *Southern Surveyor* (SS2012-02) and RV *Yokosuka* (YK06-02) cruises and are placed over the GMRT. The data from RV *Southern Surveyor* are gridded at a resolution of 30 m, while the RV *Yokosuka* data, which cover a larger area, are gridded at a lower resolution of 100 m. For further feature recognition, a slope raster and hill-shade raster calculation was preformed in ArcGIS, which is used to enhance structures and flow fields. The gray-scale image in Figure 2.3B shows shallow slopes in light gray and steep slopes in dark gray. Further structural lineament detail in Figure 2.3B is discussed below. Figure 2.3C is acoustic backscatter data collected during the SS2012-2 cruise. The relative backscatter strength is a proxy for sediment cover, surface roughness and surface hardness and provides some indirect information on relative ages and stratigraphic relationships. Areas of high reflectivity (light grey) are associated with recent faults and fresh volcanic flows such as the neovolcanic zone, and minor sediment accumulation. Areas of low reflectivity (dark grey) have thicker sediment cover and are older units.

Free-air and Bouguer gravity anomaly data and the vertical gravity gradient (VGG) are shown at a regional scale in Figure 2.4. Free-air gravity (Bonvalot et al., 2012) has a strong correlation with the topography (Figure 2.4A). The NW and NE limbs of the NFBTJ are bound by distinct positive Free-air anomalies (green lines) with local negative anomalies within rifted zones. The SW limb has a positive anomaly along the well-defined axial spreading ridge, this is flanked by a pair of low and high anomalies on either side that represent the rift and steep flanks of the SW limb. A positive free-air gravity anomaly connects the three limbs at the centre of the triple junction, which marks the topographic high of the central volcanic complex (CVC).

The Bouguer anomaly (Figure 2.4B) correlates with rock density and crustal thickness (Bonvalot et al., 2012). All three of the limbs and the CVC have generally low Bouguer gravity anomalies corresponding to increased crustal thickness, although parts of the NW limb are characterized by a positive Bouguer gravity anomaly consistent with extension and normal faulting (see below) in this part of the triple junction. The large area of low Bouguer gravity anomalies to the east of the triple junction correlates with large faults and thicker crust (Gràcia et al., 1996).

The vertical gravity gradient (VGG) derived from satellite altimetry (Sandwell et al., 2014) highlights large-scale variations in crustal structure (Figure 2.4C). The spreading axes are flanked by steep vertical gravity gradients (orange lines). Along the NW limb of the triple junction, the ~200 km-long gravity anomaly with steep vertical gravity gradients along the bounding faults. Unlike the other spreading axis, the SW limb is marked by a steep positive vertical gravity gradient (Figure 2.4C), consistent with the SW limb being the more active limb of the triple junction with an asymmetric profile (see below). Strong negative vertical gravity gradients are located along the NW and NE spreading centres.

Figure 2.5A shows magnetic data from the 2-arc minute resolution compilation, EMAG2 (Earth Magnetic Anomaly Grid: Maus et al., 2009), with broad magnetic lows corresponding to the three spreading axes of the NFBTJ and magnetic highs in at their centres. The SW limb is considered to be the most magmatically robust, supported by a strong magnetic high at its centres. Figure 2.5B, which is modified from Huchon et al. (1994), shows shipboard magnetic data profiles around the NFBTJ. The active spreading centres are represented by the red lines with two dominant spreading

centres identified by Huchon et al. (1994) in the NW and SW. The curved magnetic highs and lows to the west of the SW spreading axis correspond to the curved faults in this region (Figure 2.5A). The NW limb is bounded by magnetic anomalies; however, they are of unknown ages (orange lines). The SW spreading centre is flanked by three sets of anomalies; anomaly 'J' (1 Ma), anomaly '2' (1.65 to 2.10 Ma) and anomaly '2A' (2.45 to 3.40 Ma). Huchon et al. (1994) did not observe clear spreading anomalies in the NE limb. Figure 2.5C from Huchon et al. (1994), shows the more restricted data set corresponding to the geological map presented in this study. Crust formed within the last 1.1 Ma based on magnetic chrons is indicated by the "v" pattern, with the three active spreading axes of the NFBTJ marked by red lines. Anomaly J (yellow) and 2A (blue), corresponding to 1 Ma and 2.45-3.40 Ma, respectively, are also shown.

Teleseismic events from the Harvard Centroid Moment Tensor (CMT) catalogue (Dziewonski et al., 1981; Ekström et al., 2012) were used to investigate the type of faulting associated with the NFBTJ and adjacent structures (Figure 2.6). The CMTs represent the magnitude and direction of stress on the fault planes and are compared to mapped lineaments from our study. A total of 60 CMTs, with depths of <30 km, were identified in the study area using the ArcBeachball tool (v2.2) in ArcMap, following the method of Baxter et al. (2020). These results have been used to identify the locus of normal faulting and strike-slip faulting in the vicinity of the triple junction.

Using these data and comparisons with similar well-mapped areas of the seafloor at the same scale (e.g., 1:1,000,000 map of the Lau Basin presented by Stewart et al., 2022, and 1:500,000 maps of mid-ocean ridge spreading centres presented by Klischies et al., in prep), we isolated a variety of structures, different volcano types, and 10 different geological formations to create the geological map of the NFBTJ at 1:500,000 (Figure 2.7, Table 2.1). The approach and workflow are similar to remote predictive geological mapping (RPM) techniques used on land and are described in recent papers on submarine volcanic arcs (Anderson et al., 2016, 2017; Stewart et al., 2022) and mid-ocean ridges (Klischies et al., in prep). In these studies, geological legends were created by gathering units with similar properties, age, and origin and sorting them into distinct formations, taking into consideration the crust types (and thickness, where known), sequence of depositional events, the composition of different units, tectonic fabric and structure. In this way, for example, all of the crust of a particular age emanating from a single spreading centre is assigned to a single

formation. At the highest resolution of ship-based multibeam and backscatter, it is possible to precisely identify different volcanic and sedimentary units constrained by surface texture, acoustic reflectivity, slope breaks, and relative water depth. Common features included in the mapped formations are volcanic or tectonic ridges, mounds, discrete volcanoes, and volcanic flow fields. Correlation of units using geomorphological expression is standard practice in mapping young volcanic terranes on land (e.g., Thouret, 1999), and the superposition of units establishes key stratigraphic relationships. Complementary visual observations from towed cameras and submersibles have been compiled that provide important ground-truthing of rock types, lava morphologies and structure at the outcrop scale (see especially, *STARMER* 89 and *Yokosuka* 91 in Appendix A, Supplementary Figure 1: Gràcia et al., 1994).

Contacts between formations are based on mappable boundaries in high-precision digital elevation models (DEMs), supported by acoustic backscatter, and other geophysical data (magnetics, gravity). The contacts are drawn where a clear distinction with an adjacent formation can be made; they are interpolated between formations where a geomorphological or geophysical change is not evident. The contacts are interpreted to be conformable unless faults define them. All mapped faults are marked by narrow linear to curvilinear steps with a distinct change in relief; fault lines are drawn at the base of the fault scarps, which are identified by their high-intensity backscatter signatures. Ridges are defined by their bilateral symmetry with steep slopes on both sides. Volcanoes were outlined at the steepest inflection point nearest the base of their slopes.

The geological map is assembled as polyline and polygon shapefiles that are then combined into continuous layers to create Figure 2.7 (corresponding legend found in Table 2.1). Balanced (i.e., restorable) 3D sections of the NFBTJ map area were also produced in Surfer© (by Golden Software). Quantitative data on the mapped formations (e.g., polygon areas) have been compiled and used to derive additional information on the mapped units, such as volumes of specific magmatic features including ridges and volcanoes (e.g., calculated from measured heights or assumed unit thicknesses) that are summarized in Tables 2.2 and 2.3. Area calculations of formations exclude overlapping volcanoes.

2.5 Geological Map of the North Fiji Basin Triple Junction

The map legend for the NFBTJ (Table 2.1 and Figure 2.7) was modeled after the geological legend of the Lau Basin (Stewart et al., 2022). Individual formations were assigned based on inferred crust type, structure, magnetic character, spreading fabric, composition, age and sedimentary cover as defined in Stewart et al. (2022). Where appropriate, formations are subdivided into the "upper", "middle", and "lower" units based on the level of exposure and stratigraphic position. Stratigraphic relationships were determined, where possible, from the nature of the contacts between the units (e.g., lava flow fields erupted onto older faulted crust) and their spatial relationship to a volcanic source (e.g., distance from a spreading centre). This classification facilitates the correlation of units over larger areas, such as formations widely separated by seafloor spreading or other tectonic processes.

In the NFB, the mapped formations are grouped into two types: back-arc-rift and spreading- centre formations and relict back-arc crust formations. Crust that is dominated by back-arc rift and spreading centre formations occupies an area with a spreading fabric that can be demonstrably linked to a currently active spreading centre. The distinction between formation types is based on a clear change in the spreading fabric or the magnetic signature. Those dominated by relict back-arc formations are interpreted to have formed by rifting and seafloor spreading, but they have less well-defined spreading fabric; the associated spreading centres are either no longer preserved or cannot be identified. Commonly, the relict back-arc formations are in fault contact, for example indicated by discontinuities in the gravity gradient. Figure 2.4C is a schematic illustration of how different back-arc spreading centre formations and relict back-arc crust can be correlated across the map area.

2.5.1 Mapped formations

Ten formations have been mapped in detail as "training areas", where high-resolution data are available. These areas are used to extrapolate the geology into areas with lower resolution data but similar features (Figure 2.7 and Table 2.1). Sediments were not mapped as they are thin or absent

in most parts of the map area (<2 m thickness: Lagabrielle et al., 1994). Volcaniclastic material, where identified, is grouped with the associated coherent volcanic formations.

Axial back-arc crust (designated "upper" or uBac) has been mapped within the neovolcanic zones of the active spreading centres and typically covers the innermost rift valley floor. It consists of the eruptive products of recent spreading events, commonly from an axial volcanic high, cut by normal faults and ridges (with and without associated fissure volcanoes, Bav4, described below). Available backscatter data confirm that there is little to no sediment present on the upper formations. This formation type has been mapped within the SW limb and along sections of the NE graben, where it occupies the neovolcanic zones of the spreading centres, but it is absent along the tectonized axial valley floor of the NW limb. In the SW limb, this formation occupies a 4-km wide zone at the summit of the spreading ridge. In the NE limb, it occupies a graben-like feature only 1 km wide. Proximal back-arc crust, designated "middle" (mBac), is located outside the neovolcanic zones of the rifts but typically within the broader outer rift valleys (Figure 2.7 and see section ‘B’ in Figure 2.8). This type of crust is mostly undeformed, with little faulting, and moderately to lightly sedimented. It includes flows and volcaniclastic material that likely formed at the adjacent constructional ridge (mBar, described below) and dominates the flanks of the SW and NE limbs of the triple junction but is not present in the NW limb. Distal back-arc crust (designated "lower" or lBac) is located outside the rift valleys but adjacent to the axial spreading ridge. This crust is variably tectonized and commonly obscured by volcaniclastic and/or other sedimentary cover.

Axial volcanic ridges are locally dominated by voluminous constructional ridges (designated "upper", "middle" and "lower" back-arc ridges or uBar, mBar, and lBar) that are oriented parallel to the spreading axis and typically form the marginal highs of the neovolcanic zone. The "upper" back-arc ridges (uBar) are present along the SW limb closest to the Central Volcanic Complex of the triple junction (see below and section ‘A’ in Figure 2.8). Proximal ridges (designated "middle" or mBar) are located outside the neovolcanic zones but within the outer rift valley (see section ‘C’ in Figure 2.8). Distal ridges (designated "lower" or lBar) are located beyond the rift valley on older back-arc crust formed by off-axis volcanism or during an earlier episode of seafloor spreading (e.g., bounding the SW limbs rift valley) (see section ‘D’ in Figure 2.8). The volcanic ridges are

constructional features and include undivided flows and volcaniclastic material. They may have erupted from dikes that intrude the spreading axis or they are products of flank eruptions. The distal back-arc ridges (lBar) are increasingly faulted with distance from the neovolcanic zone and are commonly irregularly shaped blocks with low backscatter intensities; they may be bound by large scarps that are subparallel to the actively spreading segments. Their lower flanks are typically smoother than the younger ridges due to sediment cover. Some distal back-arc ridges may be tilted fault blocks that have exposed older crust and may be entirely non-volcanic (i.e., products of rifting of earlier back-arc crust, such as early NS spreading of the CSR).

The centre of the triple junction at the north end of the SW limb is dominated by a back-arc ridge (uBar) that is split by the neovolcanic zone and partly obscured by a large shield volcano at the intersection of the SW limb and the NE graben. The volcanic high is an inflated portion of the proximal volcanic ridge (mBar) and comprises several large coalesced edifices that extend along the SW limb. Together with the large back-arc volcanic field in the north, the shield volcano and the volcanic high comprise the Central Volcanic Complex of the triple junction, the largest volcanic centre in the NFB.

Relict back-arc crust, which is interpreted to have formed at a back-arc spreading ridge but is now located outside an identifiable area of active spreading, occurs throughout the map area. It generally has a smooth seafloor expression with poorly developed spreading fabric and scattered volcanoes. This crust is divided into "upper" (uRbc1) and "lower" (lRbc1) formations where the older crust is exposed by rifting (e.g., in the east-to-west transition from active back-arc crust to the relict crust adjacent to the SW spreading centre). It includes flows and volcaniclastic material that likely formed at a spreading ridge that can no longer be identified. Relict back-arc crust dominates the NW limb of the triple junction but is present only at the distal outer margins of the NE limb. In some areas, the relict back-arc crust has been intensely deformed and the tectonized crust is broken out as separate formations (i.e., tectonized relict back-arc crust, uRbc2 and lRbc2, especially in the faulted relict valley floor of the NW limb). Steep fault scarps, up to 1 km high, commonly expose upper and lower relict back-arc crust, which may be juxtaposed to actively spreading or recently active crust (e.g., adjacent to the NE limb), whereas broad extensional zones expose the relict back-arc crust along the NW limb. Large structures located ~25 km and 11 km

from the SW and NE limb, respectively, expose relict back-arc crust on normal faults that are at least ~400 m high. Based on the current spreading rates along the SW and NE limbs, this crust is at least 1.2 Ma old.

2.5.2 Volcanoes

Four different volcano types were identified in the map area: conical volcanos (Bav1), shield volcanoes (Bav2), dome volcanoes (Bav3), and fissure volcanoes (Bav4), following the classification of Stewart et al. (2022). Only those with a diameter >200 m were mapped. Caldera-like features, consisting of summit depressions and collapsed features >1 km in diameter, are uncommon (found on only one volcano at the centre of the triple junction. Smaller depressions and collapsed features < 1 km, referred to as summit craters, occur on 22 volcanoes. The conical volcanoes (Bav1), which are common on all formations, are steep-sided, cone-shaped edifices with a width:height ratio of ≤ 5:1. The average height is approximately 200 m. They may have a summit crater and commonly are cut by dike-like features. Many of the cones have radial ridges extending outward from the summits, reflecting a homogeneous or broadly isotropic stress field. The dome volcanoes (Bav3) are also present on all formations; they are generally smaller than the conical volcanoes, with an aspect ratio in plan view of 1:1 and heights of ~100 m. The fissure volcanoes (Bav4) are elongate edifices, >1 km in length and with a length:width ratio >3:1, typically with a prominent ridge that may be an exposed central dike and often with centrally located cinder cones. The average height is approximately 200 m. They are common on relict back-arc crust, where they occur in large areas of flows and volcaniclastic rocks (designated back-arc volcanic fields or Bavf, see below). Only one shield volcano (Bav2) was mapped at the summit of the Central Volcanic Complex (CVC). It has a gentle slope, width: height:ratio of ≥5:1, is 500 m high.

The large shield volcano at the summit of the CVC dominates the axial volcanic high (uBar) of the SW ridge. It is 11 km long by 7.5 km wide, and 0.5 km high and flanked by the large volcanic field (Bavf) to the north. This inflated crust is split by the 900-m wide neovolcanic zone of the SW ridge, which crosses the summit of the shield and extends 2 to 3 km onto the volcano's northern flank. A ~2 km-diameter caldera has formed at the summit, and the northern and southern rims of the caldera are cut by the extensional faults traversing the shield (Figure 2.9). A closer view of the

backscatter data in Figure 2.9B shows, of the lower reflectivity (darker/older) of the caldera rim cut by the more reflective (younger) spreading axis of the SW limb. The volcanic flow field (Bavf) emanating from the shield extends at least 25 km from the summit and partially covers the NE rift axis, but there is clear evidence of continuous rifting of the flow field along strike with the NE rift. The steep slopes partly control the bifurcation of the volcanic flow field toward the north, with high elevations in the south (uBar) encouraging flow into the NE and NW limbs. The flow field boundaries are clearly visible in Figure 2.9A and C, and the full extent of the flow field boundaries (purple) is shown in Figure 2.10. Our mapping confirms that the flows are cut by the narrow neovolcanic zone (uBac) of the NE limb but overlap the extensional fabric of the NW limb.

2.5.3 Mapped structures

Lineament mapping was carried out on the slope-shaded relief map of the study area (see Figure 2.3B). A total of 1036 lineaments were mapped (Figure 2.10), including faults, ridges, calderas rims, summit craters and flow field boundaries. 560 faults were mapped, including 108 major faults with throws of >100 m and average lengths of ~5 km. The majority of the mapped faults are normal faults identified by block tilting, with fault lines drawn on the hanging wall at the base of normal fault scarps. The largest faults are up to 30 km in length, with throws reaching up to ~500 m. Minor faults, classified by throws of less than 100 m, are 2.5 km in length on average but range from under 100 m up to 11 km long. A large number of ridge-like features (n=437) also were mapped. They are represented as distinct lineaments but may be either structural or volcanic in origin; they have an average length of 1.5 km and reach up to 9.4 km in length.

Three dominant fault orientations are identified among the 560 mapped faults: 335º, 195º, and 050º, in order of decreasing abundance and corresponding to the different spreading fabrics of the SW, NE, and NW limbs. More than 16% of the identified faults have orientations of between 190º and 201º, with an average of 195º, closely matching the orientation of the SW limb of the triple junction. 6% of the identified faults have orientations between 045º and 061º, with an average of 057º, closely matching the orientation of the NE limb of the triple junction. 17% of the identified faults have orientations between 330º and 341º, with an average of 335º, closely matching the orientation of the NW limb. The largest faults (n=108) have the same orientations (340º, 200º, and

045°: Figure 2.10). A detailed analysis of 218 faults within the spreading centre formations is shown in Figure 2.11; they have orientations of 195° in the SW limb (red), 055° in the NE limb (blue) and 335° in the NW limb (green). About 130 faults in the relict arc crust have more variable orientations ranging from 015° to 045°; a smaller number (n=71) have orientations of 145° to 160° corresponding to the early NW spreading prior to 3 Ma. The 440 volcanic ridges and other tectonic features have orientations from 140° to 240° that reflect a combination of crustal age and regional stresses (Figure 2.10).

The lack of large-scale transcurrent faulting within the map area is consistent with the stable RRR configuration of the triple junction (discussion). However, the curvature of some of the older fabric east of the SW limb may indicate a progressive change in spreading in the early stages of formation of the triple junction (e.g., rift jump or overlapping spreading centre). At least two distinct reorientations of the pre-NFBTJ spreading centres can be inferred from the NNE- and NE-trending fabrics of the relict back-arc crust in the map area and are discussed below.

2.5.4 Hydrothermal activity

All known hydrothermal vents in the NFBTJ are located within the axial back-arc crust (uBac) of the SW ridge on the Central Volcanic Complex (Figure 2.9D, Table 2.4). They extend up to 6 km south of the summit caldera in three areas: the northern, central and southern domains mapped during two cruises (*STARMER* 89 and *Yokosuka* 91: Gràcia et al., 1994). The hydrothermally active areas are characterized by similar volcanic facies, including pillow basalts, lava lakes, and massive flows. Complementary visual observations from of towed cameras and submersibles recorded by Bendel et al. (1993) have been compiled that provide important ground-truthing of rock types, lava morphologies and structure at the outcrop scale (Appendix A, Supplementary Figure 1).

The northernmost vents belong to the extensive (4 km^2) 'Le Pere Lachaise' hydrothermal system. The central hydrothermal field contains the 'White Lady' and 'STARMER II' vents that have developed on older hydrothermal deposits, associated with recent fissuring along the neovolcanic zone (Gràcia et al. 1994). The southern domain consists of mostly fossil hydrothermal vent sites

associated with tectonism along the bounding faults of the axial graben and decreasing volcanic activity further north. The current high-heat flow, intense faulting, and enhanced crustal-scale permeability on the SW limb suggest that hydrothermal activity will continue here. So far, the NW and NE limbs of the triple junction are not known to contain hydrothermal deposits. The caldera of the central volcanic shield (Bav2) would seem to be a logical location of hydrothermal venting due to high heat and ponded lavas, however, no vent sites have been located within the caldera. Any vents may have been buried by lava filling the crater.

2.6. Discussion

Larger-scale magnetic surveys (Tarling, 1967; Luyendyk et al., 1974; James and Favey, 1978; Malahoff et al., 1982 and 1994; Tanahashi et al., 1991; Joshima et al., 1994; Huchon et al., 1994) and GLORIA side-scan sonar imagery (Tiffin et al., 1989; Jarvis et al., 1991; Jarvis and Kroenke, 1993) reveal a long history of plate reorientations and changes in spreading rates in the region that coincided with the formation of the triple junction (e.g., Malahoff et al., 1994). Ship-based magnetic data confirm that the NFB has opened in several stages with different seafloor-spreading directions. Kellogg and Kansakar (1994) examined the regional gravity field and magnetic fields along the South Pandora Ridge (now Hazel Holmes), indicating a slow-spreading ridge at that location early in the history of opening of the basin. Heat flow measurements (Sclater and Menard, 1967; Wantanabe et al., 1977: Lagabrielle et al., 1997), seismic surveys and tomographic models (Skyes et al., 1969; Dubois et al., 1973; Barazangi et al., 1974; Tanahashi et al., 1991; Kisimoto et al., 1994; Van der Hilst et al., 1997; Conder et al., 2002; Hall and Spakman 2002; Amaru, 2007), and petrology (Gill, 1970; Colley and Warden, 1974; Oh et al., 2021) support a general model for basin opening influenced by mantle upwelling. Large areas of low density and low velocity under the NFB, inferred from seismic surveys, have been interpreted in terms of high mantle temperatures (Wiens et al., 2006) and correlate with regional isostatic anomalies identified by Zhang and Pysklywec (2006). The depth to the Moho was calculated by Tanahashi et al. (1991) through refraction waves and defined a ~ 3 km depth. Inflation caused by rising mantle material beneath the basin and the abnormally hot upper mantle at the centre of the NFB have contributed to voluminous mafic volcanism. In the more recent history of the basin, when the westward propagation of the Fiji Fracture Zone (FFZ) intercepted the already established SW spreading centre between ~3 Ma and 1.5 Ma, voluminous mafic magmatism was focused into the NFBTJ. Gracia et al. (1996) interpreted gravity anomalies under the triple junction and along several ridge segments to be due to mantle upwelling. Tanahashi et al. (1991) suggested the current configuration to have been in place for the last 0.5 to 1 Myr and based on magnetics chrons.

The 1:500,000 scale geological map of the NFBTJ highlights the features that have resulted from this history and can be analyzed quantitatively in terms of crustal growth and regional kinematics. The sequence of plate adjustments leading to the formation of the triple junction is summarized in

Figure 2.2, modified from previous interpretations of Chase (1971), Malahoff et al. (1982), Tanahashi et al. (1991), deAlteriis et al. (1993), Auzende et al. (1994), Huchon et al. (1994), Martin (1994), Ruellan and Lagabrielle (2005) and Heidbach et al. (2016). These events are illustrated in a palinspastic map reconstructions further below in Figures 2.12, beginning with the early emergence of the SW limb and axial volcanic high and shield volcano at the centre of the triple junction, followed by the appearance of the NE spreading centre where the FFZ first intersected the advancing SW limb. The NW rift, which is interpreted to have been an early structure, is currently undergoing mainly tectonic extension. Balanced (i.e., restorable) 3D sections (Figure 2.13) are used to show the relationship of the major structures to the inferred stratigraphic units.

2.6.1 Rates of Crustal Growth

The geological map provides a means of estimating rates of crustal growth from area-age relationships of the mapped formations. The cumulative areas for the different formations are calculated and presented in Table 2.3. The back-arc crust of the NFBTJ that can be attributed to crustal growth since the emergence of the triple junction occupies an area of 3,159 km^2 (Table 2.3) and influences at least 172 km strike length of the plate boundaries between the New Hebrides plate in the west and the Balmoral and Conway Reef plates in the east. Crust that can be assigned to the NFBTJ is clearly identified from the spreading fabric. The relict back-arc crust surrounding the NFBTJ has a dramatically different fabric that cannot be related to the presently active spreading centres. The evolution of the triple junction can be assigned to multiple stages of crustal growth since the intersection of the three active limbs at ~1.9 Ma and the initiation of a RRR-type triple junction at ~1.1 Ma (Figure 2.14).

Relict back-arc crust occupies most of the mapped area (72%). This crust formed during an earlier stage of basin opening in the centre of the NFB, possibly at different spreading centres or the same spreading centres prior to ridge reorientation and the emergence of the triple junction (i.e., a combination of the CSR and the SW limb of the NFBTJ: Jarvis et al., 1991). Where present the fabric is oblique to the presently-active SW limb of the triple junction and nearly orthogonal to the NE limb (e.g., as seen in lRbc1 on the Conway Reef Plate: Figure 2.9C). This is most reasonably interpreted as being related to the early N-S propagating rifts in the centre of the NFB at the

beginning of basin opening. The tectonic fabric of this crust has been identified in this study as the oldest of the triple junction.

The largest areas of tectonized lower relict back-arc crust (lRbc2) are associated with the NW limb and, to a lesser extent, the NE limb of the triple junction. Although the NW limb is thought to have opened at a rate of 47 mm/yr (Huchon et al., 1994), the rifting is purely extensional with negligible magmatism. This is consistent with the very few flows interpreted from GLORIA sidescan data (Jarvis et al., 1991) and with the model of spreading in the northwest being disabled from the time the connection was made between the triple junction and the FFZ (Ruellan and Lagabrielle, 2005). Tanahashi et al. (1991) interpreted the NW limb to be starved of magma and spreading obliquely. Our interpretation is that little, or no new crust has been produced in the NW limb since 1.1 Ma, although it remains unclear whether opening at 47 mm/yr could have been occurring for this time without producing new crust. Another possible explanation is that the 47 mm/yr rate is a relict spreading rate from the early opening of the basin and it has since slowed following the connection to the FFZ.

The oldest spreading- centre formations of the NFBTJ are the lower back-arc crust (lBac), which is found furthest from the actively spreading limbs (up to 5 km from the flank of the NE limb and 10 km from the lower flank of the SW limb, covering a combined area of 660 km^2). These distances, taking into account the slow spreading rate of the NE limb, correspond to a spreading age of ~500,000 yr. The young age of the 'lower' back-arc crust (i.e., >0.5 Myr) suggests that there was as much as ~1.4 Myr of rifting in the initial stages of triple junction formation before new back-arc crust began to form by active spreading, assuming the initiation of the triple junction at ~1.9 Ma. This age for the initiation of rifting corresponds closely to the width of the rift valley of the NE limb and its inferred opening rate of 18 mm/yr at ~1 Ma. An abundance of tectonized back-arc crust along the west side of NE limb highlights the intense faulting that must have occurred at the initiation of the triple junction. This early rifting stage is also reflected in the highly tectonized crust on the west side of the SW limb. The rift valley of the NW limb, which is mainly occupied by relict back-arc crust (lRbc) and lacks any new back-arc crust, covers 426 km^2, and is about 50 km wide, recording ~1 Myr of rifting without producing new crust (Huchon et al., 1994).

Proximal back-arc crust (mBac) occurs within the NE and SW limbs covering just over 5% of the mapped surface area. Growth of mBac along the NE limb took place between 0.83 Ma and 0.39 Ma and covers 37% (228 km^2) of the NE limb. The SW limb experienced growth of mBac between 0.75 Ma and 0.55 Ma, this crust covers 15% (388 km^2) of the SW limb (Table 2.5 and 2.6). The growth rate of mBac along the SW limb (1,997 m^2/yr) was more than 7X faster than that of the NE limb (275 m^2/yr).

The back-arc rift and spreading centre formation (uBac) that occupies the neovolcanic zone of the SW limb and parts of the NE graben accounts for 5% of all of the back-arc crust in the SW limb, 4% in the NE limb and none in the NW limb (Table 2.5). In the SW limb, uBac occupies up to a 4-km wide zone of the spreading ridge and extends ~74 km to the SW along the spreading axis and covers ~1,900 km^2 (Table 2.5). In the NE limb, it occupies a graben-like feature only 1 km wide that can be mapped continuously for more than 67 km from the intersection with the SW and NW limbs. This amount of crust would have taken ~1 Myr to form at a full-spreading rate of 18 mm/yr in the NE limb and 52 mm/yr in the SW limb (Huchon et al., 1994) and represents an active pulse of crustal growth. The youngest crust (uBac) that formed at the intersection of the triple junction is partly obscured by the large volcanic field (Bavf) emanating from the shield volcano (Bav2) see Figure 2.9C. However, the dominant fabric appears to be north-northeast and continuous with the NE limb of the triple junction (Figure 2.9). Lava flows of the volcanic field emanating from the Central Volcanic Complex cover an area of 431 km^2 (Table 2.5) and are older than the narrow neovolcanic zone of the NE limb but younger than the NW limb, which they overlap. The 1-km wide neovolcanic zone of the NE limb that cuts the Bavf is at least 60,000 years old (based on a full-spreading rate on the NE limb of 18 mm/yr), which corresponds to a minimum age of the rifted lava field.

Using the spreading ages of the formations and their mapped areas (Table 2.6), it is possible to derive a growth (area-age) curve for the NFBTJ (Figure 2.14). A fixed spreading rate is used for all formations of a limb to estimate growth rates through time. Spreading ages are calculated using the average width of the mapped formations and the spreading rates from Huchon et al. (1994). The calculated spreading ages agree well with independently determined ages of the formations based on magnetic chrons (Huchon et al., 1994) and therefore are used here to illustrate crustal

growth. Cumulative area (km^2) is plotted against age (Myr) and crustal growth is represented by the slope of the curve (m^2/yr), with the growth of each limb plotted individually. The NE limb marks the beginning of crustal accretion at 1.39 Ma. It is spreading at a slow (full-spreading) rate of 18 mm/yr (Huchon et al., 1994) with growth rates from 196 m^2/yr during the accretion of distal back-arc crust (lBac) up to 400 m^2/yr during the accretion of axial back-arc volcanic crust (uBac). Crustal accumulation in the SW limb began at 0.97 Ma, at an intermediate (full-spreading) rate of 52 mm/yr (Huchon et al., 1994). The fastest crustal growth rate in the SW limb was 2,715 m^2/yr during the formation of proximal back-arc crust (mBar). Due to its faster growth rate, the SW limb surpassed the NE limb in crustal abundance at approximately 0.78 Ma (Figure 2.14). No back-arc rifts and spreading centre crust was mapped along the NW limb, therefore rifting is proposed for the dominant form of extension since ~1.1 Ma.

In addition to crustal accretion along the limbs a significant proportion of anomalous volcanism is represented by the central volcanic centre (CVC) consisting of the shield volcano (Bav2) and the axial back-arc volcanic ridge (uBar). It is located at the northern termination of the SW limb. Growth rates are relatively consistent for each mapped unit throughout their crustal growth history, from ~1,700 to 2,700 m^2/yr in the SW limb, and 200 to 400 m^2/yr in the NE limb, but there is an increase of the crustal accretion rate along the NE limb at 0.4 Ma. Huchon et al. (1994) suggested that the initiation age of the current configuration of the NFBTJ was 1.1 Ma. By applying the same spreading rates as Huchon et al. (1994), we calculate that the cumulative mapped area of the NE limb would have taken ~1.4 Myr to form. Therefore the transition from RRF- to RRR-type was between 1.4 and 1.1 Ma. However, it is unclear that previously published spreading rates are representative of the current extensional regime. For example, if average spreading rates have decreased (as suggested for the NW limb), then the initiation age would be older.

2.6.2 Magmatic Productivity

The volume of new crust formed at the NFBTJ since 1.1 Ma correlates with the significant inflation of the crust and the bathymetric anomaly in the area of the triple junction. The regional geophysical data support an anomalous mantle beneath the NFB that may account for the volume of melt. The SW limb is dominated by the Central Volcanic Complex (CVC), which forms a distinct bulge in

the crust near the centre of the triple junction, consisting of the axial back-arc volcanic ridge (uBar), the shield volcano (Bav2) and the associated large volcanic flow feild (Bavf). We estimate the total uBar in the CVC amounts to 64 km^3, with the large volcanic flow field and shield volcano contributing an additional 225 km^3 (210 km^3 and 15 km^3, respectively: Table 2.5). The total volume of CVC is nearly 300 km^3 is significantly larger than the total crust formation along a comparable ~35 km length of the CSR (~140 km^3 formed in 1 Myr, based on crustal production at the current full-spreading rate of 80 mm/yr, after Ruellan and Lagabrielle, 2005, and a ridge height of 500 m). These crustal volumes within a 100-km radius of the triple junction are compared with other global triple junctions in Chapter 3.

The volume of the CVC exceeds that of some of the largest back-arc volcanoes in the oceans (e.g., ~67 km^3 Niuatahi volcano in the NE Lau Basin, with a 7 km radius and height of 1.3 km: Anderson et al., 2021; ~126 km^3 Nifonea axial volcanic in the nearby Coriolis Troughs: Anderson et al., 2016). The most recent volcanic output from the CVC is the volcanic flow field that covers the volcano's northern flank and has a volume of 209 km^3 and a surface area of 431 km^2 (Tables 2.2 and 2.5), representing about 10% of the total magmatic budget of the NBFTJ since 1.1 Ma (Figure 2.14, Table 2.2 and 2.5). The large flow field is comparable to the eruptive volumes of some of the largest recorded submarine flood basalt eruptions (581 km^2 flow field off the flank of the Nifonea axial volcano: Anderson et al., 2016). The 11 x 7.5 km shield volcano is of a size that could harbour a subvolcanic magma chamber on the order of ~15 km^3 (see Table 2.5, for polygon volumes), similar to those recently documented beneath other large oceanic shield volcanoes (18-30 km^3 estimated for Axial volcano along the Juan de Fuca Ridge: Arnulf et al., 2014). The distinctive 2-km diameter caldera on the shield appears to have formed by the retreat of 0.54 km^3 of magma from the summit (Table 2.5).

We estimate that eruption rates at the centre of the NFBTJ have been on the order of 1.4 x 10^6 m^3/yr, encompassing all crustal formations and the shield volcano and its eruptive products (uBar+uBac+mBar+mBac+lBac+Bav2+Bavf) that formed over the last 1 Myr. By comparison, eruption rates along 100 km of the CSR prior to the emergence of the triple junction are estimated to have been on the order of 0.8 x 10^6 m^3/yr. In addition to regional inflation, mantle upwelling, and high heat flow, the recent voluminous mafic magmatism of the NFBTJ resulted in a significant

increase in the supply of melt to the rift axis (e.g., Georgen and Lin, 2002). Tectonic focusing of magma is also common in other slow to intermediate-rate spreading centres in back-arc settings, such as the Nifonea axial volcano (Anderson et al., 2016). The enhanced magmatism is also likely a contributing factor in the location of the hydrothermal activity in the NFB (Bendel et al., 1993; Gracia et al., 1994; Khun et al., 2003).

The total volume of back-arc volcanoes superimposed on the NFBTJ crust (excluding the Bavf) is ~76 km^3 (Table 2.2). The abundance of small volcanoes likely reflects the same high heat flow and crustal permeability of the triple junction that promoted the growth of the large Central Volcanic Complex. Although the volcanic centres are individually small, they account for a significant part of the total magmatic output. However, the relatively few fissure volcanoes contrasts with the NE Lau Basin, where strong microplate rotation causes widespread oblique rifting, and the differential stresses and abundant strike-slip adjustments lead to extensive fissure-type eruptions (Anderson et al., 2020; Baxter et al., 2020; Stewart et al., 2022). In contrast the stress regime of a stable triple junction favours normal faulting in multiple directions thus providing more focused pathways for melts to reach the surface.

In the north, the triple junction is flanked by steep (up to 1-km high) outer walls that expose the relict back-arc crust (uRbc and lRbc) formed during an earlier stage of opening of the basin between 3 and 2 Ma. Locally thickened crust is suggested by the height of the scarps bounding the spreading segments and documented in seismic lines of the KAIYO87 expeditions (see Appendix A, Supplementary Figure 2; Tanahashi et al., 1991). As the throw of normal faults generally scale with the thickness of the crust (e.g., Rowland and Simmons, 2012), we suggest that the back-arc crust attained its greatest thickness at the original centre of the triple junction. If so, the thickened crust could retain heat and melt and allow for the emplacement of large magma chambers, with implications for local magmatic productivity. Figure 2.12 reflects this mechanism, as the limbs open via rifting of uRbc2 which is suggested to be a large relict volcanic feature formed along durring stage 1, NW-SE orientation of spreading. A conspicuous line of volcanos (Bav4) southeast of the triple junction may be located along a pre-existing structure of this type on the Conway Reef microplate, although large-scale basement structures have not been identified in the gravity or magnetics.

2.6.3 Structure and Kinematics

The geological map of the NFBTJ suggests a complicated history of rifting and spreading encompassing the magmatically robust SW limb and axial volcanic high at the centre of the triple junction, the emerging NE spreading centre, and the NW rift, which is currently undergoing mainly tectonic extension. The sequence of large-scale plate adjustments leading to this configuration is summarized in Figure 2.2; the local events are shown in Figure 2.12. Figure 2.2 summarizes the kinematic evolution of the NFB over the last 12 Ma. The opening of the NFB occurred in three stages of spreading. The first stage of spreading occurred in a NE-SW orientation from 12-7 Ma, the second stage occurred in an N-S orientation from 7-3 Ma and the third stage in an E-W orientation between 3 Ma to the present day (Ruellan and Lagabrielle, 2005). From 12-7 Ma, the spreading centres formed behind the nascent New Hebrides Arc (NE-SW). The NE-SW spreading subparallel to the arc was driven by the rollback of the Indo-Australian plate (Auzende et al., 1995; Ruellan and Lagabrielle, 2005; Martin, 2013). Between 7 and 3 Ma there was N-S spreading along the South Pandora and Tripartite ridges, based on the orientation of the trench at that time (Ruellan and Lagabrielle, 2005). No spreading fabrics from the N-S spreading were identified in the NFBTJ during this study, as these fabrics are confined to the north of the triple junction, and outside the mapped region. The third, currently active stage includes spreading and extension along the CSR. This spreading is orientated E-W. Between 1 Ma and the present, the triple junction was reconfigured from FRR- to a RRR-type triple junction.

The kinematic history for the last 3.5 Myr, based on the geological map presented here, is outlined in a palinspastic map reconstruction in Figure 2.12. This figure recreates the evolution of the NFBTJ using the geological formations compiled in Figure 2.7. The simplified lineaments shown in in Figure 2.12 are approximations of the fabrics in Figure 2.10. NW-SE fabrics are captured in all time panels (pre 3.5 Ma to present day) and originated during phase 1. These lineaments are orientated 335º and are restricted to relict back-arc crust (lRbc1 and uRbc2). In phase 2 (3.5 Ma) the CSR is a propagating rift with E-W spreading (Auzende et al., 1995). The fabric formed during this phase is still preserved in relict back-arc crust (uRbc1) but is heavily overprinted in the tectonized relict back-arc crust (lRbc2).

A RRF-type triple junction formed by 1.9 Ma. Lineaments formed during phase 2 from the propagating CSR intersected the phase 1 NW rifting at about the same time the Fiji Fracture Zone (FFZ) arrived at the triple junction. Between 1.9 and 1.1 Ma, the NE limb began to open and continued to be heavily influenced by the FFZ and associated transform faults. Back-arc ridges (lBar) initially formed at a southern limb during phase 2 were rotated into their current position as the SW limb. This process formed additional tectonized relict back-arc crust (lRbc2). By 1.1 Ma (phase 3) the transition from a RRF- to a RRR- type triple junction, and the 195° re-orientation of the SW limb was complete. No new crust is thought to have originated from the NW limb after this time. The transition from phase 1 to phase 3 is marked by the active opening rate of 47 mm/yr along the NW limb (Huchon et al., 1994).

After 1.1 Ma the structures from phase 3 were still active in all three limbs, and according to Huchon et al. (1994) they have remained active since that time. The NW limb oriented at 335° is tectonically controlled but is thought to have had a full spreading rate of 47 mm/yr. The NE limb orientated at 055° had a full spreading rate of 18 mm/yr (Huchon et al., 1994), and the structure is well preserved in the back-arc rift and spreading centre crusts. The SW limb oriented at 195° had the most complex history, preserving deformed phase 2 and phase 3 structures in the back-arc rifts and spreading centres crusts. Phase 2 structures are only present in the SW limb in lBar, uRbc1 and lRbc2. Due to the deformation of phase 2 structures during the reconfiguration between 1.9 and 1.1 Ma the lineament in these formations are notably curved with orientations ranging from ~010° to 065°.

Three rose-diagrams are inset in Figure 2.10 to show the major and minor faults in black and the ridges in gold. The orientations of the major faults are in to three main groups (phase 1 and phase 3 structures) corresponding to the orientations of the NW, SW and NE limbs, respectively 330°, 195/015°, and 050°. Fault and ridge segments in the relict back-arc crusts outside of the SW limb have distant 335° phase 1 orientations (Figure 2.12). These are all early fabrics that are associated with the last 3.5 Ma. Faults with orientations of 195° are restricted to the fabric identified in phase 3 within the back-arc rift and spreading centre crust of the SW limb. A few faults have orientation of ~050°, corresponding to phase 3 fabrics.

The shallow (<30 km) teleseismic events compiled in Figure 2.6 indicate that strike-slip faulting is still occurring in the east of the map area, whereas extensional faults occur in the northwest. There is a mixture of extension and strike-slip faulting in the NE limb but only extensional faulting in the NW. The presence of strike-slip faults in the NE limb suggests that there is an oblique compent to the active spreading. The lack of recorded seismicity along the SW arm could be explained by the lower limit of Mw > 5 for earthquakes contained in the GlobalCMT database. This may not capture many smaller Mw earthquakes, which are typical in faster spreading regimes (Eguchi et al., 1989; Conder & Wiens, 2011). Only strike-slip faults in the NE limb indicate that the FFZ continues to influence the stress regime in this region.

The NFBTJ was initiated as a RRF-type triple junction at 1.9 Ma. York (1973) confirmed this original configuration would have been unstable because the NW and SW ridges are 118º apart and, therefore, outside the proposed stability range (90º +/- 10º). In the model of York (1973), a stable FRR-type configuration requires that the two ridges have perpendicular bisectors that intersect at the same point as the bisector of the fault. This configuration persisted until 1.1 Ma when spreading began at the NE limb. The resulting change to RRR-type was a step toward a more stable configuration (McKenzie and Morgan, 1969; York, 1973; Cox and Hart, 1986; Cronin, 1992). To test the stability of the NFBTJ three methods were used in this study: a regional scale stability approach using the global plate model MORVEL56 (Argus et al., 2011), the McKenzie and Morgan-type vector stability diagram, and a simple vector addition of the E-W extension (Figure 2.15). The relative motions for each of the three plate-pairs at the NFBTJ are shown in Figure 2.15A. This method uses absolute motions in the MORVEL56 reference frame for the New Hebrides, Balmoral Reef and Conway Reef microplates. The relative motions are graphically as vector additions, with vectors in stable configurations intersecting within the velocity space of the three plates. Instead, the data for the the New Hebrides, Balmoral Reef and Conway Reef microplates indicate an unstable configuration as the vectors (dotted lines) for each pair of plate boundaries (solid line) do not intersect within the graph. The instability is caused by a high rate of spreading on the NW limb is also suggested by the MORVEL plate-motion calculator (Figure 2.15A).

The second approach uses spreading ridge orientations and spreading rates to determine if the triple junction is stable (McKenzie and Morgan-type stability diagram, Figure 2.15B). The magnitudes of the vectors are based on half-spreading rates from Huchon et al. (1994): 23.5 mm/yr (NW limb), 9 mm/yr (NE limb) and 26 mm/yr (SW limb). The perpendicular bisectors of the vectors intersect within the vector triangle; however, the vectors for the 3 limbs do not completely close, suggesting that the spreading rates proposed by Huchon et al. (1994), particularly for the NW limb, may need to be reassessed. We suggest that the spreading rate proposed for the NW limb may be greater than the current rate of opening and a shortened vector for this limb along with a faster spreading rate for the NE limb would result in a stable vector triangle. The calculations are for ridge-perpendicular extension, but a component of shear on any of the limbs, such as the NE limb which is continuous with the FFZ, could account for the instability.

A third approach to determine the stability of the triple junction is to compare the E-W component of extension for the northern limbs with the southern limb. In this case, the component of E-W extension on the two northern limbs roughly matches the E-W extension on the SW limb, although the history of extension on the NW limb remains uncertain (Figure 2.15C). To gain a better perspective on the NFBTJ stability, higher resolution magnetic surveys of the region are needed to establish spreading rates. Huchon et al. (1994) mentioned the possibility that the NW could be spreading obliquely, however, no evidence was found for such oblique spreading in the mappable structures of the NW limb.

To determine if the triple junction is stable, a velocity triangle is presented in Figure 2.15. This assumes that spreading is orthogonal on all three limbs. This assumption is necessary due to the lack of short transform segments in the region, which are used to determine relative plate motion, However, there is evidence from the CMTs (Figure 2.6) that a significant component of oblique extension may be occurring in the NE arm, which should be acknowledged as a source of uncertainty in the calculation. A second source of uncertainty is the spreading rates for the three arms of the triple junction. Only one of these, for the SW arm was calculated using magnetic anomalies. The other two, for the NW and NE arms, are predicted, assuming that the triple junction is stable (Huchon et al., 1994). Additional magnetic data should be collected to test the predicted spreading rates, as the geological mapping presented here suggests that extension is occurring at a

much lower rate in the NW arm in particular. Based on the results of the velocity triangles, the NFBTJ is undergoing constant readjustment, in response to micro-plate reorganization within a dynamic back-arc setting (e.g., double saloon-door model). The triple junction may experience further adjustments, such as the abandonment of limbs, as the NFB continues to extend.

Taking into consideration the location of the J magnetic anomalies (e.g., Martin, 2013), the NW limb is either very fast or very old (large distance to the J anomaly). Burke and Dewey (1973) previously interpreted the NW limb to be in a pre-spreading phase, whereas LaFoy et al. (1990) considered it to reactivate the early NW-SE spreading centre of the NFB, which was present at 4 to 3 Myr. Huchon et al. (1994) and Auzende et al. (1995) considered the NW limb to be a spreading segment of the triple junction that has been abandoned in favour of the NE graben. This study shows that it is very old. The NW limb has a very different geological character than the SW or NE limbs and most likely has been in a non-magmatic rifting state for at least the last 1.1 million years, whereas the SW limb and NE limb are actively generating new back-arc crust. If the NW limb was spreading at 47 mm/yr, it would imply that the entire width of the lRbc2 (~10 km) took only 0.2 Myr to form, which is much faster than suggested by the present reconstruction. As suggested above, a likely explanation is that the 47 mm/yr rate is a relict spreading rate from the early opening of the basin, and it has since slowed following the connection to the FFZ. Relict back-arc crust at the junction of the rift is covered by the volcanic flow field (Bavf) from the Central Volcanic Complex, and the lack of volcanism and mainly tectonic fabric confirms that the NW limb is not currently undergoing magmatic extension. The highly tectonized valley floor with no neovolcanic zone is more typical of a slow-spreading ridge (Carbotte et al., 2016). Together, these observations suggest that the NW limb may eventually become a failed rift, giving way to the expansion of the NE limb and/or SW limb, as Mitchell et al. (2011) suggested. The NE graben, which was originally classified as a fault by Bird (2003), Taylor et al. (2000) and Auzende et al. (1995), is shown here to have been actively spreading since at least 1.1 Ma. This is consistent with the positions of the J magnetic anomaly on crust adjacent to the SW and NE limbs (Huchon et al., 1994; Martin, 2013).

Distinct reorientations of the pre-NFBTJ spreading centres have been mapped in the relict back-arc crust (Figures 2.2 and 2.12) and appear to record a progressive rotation that could account for

the curvature of some of the older fabric. Some curved structures may have been a result of a rift "jump" with the typical overlapping spreading fabric as proposed by Patriat and Courtillot (1984). Both the NW and SW limbs are asymmetrical in cross-section, with their deepest parts in the west (Figure 2.13). One possible explanation is that clockwise rotation of the New Hebrides Arc promoted asymmetric spreading during the initiation of the triple junction. When Fiji stopped rotating at 3 Ma, the New Hebrides Arc continued to rotate, causing northward propagation of the spreading centres in the back-arc region and accelerated opening of the basin toward the west. This accelerated opening may be connected to the complicated relationship between the NFBTJ and the CSR segments in the south (Auzende et al., 1988, 1992, 1995; Gracia et al., 1994; Tanahashi et al., 1994; Huchon et al., 1994). A northward propagating rift of the CSR is currently migrating through the SW limb of the NFBTJ and capturing melt from it (Auzende et al., 1998; de Alteriis et al., 1993). In addition, the southern part of the SW axial ridge beyond the map area is fragmented into two smaller segments forming an overlapping spreading centre (OSC) with the northward propagating rift tip of the CSR (de Alteriis et al., 1993). A similar process could have taken place between 3.5 and 1.9 Ma which is indicated in Figure 2.12 and discussed in detail above.

2.7 Summary and Conclusions

The NFBTJ is a type locality for triple junction formation. This study compiled high-resolution multibeam, geophysical and ground-truthing data to construct the first geological map of the NFBTJ at a 1:500,000 scale. Quantitative analysis and interpretation of the map has revealed rift propagation, plate boundary rotations, and eruptive histories that highlight previously unrecognized near and far-field geodynamic influences on plate fragmentation and crustal growth during triple junction formation, including important magmatic and tectonic controls on the initiation and evolution of the triple junction, and the transition from an unstable FRR- to a stable RRR- type configuration.

The early NFBTJ was established in the centre of the NFB at 1.9 Ma when the westward propagating FFZ intercepted an already established spreading centre to the south and an older NW spreading centre in the north, forming an FRR-type triple junction. However, the first few hundred thousand years of the triple junction evolution were mainly in a rifting stage, extending toward the northeast, and the formation of the present RRR-type triple junction occurred as early as 1.4 Ma. The beginning of spreading along the NE limb coincided with the reorientation of the northern portion of the CSR to its present configuration along the SW limb. Huchon et al. (1994) suggested that the initiation age of the current configuration of the NFBTJ was 1.1 Ma. By applying the same spreading rates as Huchon et al. (1994), we calculate that the cumulative mapped area of the NE limb would have taken ~1.4 Myr to form. Therefore the transition from RRF- to RRR-type was between 1.4 and 1.1 Ma. The evolution from an FRR- to an RRR-type configuration was related to the emergence of a new spreading centre on the Conway Reef Plate at the location of the intersecting Fiji Fracture Zone (FFZ). Thus, the initiation of spreading on the NE limb of the triple junction likely coincided with the termination of the counter-clockwise rotation of the Fiji Platform. The NE limb began accreting crust ~400, 000 years before the SW limb. The present configuration of the triple junction has remained stable since its transition to a RRR-type (Huchon et al., 1994), contributing to significant magmatic productivity in the centre of the NFB. This study highlights the importance of the FFZ and its role in the kinematics of the evolution of the NFBTJ, focusing melts when it intersected the EW and the NE-SW spreading centres. The initial

interaction with the transform fault allowed rifting and basin opening to accelerate relative to the SW limb.

The convergence of multiple spreading centres at the NFBTJ had important implications for crustal growth in the NFB. Although little to no new crust has been produced in the NW limb, voluminous magmatism has occurred at the centre of the triple junction, particularly at the northern termination of the SW limb, over the last 0.3 Myr. The Central Volcanic Complex (CVC) and associated flow field (Bavf) are estimated to have grown in place at a rate of 3,000 m^2/yr, thus dominating the recent history of the NFBTJ. By contrast, earlier crustal growth along the SW and NW spreading segments, prior to the emergence of CVC, is estimated to have been ~1,650 m^2/yr and 200 m^2/yr respectively. Area-age relationships of the geological formations of the NFBTJ reveal 3 distinct rates of crustal growth for each of the three limbs of the triple junction. The NE limb started accreting crust by 1.4 Ma and experienced growth rates up to 400 m^2/yr. The SW limb had a longer period of initial rifting with crustal accretion not starting until 1.0 Ma. Despite its delayed crustal accretion this intermediate-spreading centre rifting phase the crustal growth rates range from 1,083 m^2/yr to 2374 m^2/yr. The crustal growth rate in the NW limb within last 1.1 Ma is considered to be 0 m^2/yr as it is only rifting existing crust and not producing new crust.

The high crustal growth rates at the NFBTJ contrast with the back-arc crust elsewhere in the NFB and in other back-arc basins (e.g., Lau Basin: Stewart et al., 2022). The recent (<1 Ma) voluminous mafic magmatism represented by the CVC, ~ 300 km^3, may be related to the high heat flow, intense faulting, and enhanced crustal-scale permeability of the triple junction, resulting in a significant increase in the supply of melt. High-standing normal faults at the margins of the actively spreading limbs expose thick crust that also may have promoted high heat flow and melt production. High heat flow has been linked to hydrothermal activity within the neovolcanic zone of the SW limb. This hydrothermal activity has produced an extensive vent field (4 km^2) containing massive sulfide deposits (Bendel et al., 1993). Hydrothermal vents have only been found along the SW limb, but due to the geological similarities observed in the neovolcanic zone of the NE limb, it is possible that additional hydrothermal vents may be discovered in the NFBTJ. These findings have implications for understanding the origins of similarly anomalous mafic magmatism in ancient

greenstone belts (e.g., possibly triggered by the coincidence of mantle upwelling and structural permeability of triple junctions).

The study shows that the history of triple junction formation can be reconstructed effectively by geological mapping. The quantitative analysis of the map units highlights important episodes of crustal growth. In the NFB, an abundance of tectonized back-arc crust bordering the three limbs of the triple junction prolonged rifting that must have occurred at the initiation of the triple junction followed by pulses of crustal growth culminated with the CVC. Simple vector addition of the spreading rates on the NW, NE, and SW limbs, indicates a stable triple junction configuration requires a slow spreading rate on the NW limb, which, may eventually become a failed rift, giving way to the expansion of the NE limb and/or SW limb. Suggested future research should include but is not limited to rock sampling to constrain the magmatic evolution of the TJ, Ar-Ar age dating to constrain the spreading rates, and possible dating of sediments (Clague et al., 2013).

Figures

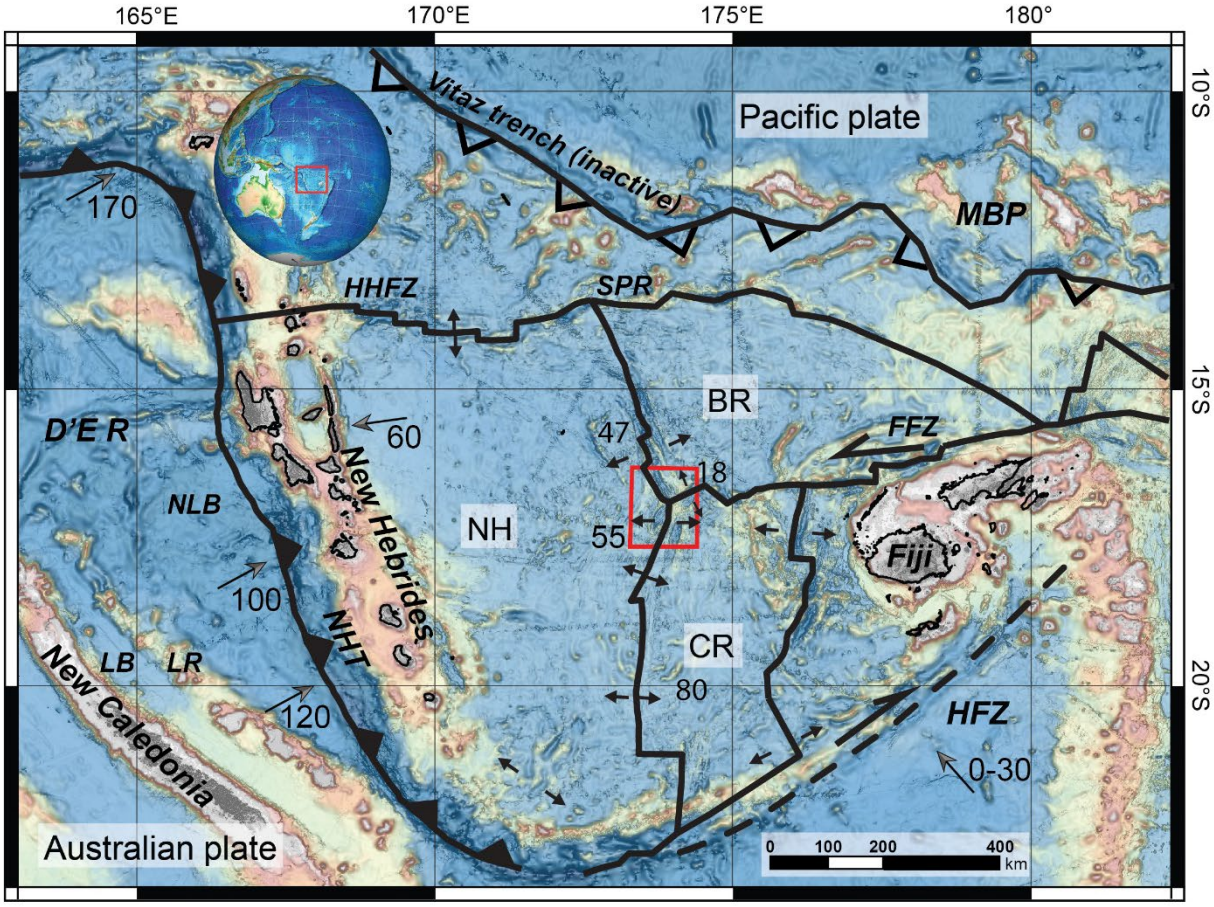

Figure 2.1 Multibeam bathymetry compilation and regional tectonic map of the North Fiji Basin with interpreted plate boundaries, emerging microplates, spreading centres, and other major structures. Major plate and microplate boundaries are from Bird (2003) and indicated with full black lines; inferred boundaries are indicated by dashed lines. Full lines with black triangles are active subduction zones; open tringles indicate inactive subduction zones. Half arrowheads indicate fracture zones with sense of motion indicated. GPS velocities (mm/yr) and azimuth (long gray arrows) are from Ruellan and Lagabrielle (2005). Full-spreading rates (mm/yr) and direction of spreading (short black arrows) are from Auzende et al. (1988, 1995), Huchon et al. (1994), Maillet et al. (1989), Ruellan et al. (1989), and Lagabrielle et al. (1996). The North Fiji Basin Triple Junction study area is outlined in red. MBP = Melanesian Boarder Plateau, HHFZ - Hazel Holme Fracture Zone; SPR - South Pandora-Tripartite Ridge; FFZ - Fiji Fracture Zone; CSR – Central Spreading Ridge; HFZ - Hunter Fracture Zone; NH - New Hebrides; CR - Conway Reef; BR - Balmoral Reef.

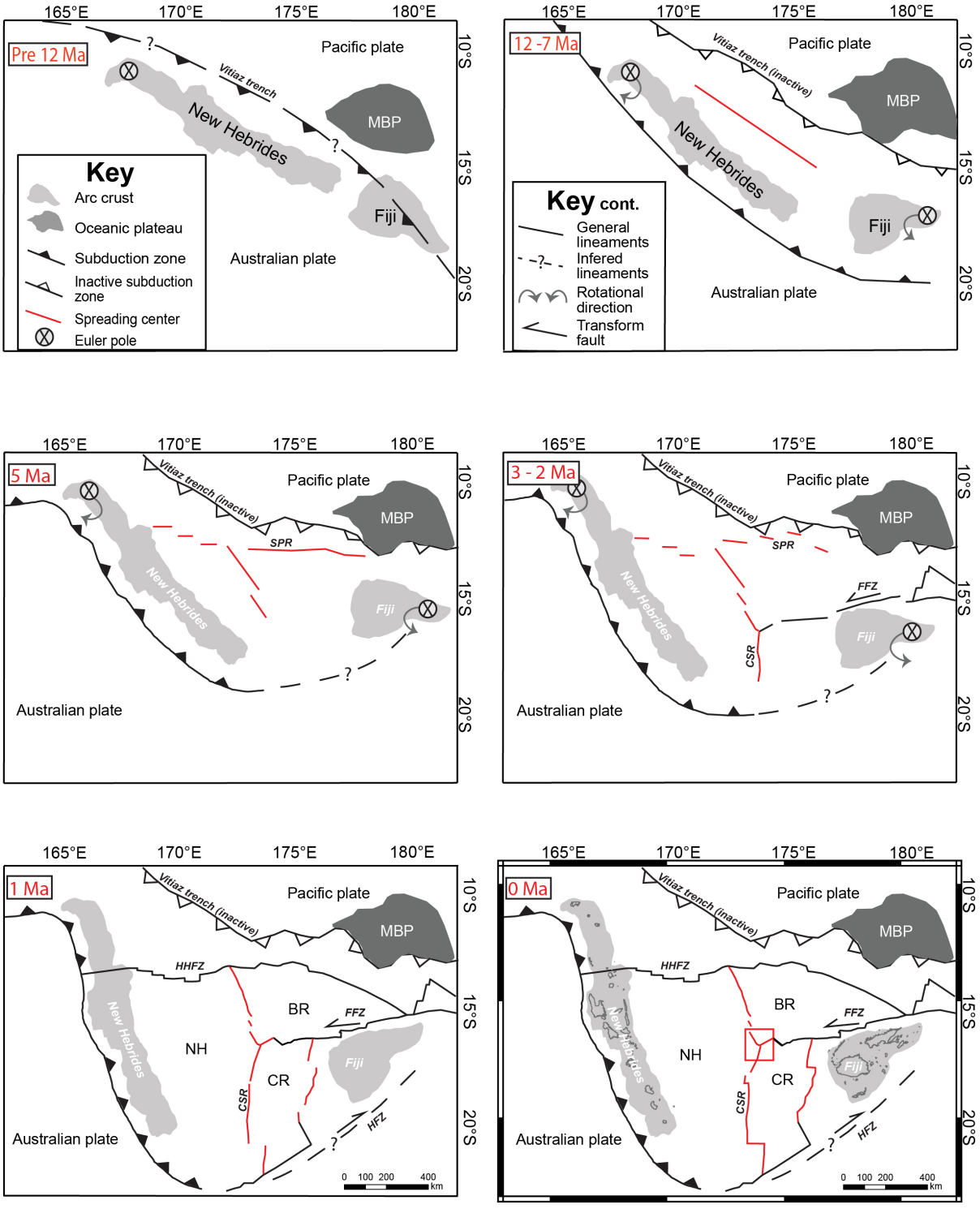

Figure 2.2 Schematic illustration of the opening of the North Fiji Basin and the emergence of the North Fiji Basin Triple Junction (NFBTJ). **Pre-12 Ma)** Subduction of the Pacific Plate to the

southwest under the Vitiaz Arc. **12 - 7 Ma)** Subduction was interrupted by the collision of the Melanesian Border Plateau (MBP) along the Vitiaz Trench causing a polarity reversal that initiated subduction of the Australian Plate along the New Hebrides Trench (Auzende et al., 1995; Taylor, 2000; Ruellan and Lagabrielle, 2005; Schellart et al., 2006; Martin, 2013). Back-arc basin spreading caused by rollback of the Indo-Australian slab formed new crust along a now extinct NW-SE spreading centre that was oriented parallel to the rotating New Hebrides arc (Auzende et al., 1995; Martin, 2013). **5 Ma)** Further opening of the back-arc basin occurred along two new spreading centres oriented NW and NS following the rotating New Hebrides arc. **3 - 2 Ma)** With reduced rotation of the Fiji Platform, the Fiji Fracture Zone (FFZ) emerged and propagated westward until it intercepted the already established spreading centres, creating the NFBTJ (Martin, 1994). The original configuration was a Ridge-Ridge-Fault-type (RRF) triple junction, with spreading on the NW and SW limbs. **1 Ma)** Spreading initiated along the NE limb transitioning the triple junction to a Ridge-Ridge-Ridge-type. **0 Ma)** Present configuration of the NFB and NFBTJ. The NFBTJ study area is outlined in red. MBP - Melanesian Boarder Plateau; HHFZ - Hazel Holme Fracture Zone; SPR - South Pandora-Tripartite Ridge; FFZ - Fiji Fracture Zone; HFZ - Hunter Fracture Zone; NH - New Hebrides; CR - Conway Reef ; BR - Balmoral Reef.

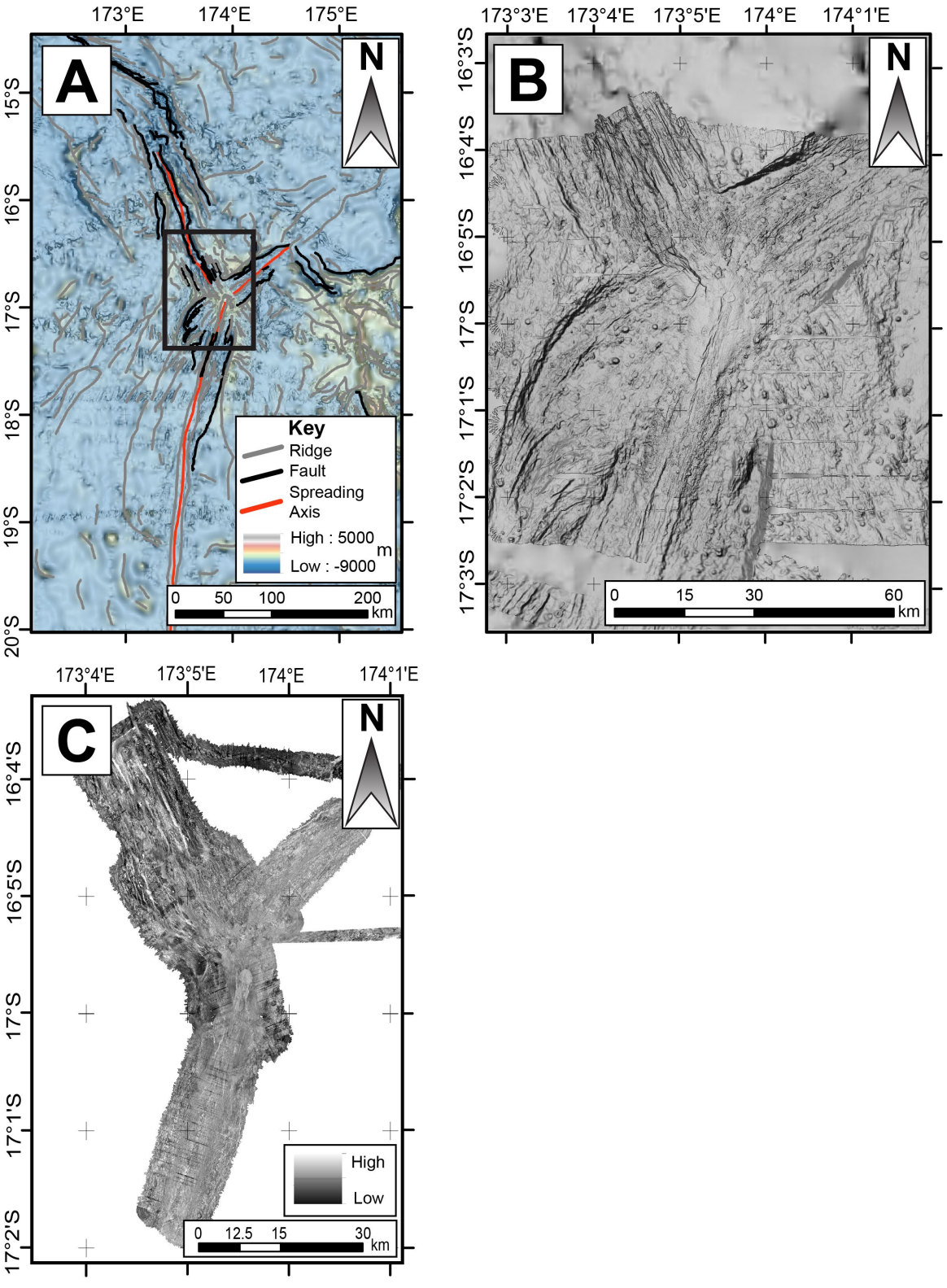
A
N
173°E
174°E
175°E
15°S
16°S
17°S
18°S
19°S
20°S
Key
Ridge
Fault
Spreading Axis
High : 5000 m
Low : -9000
0 50 100 200 km
B
N
173°3'E
173°4'E
173°5'E
174°E
174°1'E
16°3'S
16°4'S
16°5'S
17°S
17°1'S
17°2'S
17°3'S
0 15 30 60 km
C
N
173°4'E
173°5'E
174°E
174°1'E
16°4'S
16°5'S
17°S
17°1'S
17°2'S
High
Low
0 12.5 15 30 km

Figure 2.3 A) Regional lineament map of large-scale ridges, faults and spreading axes superimposed on bathymetric data of the Global Bathymetric Chart of the Oceans (GEBCO Compilation Group, 2021). Spreading fabrics (mostly ridge lineaments) are shown in grey, major faults with throws of >100 m are in black, and spreading axes are in red. The three longest spreading segments, corresponding to the limbs of the NFBTJ are oriented SW, NW and NE. Major NW-trending faults to the east of the triple junction are apart of the Fiji Fracture Zone (FFZ). Most of the spreading fabric mimics the three active spreading axes, except south of 19ºS and in the northeast of the map area, east of ~174.6 E. Inset black box represents this studies geological map (Figure 2.7) extent. **B**) Integrated DEM (gray scale) with slope-shaded enhancement (calculated slope raster and hill-shade) of Global Multi-Resolution Topography Data Synthesis (GMRT) bathymetric grid (v3.7) (Ryan et al., 2009). MBES data were incorporated from the *RV Southern Surveyor* (SS2012-02) and *RV Yokosuka* (YK06-02) cruises and superimposed onto the GMRT. The RV Southern Surveyor data are at a resolution of 30 m; the RV Yokosuka data cover a larger area at a lower resolution of 100 m. **C)** Backscatter data collected during the SS2012-02 cruise. Relative backscatter strength is a proxy for the accumulation of sediment cover and provides a relative of the underlying formations. Low sediment accumulation has a high reflectivity and appears as lighter gray. Areas of high reflectivity are associated with recent faults and fresh volcanic flows such as in the neovolcanic zones of the active rift, areas of low reflectivity (dark grey) have thicker sediment deposits and are older units. See Appendix A, Supplementary Figure 3 - 5 for enlarged images.

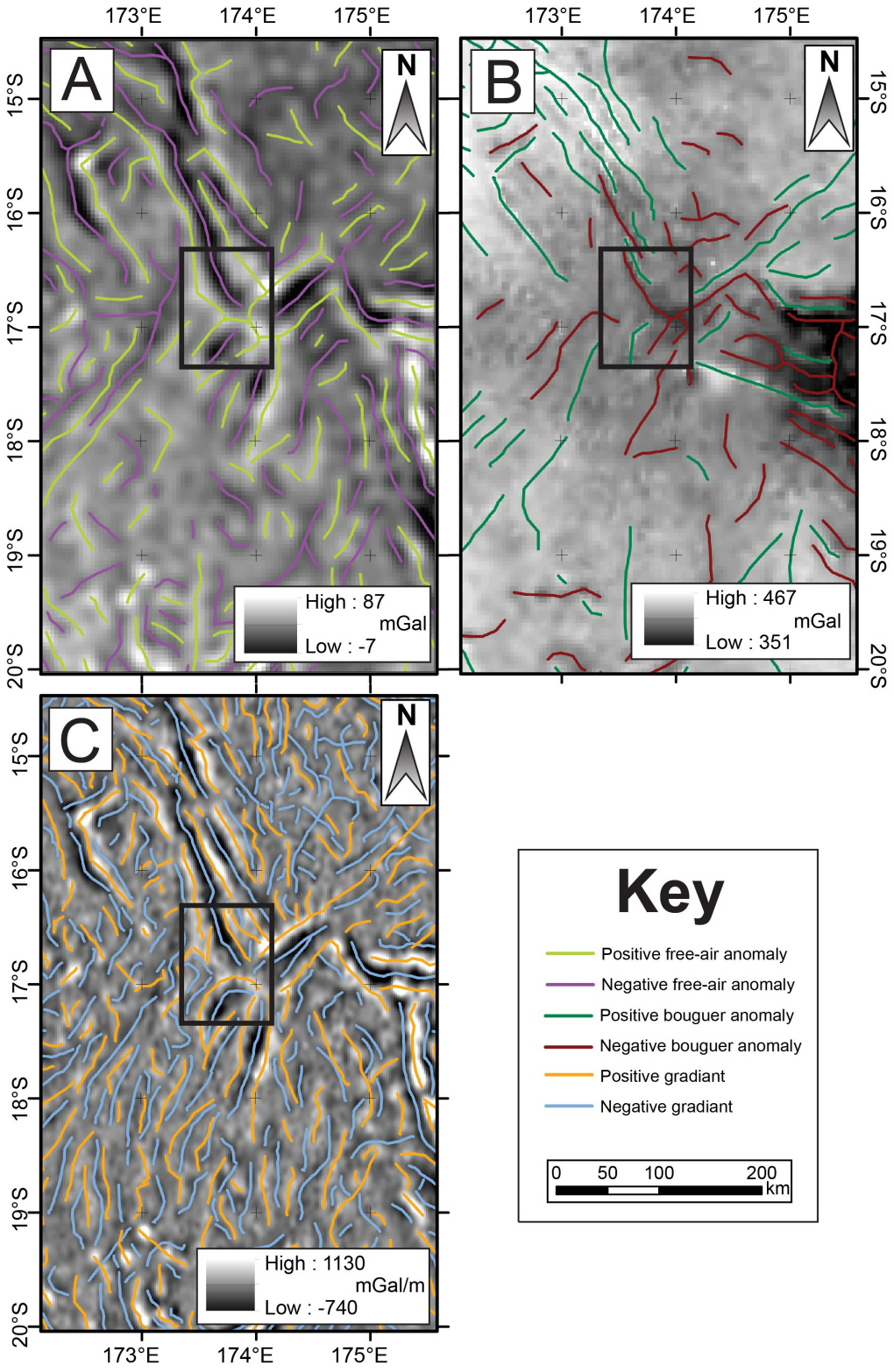

Figure 2.4 Free-air gravity, Bouguer gravity anomaly and vertical gravity gradient (VGG) of the NFBTJ. Inset black boxes represents this studies geological map (Figure 2.7) extent. **A)** Free-air

gravity from Bonvalot et al. (2012) shows a strong correlation with the bathymetry. Parallel gravity highs (green lines) and local gravity lows (purple) correspond to rift zones in the NW and NE limbs and the axial spreading centre of the SW limb. A gravity high connects the three limbs at the centre of the triple junction, which marks the central volcanic complex (CVC). **B)** The Bouguer anomaly map shows the relative densities of the crust (Bonvalot et al., 2012). Overall, the triple junction is marked by low gravity anomalies (burgundy) reflecting regionally inflated crust. Gravity lows are also dominant east of the triple junction, where the region has thicker crust and is highly faulted. **C)** The vertical gravity gradient (VGG) derived from satellite altimetry (Sandwell et al., 2014) highlights the three spreading axes which are flanked by steep vertical gravity gradients (orange lines). Strong negative (blue) gradients follow the NW and NE spreading centres; steep positive vertical gravity gradient mark the SW limb.

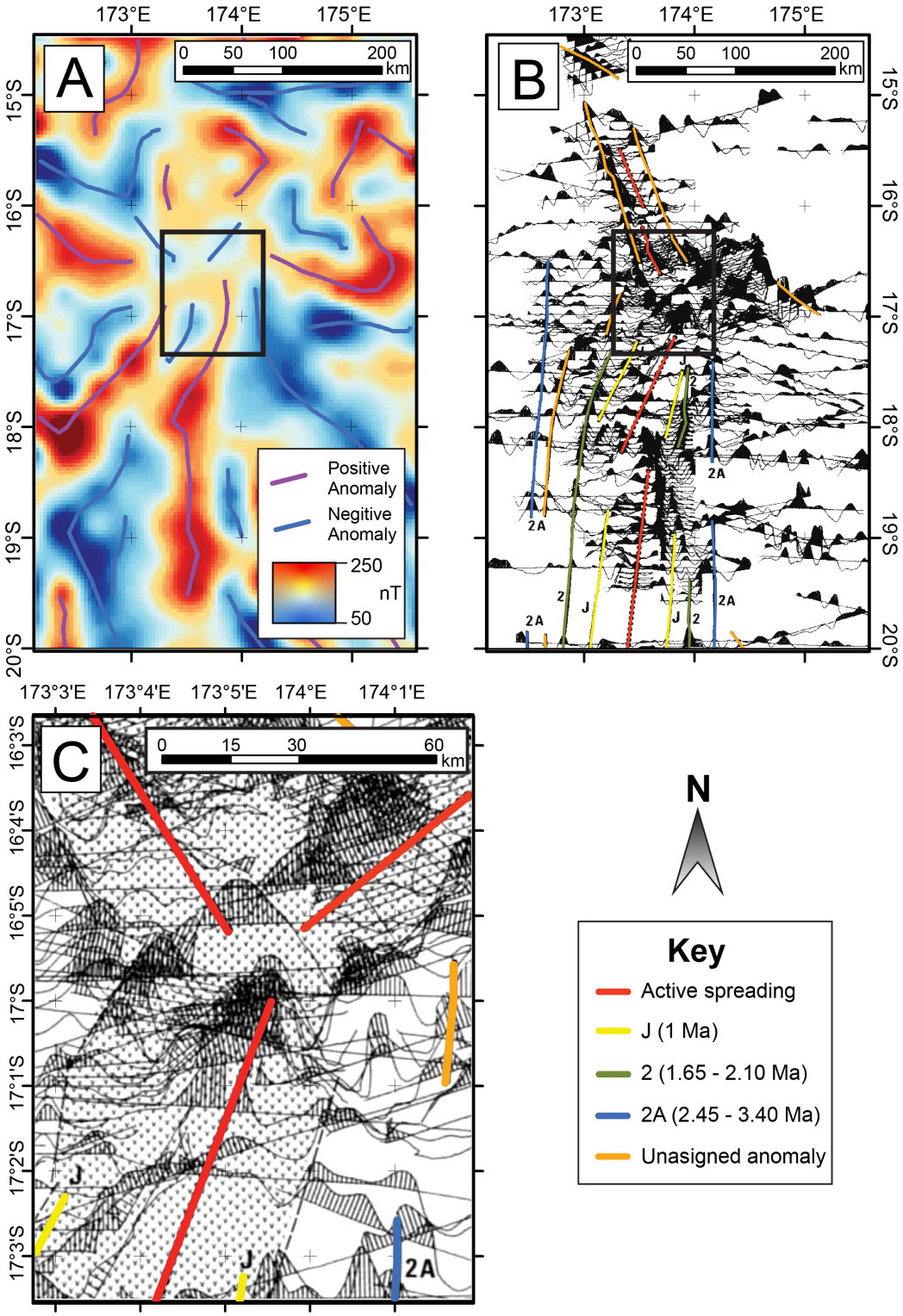

Figure 2.5 A) Magnetic anomalies from the 2-arc minute resolution compilation, EMAG2 (Earth Magnetic Anomaly Grid: Maus et al., 2009), with broad negative anomalies (blue) corresponding

to the three spreading axes of the NFBTJ positive anomaly (purple) at their intersection. The Curved magnetic high and lows to the west of the SW spreading axis correspond to the curved faults in this region. Inset black box represents this studies geological map (Figure 2.7) extent. **B)** Magnetic anomalies modified from Huchon et al. (1994) corresponding to the active spreading centres (red lines) of the NW and the SW limbs. The NW spreading centre is bounded by magnetic anomalies of unknown ages (orange lines). The SW spreading centre is bound by three sets of anomalies, from youngest to oldest: anomaly 'J' (1 Ma), anomaly '2' (1.65 to 2.10 Ma) and anomaly '2A' (2.45 to 3.40 Ma). No clear spreading anomalies are identified along the NE limb, possibly because of the strike-slip faulting associated with the FFZ. Inset black box represents this studies geological map (Figure 2.7) extent. **C)** Close-up of the magnetic anomaly map from Huchon et al. (1994) showing crust formed within the last 1.1 Ma indicated by the "v" pattern, and magnetic chrons corresponding to the three active spreading axes of the NFBTJ marked by red lines. Anomaly J (yellow) and 2A (blue), correspond to 1 Ma and 2.45-3.40 Ma, respectively.

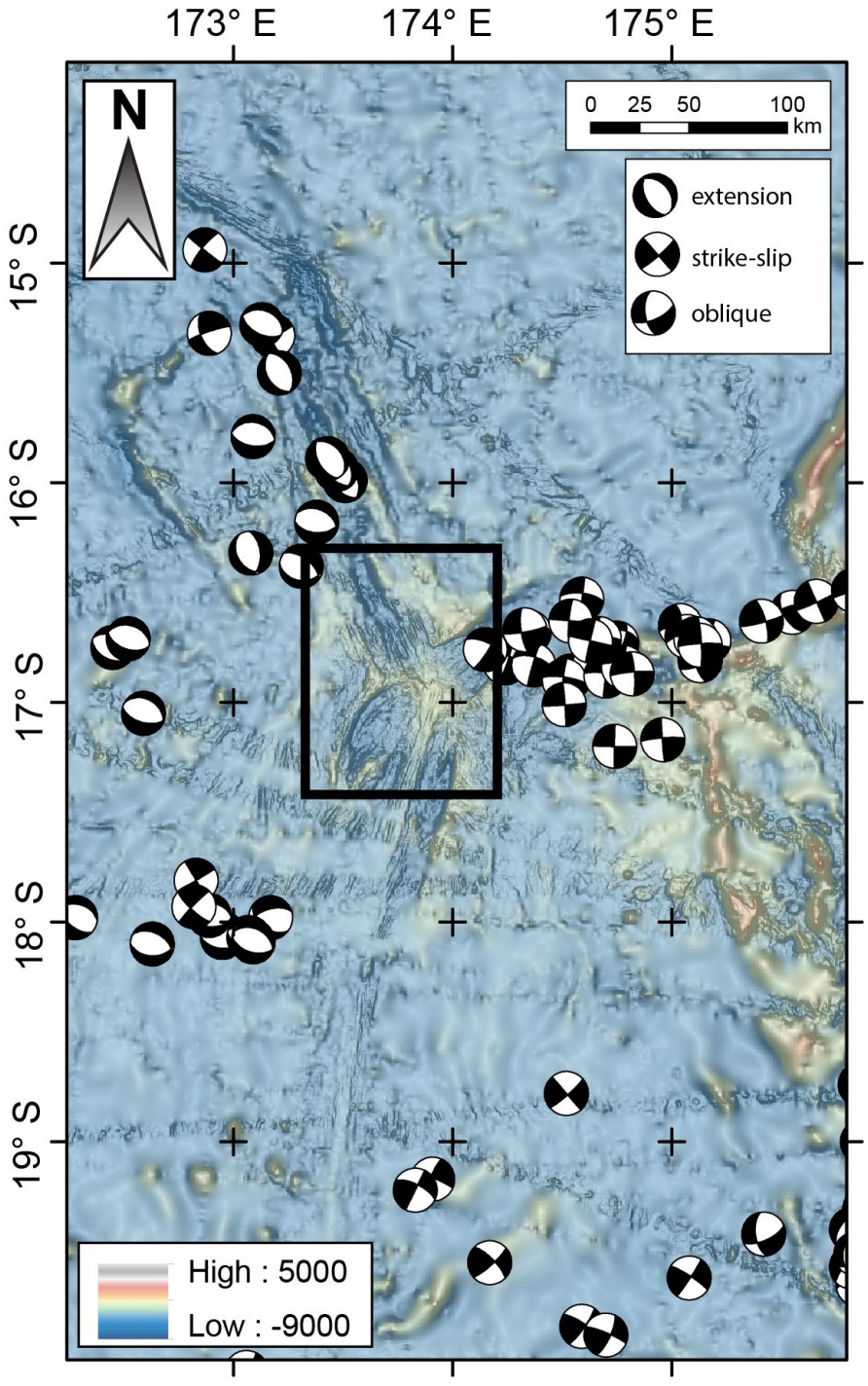

Figure 2.6 Harvard Centroid Moment Tensors (CMTs) for earthquakes in the vicinity of the NFBTJ. Epi centres of shallow (<30 km) teleseismic events (Mw>5) are shown in the central NFB

from the open-source catalogue of Dziewonski et al. (1981) and Ekström et al. (2012). The calculated fault-plane solutions, plotted using the ArcBeachball tool (v.2.2) (Tiesheng, 2016), indicate mainly strike-slip faulting in the east of the map area, including along the NE limb of the NFBTJ, whereas extensional faults occur along the NW limb. The lack of recorded seismicity along the SW arm could be explained by the lower limit of Mw > 5 for earthquakes contained in the GlobalCMT database. This may not capture many smaller Mw earthquakes, which are typical in faster spreading regimes (Eguchi et al., 1989; Conder & Wiens, 2011). The CMTs dataset overlay bathymetric data of the Global Bathymetric Chart of the Oceans (GEBCO Compilation Group, 2021). Inset black box represents this studies geological map (Figure 2.7) extent.

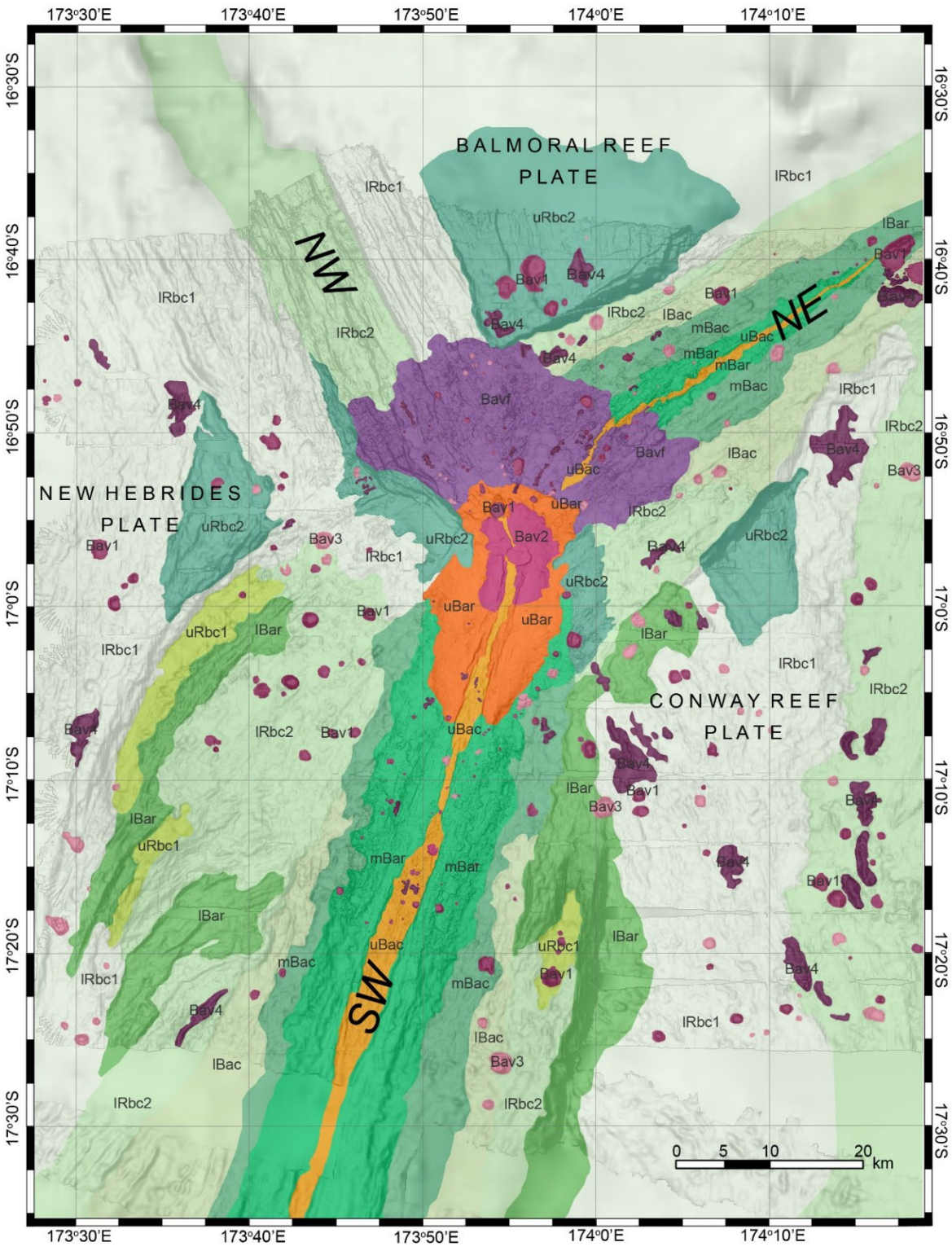

Figure 2.7 Reduced and simplified version of the 1:500,000 geological map of the NFBTJ. The corresponding legend is in Table 2.1. The complete map sheet including legend and marginal notes

is provided at the original scale in Appendix B. The legend used for this map was adapted from the geological legend of the Lau Basin, following the lithostratigraphic classification scheme of Stewart et al. (2022). NE - Northeastern oriented limb; NW – Northwestern orientated limb; SW – Southwestern orientated limb.

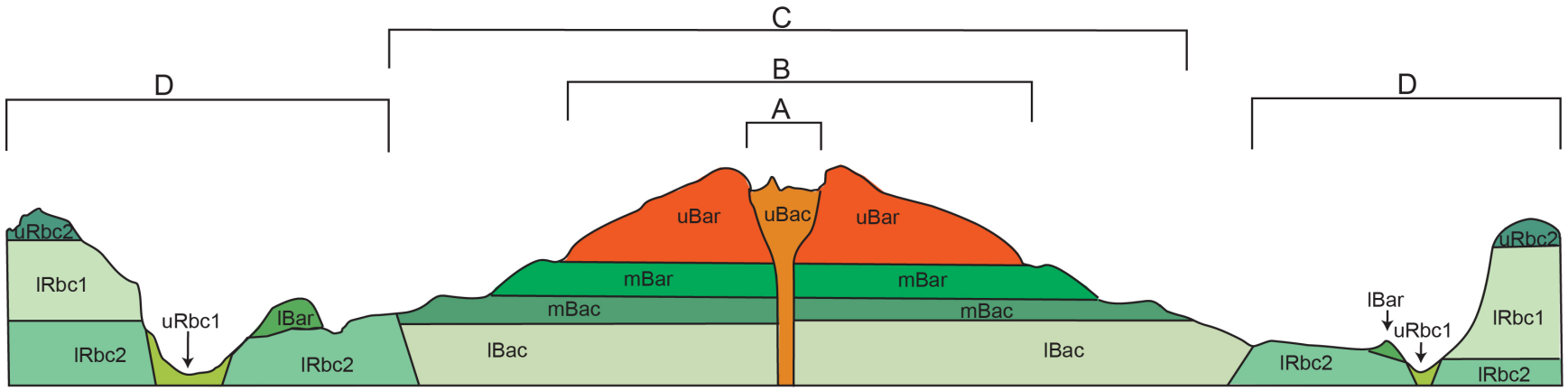

Figure 2.8 Schematic illustration of stratigraphic correlations depicted in the 1:500,000 scale geological map of the NFBTJ A) neovolcanic zone and inner rift valley, B) outer rift valley and flanks of the axial volcanic zone, C) "middle" and "lower" back-arc crust, D) relict back-arc crust. This illustration is not to scale. See Table 2.1 for corresponding legend.

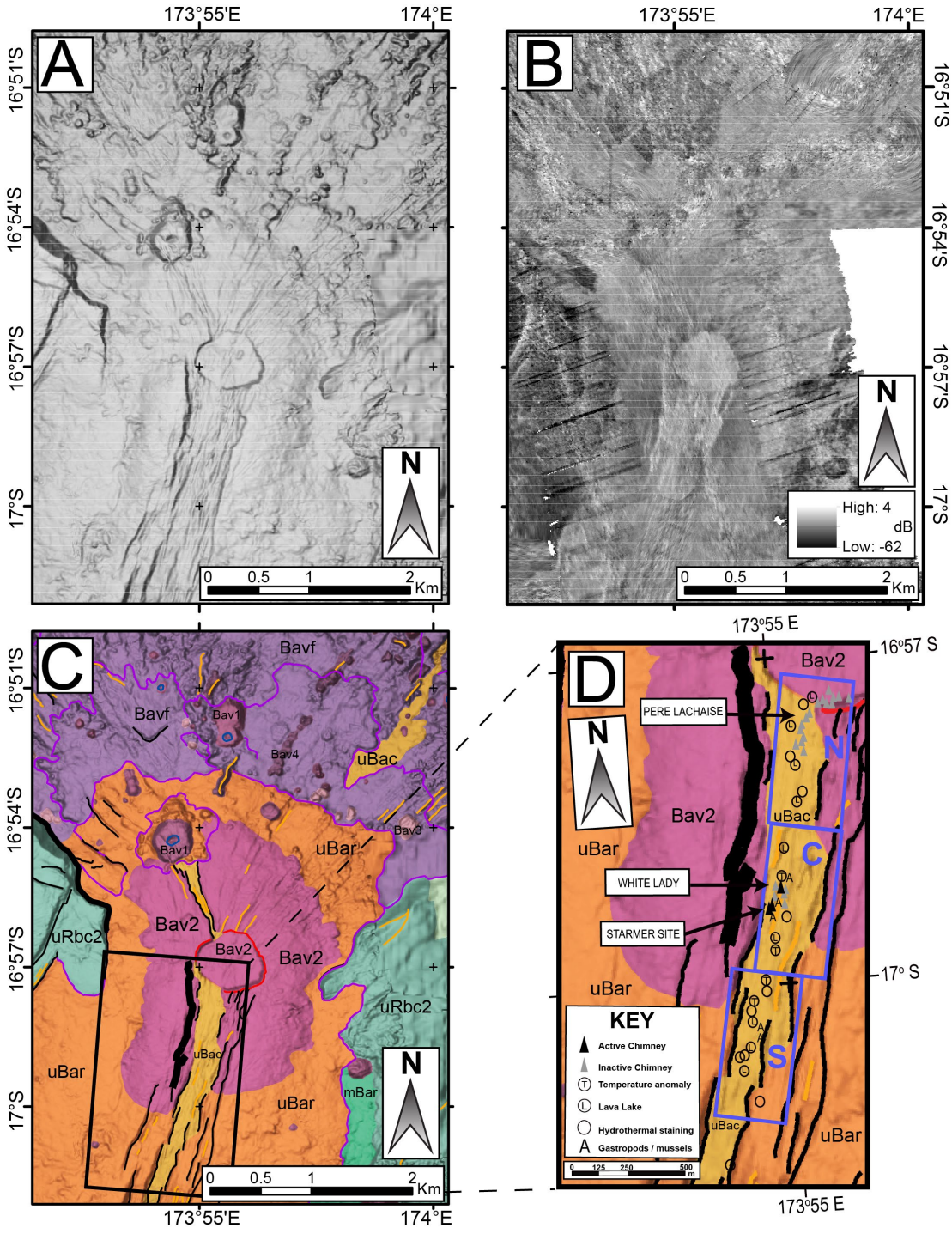

Figure 2.9 Detailed view of geological map and hydrothermal vent locations on the Central Volcanic Complex of the NFBTJ. **A**) Integrated DEM presented in gray scale and including multibeam echosounder (MBES) data collected during the RV *Southern Surveyor* (SS2012-02)

and RV *Yokosuka* (YK06-02) cruises and superimposed onto the GMRT. The RV *Southern Surveyor* data are at a resolution of 30 m; the RV *Yokosuka* data cover a larger area at a lower resolution of 100 m. A calculated slope raster and hill-shade preformed in ArcGIS was used for enhancement. **B)** Backscatter data collected during the SS2012-02 cruise. These data show the lower reflectivity (darker/older) of the caldera rim cut by the more reflective (younger) spreading axis of the SW limb. The volcanic flow field (Bavf) emanating from the shield extends at least 25 km from the summit and partially covers the NE rift axis, but there is clear evidence of continuous rifting of the flow field along strike with the NE rift. The steep slopes partly control the bifurcation of the volcanic flow field toward the north, with high elevations in the south (uBar) encouraging flow into the NE and NW limbs. The flow field boundaries are clearly visible in Figure 2.9A, and the full extent of the flow field boundaries (purple) is shown in Figure 2.10. **C)** A Portion of the geological map (Figure 2.7) with superimposed (see Figure 2.10). The corresponding legend is in Table 2.1. The large shield volcano at the summit of the Central Volcanic Complex comprises the axial volcanic high (uBar) of the SW ridge capped by the shield volcano (Bav2) and flanked by the large volcanic field (Bavf) to the north. The shield volcano is 11 km long by 7.5 km wide, and 0.5 km high. This inflated crust is split by the 900-m wide neovolcanic zone of the SW ridge, which crosses the summit of the shield and extends 2 to 3 km onto the volcano's northern flank. A ~2 km-diameter caldera (red line) has formed at the summit, and the northern and southern rims of the caldera are cut by the extensional faults traversing the shield. The full extent of the flow field boundaries (purple) is shown in Figure 2.10. Our mapping shows that the flows are cut by the narrow neovolcanic zone (uBac) of the NE limb but overlap the extensional fabric of the NW limb. The black box shows the location of the area of hydrothermal activity. **D)** Close –up of the area of hydrothermal activity on the axial volcanic high of the SW limb (black box in C). All known hydrothermal vents in the NFBTJ (Table 2.4) are located on the axial back-arc crust (uBac) of the SW ridge. They extend for 6 km south of the summit caldera in three locations (blue boxes): the northern, central and southern domains mapped during two cruises (STARMER 89 and *Yokosuka* 91: Gràcia et al., 1994). The hydrothermally active areas are characterized by similar volcanic facies, including pillow basalts, lava lakes, and massive flows. Visual observations from towed cameras and submersibles reported by Bendel et al. (1993) provide important ground-truthing of rock types, lava morphologies and structure at the outcrop scale (Appendix A, Supplementary Figure 1).

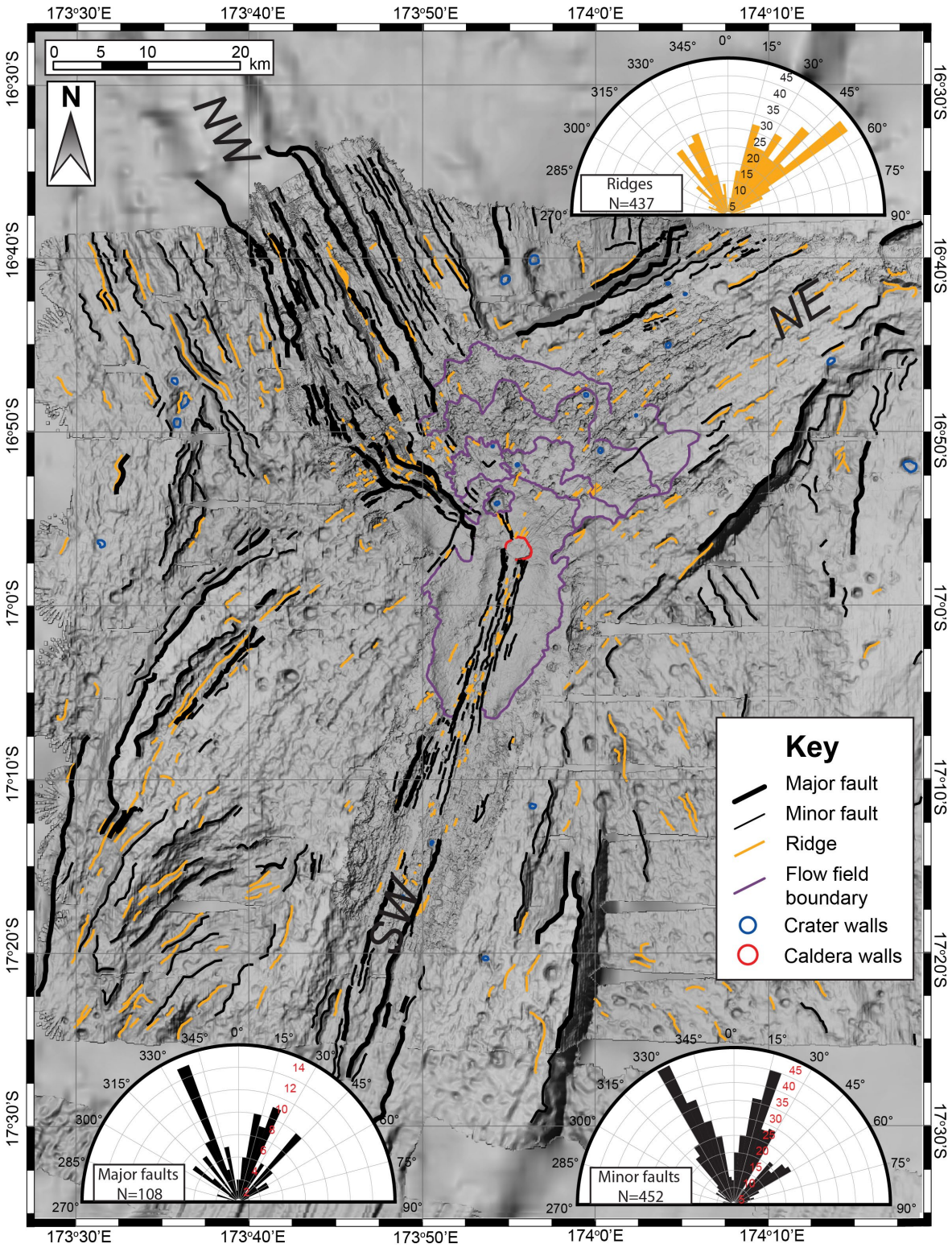

Figure 2.10 Lineament map of the North Fiji Basin Triple junction (NFBTJ). A total of 1036 lineaments were mapped including faults, ridges, calderas rims, summit craters and flow field

boundaries. 560 faults were mapped, including 108 major faults (thick black lines) with throws of >100 m and average lengths of ~5 km. 452 minor faults (thin black lines) were found, with throws of less than 100 m, and lengths from less than 100 m to 11 km long. 437 distinct ridges were mapped (orange lines) with an average length of 1.5 km up to 9.4 km. Summit depressions and collapsed features related to volcanism are included, referred to as "calderas" and indicated in red if >1 km in diameter or "volcanic craters" indicated in blue if < 1 km in diameter. Flow field boundaries are indicated in purple. Top right inset: orientations of 437 ridges, from 140º to 240º. Bottom left inset: dominant orientations of a subset of 108 major faults at 340º, 200º, and 045º. Bottom right inset: orientations of a subset of 452 minor faults at 335º, 195º, and 050º. NE - Northeast limb of the NFBTJ; NW – Northwest limb; SW – Southwest limb; N – Number of measured lineaments.

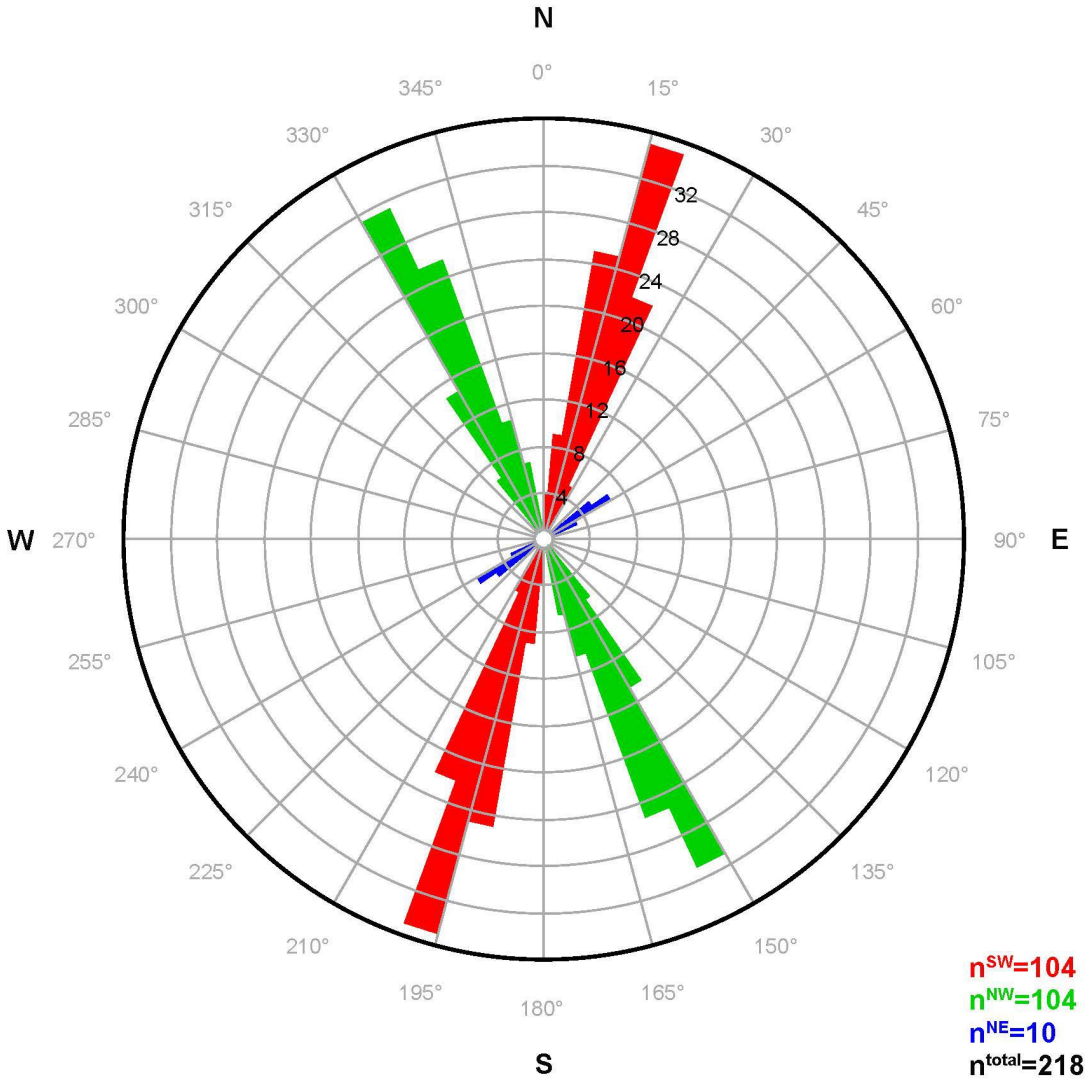

Figure 2.11 Orientations of faults within the back-arc rifts and spreading centre formations of the NE and SW limbs, as well as the tectonized relict back-arc crust the NW limb. SW limb (red), NW limb (green) and NE limb (blue). The SW limb contains 104 faults with orientations of ~195º, the NW limb contains 104 faults with orientations of ~335º, and NE limb contains only 10 faults with orientations of ~055º. NE - Northeast limb; NW – northwest limb; SW – southwest limb; N – number of measured lineaments.

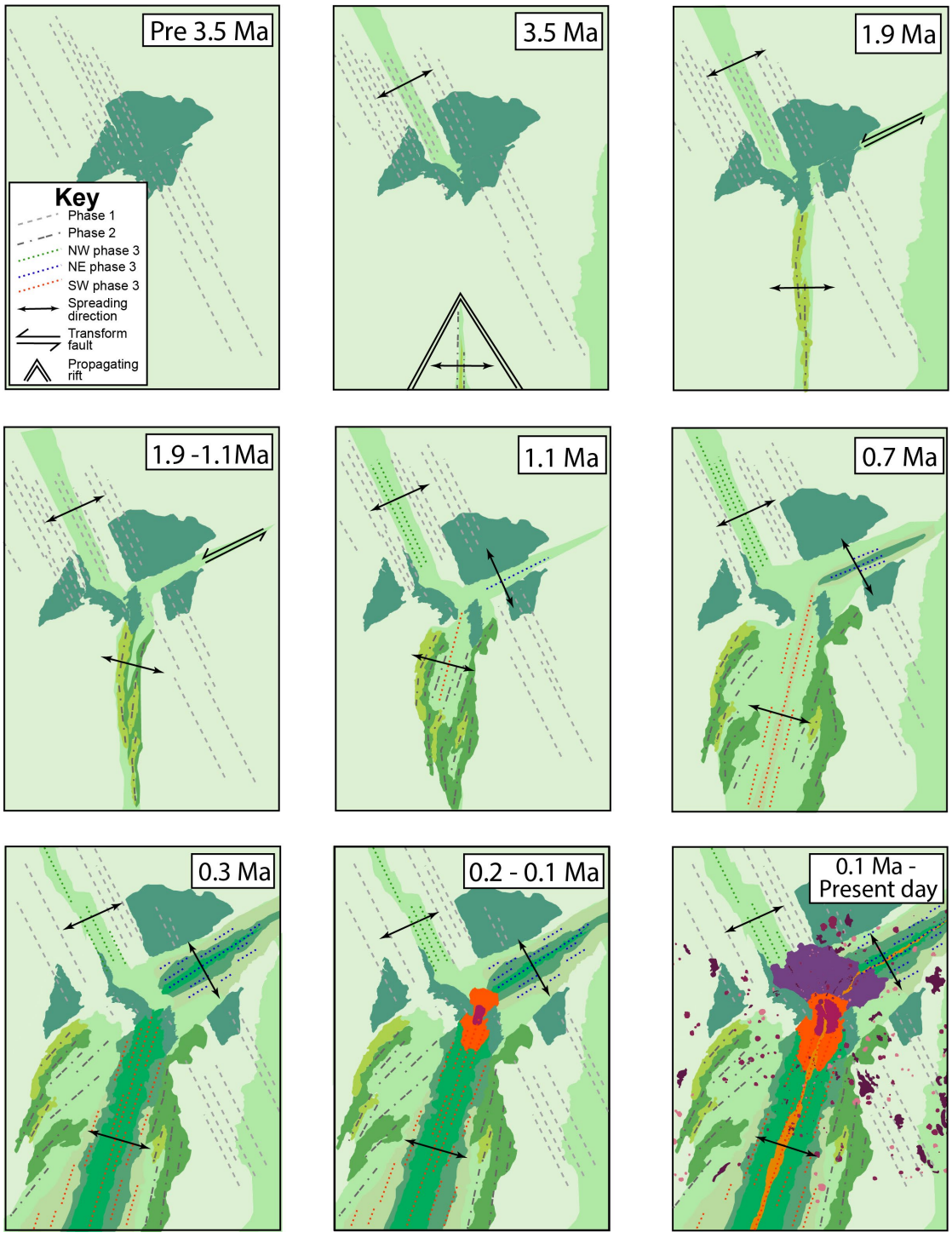

Figure 2.12 Schematic reconstruction of the NFBTJ through time based on the mapped formations from Figure 2.7 (Table 2.1, corresponding legend). The simplified lineaments are approximations of the fabrics seen in lineament map (Figure 2.10), and are categorized into three phases based on

spreading origins. Volcanic edifices and flow fields are only the last panel for simplicity. **Pre 3.5 Ma)** A large early volcanic centre included the preserved uRbc2, and lRbc1 crust and structures of phase 1. **3.5 Ma)** The NW limb had emerged by 3.5 Ma by rifting of lRbc1 and lRbc2; no new crust is thought to have originated from this spreading centre and so this is considered a continuation of phase 1. A northward propagating rift in the south of the map area introduced phase 2 structures (EW spreading), which are still preserved in relict back-arc crust (uRbc1). This fabric is preserved the tectonized relict back-arc crust (lRbc2). **1.9 Ma)** a RRF-type triple junction is formed by the northward propagating rift with phase 2 intersecting the phase 1 NW rifting. The Fiji Fracture Zone (FFZ) easterly intersection of the two stablished limbs at this time. **1.9 - 1.1 Ma)** NE limb began opening and continued to be heavily influenced by the FFZ. Phase 2 structures are preserved in lBar as the opening of the southern limb began and rotated to its current position as the SW limb. The relict back-arc crust (lRbc2) was further tectonized during this process. Phase 2 structures are also present in the SW limb in lBar, uRbc1 and lRbc2 crust, and deformation of the fabric during 1.9 – 1.1 MA accounts for the curvature, which ranges from ~010º to 065º. **0.7 Ma)** Phase 3 resulted in the transition from a RRF- to a RRR-type triple junction with the re-orientation of the SW limb to 195º. According to Huchon et al. (1994) the SW limb has been actively spreading since ~1.1 Ma. The NE limb achieved a full spreading rate of 18 mm/yr (Huchon et al., 1994) by at least 1.1 Ma. Structures formed at this time (phase 3) have an average orientation of 055º preserved in back-arc rift and spreading centre crust that was formed along the spreading centre. Spreading of the NW limb was also is initiated at this time with a full spreading rate of 47 mm/yr, oriented at 335º. However, since at least 1.1 Ma, the NW limb has undergone mainly tectonic with no new crust currently being produced. **0.3 Ma)** The SW limb, which has had a more complex history, has cut both phase 2 and phase 3 structures. Phase 3 structures in the SW are oriented at 195º and are confined to back-arc rift and spreading centre crust formation but not preserved in lBar. The faster spreading SW limb has overtaken the NE limb as the dominant spreading centre. **0.2 - 0.1 Ma)** A central volcanic complex (CVC) began to form at the centre of the triple junction. Phase 3 fabrics continue to develop in the NW, NE and SW limbs. **0.1 Ma – Present day)** Further inflation of the CVC has occurred to the present day, with the eruption of the shield volcano creating massive flow fields (Bavf) to the north of the CVC. Phase 3 structures (both NE and SW) are still being created along the young active neovolcanic spreading centres cross the CVC and associated flows.

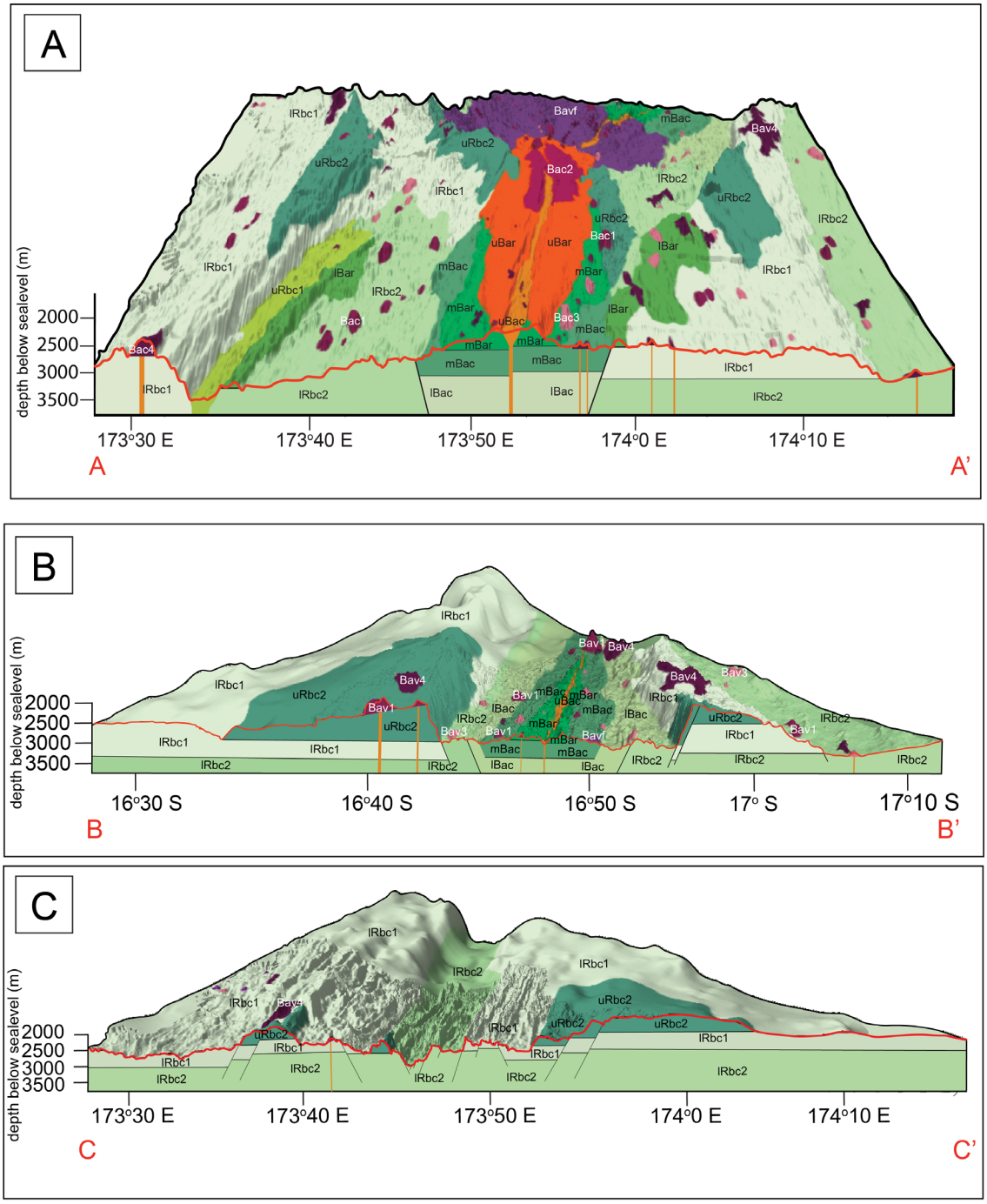

Figure 2.13 3-D perspectives and cross sections of the NW, NE and SW limbs of the NFBTJ. 6x vertical exaggeration. All contacts are considered to be conformable unless defined by faults. **A)** SW limb **B)** NE limb **C)** NW limb. The location of cross section are shown in Appendix A, Supplementary Figure 6.

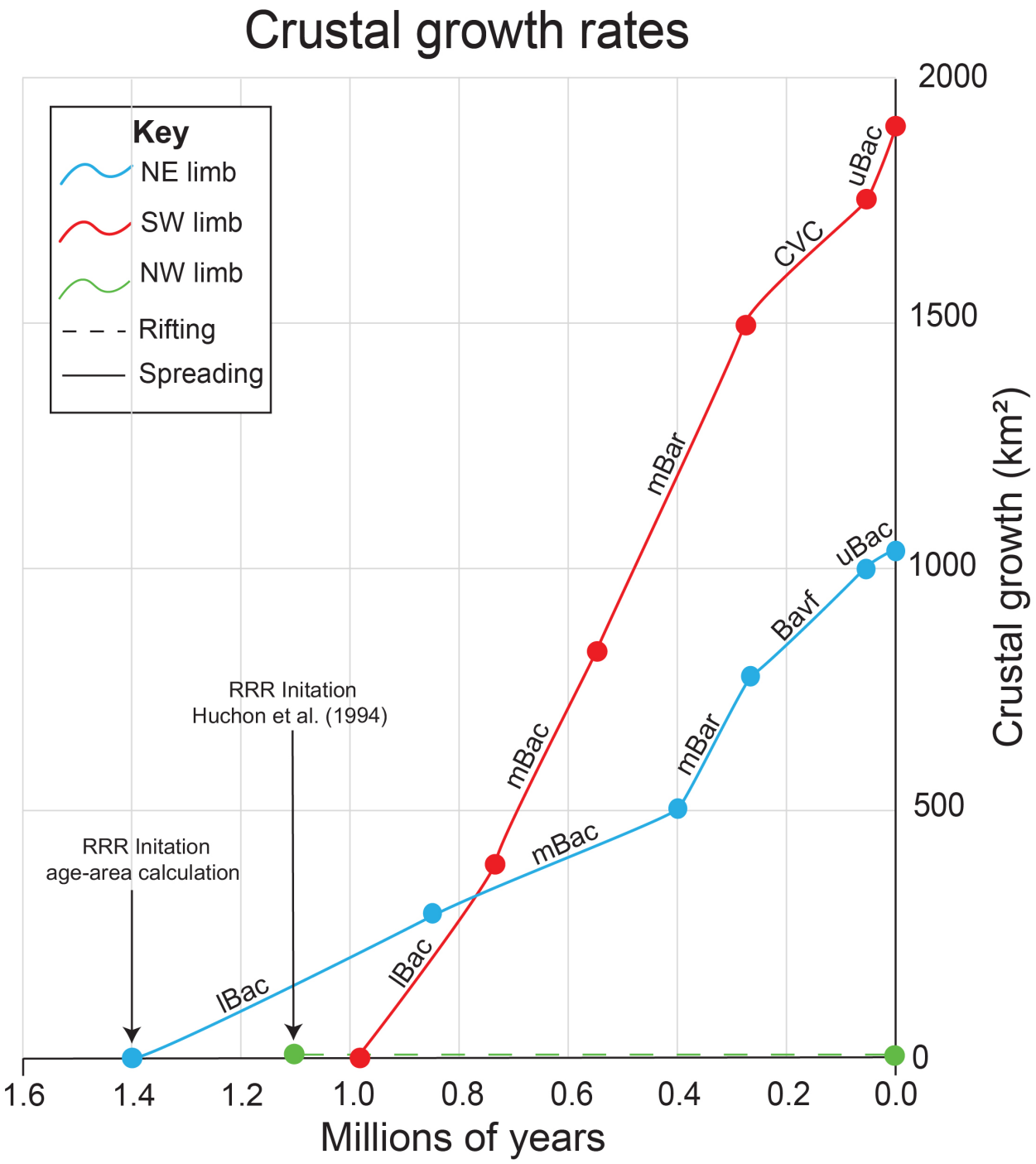

Figure 2.14 Growth curves (area-age) for each limb of the NFBTJ from calculated ages (Table 2.6) of the formations and their mapped areas. The NE (blue), SW (red) and NW (green) limbs have distinct histories of crustal growth since ~1.5 Ma. Spreading ages are calculated using the

average width of the mapped formations and the spreading rates from Huchon et al. (1994). A fixed spreading rate is used for all formations of a limb to estimate growth rates through time. The calculated spreading ages agree well with independently determined ages of the formations based on magnetic chrons (Huchon et al., 1994) and therefore are used here to illustrate crustal growth. Cumulative area (km2) is plotted against age (Myr) and crustal growth is represented by the slope of the curve (m2/yr), with the growth of each limb plotted individually. Rifting phases are indicated by dotted lines (no accumulation of area) and spreading is indicated by solid lines. The NE limb marks the beginning of crustal accretion at 1.4 Ma. It is spreading at a slow (full-spreading) rate of 18 mm/yr. Crustal accumulation in the SW limb began at 1 Ma, at an intermediate (full-spreading) rate of 52 mm/yr. Due to its faster growth rate, the SW limb surpassed the NE limb in crustal abundance at approximately 0.8 Ma. No back-arc and spreading centre crust was mapped along the NW limb, therefore rifting is proposed for the dominant form of extension since 1.1 Ma. Huchon et al. (1994) suggested that the initiation age of the current configuration of the NFBTJ was 1.1 Ma. By applying the same spreading rates as Huchon et al. (1994), we calculate that the cumulative mapped area of the NE limb would have taken ~1.4 My to form. Therefore the transition from RRF- to RRR-type was between 1.4 and 1.1 Ma. CVC= Central Volcanic Complex; refer to Table 2.1 for mapped formation and volcanic edifices abbreviations.

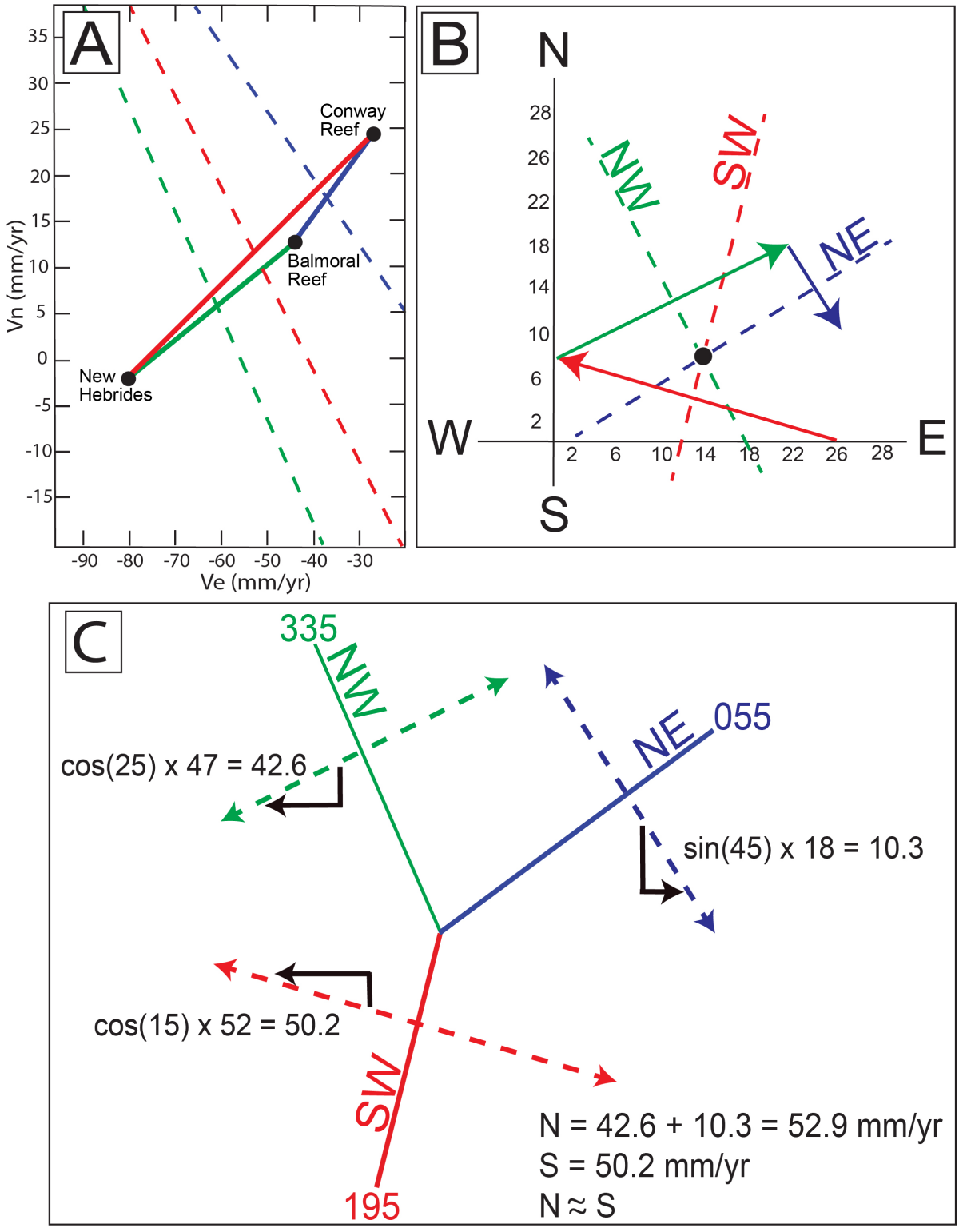

Figure 2.15 Three different models used to asses the stability of the NFBTJ. Based on regional-scale vectors from MORVEL56 (Argus et al., 2011), the McKenzie and Morgan-type vector

stability diagram, and a simple vector addition of the E-W extension. **A)** This method uses absolute motions of the plates from the MORVEL56 reference frame for the New Hebrides, Balmoral Reef and Conway Reef microplates. In a stable configuration the bisectors (dotted lines) for each pair of plate boundaries (solid line) should intersect within the plotted triangle (Argus et al., 2011). The apparent instability in this model is caused by a high rate of spreading on the NW limb. **B)** In the McKenzie and Morgan-type stability diagram, the lengths of the vectors correspond to the half-spreading rates from Huchon et al. (1994): 23.5 mm/yr (NW limb), 9 mm/yr (NE limb) and 26 mm/yr (SW limb). In this plot, the perpendicular bisectors of the vectors intersect within the vector triangle, indicating that the orientations of the vectors are stable; however, this method shows that the vectors for the 3 limbs of the triple junction do not completely close, indicating an error in the proposed spreading rates. We suggest that the spreading rate proposed for the NW limb is probably greater than the current rate of opening and a shortened vector for this limb is required for a stable configuration of the triple junction. **C)** A simple vector addition of the full spreading rates on the NW (47 mm/yr), NE (18 mm/yr) and SW (52 mm/yr) limbs shows that the component of E-W extension on the two northern limbs roughly matches the E-W extension on the SW limb. However history of extension on the NW limb remains uncertain. NE – Northeastern limb; NW - Northwestern limb; SW - Southwestern limb; N - North; S – South.

Tables

Table 2.1 Description of the formation types on the North Fiji Basin Triple Junction

BACKARC VOLCANOES	
Bav1	**Conical volcano** Cone-shaped edifice composed of lava flows and volcaniclastic material erupted onto backarc crust, commonly with a summit crater or caldera and/or cut by dike complexes (width:height ≤5)
Bav2	**Shield volcano** Mound-shaped edifice composed of lava flows extruded onto backarc crust, commonly with a central caldera (width:height >5)
Bav3	**Dome volcano** Dome-shaped edifice composed of lava flows extruded onto backarc crust or onto an axial volcanic ridge (length:width ~1)
Bav4	**Fissure volcano** Elongate volcanic edifice composed mostly of lava flows extruded onto backarc crust, commonly with a central dike (length:width >3)
Bavf	**Volcanic field** A broad area of lava flows and volcaniclastic material surrounding a number of closely-spaced volcanoes
BACKARC RIFTS AND SPREADING CENTRES	
Upper uBar	**Axial backarc volcanic ridge** Volcanic ridge marking the active spreading center, commonly with discrete volcanic edifices (cones and domes), dike complexes, or calderas
uBac	**Axial backarc crust** Undivided backarc crust in the inner rift valley of an active spreading center
Middle mBar	**Proximal volcanic or tectonic ridge** Elongate volcanic edifice or coalesced ridges in the outer rift valley or on the flank, adjacent to an active spreading center or axial volcanic ridge
mBac	**Proximal backarc crust** Undivided backarc crust in the outer rift valley, adjacent to an active spreading center or axial volcanic ridge (may include products of off-axis volcanism)
Lower lBar	**Distal volcanic ridge** Elongate volcanic edifice or coalesced ridges on distal backarc crust (may include products of off-axis volcanism or earlier seafloor spreading from a distant ridge; commonly obscured by volcaniclastic cover)
lBac	**Distal backarc crust** Undivided backarc crust beyond the outer rift valley and flank of an active spreading center (may include products of off-axis volcanism)
RELICT BACKARC	
Upper uRbc1	**Upper relict backarc crust** Undivided backarc crust outside an identifiable area of active spreading (may be a product of intraplate volcanism, rifting of earlier backarc crust, or an unknown spreading center)
uRbc2	**Upper tectonized relict backarc crust** Intensely deformed backarc crust outside an identifiable area of active spreading
Lower lRbc1	**Lower relict backarc crust** Earliest exposed extrusive and intrusive rocks in the backarc and outside an identifiable area of active spreading
lRbc2	**Lower tectonized relict backarc crust** Intensely deformed earliest exposed extrusive and intrusive rocks in the backarc and outside an identifiable area of active spreading

Table 2.2 Summary statistics for the different volcano types of the North Fiji Basin Triple Junction (including surface area and volumes).

Volcanic Feature	Abv.	Area (km^2)	Volume (km^3)	N	Area/N (km^2)	Vol./N (km^3)	Area % of total volcanos	Vol. % of total volcanos
cone	bav1	131.54	15.59	176	0.75	0.09	14.6	5.5
shield	bav2	61.29	15.07	1	61.29	15.07	6.8	5.3
dome	bav3	72.62	8.31	76	0.96	0.11	8.1	2.9
fissure	bav4	202.52	37.70	62	3.27	0.61	22.5	13.2
flow field	bavf	431.25	209.22	1	431.25	209.22	48.0	73.2
Total	n/a	**899**	**286**	**316**	**n/a**	**n/a**	**100.0**	**100.0**

Note: Volumes are calculated using an ArcGIS polygon volume function, determined above a minimum elevation value (Zmin) for each polygon in the 1:500,000 geological map of the area. N – Number of individual mapped volcanic features. See Table 2.1 for further descriptions of mapped volcanic features.

Table 2.3 Summary statistics for the principal formation types of the North Fiji Basin Triple Junction (including total areas and estimated volumes).

Formation	Abv.	Area (km^2)	Volume (km^3)	N	Area % of total crust	Volume % of total crust
Axial back-arc volcanic ridge	uBar	189	64	1	1.67	0.82
axial back-arc crust	uBac	161	54	3	1.43	0.69
Proximal volcanic or tectonic ridge	mBar	816	517	4	7.24	6.67
Proximal back-arc crust	mBac	612	291	4	5.43	3.75
distal volcanic ridge	lBar	720	593	3	6.39	7.64
Distal back-arc crust	lBac	661	251	4	5.87	3.24
Upper relict back-arc crust	uRbc1	147	36	3	1.31	0.46
Upper tectonized relict back-arc crust	uRbc2	890	598	5	7.90	7.71
Lower relict back-arc crust	lRbc1	3754	3169	4	33.32	40.85
Lower tectonized relict back-arc crust	lRbc2	3316	2185	7	29.43	28.17
Total	n/a	**11266**	**7758**	**38**	**100**	**100**
Active back-arc rift and spreading centre total	n/a	3159	1770	19	28.0	22.8
Relict back-arc crust	n/a	8108	5988	19	82.0	77.2

Note: Area and volumes are calculated using an ArcGIS polygon volume function, determined above a minimum elevation value (Zmin) for each polygon in the 1:500,000 geological map of the area. Contacts between formations are based on mappable boundaries in high-precision digital elevation models (DEMs), supported by acoustic backscatter, and other geophysical data (magnetics, gravity). Contacts between the formations are drawn where a clear distinction with an adjacent formation can be made; they are interpolated between formations where a geomorphological or geophysical change is not evident. Unless defined by faults, all contacts are interpreted to be conformable. N – Number of individual mapped formation polygons. See Table 2.1 for further descriptions of mapped formations.

Table 2.4 List of active hydrothermal vent sites of the SW limb of the NFBTJ.

Domain	Dominant structural orientations	Activity	Vent field ID	Name Alias	Vent Sites	Organisms	Spreading Rate (mm/yr)	Host Rock	Deposit Type	Sulfides	Width of Axial Graben	Dive info
Northern	015, 020, 055, 160	inactive	Pere Lachaise	Station 4, Triple Junction	n/a	Dead mussels & clams	55.5	MORB, E-MORB, minor BABB	PMS	Yes	2 km	1989 submersible *Nautile* did not find activity; 1991 submersible *Shinkai 6500* did not find activity
Central	015, 020	active, confirmed	White Lady	17 S active site, Station 4, Triple Junction	Kaiyo, LHOS, Mussel Hill, STARMER II, White Lady	Gastropods, clam, mussel, shrimp and crabs					2 km	1988 towed camera and plume; 1989 submersible *Nautile*
Southern	020	active, confirmed	Sonne 99	SONNE 99, Sonne99, SO-99, SO99, SO 99, Station 4, Triple Junction	Corner Mound, Yogi Mound	Mussel and clams					2.5 km	1995 deep tow video and TV-grab

Note: Northern, Central and Southern domains are defined by Bendel et al., (1993). PMS = Polymetallic Massive Sulfides Full Spreading is a point value at the location of hydrothermal vent represented in mm/yr Host Rock: BABB = Back-Arc Basin Basalts, MORB = Mid-Ocean Ridge Basalts, E-MORB = Enriched (mantle) Mid-Ocean Ridge Basalts. Source: The data presented is from the InterRidge Global Vents Database, Beaulieu and Szafranski (2020), and the STAMER 89 and Yokosuka 91 research cruises (Gràcia et al., 1994).

Table 2.5 Summary statistics of each limb of the triple junction and the Central Volcanic Complex

SW limb

Abv.	Area (km^2)	Volume (km^3)	Area (%)	Volume (%)
uBac	137	42	5	3
uBar	189	64	7	4
mBar	731	477	29	31
mBac	384	186	15	12
lBac	388	175	15	11
lBar	720	593	28	39
Total	**2548**	**1536**	**100**	**100**

NE limb

Abv.	Area (km^2)	Volume (km^3)	Area (%)	Volume (%)
uBac	24	12	4	5
mBar	85	40	14	17
mBac	228	105	37	45
lBac	273	76	45	33
Total	**610**	**234**	**100**	**100**

NW limb

Abv.	Area (km^2)	Volume (km^3)	Area (%)	Volume (%)
lRbc2	**426**	**245**	**100**	**100**

CVC

Name	Abv.	Area (km^2)	Volume (km^3)
Shield volcano	Bav2	61.29	15.07
Axial ridge	uBar	188.56	63.88
Total	**CVC**	**249.85**	**78.95**
Volcanic flow field	Bavf	431.25	209.22
Caldera	n/a	5.18	0.54

Note: Areas and volumes are calculated using an ArcGIS polygon volume function, determined above a minimum elevation value (Zmin) for each polygon in the 1:500,000 geological map of the area. NE - Northeastern oriented limb; NW – northwestern orientated limb; SW – southwestern orientated limb; CVC – Central Volcanic Complex.

Table 2.6 Area-age calculations of each limb of the triple junction and the Central Volcanic Complex

SW LIMB	Approximate width (km)	Time-lapse (Myr)	Area (km^2)	Cumulative Area (km^2)	Start (Ma)	End (Ma)	Change in Area (km^2)	Change in time (Myr)	Growth rate (km^2/Myr)	Growth rate (m^2/yr)
uBac	1.5	0.1	137	1890	0.1	0.0	137	0.1	2375	2375
CVC	6.0	0.2	250	1753	0.3	0.1	250	0.2	1083	1083
mBar	7.0	0.3	731	1503	0.5	0.3	731	0.3	2715	2715
mBac	5.0	0.2	384	772	0.7	0.6	384	0.2	1997	1997
lBac	6.0	0.2	388	388	1.0	0.7	388	0.2	1681	1681

NE LIMB	Approximate width (km)	Time-lapse (Myr)	Area (km^2)	Cumulative Area (km^2)	Start (Ma)	End (Ma)	Change in Area (km^2)	Change in time (Myr)	Growth rate (km^2/Myr)	Growth rate (m^2/yr)
uBac	0.5	0.1	24	1041	0.1	0.0	24	0.1	400	400
Bavf	n/a	n/a	431	1017	0.3	0.1	431	0.2	n/a	n/a
mBar	3.0	0.3	85	586	0.4	0.3	85	0.4	218	218
mBac	4.0	0.4	228	501	0.8	0.4	228	0.8	275	275
lBac	5.0	0.6	273	273	1.4	0.8	273	1.4	196	196

NW LIMB	Approximate width (km)	Time-lapse (Myr)	Area (km^2)	Cumulative Area (km^2)	Start (Ma)	End (Ma)	Change in Area (km^2)	Change in time (Myr)	Growth rate (km^2/Myr)	Growth rate (m^2/yr)
Rifting	10.0	0.2	n/a	n/a	1.1	0.0	n/a	1.1	n/a	n/a

	Approximate width (km)	Time-lapse (Myr)	Area (km^2)	Cumulative Area (km^2)	Start (Ma)	End (Ma)	Change in Area (km^2)	Change in time (Myr)	Growth rate (km^2/Myr)	Growth rate (m^2/yr)
uBar	6.0	0.2	198	n/a	n/a	n/a	n/a	n/a	n/a	n/a
Bav2	n/a	n/a	61	n/a	0.3	0.1	n/a	n/a	n/a	n/a
CVC	**6.0**	**0.2**	**259**	**n/a**	**0.3**	**0.1**	**259**	**0.2**	**1083**	**1083**
Bavf	n/a	n/a	431	n/a	n/a	n/a	431	0.2	n/a	n/a
CVC + Bavf	**6.0**	**0.2**	**690**	**690**	**0.3**	**0.1**	**690**	**0.2**	**3000**	**3000**

Note: All spreading is assumed to be symmetrical and consistently spreading at full rates of 52 mm/yr, 18 mm/yr and 47 mm/yr for the SW, NE and NW limbs respectively. Spreading ages are calculated using the average width of the mapped formations and the spreading

rates from Huchon et al. (1994).. A fixed spreading rate is used for all formations of a limb to estimate growth rates through time. The calculated spreading ages agree well with independently determined ages of the formations based on magnetic chrons (Huchon et al., 1994) and therefore are used here to illustrate crustal growth No back-arc and spreading centre crust was mapped along the NW limb, therefore rifting is proposed for the dominant form of extension since ~1.1 Ma. Huchon et al. (1994) suggested that these spreading rates have been active for at least 1.1 Myr. Surface area (km^2) are calculated using an ArcGIS polygon volume function, determined above a minimum elevation value (Zmin) for each polygon in the 1:500,000 geological map of the area. Contacts between formations are based on mappable boundaries in high-precision digital elevation models (DEMs), supported by acoustic backscatter, and other geophysical data (magnetics, gravity). Contacts between the formations are drawn where a clear distinction with an adjacent formation can be made; they are interpolated between formations where a geomorphological or geophysical change is not evident. Unless defined by faults, all contacts are interpreted to be conformable. NE - Northeastern oriented limb; NW – northwestern orientated limb; SW – southwestern orientated limb, CVC - Central Volcanic Complex; refer to Table 2.1 for mapped formation and back-arc volcano abbreviations.

Chapter 3: A Global Database of Triple Junctions in the Oceans: Lessons for the North Fiji Basin

3.1 Introduction

McKenzie and Morgan (1969) were the first to describe triple junctions in the oceans. They used the plate boundaries to develop the nomenclature, assigning the different boundary types to active spreading centres (R=ridge), subduction zone boundaries (T=trenches), and transcurrent faults (F=faults). For example, in their classification, a triple junction where three spreading centres meet is designated RRR-type (ridge-ridge-ridge). They identified 16 different types of triple junctions. The number of triple junctions expected on the Earth's surface can be calculated simply from the number of major and minor plates. Applying Euler's equation, the 52 plates of Bird (2003) require a minimum of 106 triple junctions. In Euler's formula (V-E+F = 2), F = number of plates, E = number of plate boundaries, and V = number of triple junctions. In the case if Bird (2003), the number of boundaries for 52 hexagonal 6-sided plates is (52 x 6)/2, divided by 2 because each boundary is counted twice. This gives V-156+52 = 2 or V = 106. From a global database of triple junctions assembled in this study, we have identified 117 triple junctions at the plate boundaries, close to the number estimated from Bird's (2003) 52-plate model. They include 54 oceanic triple junctions, 25 continental triple junctions, and 38 ocean-continent triple junctions (Figure 3.1 and Appendix D). These numbers are only for the minor and major plates that are 1 to 20 million km^2, respectively (defined by Bird, 2003). However, many more triple junctions may be associated with hundreds of microplates (<<1 million km^2), which have not been mapped in detail and are not included in Bird (2003). In total, they account for a significant proportion of the crustal accretion and deformation at global plate boundaries.

A quantitative analysis of triple junctions in different settings identifies several common features. Triple junction formation and configuration are closely linked to near- and far-field geodynamic influences that drive both crustal growth and destruction of plates. Magmatically robust triple junctions, typical of oceanic spreading centres, have long been correlated to mantle plumes (Burke and Dewey, 1973). These "hot" triple junctions are thought to experience more mantle melting

and underplating by mantle melts, resulting in increased thickness and buoyancy of the crust. This type of crust retains heat and melt and allows for the emplacement of large magma chambers that produce large volcanic edifices and also may drive large-scale hydrothermal convection. Increased buoyancy of triple-junction crust due to higher temperatures related to mantle upwelling might also influence its preservation in ancient greenstone belts. However, it remains uncertain whether anomalous melting associated with triple junctions is a consequence of plume rise or if triple junctions simply tap the mantle more readily than at other types of plate boundaries.

Extensive theoretical modelling of triple junction formation has been carried out in the classic studies of McKenzie and Morgan (1969), Patriat and Courtillot (1984), and Cronin (1992). However, few studies have examined the physical attributes of actual triple junctions in the oceans, largely due to the lack of seafloor data at relevant locations. Here we have compiled the attributes of well-studied triple junctions worldwide and compare their observed stability, stress regimes and magmatic productivity to the North Fiji Basin Triple Junction (NFBTJ). The NFBTJ highlights some potentially geodynamic drivers that are related to the anomalous size, heat flow and magmatic productivity of the North Fiji Basin (e.g., Lagabrielle et al., 1997). We examine the influence of crustal type and geodynamic setting on their formation and evolution, including anomalies associated with mantle plumes and Large Igneous Provinces (LIPs). Significant volume addition at triple junctions occurs as a result of horizontal accretion due to seafloor spreading, increased height due to crustal buoyancy, and increased magmatic productivity at axial volcanic highs. We suggest that fundamental differences in triple junctions between mid-ocean ridges (MOR) and back-arc basins (BAB) may be explained by these differences and highlight observations from the specific evolution of the NFBTJ.

3.2 Previous Work

McKenzie and Morgan (1969) identified the geometries of all possible configurations of triple junctions. They constructed stability diagrams (velocity triangles) to demonstrate the most stable configurations and concluded that only 14 of 16 triple junction configurations are stable, meaning unless an external force acts on the system, the orientations of the limbs of the triple junction will remain constant. Two combinations (FFF and RRF) were identified as unstable, requiring that they continually adjust until a stable configuration is reached (McKenzie and Morgan, 1969).

Subsequent studies by Burke and Dewey (1973), York (1973), Patriat and Courtillot (1984), Cronin (1992), Bird et al. (1999), Georgen and Lin (2002), and Sissions et al. (2003) further investigated the most stable triple junction configurations. York (1973) challenged the assertion that RRF-type triple junctions are always unstable, proposing that an orthogonal arrangement of boundaries is a stable configuration. McKenzie and Morgan (1969) considered the instability of RRF-type triple junction as a consequence of the particular configuration in which the ridges form a straight line with the fault intersecting perpendicular to this line. York (1973) proposed that a stable configuration exists when the two ridges have perpendicular bisectors that intersect at the exact location as the fault's bisector. Patriat and Courtillot (1984) further introduced oblique or asymmetrical spreading and rift propagation, which are common among MOR and BAB spreading centres. Cronin (1992) proposed nine additional triple junction types and identified 125 configurations based on additional variables (e.g., dextral or sinitral transform faults; trenches that can rotate either clockwise or counter-clockwise, etc.). Cronin (1992) also considered the 3D structure of triple junctions, noting that transform boundaries and ridges have a vertical interface, whereas subduction trench boundaries have an inclined interface that can influence the behaviour of the triple junction. Cronin (1992) argued that most triple junctions are inherently unstable and that it is more important to understand how a triple junction varies over time rather than its particular configuration at any given moment. Gerya and Burov (2018) recently attempted to demonstrate the behaviour of RRR-type triple junctions through high-resolution 3-D thermomechanical numerical modeling. They found that the asymmetrical geometry of triple junctions is due to the increasing length of the slowest spreading limb while simultaneously shortening occurs at the two other faster limbs.

Factors such as crustal type, mantle structure, near- and far-field plate interactions (especially rotation), and boundary types determine the types of stresses that are accommodated by triple junctions and how the different limbs of the triple junction react. These factors dictate the long-term stability-such as the failure of a limb or extinction of the triple junction. The overall magmatic productivity of a triple junction is also dependent on highly variable magma supply to the different limbs. Burke and Dewey (1973) were among the first to consider the relationship of triple junctions to resource potential, noting triple junction reactivation of old, failed rifts as a trigger for developing basins that host hydrocarbon accumulations and mineralization. Here, we also show that high heat flow and magmatic productivity of triple junctions are crucial for hydrothermal activity in the oceans.

3.3 Methods and Data

To better understand the controls on triple junction stability, we have reviewed the literature on triple junctions in a full range of geodynamic settings in which they occur. By inspection of global geophysical datasets, we have identified 117 triple junctions in the oceans, both in continental crust and oceanic crust (Appendix D). A subset of these (46 of 117) are classified as oceanic triple junctions and are the focus of this study (listed in Table 3 and Appendix E, shown in Figure 3.2). The classification scheme used is given in Appendix C, Supplementary Table 1. Plate boundaries used for the identifications of the triple junctions are from the unpublished GEOMAR Global Microplates Atlas, modified from Bird (2003) and based on a reassessment of the global gravity gradient grid (Sandwell et al., 2014). The selection of triple junctions was also referenced to the 1:25,000,000 Geological Map of the World from CGMW (Commission for the Geological Map of the World: Bouysse, 2014) and the Tellus Database of Sedimentary Basins (Robertson CGG, 2017). Attributes of the triple junctions were assigned by inspection of the Global Bathymetric Chart of the Oceans (GEBCO Compilation Group, 2021) and the Global Multi-Resolution Topography datasets (GMRT: Ryan et al., 2019). High-resolution ship-based multibeam surveys were also inspected, with individual research cruises identified in the database. The available datasets were compared to global gravity (Sandwell et al., 2014) and global magnetics (EMAG2: Maus et al., 2009) to identify the shapes and geophysical attributes of the individual triple junctions. Spreading ridges were classified using the Global Seafloor Fabric and Magnetic Lineation database project (GSFML: Seton et al., 2014), and spreading rates were determined from magnetic picks from the Global Plate Motion Vectors database (MORVEL: DeMets, et al., 2010). Additional spreading rate data constraints were taken from Seton et al. (2020). These data are compiled in, Appendix C: Supplementary Table 2 and 3 and Appendix D: Global triple junction database.

Table 3.1 list the attributes of Oceanic triple junction in the database (summarized from Appendix E) triple junction ID, latitude and longitude of the triple junction; general geolocation; the geodynamic setting; known triple junction names; general triple junction type, and plate names. Additional data includes the orientation of each limb of the triple junctions, the angle between each limb, the certainty of limb boundary classification; initiation age of the triple junction; spreading

rate category and average spreading rate within a 100-km radius (see explanation below); the vertical global gravity gradient (mgal/m) at the centre of the triple junction; the research cruises ID(s) that surveyed within 1 km of the triple junction centre; the volume addition within a 100-km radius (see below); known hydrothermal vent fields within a 100-km radius; the number of vent fields and any associated volcanos; the names of overlapping hotspots within 100 km, 500 km, and 1000 km; the name, location and age of large igneous provinces (LIPs) coincident with the triple junction; the name of sedimentary basins coincident or otherwise associated with the triple junction from the Tellus Database; seabed lithology; other geomorphological features; and important references. Detailed descriptions of abbreviations and descriptions is contained in Appendix C, Supplementary Table 1.

The Triple junction classifications are based on boundary types (R=ridges, T=trenches, and F=faults) and are assigned where the limbs are clearly defined (Appendix D). If the boundary type is unclear or has attributes of structures other than ridges, faults or trenches the letter X is assigned (e.g., RTX). To capture the large variation in boundary types, an additional data column was included which contains 34 different specific boundary types (e.g., CMAF = continental margin arc fault: see Appendix C, Supplementary Table 1 and Appendix D). The triple junction classifications are assigned a "certainty" score based on the number of limbs that are clearly distinguished in the inspected data: '0' for a low degree of certainty (all 3 limbs are uncertain), '1' for a triple junction with 1 limb identified, '2' for 2 limbs identified, and 3 for all limbs identified.

In each case, the limb, plates and interlimb angles are identified beginning with the first limb east of north (Limb 1) and continuing clockwise from Limb 2 and 3 (Figure 3.3). Plates A, B and C are assigned beginning to the right of 'Limb 1' and progressing clockwise. The cited spreading rate refers to the maximum total separation of the two dominant plates, generally classified as slow (<50 mm/yr), intermediate (50-80 mm/yr), and fast (>80 mm/yr) (Seton et al., 2020). These data are from the global plate vector data (MORVEL: DeMets, et al. 2010), but may also be from published data, often established from magnetic chrons (GSFML: Seton et al., 2014). Where accepted names have been published, they are also assigned. Different research cruises that have focused on specific triple junction locations are identified (Cruise ID from the GEBCO Compilation Group, 2021); however, only 24 of the triple junctions in the database are directly

covered by ship track data. Spatial relationships to large igneous provinces (LIPs: Johansson, et al., 2018) and mantle plumes (Whittaker et al., 2015) are also referenced in the compiled data. Additional attributes of the triple junctions listed in Appendix D and E were compiled from global seafloor sediment lithology (Dutkiewicz et al., 2015) and global seafloor geomorphology (Harris et al., 2014), including the identification of associated or nearby rift valleys, trenches, abyssal hills and plains, plateaus, orogenic crust, and sedimentary basins.

Using the data compiled in Appendix E, we derived additional attributes such as magmatic productivity and average spreading rates. Crustal growth and volume addition associated with the individual triple junctions were estimated by measuring the volume of crust in a 100 km radius surrounding the triple junction. Volumes were calculated using an ArcGIS polygon volume function, which calculates the volume and surface area between a polygon and a surface defined by a triangular irregular network (TIN). The volume addition at each triple junction was determined between the minimum elevation value (Zmin) of the TIN and the overlying polygon. To obtain a representative spreading rate for each triple junction, we used a 100-km radius circle to average the values published in Seton et al. (2020) (Table 3.2, Table 3.3, Appendix E and see Appendix C, Supplementary Table 1 for further spreading rate data). Example of these calculation and specific examples for individual limb rates of select triple junctions are discussed below (Chapter 3.6).

3.4 Summary Statistics

Half of the triple junctions in the oceans are in oceanic crust (O-type). Of these, 9 have at least 1 limb that is incompletely defined and are excluded from further investigation. Among the remaining 46 oceanic triple junctions, there are four main types: FRR-type (n=14), FTT-type (n=12), RRR-type (n=10) and RFF-type (n=6). Four other triple junction configurations were also identified (TTT-, RTT-, TFF-, and FFF-, type), with one example each. 22 are located at mid-ocean ridge spreading centres, 15 are in arc-trench systems (e.g., in island arcs), and 9 are in back-arc basins (mostly at back-arc spreading centres). Although most of the oceanic triple junctions have at least one spreading centre boundary, 31 are bound by faults, including 17 with at least one trench boundary. The dominant types are consistent with previous compilations (e.g., Mitchell et al., 2011), although the specific geodynamic settings were not previously identified. RRF, RRR, and RFF-type triple junctions are confined to mid-ocean spreading centres and back-arc basins. TTF-type triple junctions are found in both arc-trench systems and back-arc basins. TFF-type and TTT-type are restricted to arc-trench systems, and RTT-type and FFF-type are restricted to back-arc basins.

Fourteen of the triple junctions in the oceans are in continental crust (C-type), either in continental back-arcs or rifted margin settings. Many of the triple junctions along continental margins are catchments for sediment and coincide with well-known sedimentary basins (e.g., North New Guinea Basin, Gulf of California, and Red Sea). They are commonly dominated by strike-slip regimes. Six are in collisional zones, and 3 are related to continental margin arcs (see Appendix D). Many of these triple junctions have at least one undefined limb (18 of 24 continental triple junctions). Five are FFF-type triple junctions and 2 are FRR-type. There are 38 triple junctions at ocean-continent boundaries (OC-type) mostly occurring at continental margin arcs and in continental margin back-arc basins; 8 have at least one undefined limb, and 18 triple junctions are FTT type (Appendix D).

Although most of the triple junctions in the oceans are still active, some in the continental margin and ocean-continent settings have an initiation age as old as 150 Ma (e.g., an XFF-type oceanic triple junction off the coast of Mozambique: Seton et al., 2020). The longevity of some triple

junctions suggests that their structural integrity and function may be preserved long after they are initiated. This is supported by the number of buried triple junctions that have been documented with the most recent global vertical gravity gradient (Matthews et al., 2011; Macleod et al., 2017).

3.5 Results

Well-known examples of RRR-type triple junctions are in the Indian Ocean (Rodriguez Triple Junction; #71 in Table 3.1) and at the East Pacific Rise west of the Galapagos Islands (Galapagos Triple Junction; #88). Examples of FRR-type triple junctions are in the Atlantic Ocean (Fifteen-Twenty Fracture Zone Triple Junction; #51, Arabian Sea (Aden-Owen-Carlsberg Triple Junction; #73), and the eastern Pacific Ocean (Mendocino Triple Junction; #96). An example of an RFF-type triple junction occurs at the spreading axis of the South Atlantic (Bouvet Triple Junction; #80). A RTT-type triple junction (#44) is located north of the Lau Basin, where the Tonga and Niuafo'ou microplates meet the subducting Pacific Plate along the Tonga trench. An example of a FTT-type triple junction (#114) is located in the Mid-Atlantic, where the Greater Gonave, Caribbean and North American plates meet. A TFF-type triple junction (#53) is located in the southern Atlantic Ocean between the South America, Antarctica and Sandwich plates, and an example of a TTT-type triple junction (#24) can be found where the Manus-Kilinailau trench, Mussau trough and the Manus trench meet.

The relative importance of triple junction types in different geodynamic settings is illustrated in Figure 3.4, which shows the proportion of triple junctions in the three main oceanic settings (mid-ocean ridge, back-arc basin, and arc-trench systems). The plot illustrates the importance of RRR-type, FRR-type, and RFF-type triple junctions at MOR and back-arc spreading centres, and fault or trench boundaries in arc-trench systems. The accurate classification of the triple junctions is highly dependent on the availability of ship-based multibeam, with about half of the triple junctions crossed by at least one ship track from at least one research cruise. The clusters in Figure 3.4 are related to different crustal types, stress regimes, and magmatic budgets. Fault (F) boundaries are the most common boundary type in 33 of 46 triple junctions and in all three geodynamic settings. The majority of the triple junctions classified as 'arc-trench systems' with trench boundaries (T) are found along the Izu Bonin-Mariana arc-back-arc system and within the Melanesian Archipelago (10 of 15). Ridge (R) boundaries occur in 31 of 46 oceanic triple junctions.

The geometry of the different triple junction types, represented by the angles between each limb, are shown in Figure 3.5. A high proportion of the spreading- centres in triple junctions of MOR settings are at right angles to the other limbs (90 degrees or 270 degrees; up to 70 degrees). In contrast, the geometry of triple junctions in arc-trench system and back-arc basin settings show a much greater range of orientations, consistent with oblique spreading or strike-slip deformation in collisional settings. As a result, triple junctions in back-arc basins and other subduction-related settings are far less stable than triple junctions at mid-ocean ridges (e.g., York, 1973).

The inflation of the crust at triple junctions is associated with spreading ridges, and three processes of volume addition along ridge boundaries are illustrated in Figure 3.6. These processes are linked and thought to be controlled by significant heat flow anomalies and tectonics. Additional volume of crust typically seen along fast spreading MORs is caused by a hot rising mantle, crustal thinning, and an upward bow in the crust (Figure 3.6A). At slow spreading ridge, where tectonic extension exceeds magmatic extension (Sinton and Detrick, 1992), pathways are created in which repeated injection of dykes into faulted crust causes inflation of the ridge, as well as significant point source magmatism in the neovolcanic zone (Figure 3.6B). This may be compounded by volcanic flows and or edifices resulting in a vertical accumulation of volcanic masses (figure 3.6C). Some of the inflated ridge segments at triple junctions are clearly influenced by their proximity to mantle plumes or hot spots.

We estimated volume addition surrounding triple junctions in the oceans by measuring the volume of the crust within a 100-km radius of the triple junction (Table 3.2 and Figure 3.7). The approach provides a first-order approximation of volume addition associated with the 46 oceanic triple junctions, which are grouped by geodynamic setting and triple junction type in Figure 3.7A. Volumes were calculated using an ArcGIS polygon volume function, which calculates the volume and surface area between a polygon and a surface. The surface, and terrain in this cases is defined by a triangular irregular network (TIN). The volume addition is measured between the minimum elevation value (Zmin) of the TIN and the overlying polygon. The datum used (Z-min) in each case is described in the figure captions and data Tables. The majority of triple junctions at mid-ocean ridges and in back-arc basin are characterized by a volume addition relative to background (beyond 100 km radius) of less than 100,000 km^3. Much greater volume addition (more than

100,000 km^3) is associated with triple junctions close to continental margins and arc trenches because of the overall greater crustal thickness. The average volumetric anomaly for 1 Myr of crustal growth associated with a RRR-type triple junction is 22,000 km^3 or about 0.02 km^3/yr. For comparison, typical horizontal accretion at mid-ocean ridges is on the order of ~0.03 km^3/yr for every 100 km of ridge length (e.g., assuming global accretion rates at MORs between ~18-21 km^3/yr and a total MOR length of ~60,000 km: Deligne and Sigurdsson, 2015; LaFemina, 2015).

The different triple junction types at MOR settings (e.g., RRF, RRR, RFF: Figure 3.7B show more uniform volume addition than in arc-trench systems; however, there are variations (e.g., Figure 3.7A and B) especially among the triple junctions with volume addition of <100,000 km^3: Figure 3.7C). On average, RFF-types have the largest volume addition at MOR settings. FRR-type triple junctions in large back-arc basins like the NFB have comparable volume addition to those located along mid-ocean spreading centres. In both cases, there is a close association of volume addition with mantle plumes such as near Galapagos (triple junction #91).

An average spreading rate within a 100-km radius of each triple junction was calculated using the global full-spreading rate data from Seton et al. (2020) (Appendix C, Supplementary Table 1). The results and the spreading-rate designation (slow, intermediate and fast) are presented in Tables 3.1 and 3.2. 41 of the 46 oceanic triple junctions have average spreading rates of 15.8 to 158.6 mm/yr, with a mean of all triple junctions of 75 mm/yr (standard deviation of 46.8 mm/yr). This is more than double the global MOR average (18-21 mm/yr: Deligne and Sigurdsson, 2015). The average spreading rates are grouped according to the 8 different triple junction types in Figure 3.8A. RFF-type triple junctions spread at slow rates (avg. 49.6 mm/yr). FRR- and FTT-type triple junctions spread on average at intermediate speeds, 53.8 and 76.1 mm/yr, respectively. RRR-type triple junctions have the highest full-spreading rates of 118 mm/yr and are associated with microplates bordering fast-spreading mid-ocean ridges, including the Galapagos microplate (triple junction #91), the Easter Microplate (#92) and the Juan Fernandez Microplate (#93 and #94) (Appendix E). Spreading rates vary between the individual limbs of triple junctions, owing to partitioning of strain in non-isotropic stress regime, but a detailed comparison is not possible because of the lack of spreading rate information.

A slow-spreading rate typically results in a deep rift valley with rough and faulted terrain, whereas a fast-spreading centre may have less relief overall but possibly significant regional inflation of the crust (e.g., MacDonald, 1982). However, there is no obvious correlation between volume addition at triple junctions and spreading rates. Spreading rates show the greatest variability in triple junctions at mid-ocean ridges, from very fast to slow (Figure 3.8A), whereas spreading rates at 2/3 of triple junctions in back-arc basins fall into the relatively narrow range of intermediate and slow spreading (average of ~68 mm/yr). Triple junctions with volume addition of <100,000 km3 have full spreading rates ranging from 18.8 to 158.6 mm/yr (Figure 3.8C). Two very similar triple junctions with the same spreading rates can have very different crustal volumes. For example, RRR-type triple junctions at the Easter microplate and Juan Fernandez microplate (#92 and #94) are located only 1,000 km apart and have the same fast spreading rates (~158 mm/yr), but triple junction #92 has a volume addition of 23,533 km^3, whereas #94 shows nearly twice the volume addition (54,620 km^3). More research is needed to understand this variability.

In Table 3.3, we compare volume addition with spreading rate at several representative MORs spreading centres and triple junctions in the Pacific Ocean, the North Fiji Basin, and along the Mid Atlantic Ridge. We selected three representative MORs (i) along the EPR (fast spreading), (ii) along the GSC (intermediate spreading) and (iii) along the MAR (slow spreading), based on the classification of Carbotte et al. (2016) with spreading rates similar to that of average spreading rates of the triple junctions. The comparison shows a large range of volume addition for the different types of boundaries, but on average the inflation is nearly 1.7 times greater at the triple junctions than at the MOR segment (see Table 3.3).

The fast-spreading EPR is characterized by an 8-10 km wide elongated axial high (Carbotte et al., 2016) with an average spreading rate of 99.4 mm/yr. The volume addition across at a central 100-km radius portion of the ridge at 45ºS, 22ºE, is 15,571 km^3. A typical RRR-type triple junction with a comparable average spreading rate (e.g., 120.4 mm/yr at #75 in Table 3.3 and Appendix E) has a volume addition of 29,443 km^3 measured at the central 100-km radius portion of the ridge that is nearly is nearly twice that of the EPR and influences 305 km of the spreading ridge. The intermediate-rate GSC at 104ºS, 13ºE comprises a series of rifted axial highs and shallow rift valleys (Carbotte et al., 2016) with a spreading rate of 43.9 mm/yr. The volume addition across at

a central 100-km radius portion of the ridge has a volume of 19,327 km^3 and influences 230 km of the spreading centre. A typical triple junction with a comparable average spreading rate (e.g., 71.4 mm/yr at # 86 in Table 3.1 and Appendix E) has a volume of 62,958 km^3 measured at a central 100-km radius portion of the triple junction, nearly 3 times larger than the volume addition of the GSC segment and influences ~225 km of the associated spreading centres. The slow-spreading MAR at 93°S, 2.4°E has a spreading rate of 25.8 mm/yr and volume addition measured at a central 100-km radius of 50,768 km^3, influencing 195 km of the spreading centre. A typical triple junction with a comparable average spreading rate (e.g., 28.6 mm/yr at #51 in Table 3.3 and Appendix E) has a volume of 53,933 km^3, similar to but still larger than the volume addition of the MAR example, and inflation that influences ~203 km of the associated spreading centres.

To determine whether there are any possible links to large igneous provinces (LIPs) or hotspots we also examined their spatial relationships. Appendix E and Figure 3.9 show the number of hotspots within 100, 500, and 1000 km of a triple junction. Globally, 16 triple junctions overlap with hotspots; 4 triple junctions (#31, 55, 61, and 107) are within 100 km of a hotspot (Appendix D: Johansson et al. 2018; Ernst and Buchan, 2003; Fletcher et al., 2018). Using the hotspot database of Whittaker et al. (2015) (Appendix A, Supplementary Figure 2), 36 triple junctions are in "zones of potential interaction" within 1,000 km of hotspots (see Fletcher and Wyman, 2015); 9 are within 500 km, and 1 is within 100 km of a hotspot (Appendix D). Figure 3.9 shows the distribution of oceanic triple junctions and the scale of the three zones of potential interaction. 2% within 100 km of a hotspot (Figure 3.9A), 9% within 500 km (Figure 3.9B), and 35% within 1,000 km (Figure 3.9C). Most of the plume-influenced triple junctions are found along mid-ocean spreading centres, except for the arc-trench triple junction influenced by the Samoa hotspot (#44 in Appendix E, Figure 3.9C). Of the 22, oceanic-type triple junctions at MORs, over 70% (16 triple junctions) are within 1,000 km of a mantle plume.

As a result of increased spreading, triple junctions in proximity to a mantle plume are commonly centres of increased magmatic productivity. This is evidenced by the large volcanic centres commonly found at the intersections of the actively spreading limbs of the triple junctions. Examples of such large volcanoes include the Lobster and Dugong volcanos in the Lau Basin (#104 in Table 3.1), the Fayal/Faial stratovolcano (and associated cones and domes) along the

northern Mid-Atlantic Ridge (#82 in Table 3.1), and the Plat Pays and Morne stratovolcanoes that make up the Caribbean island of Dominica (#52 in Table 3.1) (see Tables 3.1; Appendix C, Supplementary Table 4 and 5). All are within 100 km of a region of mantle upwelling. The Lobster volcano is estimated to be ~600 km^3 in volume (Ryan et al., 2022). The Dugong volcano has a diameter of 45 km with a 5 km-diameter caldera. Fayal/Faial (a subaerial stratovolcano), is 1 km in height, and has an area of 173 km^2, with an estimated volume of ~100 km^3. These are comparable to some of the largest back-arc volcanoes in the oceans (e.g., ~67 km^3 Niuatahi volcano in the NE Lau Basin, with a 7 km radius and height of 1.3 km: Anderson et al., 2021; ~126 km^3 Nifonea axial volcanic in the nearby Coriolis Troughs: Anderson et al., 2016). Many of these volcanoes have distinctive summit calderas. The Plat Pays and Morne volcanoes have an elevation of 940 m above sea level and contain at least a dozen small (under 1 km diameter) calderas/craters that collectively have a volume of at least 10 km^3 (Global Volcanism Program, 2013). Atop the Fayal/Faial volcano is a 400-m deep caldera, which is 2 km in diameter.

The significant volume addition at triple junctions, as a result of enhanced seafloor spreading, increased crustal buoyancy, and magmatic productivity should also be reflected in increased hydrothermal activity. The average temperature for the observed hydrothermal vent sites is 273^{oC}. The average depth of MORs is 2,500 m (below sea-level) (Macdonald, 2019), and the average depth of the vents identified at a triple junction is 2,250 m. Triple junctions represent ~5% of the total length of the global MOR. However, the frequency of hydrothermal vents is significantly greater than elsewhere on the MORs: 29% of all known (confirmed and inferred) hydrothermal vent fields are within 100 km of a triple junction (InterRidge Global Vents Database; Beaulieu and Szafranski, 2020; Appendix C, Supplementary Table 4; Appendix D and E). Of the 197 vents fields at this distance from a triple junction, 146 are in oceanic crust (i.e., at a mid-ocean spreading centre), 38 are within 100 km of a back-arc basin spreading centre, and 38 are in arc-trench systems. The smaller number of known vent fields at triple junctions in arc and back-arc settings, despite the large magmatic productivity suggest that these triple junctions are likely underexplored for hydrothermal activity.

3.6 Comparisons with the North Fiji Basin Triple Junction

The NFBTJ has an average full spreading rate of 71.4 mm/yr, as defined in Seton et al. (2020), a volume addition of 62,958 km^3, and 4 known hydrothermal vent fields with polymetallic sulfides deposits. The SW limb is a well-defined spreading centre with a spreading rate of 52 mm/yr (Huchon et al., 1994). The NW is a tectonically-controlled limb, with minor magmatic productivity and a spreading rate of 47mm/yr (Huchon et al., 1994). The NE limb is the slowest of the three limbs (18 mm/yr) (Chapter 2). The NE and SW limbs have distinctive neovolcanic zones but there is no discernible neovolcanic zone in the NW limb. A comparison of the NFBTJ with other well-established oceanic triple junction shows the important similarities between the structures developed in mature back-arc basins and at the mid-ocean ridges. The NFBTJ is a close analog of MOR-type triple junctions but manifests the influence of plate rotation typical of convergent margins. The NFBTJ was initially identified as an RRF-type triple junction (Table 3.1, Appendix E), and applying the criteria of York (1973), this is considered unstable because the two assigned ridges are outside the proposed stability range of 90º +/- 10º. However, the boundary between the Balmoral Reef and Conway Reef, defined initially as an oceanic back-arc fault (OBAF) is now recognized as an active spreading centre (this study, Chapter 2). Careful mapping of the NFBTJ shows that it has evolved from an unstable RRF- to an RRR-type triple junction.

A significant difference between the NFBTJ and other back-arc basin triple junctions is related to the rotation of the New Hebrides microplate. Because the NFB is opening in response to the retreat of the New Hebrides Arc, and not simply a direct consequence of slab rollback at the Australian margin (Schellart et al., 2002). The NFBTJ is more similar to a MOR-type triple junction, with little or no direct influence from a subducting slab. This is consistent with the large size and age of the NFB, which bears a closer resemblance to crust formed at a mid-ocean ridge than to crust in back-arc basin. Like other oceanic arc-back-arc triple junctions, the NFBTJ has a much wider range of inter-limb angles (from 44º to 186º for most back-arc basin triple junctions: Figure 3.5), consistent with plate rotation and asymmetry being significant factors in their construction and evolution.

We also compared the NFBTJ to three well-studied triple junctions; i) the Mangatolu triple junction, located in the Lau Basin (not recorded in Table 3.l), ii) the Rodriguez triple junction in the Southern Indian Ocean (#71), and iii) a well-known triple junction on the Juan de Fuca plate (#96) illustrates the similarities and differences between the NFBTJ and a young back-arc basin triple junction (Mangatolu), a mature and very stable MOR triple junction (Rodriguez), and a very dynamic triple junction in the Juan de Fuca. All three examples include oceanic back-arc spreading centres and associated transform faults boundaries. The MTJ is located in the Lau basin at the intersection of the Tonga and Niuafo'ou microplates in the southwest and an unnamed microplate in the north (Mensing, 2019). The Rodriguez triple junction is at the intersection of the Capricorn, Antarctic, and Somalia plates, which are much larger plates than those around the NFBTJ. The Juan de Fuca triple junction is located at the intersection of the Pacific Plate and the Gorda and Juan de Fuca microplates, which are remnants of the Farallon paleoplate.

Like the NFBTJ, the MTJ is classified as a RRR-type triple junction, and each limb would be classified as an Oceanic Back-Arc Spreading centre and associated transform fault (OBASCt: Appendix C, Supplementary Table 1). The RTJ is also a RRR-type triple junction (McKenzie and Sclater, 1971; Munschy and Schlich, 1989), and each limb is classified as an OCSt (Oceanic Spreading centre with associated transform faults: Appendix C, Supplementary Table 1). Magnetic data for the RTJ suggest a transition from FRR- to an RRR-type (Klischies, 2022), similar to the NFBTJ. The JDF triple junction is a FRR-type triple junction composed of two boundary types: an Oceanic Fault with associated transforms (Oft) and two OSCt boundaries. The first limb is the eastern extension of the Blanco Fracture Zone.

Although the much younger than the NFBTJ, the MTJ has very similar spreading rates. The northern limb has a full spreading rate of 37 mm/yr, the southern limb has a rate of 30 mm/yr, and the western limb is mainly in a stage of tectonic rather than magmatic extension (Mensing, 2019). Like the NW limb of the NFBTJ, the western limb of the MTJ shows no signs of active volcanism but is characterized by highly tectonized back-arc crust. The NFBTJ is a volumetrically large triple junction (62,958 km^3) this is consistent with its longevity, and the growth rates of ~0.022 km^3/yr per 100 km at the Central Volcanic Complex (Chapter 2) are several times higher than have been estimated for the currently active spreading centres in the MTJ (0.0013 km^3/yr: Mensing, 2019).

The cumulative volume of triple junction formations are similar, formations at the NFBTJ is 8,044 km^3 over 10,000 km^2 (Chapter 2), MTJ is estimated to be 6,895 km^3 over 9,000 km^2 (Mensing, 2019). Unlike the NFBTJ, MTJ lacks a central shield volcano at the intersection of the three limbs. However, there is extensive off-axis volcanism along the MTJ in response to the distributed extension and microplate rotation characteristic of the opening of the NE Lau Basin (Stewart et al., 2022). Also unlike the NFBTJ, which is far from the nearest subduction zone, the emergence of the MTJ is strongly influenced by the nearby subducting Pacific Plate with rock compositions dominated by BABB compared to MORB in the NFB (Tain et al., 2011; Zhang et al., 2018; Beaulieu and Szafranski, 2020; Oh et al., 2021; Haase et al., 2022). Proximity to the Samoan hot spot suggests that mantle plume material may be present in the vicinity of the MTJ, and active hydrothermal systems have been discovered along both the NE and southern limbs.

The RTJ is of a similar size to the NFBTJ, although they have very different geometries, with a distinctive "T" shape and limbs at 186 º, 241 º and 334 º in the RTJ. In contrast, the NFBTJ has nearly identical 120-degree angles between neighbouring limbs. The unusual configuration of the RTJ is explained by larger-scale tectonic controls in the Indian Ocean (Klischies, 2022), whereas smaller microplates are responsible for the configuration, of the MTJ. The far-field dynamics of the Indian Ocean are responsible for generally slower average spreading at the RTJ (46.3 mm/yr) than at the NFBTJ (71.4 mm/yr: Seton et al., 2020). The Southeast Indian Ridge (SEIR) is spreading at an intermediate-spreading rate of 53 mm/yr, the Central Indian Ridge (CIR) is spreading at 22 mm/yr, and the Southwest Indian Ridge (SWIR) is a slow-spreading ridge at 12 mm/yr. In contrast, the NFBTJ has two intermediate-rate spreading limbs at 52 mm/yr and 47 mm/yr and one slow-spreading limb at 18 mm/yr, although we have shown that the proposed spreading rate of the NW limb results in an unstable configuration and probably is too high. As in the NFBTJ, the SWIR limb lacks an axial neovolcanic zone, and the CIR limb is also dominated by tectonic extension, similar to the NE and NW limbs of the NFBTJ. Unlike the RTJ has remained remarkably stable throughout its history. Volume addition at the RTJ (49,714 km^3) is similar to that at the NFBTJ (62,958 km^3) (Table 3.2), and both triple junctions are host to a number of vigorous hydrothermal vent fields (Klischies, 2022; Beaulieu and Szafranski, 2020). However, some aspects of the RTJ may reflect proximity to a regional hotspot. The RTJ is within 1,000 km of the Rodrigues hotspot and likely has been influenced by the associated mantle upwelling.

The triple junction at the intersection of the Blanco Fracture Zone with the Gorda Ridge and southern Juan de Fuca Ridge (JDF) also have 'T' shapes with limbs at 78°, 211°, and 285°, similar to the RTJ. The average spreading rate of the triple junction is 66 mm/yr (Seton et al., 2020), with the Gorda Ridge spreading at a full rate of 56 mm/yr. The Gorda Ridge has a rift valley of 1 km depth at the centre, similar to a slow-spreading ridge, with abundant seismicity indicating a thicker, stronger lithosphere (Hooft and Detrick, 1995). The valley depth also increases with distance from the triple junction centre. In contrast, the southernmost segment of the Juan de Fuca ridge is characterized by a rifted axial high, typical of fast- and intermediate-rate spreading ridges. The third limb, the Blanco Fault Zone, has offset Juan de Fuca Ridge segment (JDF) by about 400 km and also exhibits localized spreading along the transform (Braunmiller and Ná´bělek, 2008). Because the JDF spreading segment is terminated by a transform fault, a large volume of melt has not developed here, and the crust is not inflated as at the RRR-type triple junctions, NFBTJ and RTJ. Instead volume addition at the termination of the JDF spreading centre is less than 8,000 km^3, or about 8 times smaller than the NFBTJ. Active volcanism occurs along the North Gorda Ridge segment and Southern Juan de Fuca segment, with localized hydrothermal activity, but much less than at the NFBTJ and RTJ (Beaulieu and Szafranski, 2020). The possibility of seafloor spreading within the fracture zone (Braunmiller and Ná´bělek, 2008) may indicate that similar processes are possible in the analogous Fiji Fracture Zone at the NFBTJ. The triple junctions at the intersections of the Blanco Fracture Zone with the Gorda Ridge and southern Juan de Fuca Ridge are within a 1,000 km of the Cobb hotspot, but it is unclear to what extent the hotspot might have influenced the ridge segments, given the limited volume addition and the geochemistry of the associated melts (MORB-dominated and lacking a plume signature) (Chadwick et al., 2005).

The comparisons of the NFBTJ to typical MOR triple junctions suggests that it rapidly evolved from a subduction-dominated setting to a mature back-arc basin with distinctive MOR-like characteristics. The NFBTJ is a volumetrically large triple junction with geochemical signatures typical of MORB and OIB (ocean island basalt) rather than BABB, and lacking the influence of a slab input (Johnson and Sinton, 1990; Oh et al., 2021). The comparison with other oceanic triple junctions, however, shows considerable variability in triple junction configuration and. One limb of the triple junction is almost always dominant, reflecting prevailing regional stress regimes, but

all configurations appear capable of evolving rapidly (e.g., in <1 million years), becoming more or less stable over time.

3.7 Conclusions

The global database highlights a number of important controls on triple junction configuration that are manifested in the NFBTJ. Some triple junctions in mature back-arc basin and MOR spreading centre environments, such as the NFBTJ and RTJ, have large crustal volumes reflecting their longevity and probable link to upwelling mantle. In contrast, other triple junctions that are still emerging (e.g., as at the MTJ) are relatively small. Map data that are now readily available for some triple junctions allow quantitative analysis of their evolution, which differs according to geodynamic setting, triple junction type, limb orientation and boundary types, microplate interactions, average spreading rates and proximity to mantle plumes. These in turn influence magmatic productivity, and hydrothermal activity. An important finding is the growth of large triple junction boundaries in back-arc basin settings are similar to those of MOR. The example of the NFBTJ is nearly identical to MOR-type triple junctions and more closely related to large-scale plate interactions rather than subduction along the New Hebrides Trench. Oblique collision and rotations, which are common in subduction settings commonly result in transient microplate configurations and unstable triple junctions whereas stresses typical of MOR spreading centers are commonly isotropic, resulting in more stable triple junctions (e.g., RRR-type). The long-term evolution of the NFBTJ appears to have been an important contributing factor in the stability and size of the North Fiji Basin, with implications for localizing magmatic productivity and hydrothermal activity in other large back-arc basins.

Figures

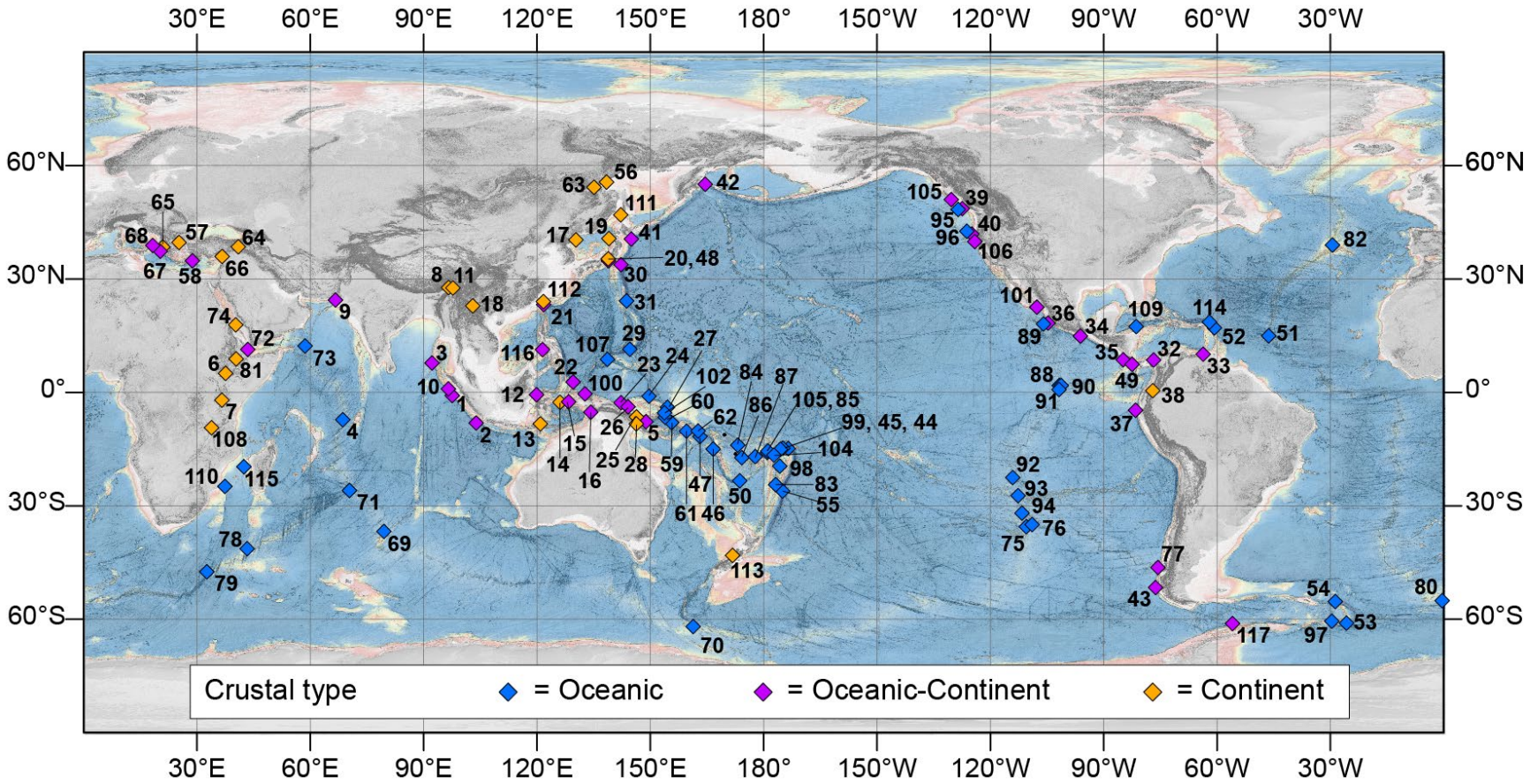

Figure 3.1 Global distribution of the 117 triple junctions included in the Database of Global Triple Junctions (ID numbers correspond to Appendix D). Coloured icons distinguish crustal types: continental crust (yellow, n=25), oceanic crust (blue, n=54), and ocean-continent crustal boundaries (fuchsia, n=38)

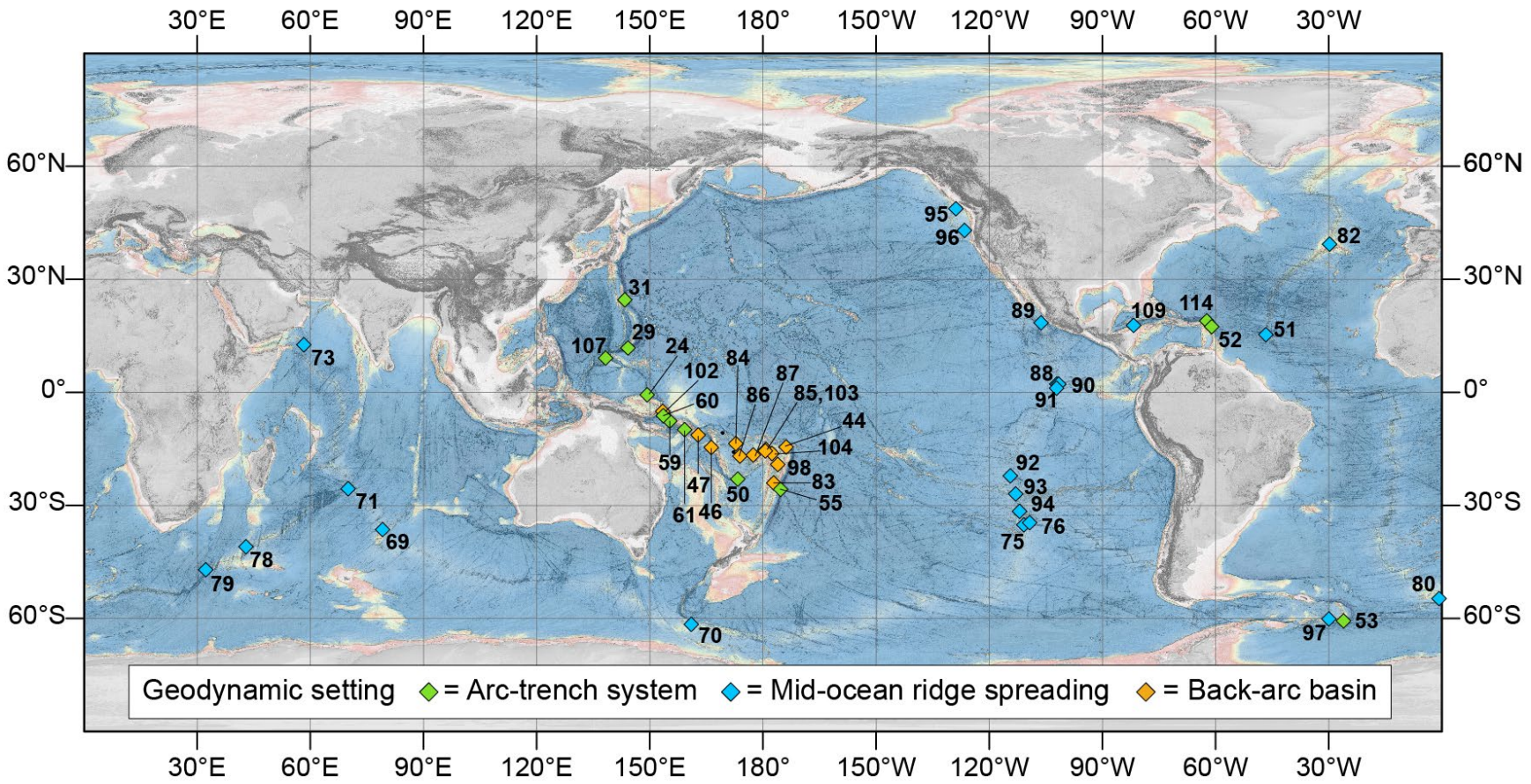

Figure 3.2 Global distribution of the 46 oceanic triple junctions analyzed in this study (Table 3.1; Appendix E). Coloured icons distinguish geodynamic settings: back-arc basin (orange, n=9), mid-ocean ridge spreading centre (blue, n= 22), and arc-trench systems (green, n=15).

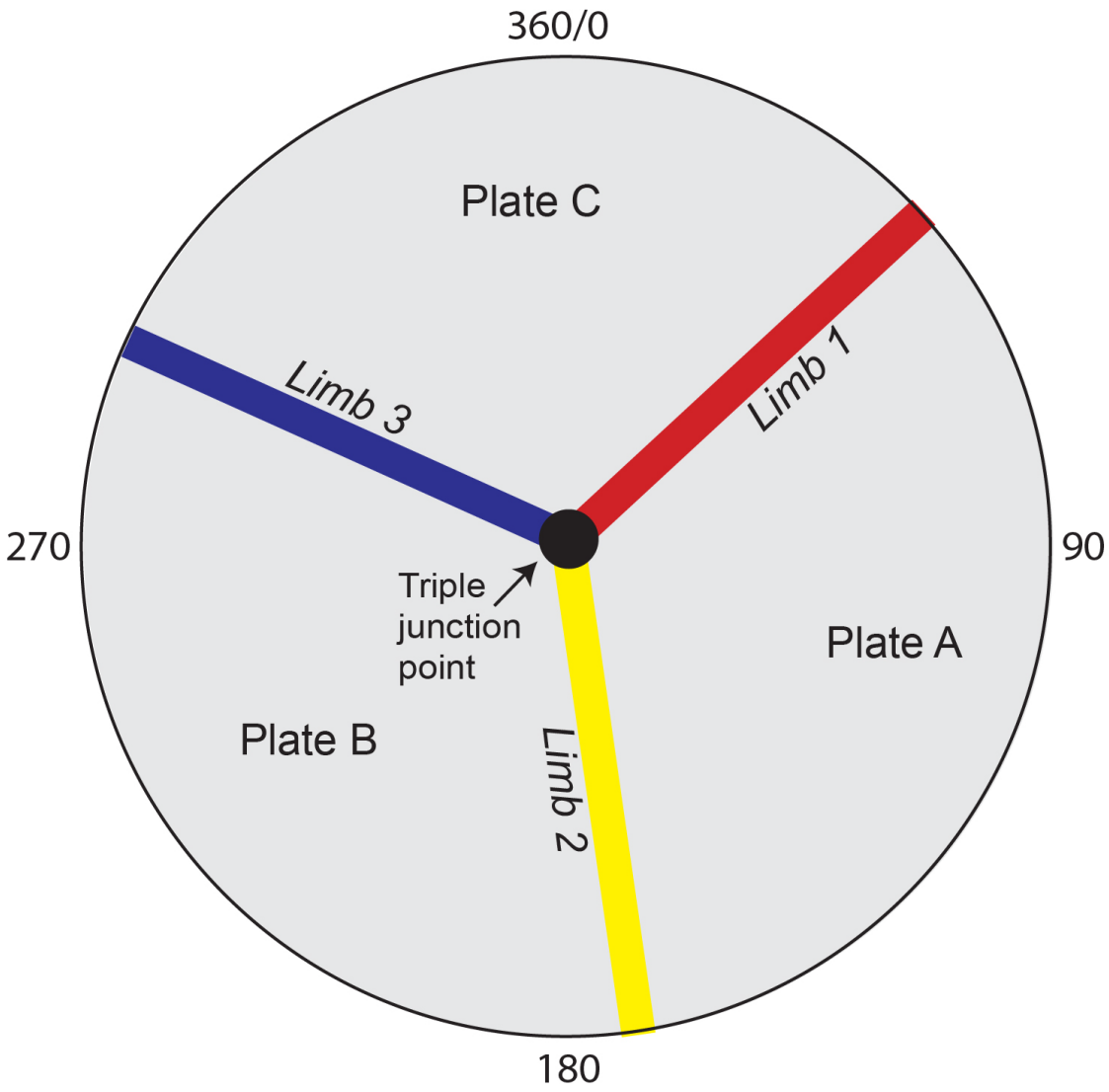

Figure 3.3 Illustration of segment labelling used in the global database of triple junctions. The first limb east of north is assigned limb 1, followed by limb 2 and limb 3 in a clockwise rotation. Plate A is the first plate clockwise from limb 1 (i.e., between limb 1 and limb 2). Plate B is between limb 2 and limb 3. Plate C is located between limb 3 and limb 1.

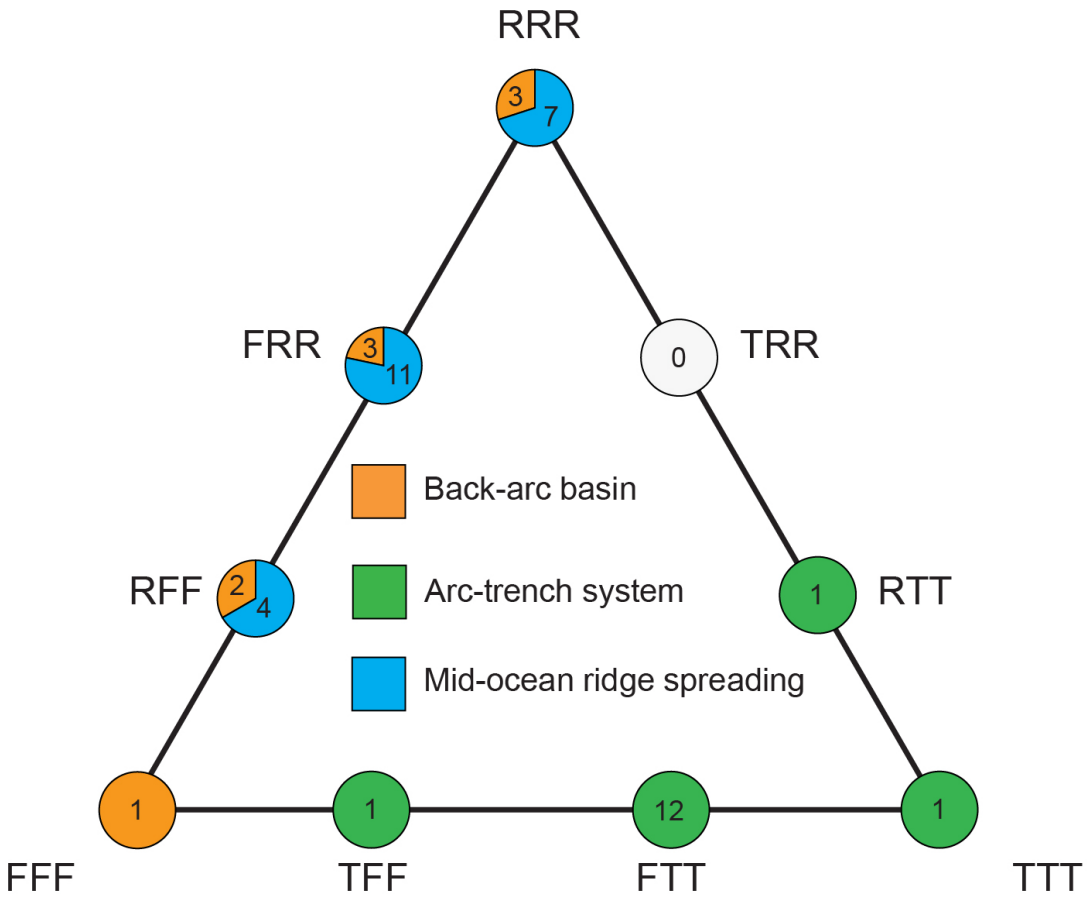

Figure 3.4 Schematic illustration of the distribution of triple junction types in different geodynamic settings. Numbers refer to the 46 oceanic triple junctions in the global database (Table 3.1) and their settings: back-arc basins (orange), arc-trench systems (green), and mid-ocean spreading centres (blue). RRR-, FRR-, and RFF-type triple junctions occur in back-arc basins and mid-ocean spreading centres. 15 triple junctions in arc-trench systems are FTT-, TFF-, TTT- and RTT-type. No TRR-type triple junctions were identified in the compilation. Abbreviations and descriptions of entries are found in Appendix C, Supplementary Table 1.

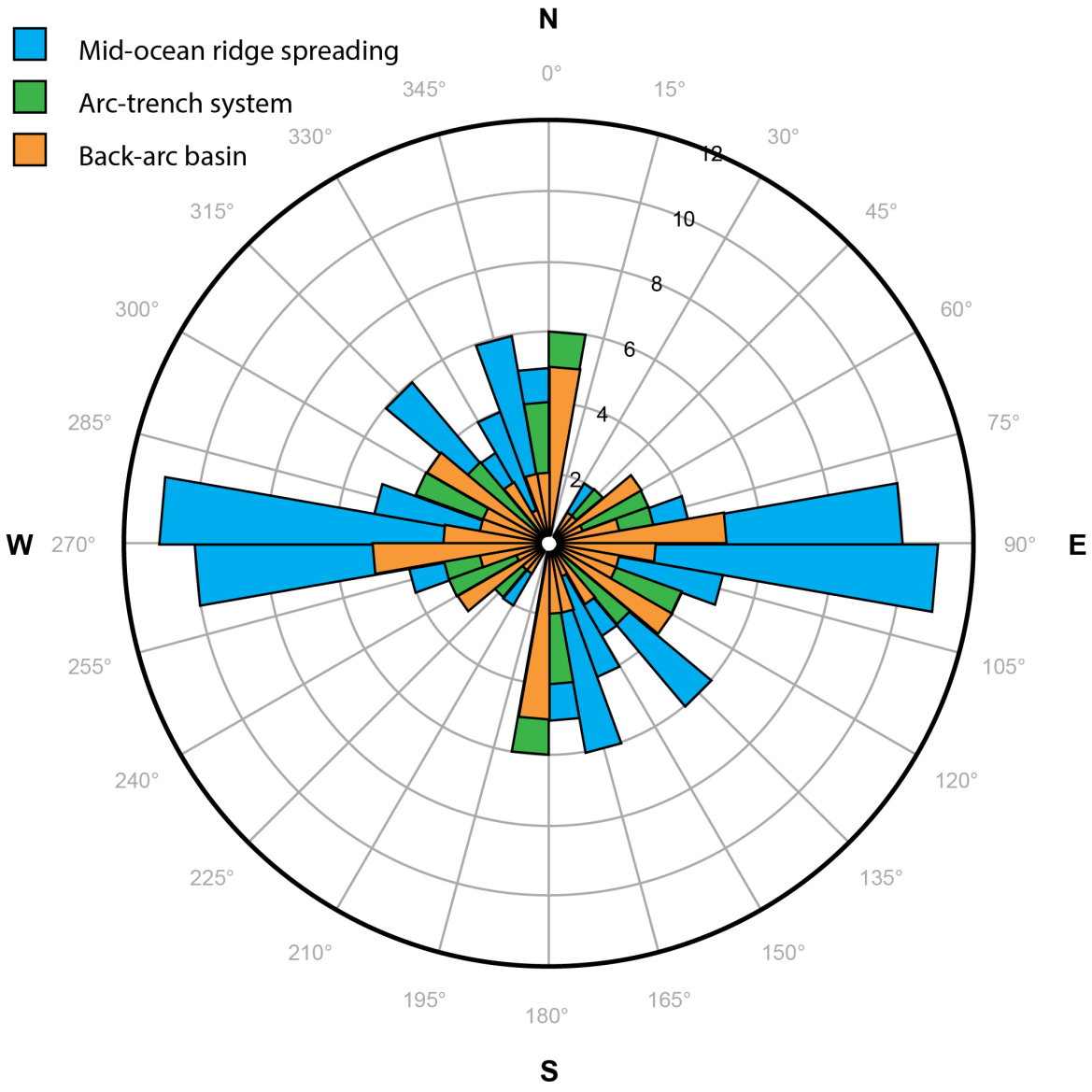

Figure 3.5 Distribution of the inter-limb angles of oceanic triple junctions classified by their geodynamic setting (from the Database of Oceanic Triple Junction: Table 3.1): blue (mid-ocean ridge spreading centres), green (arc-trench systems), and orange (back-arc basins). A high proportion of the triple junctions at mid-ocean ridge spreading centres have nearly orthogonal limbs (90 and 270 degrees). In contrast, triple junctions in arc-trench systems and back-arc basin settings show a wide range of inter-limb angles consistent with oblique spreading or strike-slip deformation in collisional settings. The geometry of triple junctions in back-arc basins and other subduction-related settings is less and far less stable than triple junctions at mid-ocean ridges with orthogonal intersections.

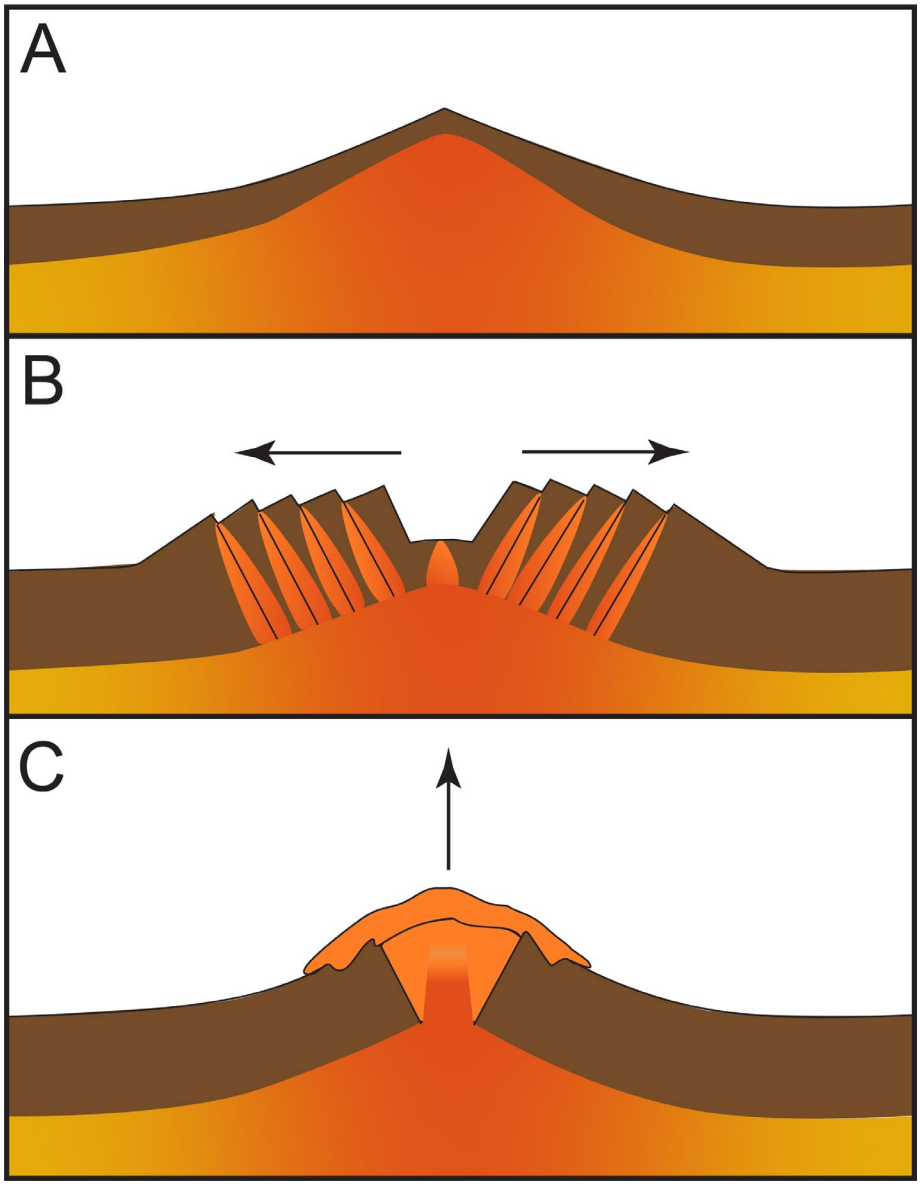

Figure 3.6 The three panels show three scenarios, all with similar crustal inflation due to mantle upwelling and thermal buoyancy. Crustal inflation without additional volume due to magmatism is indicated in A). Volume addition by intrusion is indicated in B). Volume addition by seafloor volcanism is indicated in C). **A)** Crustal volume at an inflated spreading centre, typical of fast spreading MOR. Despite crustal thinning, the surrounding crust is bowed upwards by a hot rising mantle causing overall inflation of the ridge. **B)** Volume addition at a typical slow-spreading mid-ocean ridge where tectonic extension exceeds magmatic extension (Sinton and Detrick, 1992). Accretion is mainly by intrusion. **C)** Volume addition at a typical MOR dominated by magmatic

extension and eruption onto the seafloor. Similar inflation occurs at hotspots represented at the surface as axial highs and central volcanic complexes.

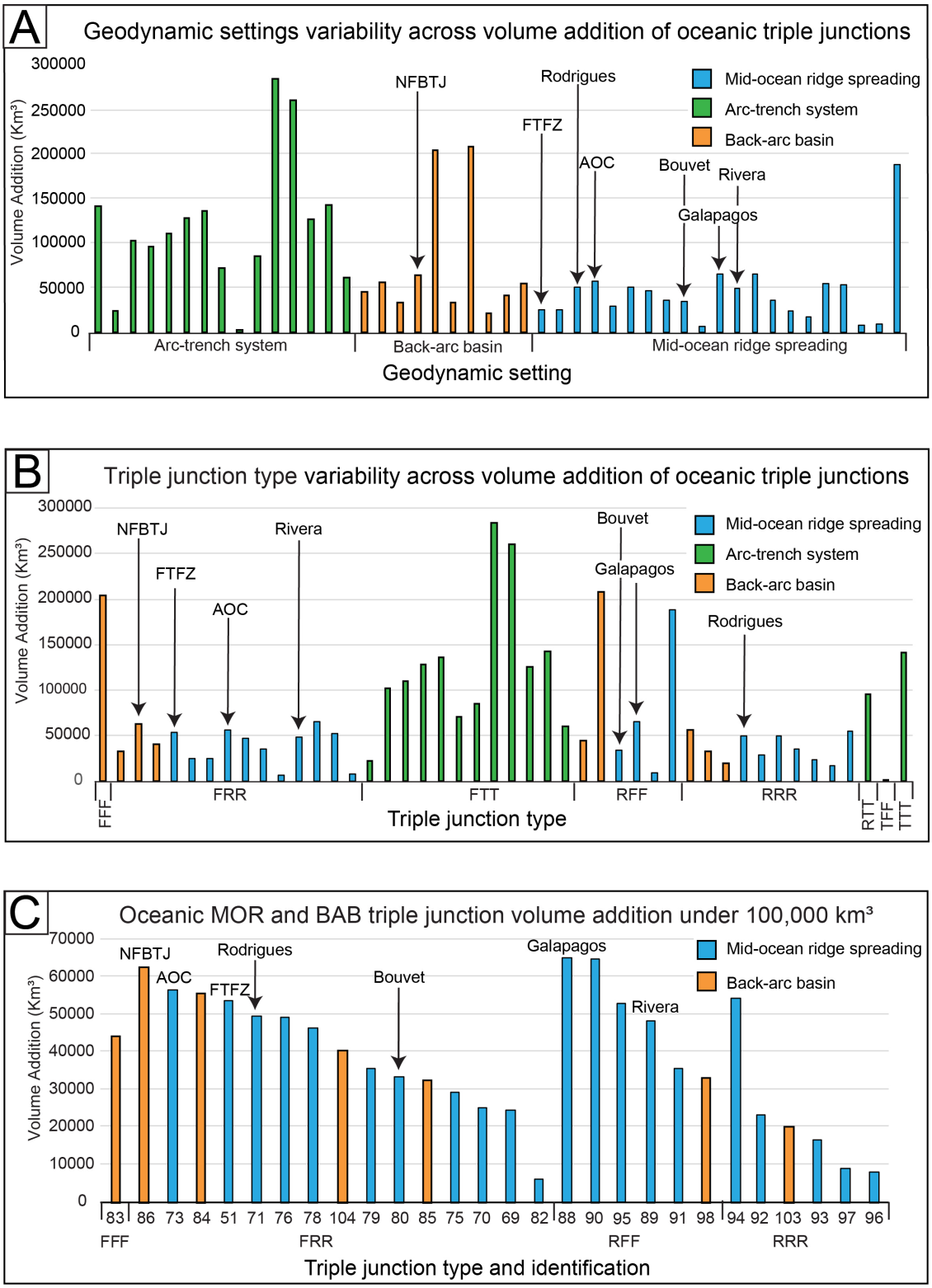

Figure 3.7 Volume addition associated with triple junctions sorted by geodynamic setting and triple junction types. Volume addition is represented by the volume (km^3) of crust above a datum

(Zmin) surrounding the triple junction up to 100 km from the triple junction centre (from the Database of Oceanic Triple Junction: Table 3.1). Volumes were calculated using an ArcGIS polygon volume function, which calculates the volume and surface area between a polygon and a surface. The surface, and terrain in this cases is defined by a triangular irregular network (TIN). A TIN is a form of vector-based digital geographic data, constructed by triangulated a set of vertices (points). The vertices are connected with a series of edges to form a network of triangles the edges of TINs form continuous, non-overlapping triangular facets and can be used to capture the position of linear features that play an important role in defining a complex surface. The volume addition is measured between the minimum elevation value (Zmin) of the TIN and the overlying polygon. **A)** Volume addition for 46 oceanic triple junctions grouped by geodynamic setting: blue (mid-ocean ridge spreading centres), green (arc-trench systems), and orange (back-arc basins). The majority of triple junctions at mid-ocean ridge spreading centres and in back-arc basins have volumes of less than 100,000 km^3. Larger volumes are calculated in proximity to continental crust and arc trenches owing to low Zmin values. **B)** Volume addition for oceanic triple junctions grouped by triple junction type. A variety of triple junction types occur in MOR settings (e.g., RRF, RRR, RFF), but there is a narrow range of low volume addition for this setting. **C)** Volume addition for a subset group of 28 oceanic triple junctions (all <100,000 km^3) showing FRR-type triple junctions in large back-arc basins like the NFB have volume addition comparable to those located along mid-ocean spreading centres (see text for discussion). Numbers refer to the triple junction ID in Table 3.1. NFBTJ= North Fiji Basin Triple junction, FTFZ=Fifteen Twenty Fracture Zone, AOC= Aden-Owen-Carlsberg. Additional abbreviations and descriptions of entries are found in Appendix C, Supplementary Table 1.

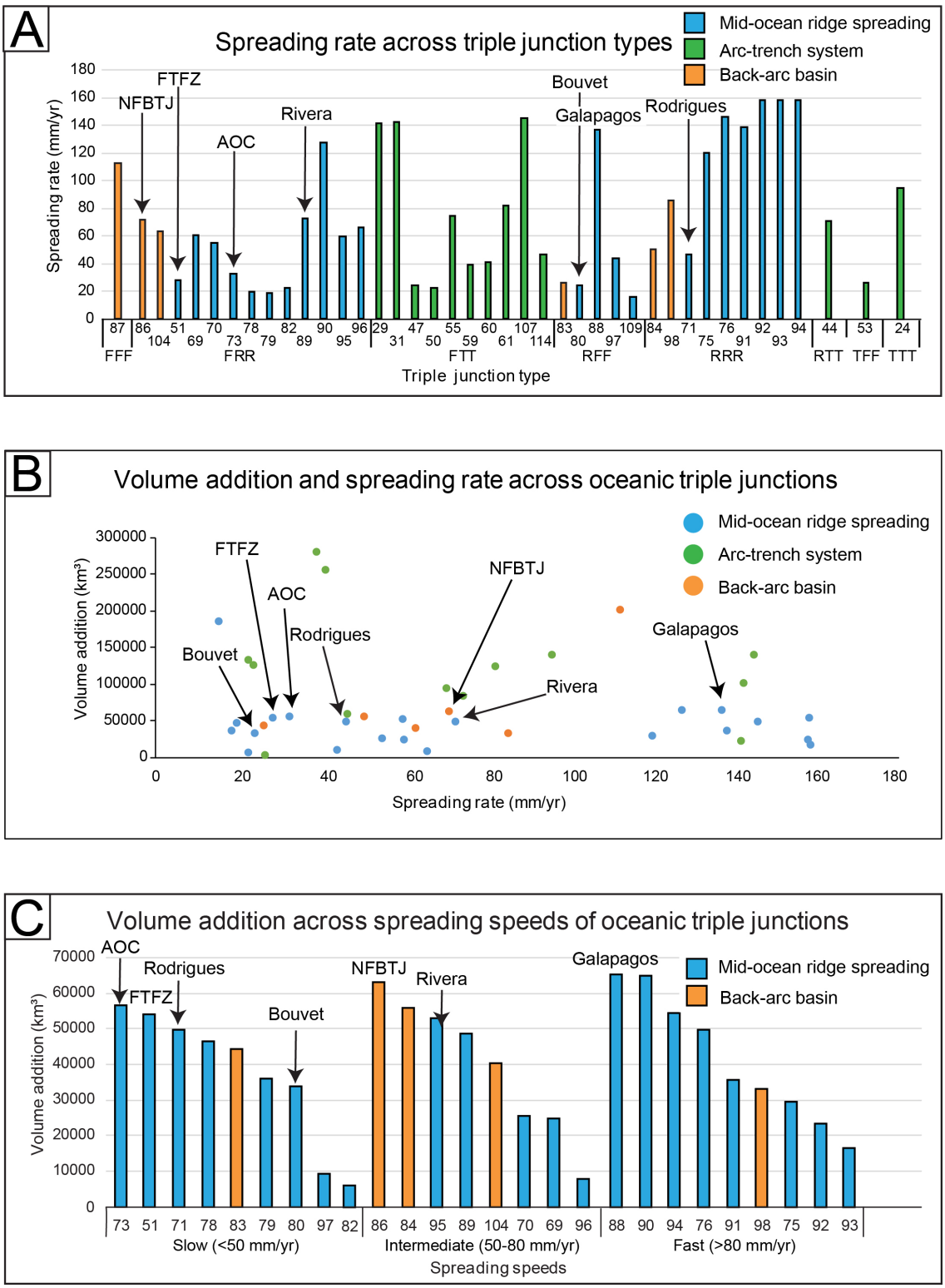

Figure 3.8 Average spreading rates of oceanic triple junctions sorted by geodynamic setting and triple junction types. Average spreading rates in mm/yr are determined within a 100-km radius of

the triple junction from data reported in Seton et al. (2020). Volume addition is represented by the volume (km^3) of crust above a datum (Zmin) surrounding the triple junction up to 100 km from the triple junction centre (from the Database of Oceanic Triple Junction: Table 3.1). **A)** Average spreading rates of different triple junction types (FFF, FRR, FTT, RFF, RRR, RTT, TFF and TTT-type) according to geodynamic setting. Numbers refer to the triple junction ID in Table 3.1. RFF-type triple junctions spread at slow rates (avg. 49.6 mm/yr); FRR- and FTT-type triple junctions spread at intermediate speeds, 53.8 and 76.1 mm/yr, respectively. RRR-type triple junctions have the highest full-spreading rates of 118 mm/yr. **B)** Volume addition (km^3) and average spreading rates of individual triple junctions. Triple junctions at mid-ocean ridges and in back-arc basins show a wide range of spreading rates but overall a narrow range of volume addition compared to triple junctions in arc-trench systems. **C)** Range of volume addition at triple junctions with a volume of <100,000 km^3 and slow-, intermediate-, and fast-spreading rates at mid-ocean ridges and back-arc basin spreading centres. Although triple junctions at mid-ocean ridges show the greatest variability in average spreading rate, there is no obvious correlation between volume addition and spreading rates (see text for discussion). NFBTJ= North Fiji Basin Triple junction, FTFZ=Fifteen Twenty Fracture Zone, AOC= Aden-Owen-Carlsberg. Additional abbreviations and descriptions of entries are found in Appendix C, Supplementary Table 1.

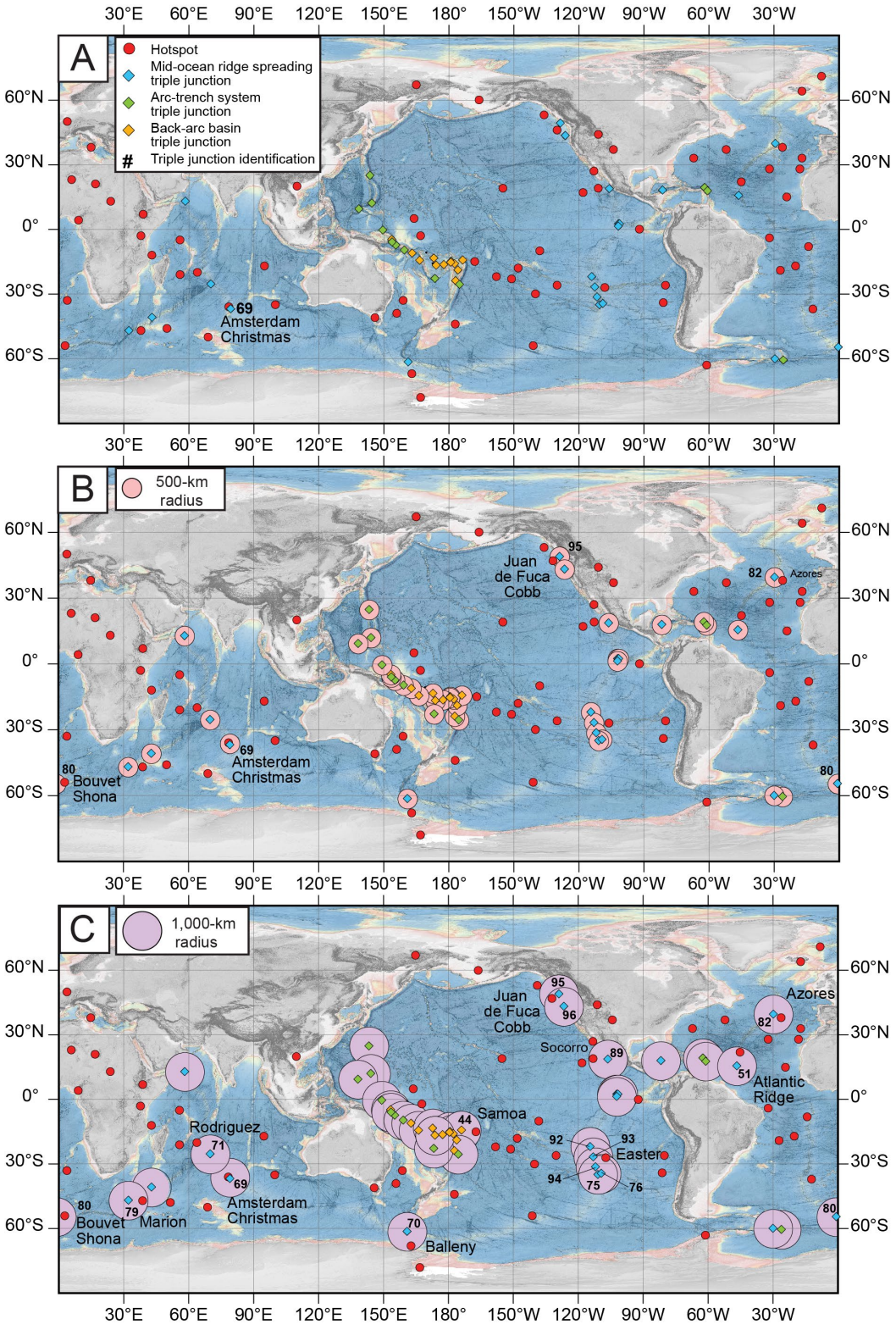

Figure 3.9 Distribution of oceanic triple junctions in relation to global hotspots (red circles from Whittaker et al., 2015). 46 triple junctions in different settings are represented by diamonds: blue

(mid-ocean ridge spreading centres), green (arc-trench systems), and orange (back-arc basins). Potential zones of influence are shown at distances of 100-, 500-, and 1,000-km from each triple junction. Triple junction ID numbers are indicated in each case where a hotspot falls within 100, 500, and 1,000 km of a triple junction **A)** One triple junction (#69) occurs immediately above a well known mantle plume at the Amsterdam Christmas hotspot. **B)** Three triple junctions are within the 500 km of a hot spot, including in the Azores (triple junction #82) and Cobb hotspot on the Juan de Fuca Plate (triple junction #95). **C)** 17 triple junctions (37%) are within 1,000 km of an oceanic hotspot: Samoa (deep mantle; #44), Azores (deep mantle; #82), Balleny (secondary/tertiary; #70), Amsterdam Christmas (#69), Marion (secondary/tertiary; #78 and #79), Atlantic (#51), Socorro (secondary/tertiary; #89), Juan de Fuca Cobb (mid-mantle; #95 and #96), Rodriguez (#71), Easter (deep mantle; #75, #76, #92, #93, and #94). All are found along mid-ocean ridge spreading centres, except for the Samoa hotspot.

Tables

Table 3.1 Excerpt from the Database of Oceanic Triple Junctions (Appendix E) providing details of the 46 oceanic triple junctions considered in this study.

ID	Latitude	Longitude	Geolocation	Geodynamic Setting	Known TJ Names	General TJ Type	Plate A	Plate B	Plate C
114	19.04	-62.36	Caribbean	ATS	n/a	FTT	Caribbean	Greater Gonave	North America
52	17.50	-61.04	Caribbean	ATS	n/a	FTT	South America	Caribbean	North America
50	-22.95	173.31	Hunter Ridge	ATS	n/a	FTT	Australia	New Hebrides	Conway Reef
29	12.00	144.29	Mariana	ATS	n/a	FTT	Pacific	Philippine Sea	Mariana
31	24.62	143.39	Mariana	ATS	n/a	FTT	Mariana	Philippine Sea	Pacific
107	9.17	138.28	Philippine Sea	ATS	n/a	FTT	Pacific	Caroline	Philippine Sea
61	-9.85	159.24	Soloman Islands	ATS	n/a	FTT	Australia	Woodlark	Solomon
59	-7.55	155.29	Soloman Sea	ATS	n/a	FTT	Woodlark	Solomon Sea	Solomon
60	-6.16	153.58	Soloman Sea	ATS	n/a	FTT	Solomon	Solomon Sea	South Bismark
46	-14.61	166.28	Southwest Pacific	ATS	n/a	FTT	Vitaz	New Hebrides	Australia
47	-11.29	162.81	Southwest Pacific	ATS	n/a	FTT	Australia	Solomon	Vitiaz
55	-25.69	-175.30	Southwest Pacific	ATS	n/a	FTT	Pacific	Kermadec	Tonga
44	-14.48	-173.87	Southwest Pacific	ATS	n/a	RTT	Tonga	Niuafo'Ou	Pacific
53	-60.59	-26.03	Alantic	ATS	n/a	TFF	South America	Antarcticia	Sandwich
24	-0.63	149.33	Southwest Pacific	ATS	n/a	TTT	North Bismarck	Caroline	Pacific
87	-16.56	177.45	Southwest Pacific	BAB	n/a	FFF	Australia	Conway Reef	Balmoral Reef
85	-15.52	-179.38	Southwest Pacific	BAB	n/a	FRR	Australia	Balmoral Reef	Vitaz
86	-16.86	173.91	Southwest Pacific	BAB	NFBTJ	FRR	Conway Reef	New Hebirdes	Balmoral Reef
104	-16.20	-177.63	Southwest Pacific	BAB	n/a	FRR	Niuafo'Ou	Australia	Vitiaz
83	-24.00	-177.17	Southwest Pacific	BAB	n/a	RFF	Tonga	Kermadec	Australia
102	-5.00	153.41	Southwest Pacific	BAB	n/a	RFF	Solomon	South Bismarck	North Bismarck
84	-13.53	172.80	Southwest Pacific	BAB	n/a	RRR	Balmoral Reef	New Hebirdes	Vitiaz
98	-19.07	-176.07	Southwest Pacific	BAB	n/a	RRR	Tonga	Australia	Niuafo'Ou
103	-15.08	-179.22	Southwest Pacific	BAB	n/a	RRR	Futuna	Australia	Vitiaz
82	39.40	-29.77	Alantic	MORS	n/a	FRR	Eurasia	Africa	North America
70	-61.52	160.99	Antarctica	MORS	n/a	FRR	Antarctica	Australia	Pacific
73	12.70	58.27	Arabian Sea	MORS	AOC	FRR	India	Somalia	Arabia
69	-36.36	79.10	Indian Ocean	MORS	n/a	FRR	Australia	Antarctica	Capricorn
78	-40.93	42.91	Indian Ocean	MORS	n/a	FRR	Somalia	Antarcticia	Lwandle
79	-47.06	32.24	Indian Ocean	MORS	n/a	FRR	Lwandle	Antarctica	Africa
51	15.37	-46.64	Mid-Alantic Ridge	MORS	FTFZ	FRR	Africa	South America	North America
89	18.51	-106.27	Pacific	MORS	Rivera	FRR	Cocos	Pacific	Rivera
90	2.23	-101.55	Pacific	MORS	n/a	FRR	Nazca	Galapagos	Cocos
95	48.81	-128.87	Pacific	MORS	n/a	FRR	Juan De Fuca	Pacific	Explorer
96	43.00	-126.59	Pacific	MORS	n/a	FRR	Gorda	Pacific	Juan De Fuca
80	-54.69	-0.73	Alantic	MORS	Bouvet	RFF	Antarctica	South America	Africa
97	-60.10	-29.93	Alantic	MORS	n/a	RFF	Antarctica	Scotia	Sandwich
109	17.81	-81.75	Caribbean	MORS	n/a	RFF	Greater Gonave	Caribbean	North America
88	2.27	-102.08	Pacific	MORS	Galapagos	RFF	Cocos	Galapagos	Pacific
71	-25.56	70.04	Indian Ocean	MORS	Rodrigues	RRR	Capricorn	Antarctica	Somalia
75	-35.10	-110.81	Pacific	MORS	n/a	RRR	Antarctica	Pacific	Juan Ferandez
76	-34.55	-109.25	Pacific	MORS	n/a	RRR	Antarctica	Juan Fernandez	Nazca
91	1.16	-102.17	Pacific	MORS	n/a	RRR	Nazca	Pacific	Galapagos
92	-22.09	-114.39	Pacific	MORS	n/a	RRR	Nazca	Easter	Pacific
93	-26.92	-113.01	Pacific	MORS	n/a	RRR	Nazca	Pacific	Easter
94	-31.52	-111.98	Pacific	MORS	n/a	RRR	Nazca	Juan Fernandez	Pacific

Note: Details of abbreviations, definitions of the attributes, and classification schemes can be found in Appendix C, Supplementary Table 1. Further attributes of these triple junctions are

presented in Appendix E. 9 of the original 54 oceanic triple junctions identified in Appendix D have at least one limb undefined (indicated by an “X”) and are excluded from Table 3.1. NFBTJ= North Fiji Basin Triple Junction, AOC= Aden-Owen-Carlsberg.

Table 3.2 Average spreading rates and volume addition of 41 oceanic triple junctions from the Database of Oceanic Triple Junctions (Appendix E).

ID	Geodynamic Setting	Known TJ Names	General TJ Type	Speed	Full Spreading Rate (mm/yr)	Volume Addition (km^3)
24	ATS	n/a	TTT	Fast	96.1	141394
29	ATS	n/a	FTT	Fast	141.7	23052
31	ATS	n/a	FTT	Fast	142.4	101866
44	ATS	n/a	RTT	Inter.	70.8	95527
47	ATS	n/a	FTT	Slow	24.1	127563
50	ATS	n/a	FTT	Slow	22.9	135445
53	ATS	n/a	TFF	Slow	26.7	1720
55	ATS	n/a	FTT	Inter.	74.8	84547
59	ATS	n/a	FTT	Slow	39.4	284056
60	ATS	n/a	FTT	Slow	41.3	260228
61	ATS	n/a	FTT	Fast	82.5	126037
107	ATS	n/a	FTT	Fast	144.8	142582
114	ATS	n/a	FTT	Slow	46.8	60568
	Averages and statistics		FTT=10 TTT=1 TFF=1 RTT=1	Fast=5 Inter.=2 Slow=6	73.4	121891
83	BAB	n/a	RFF	Slow	26.4	44459
84	BAB	n/a	RRR	Inter.	50.8	55904
86	BAB	NFBTJ	FRR	Inter.	71.4	62958
87	BAB	n/a	FFF	Fast	112.7	204051
98	BAB	n/a	RRR	Fast	85.6	33103
104	BAB	n/a	FRR	Inter.	63.3	40461
	Averages and statistics		RFF=1 RRR=2 FRR=2 FFF=1	Fast=2 Inter.=3 Slow=6	68.4	73489
51	MORS	FTFZ	FRR	Slow	28.6	53933
69	MORS	n/a	FRR	Inter.	60.3	24650
70	MORS	n/a	FRR	Inter.	55.2	25363
71	MORS	Rodrigues	RRR	Slow	46.3	49714
73	MORS	AOC	FRR	Slow	32.8	56729
75	MORS	n/a	RRR	Fast	120.4	29443
76	MORS	n/a	RRR	Fast	145.7	49588
78	MORS	n/a	FRR	Slow	20.0	46634
79	MORS	n/a	FRR	Slow	18.8	35869
80	MORS	Bouvet	RFF	Slow	24.4	33688
82	MORS	n/a	FRR	Slow	22.8	6196
88	MORS	Galapagos	RFF	Fast	137.3	65426
89	MORS	Rivera	FRR	Inter.	72.9	48530
90	MORS	n/a	FRR	Fast	127.4	64957
91	MORS	n/a	RRR	Fast	138.5	35686
92	MORS	n/a	RRR	Fast	157.9	23533
93	MORS	n/a	RRR	Fast	158.6	16637
94	MORS	n/a	RRR	Fast	158.4	54620
95	MORS	n/a	FRR	Inter.	60.1	52877
96	MORS	n/a	FRR	Inter.	66.0	7994
97	MORS	n/a	RFF	Slow	44.1	9232
109	MORS	n/a	RFF	Slow	15.8	188297
	Averages and statistics		FRR=12 RRR=7 RFF=4	Fast=8 Inter.=5 Slow=9	77.8	44527.1

Note: To obtain a representative spreading rate for each triple junction, we used a 100-km radius circle to average the spreading rate data published in Seton et al. (2020), for further detail see

Appendix C, Supplementary Table 2. Speed is categorized according to the full spreading rate in mm/yr from Seton et al. (2020) into three groups: slow (<50 mm/yr), inter. (50-80 mm/yr), and fast (>80 mm/yr). Crustal growth and inflation associated with the individual triple junctions were estimated by measuring the volume of crust in a 100 km radius surrounding the triple junction. Volumes were calculated using an ArcGIS polygon volume function, which calculates the volume between a polygon and a surface. The surface is defined by a triangular irregular network (TIN). The volume addition is measured between the minimum elevation value (Zmin) of the TIN and the overlying polygon. Abbreviations: NFBTJ= North Fiji Basin Triple Junction, AOC= Aden-Owen-Carlsberg, FTFZ= Fifteen Twenty Fracture Zone. Additional abbreviations and descriptions of entries are found in Appendix C, Supplementary Table 1.

Table 3.3 Comparison of spreading rates and volume addition between mid-ocean ridge spreading centres and representative triple junctions

	ID	Speed	Speed (mm/yr)	General TJ Type	Cumulative Ridge Length (km)	Volume Addition (km^3)
Triple Junctions	75	Fast	120.4	RRR	305	29443
	86	Inter	71.4	FRR	225	62958
	51	Slow	28.6	FRR	203	53933
MORs	EPR	Fast	99.4	/	205	15571
	GAL	Inter/slow	43.9	/	230	19327
	MAR	Slow	25.8	/	195	50768

Notes: Data for the MORs are from Carbottte et al. (2016). The representative triple junctions are #75 in the South Pacific (fast-spreading), #86 at the North Fiji Basin Triple Junction (intermediate-spreading), and #51 at the Fifteen Twenty Fracture Zone (slow-spreading). General triple junction (TJ) types are listed in Appendix C (Supplementary Table 2.) To obtain a representative spreading rate for each triple junction, we used a 100-km radius circle to average the spreading rate data published in Seton et al. (2020), for further detail see Appendix C, Supplementary Table 2. Speed is categorized according to the full spreading rate in mm/yr from Seton et al. (2020) into three groups: slow (<50 mm/yr), inter. (50-80 mm/yr), and fast (>80 mm/yr). Crustal growth and inflation associated with the individual triple junctions were estimated by measuring the volume of crust in a 100 km radius surrounding the triple junction. Volumes were calculated using an ArcGIS polygon volume function, which calculates the volume between a polygon and a surface. The surface is defined by a triangular irregular network (TIN). The volume addition is measured between the minimum elevation value (Zmin) of the TIN and the overlying polygon. Abbreviations: MORs=Mid-Ocean Ridges, EPR=Eastern Pacific Rise, GAL=Galapagos spreading centre, MAR= Mid-Atlantic Ridge. Additional abbreviations and descriptions of entries are found in Appendix C, Supplementary Table 1.

Chapter 4: Summary and Conclusions

Triple junctions are a fundamental element of plate tectonic theory (Bird, 2003) yet the processes that control triple junction formation and evolution are not well understood. Numerous researchers have focused on triple junction stability to better understand their evolution, but there is a lack of quantifiable data on the structures, magmatism, crustal accretion rates and volumes produced at these plate boundaries. This study focused on a triple junction in the centre of the North Fiji Basin (NFB), which is one of the largest intraoceanic back-arc basins in the world and a type locality for triple junction formation in this setting. The NFB opened in response to the collision of the Melanesian Plateau with the Indo-Australian Margin. This caused a regional subduction polarity reversal and fragmentation of the existing Vitiaz Arc. The North Fiji Basin Triple Junction (NFBTJ) was established at the centre of the NFB at ~2 Ma, when the already established Central Spreading Ridge (CSR) in the south of the basin, and a pre-existing northwest-trending spreading centre in the north were intersected by the westward propagating Fiji Fracture Zone (FFZ) in the east. This resulted in the emergence of a fault-ridge-ridge (FRR-type) triple junction. Between 1.3 Ma and 1 Ma, the NW limb and SW limb of the triple junction were the dominant spreading centres. The SW limb, which was continuous with the CSR, was rotated clockwise into its present position around 1.1 Ma, and the NE limb transitioned from dominantly tectonic extension to a spreading regime. This isolated the NFBTJ from the FFZ and created the currently stable ridge-ridge-ridge (RRR-type) configuration. No major reorganization of the NFBTJ occurred after 1 Ma.

A new compilation of marine geophysical data (hydroacoustics, magnetics, and gravity) was used to construct the first comprehensive geological map of the NFBTJ at 1:500,000, covering an area of 10,000 km^2. The study investigated the relationship between the different geological formations, mapped structures, magmatism and hydrothermal systems; including a quantitative analysis of crustal growth and structural evolution at each of the three limbs of the triple junction. The NE limb is a 57 km-long and 30-km-wide rift graben that terminates at a strike-slip discontinuity in the north where it joins the westward extension of the Fiji Fracture Zone (FFZ). The NW limb is a broad, 30-km-wide zone of normal faulting with volumetrically minor eruptions. Although extension along the NW limb is thought to have reached ~47 mm/yr, this part of the triple junction is now in a rifting stage and does not appear to be actively spreading. The SW limb is at least 73-

km-long and up to 55-km-wide rift zone with a well-developed spreading ridge, dominated by the Central Volcanic Complex (CVC) to the north. The CVC is a 27-km-long, 15-km-wide, and 0.4-km-high magmatically robust centre of the triple junction, comprising a large axial shield volcano and an inflated volcanic ridge. A recent eruption (~0.06 Ma) of the axial shield volcano created a summit caldera ~2 km in diameter, and produced a volcanic flow field of at least 200 km^3 on the northern flank of the CVC. Relict back-arc crust, possibly originating from older spreading centres, surrounds the NFBTJ and shows a range of spreading fabrics. Notably curved fabric in the SW of the map area possibly indicates that an abandoned spreading centre or an overlapping spreading centre may have been present during the earliest stages of formation of the NFBTJ. The present configuration of the triple junction and the observed changes in crustal fabric are thought to be related to reorganisation of the New Hebrides and Conway Reef microplates, as rotation of the Fiji Platform ended and westward migration of the New Hebrides Arc continued.

We show that the history of formation and evolution of the NFBTJ can be quantitatively assembled from a palinspastic reconstruction of the 1:500,000 geological map created in this study with precise area-age relationship established for the last 1.4 Myr. The mapping highlighted the role of different crustal types, the different near- and far-field stresses, and the possible link to local mantle upwelling. The structure and thickness of the crust affected how stresses were accommodated at the triple junction, including which limbs propagated or became extinct and how this influenced magmatic productivity and crustal growth. The long-lived microplate evolution of the basin was dominated by high regional heat flow and numerous propagating spreading centres. Volume addition at the centre of the NFB suggests an anomalous hot upper mantle that likely contributed to the formation and stability of the triple junction. Area-age relationships show two pulses of crustal growth occurred after the spreading centres were intercepted by the migrating FFZ and in response to continuing migration of the New Hebrides Arc. The rapid evolution from a FRR-type triple junction to a RRR-type triple junction was caused by continuing plate rotation after the arrival of the FFZ. Given what is known about the spreading rates and the volume of crust created at the NFBTJ, it is clear that the triple junction has been an important locus of crustal growth in this part of the NFB, greatly exceeding the growth rate of relict back-arc crust prior to the initiation of the triple junction.

A quantitative analysis of other triple junctions from a new global database show that the NFBTJ is one of the largest features of this kind in the oceans. The crustal volumes are similar to some of the largest MOR triple junctions, and show that similar large-scale plate interactions leading to triple junction formation can occur in back-arc basins. On average, volume addition at triple junctions is as much as 3 times greater than that of MOR spreading centres with comparable spreading rates. The inflation of the crust associated with many triple junctions is considered to be a result of the additional heat caused by local mantle upwelling, in addition to the calculated volume additions. This vertical crustal buoyancy may contribute to enhanced preservation of this type of crust in the geological record. Moreover, back-arc basin triple junctions, such as the NFBTJ, located on the upper plate of a subduction zone are more likely to be persevered than those located on the subducting plate (e.g., RTJ).

Globally 36 triple junctions are located within 1,000 km of a hotspot; 10 are within 500 km. Of the 22 oceanic triple junctions at mid-ocean ridge spreading centres, over 70% (16 triple junctions) are within 1000 km of a hotspot. Several back-arc basins are also likely within the influence of a plume (e.g., Samoan hotspot near the NE Lau Basin). Although significant hydrothermal activity is associated with some triple junctions, the small number of vents compared to oceanic spreading centres suggest that they may be underexplored for hydrothermal activity. Because the NFBTJ has acted as a locus for high heat flow, faulting, and crustal-scale permeability for several million years, there is the possibility of significant, now extinct off-axis hydrothermal systems in the area requiring further detailed mapping off-axis. An important aspect of triple junctions is that the most stable configuration is a RRR-type. Therefore these types of triple junctions are likely to have had the greatest impact on crustal growth in the geological record. The NFBTJ is an important example that may be compared to pulses of crustal growth and mineral endowment in ancient greenstone belts.

References

Amaru, M. L., 2007, Global travel time tomography with 3-D reference models (Vol. 274). Doctoral thesis, Utrecht University, Netherlands, **v.274**, p.1-174 doi:10.1016/j.epsl.2016.02.002

Anderson, M. O., Chadwick, W. W., Hannington, M. D., Merle, S. G., Resing, J. A., Baker, E. T., Butterfield, D. A., Walker, S. L., and Augustin, N., 2017, Geological interpretation of volcanism and segmentation of the Mariana back-arc spreading centre between 12.7°N and 18.3°N. Geochemistry, Geophysics, Geosystems, **v. 18**, p. 2240–2274, doi:10.1002/2017GC006813

Anderson, M. O., Hannington, M. D., Haase, K., Schwarz-Schampera, U., Augustin, N., McConachy, T. F., and Allen, K., 2016, Tectonic focusing of voluminous basaltic eruptions in magma-deficient back-arc rifts. Earth and Planetary Science Letters, **v. 440**, p. 43–55

Anderson, M. O., Norris-Julseth, C., Rubin, K. H., Haase, K., Hannington, M. D., Baxter, A. T., and Stewart, M. S., 2021, Geologic and Structural Evolution of the NE Lau Basin, Tonga: Morphotectonic Analysis and Classification of Structures Using Shallow Seismicity. Frontiers in Earth Science, **v. 9**, 426 p., doi:10.3389/feart.2021.665185

Argus, D.F., Gordon, R.G. and DeMets, C., 2011, Geologically current motion of 56 plates relative to the no-net-rotation reference frame. Geochemistry Geophysics Geosystems, **v. 12(11)**, 13 p, dio:10.1029/2011GC003751

Arnulf, A.F., Harding, A.J., Kent, G.M., Carbotte S.M., Canales J.P., and Nedimović, M.R., 2014, Anatomy of an active submarine volcano, Geology, **v. 42(8)**, p. 655–658, doi:10.1130/G35629.1

Auzende, J. M., Honza, E., Maze, J. P., Bendel, V., Eissen, J. P., Gracia-Mont, E., Huchon, P., Lafoy, Y., Lagabrielle, Y., Ruellan, E., Iwabuchi, Y., Jossima, M., Kissimoto, k., Matsumoto T., Mitsuzawa K., Momma H., Naganuma T., Naka J., Nojiri Y., Otsuka K., Tanahashi M., Tanaka T., and Urabe T., 1992, Comments on the seabeam map of the North Fiji basin ridge between 16° 10'S and 21° 40'S. Ofioliti, **v.17(1)**, p 43-53.

Auzende, J. M., Pelletier, B., and Eissen, J. P., 1995, The North Fiji Basin Geology, Structure, and Geodynamic Evolution. Back-arc Basins: Tectonic and Magmatism, Springer, Boston, p 139-175, doi:10.1007/978-1-4615-1843-3_4

Auzende, J. M., Rissen, J. P., Lafoy, Y., Gente, P., and Charlou, J. L., 1988, Seafloor spreading in the north Fiji basin (Southwest Pacific). Tectonophysics, **v. 146(1-4)**, p. 317-352, doi:10.1016/004-1951(88)90098-4

Barazangi, M., Isacks, B., Dubois, J., & Pascal, G., 1974, Seismic wave attenuation in the upper mantle beneath the southwest Pacific. Tectonophysics, **v. 24(1-2)**, p 1-12, doi:10.1016/0040-1951(74)90127-9

Baxter, A. T., Hannington, M. D., Stewart, M. S., Emberley, J. M., Breker, K., Krätschell, A., Petersen, S., Brandl, P. A., Klischies, M., Mensing R., and Anderson, M. O., 2020, Shallow seismicity and the classification of structures in the Lau back-arc basin. Geochemistry, Geophysics, Geosystems, **v. 21**, 25 p, doi:10.1029/2020GC008924

Beaulieu, S. E., & Szafranski, K., 2020, InterRidge Global database of active submarine hydrothermal vent fields, Version 3.4, URL: http://vents-data. interridge.org

Bendel, V., Fouquet, Y., Auzende, J. M., Lagabrielle, Y., Grimaud, D., and Urabe, T., 1993, The White Lady hydrothermal field, North Fiji back-arc basin, Southwest Pacific. Economic Geology, **v. 88(8)**, p 2237–2245, doi:10.2113/gsecongeo.88.8.2237

Bird, P., 2003, An updated digital model of plate boundaries. Geochemistry, Geophysics, Geosystems, **v. 4(3)**, p 25-28, doi:10.1029/2001GC000252

Bird, R. T., Tebbens, S. F., Kleinrock, M. C., and Naar, D. F., 1999, Episodic triple-junction migration by rift propagation and microplates. Geology, **v. 27(10)**, p 911-914, doi:10.1130/0091-7613

Bonvalot, S., Balmino, G., Briais, A., M. Kuhn, Peyrefitte, A., Vales N., Biancale, R., Gabalda, G., Reinquin, F., and Sarrailh, M., 2012, World Gravity Map. Commission for the Geological Map of the World. Eds. BGI-CGMW-CNES-IRD, Paris

Bouysse, P., 2014, Geological Map of the World (third edition, revised): Paris, France, Commission for the Geological Map of the World, 2 sheets, scale 1:35,000,000, doi:F10.14682/2014CGM3R.

Braunmiller, J., & Nábělek, J., 2008, Segmentation of the Blanco Transform Fault Zone from earthquake analysis: Complex tectonics of an oceanic transform fault. Journal of Geophysical Research: Solid Earth, **v. 113**, 23 p, doi:10.1029/2007JB005213

Burke, K., & Dewey, J. F. (1973). Plume-generated triple junctions: key indicators in applying plate tectonics to old rocks. The Journal of Geology, **v. 81(4)**, p 406-433

Carbotte, S. M., Smith, D. K., Cannat M. and E. M Klein, 2016, Tectonic and magmatic segmentation of the Global Ocean Ridge System: a synthesis of observations. Geological Society of London, **v. 420**, p 249-295, doi:10.1144/SP420.5

Chadwick, J., Perfit, M., Ridley, I., Jonasson, I., Kamenov, G., Chadwick, W., Embley, R., Le Roux, P. and Smith, M., 200, Magmatic effects of the Cobb hot spot on the Juan de Fuca Ridge. Journal of Geophysical Research: Solid Earth, **v. 110(B3)**, 16 p, dio:10.1029/2003JB002767

Chase, C. G., 1971, Tectonic history of the Fiji Plateau. Geological Society of America Bulletin, **v. 82(11)**, p 3087-3110, dio:10.1130/0016-7606(1971)82[3087:THOTFP]2.0.CO;2

Chaytor, J. D., Goldfinger, C., Dziak, R. P., and Fox, C. G., 2004, Active deformation of the Gorda plate: Constraining deformation models with new geophysical data. Geology, **v. 32(4)**, p 353-356, doi:10.1130/G20178.1

Clague, D.A., Dreyer, B.M., Paduan, J.B., Martin, J.F., Chadwick, W.W., Caress, D.W., Portner, R.A., Guilderson, T.P., McGann, M.L., Thomas, H. and Butterfield, D.A., 2013, Geologic history of the summit of Axial Seamount, Juan de Fuca Ridge. Geochemistry, Geophysics, Geosystems, **v. 14(10)**, p 4403-4443, dio:10.1002/ggge.20240

Colley, H., and Warden, A. J., 1974, Petrology of the New Hebrides. Geological Society of America Bulletin, **v. 85(10)**, p 1635-1646, dio:10.1130/0016-7606(1974)85<1635:POTNH>2.0.CO;2

Collot, J., Patriat, M., Sutherland, R., Williams, S., Cluzel, D., Seton, M., Pelletier, B., Roest, W.R., Etienne, S., Bordenave, A. and Maurizot, P., 2020, Geodynamics of the SW Pacific: a

brief review and relations with New Caledonian geology. Geological Society, London, Memoirs, **v. 51(1)**, p 13-26, dio:10.1144/M51-2018-5

Conder, J. A., Wiens, D. A., and Morris, J., 2002, On the decompression melting structure at volcanic arcs and back-arc spreading centres. Geophysical Research Letters, 29(15), 17-1 Contributions to Mineralogy and Petrology, **v. 27(3)**, p 179-203, dio:10.1029/2002GL015390

Cox, A., and Hart, R. B., 1986, Plate Tectonics: How It Works (1st ed.) John Wiley & Sons, 2009. p 51-84

Cronin, V. S., 1992, Types and kinematic stability of triple junctions. Tectonophysics, **v. 207(3-4)**, p. 287-301, dio:10.1016/0040-1951(92)90391-I

de Alteriis, G., Ruellan, E., Auzende, J. M., Ondréas, H., Bendel, V., Gràcia-Mont, E., Lagabrielle, Y., Huchon, P. and Tanahashi, M., 1993, Propagating rifts in the North Fiji Basin (southwest Pacific). Geology, **v. 21(7)**, p 583-586, doi:10.1130/0091-7613(1993)021<058

Deligne, N. I., and Sigurdsson, H., 2015, Global rates of volcanism and volcanic episodes. In The encyclopedia of volcanoes (second edition), Academic Press, p 265-272, dio:10.1016/B978-0-12-385938-9.00014-6

DeMets, C., Gordon, R. G., and Argus, D. F., 2010, Geologically current plate motions. Geophysical journal international, **v. 181(1)**, p 1-80, dio:10.1111/j.1365-246X

Dubois, J., Pascal, G., Barazangi, M., Isacks, B. L., and Oliver, J, 1973, Travel times of seismic waves between the New Hebrides and Fiji Islands: A zone of low velocity beneath the Fiji Plateau. Journal of Geophysical Research, **v. 78(17)**, p 3431-3436, dio:10.1029/JB078i017p03431

Dziewonski et al., 1981; Dziewonski, A. M., Chou, T. A., and Woodhouse, J. H., 1981, Determination of earthquake source parameters from waveform data for studies of global and regional seismicity. Journal of Geophysical Research: Solid Earth, **v. 86(B4)**, p 2825-2852, dio:10.1029/JB086iB04p02825

Ekström, G., Nettles, M., and Dziewoński, A. M., 2012, The global CMT project 2004–2010: Centroid-moment tensors for 13,017 earthquakes. Physics of the Earth and Planetary Interiors, **v. 200**, p 1-9, dio:10.1016/j.pepi.2012.04.002 002

Ernst, R. E., and Buchan, K. L., 2003, Recognizing mantle plumes in the geological record. Annual Review Earth Planetary Science, **v. 31**, p 463-523, doi:10.1146/annurev.earth.31.100901.145500

Falvey, D. A., 1978, Analysis of palaeomagnetic data from the New Hebrides. Exploration Geophysics, **v. 9(3)**, p 117-123. dio:10.1071/eg978117

Fletcher, A. W., Abdelsalam, M. G., Emishaw, L., Atekwana, E. A., Laó-Dávila, D. A., and Ismail, A., 2018, Lithospheric controls on the rifting of the Tanzanian craton at the Eyasi basin, eastern branch of the East African rift system. Tectonics, **v. 37**, p 2818–2832, dio:10.1029/ 2018TC005065

Fletcher, M., and Wyman, D. A., 2015, Mantle plume–subduction zone interactions over the past 60 Ma. Lithos, **v. 233**, p 162-173, dio:10.1016/j.lithos.2015.06.026

GEBCO Compilation Group, 2021, GEBCO 2021 Grid, doi:10.5285/c6612cbe-50b3-0cff-e053-6c86abc09f8f

Georgen, J. E., and Lin, J., 2002, Three-dimensional passive flow and temperature structure beneath oceanic ridge–ridge–ridge triple junctions. Earth and Planetary Science Letters, **v. 204(1-2)**, p 115-132, dio:10.1016/S0012-821X(02)00953-6

Gerya, T., and Burov, E., 2018, Nucleation and evolution of ridge-ridge-ridge triple junctions: Thermomechanical model and geometrical theory. Tectonophysics, **v. 746**, p 83-105, dio:10.1016/j.tecto.2017.10.020

Gill, J. B., 1970, Geochemistry of Viti Levu, Fiji, and its evolution as an island arc. Contributions to Mineralogy and Petrology, **v. 27(3)**, p. 179-203, doi:10.1007/BF00385777

Global Volcanism Program, 2013, Volcanoes of the World. **v.** 4.11.0. (2020), *In* Venzke, E (*Eds*). Smithsonian Institution, dio:10.5479/si.GVP.VOTW4-2013

Gràcia, E., Ondréas, H., Bendel, V., and Group, S., 1994, Multi-scale morphologic variability of the North Fiji Basin ridge (Southwest Pacific). Marine Geology, **v. 116(1-2)**, p 133-151, dio:10.1016/0025-3227(94)90173-2

Gràcia, E., Tisseau, C., Maia, M., Tonnerre, T., Auzende, J. M., and Lagabrielle, Y., 1996, Variability of the axial morphology and of the gravity structure along the Central Spreading Ridge (North Fiji Basin): Evidence for contrasting thermal regimes. Marine Geophysical Researches, **v. 18(2)**, p 249-273, doi:10.1007/BF00286080

Haase, K. M., Schoenhofen, M. V., Storch, B., Beier, C., Regelous, M., Rubin, K., and Brandl, P. A., 2022, Effects of the hydrous domain in the mantle wedge on magma formation and mixing at the Northeast Lau Spreading centre, SW Pacific. Geochemistry, Geophysics, Geosystems, **v.23(3)**, 22 p, doi:10.1029/2021GC010066

Hall, R., and Spakman, W, 2002, Subducted slabs beneath the eastern Indonesia–Tonga region: insights from tomography. Earth and Planetary Science Letters, **v. 201(2)**, p 321-336. doi:10.1016/S0012-821X(02)00705-7

Harris, P. T., Macmillan-Lawler, M., Rupp, J., and Baker, E. K., 2014, Geomorphology of the oceans. Marine Geology, **v. 352**, p 4-24, dio:10.1016/j.margeo.2014.01.011

Heidbach, O., Rajabi, M., Cui, X., Fuchs, K., Müller, B., Reinecker, J. Reiter, K., Tingay, M., Wenzel, F., Xie, F. and Zoback, M., 2018, The World Stress Map database release 2016: Crustal stress pattern across scales. Tectonophysics, **v. 744**, p 484-498, dio:10.1016/j.tecto.2018.07.007

Hooft, E. E., and Detrick, R. S., 1995, Relationship between axial morphology, crustal thickness, and mantle temperature along the Juan de Fuca and Gorda Ridges. Journal of Geophysical Research: Solid Earth, **v. 100(B11)**, p 22499-22508, dio:10.1029/95JB02502

Huchon, P., Gràcia, E., Ruellan, E., Joshima, M., and Auzende, J. M., 1994, Kinematics of active spreading in the central North Fiji Basin (Southwest Pacific). Marine Geology, **v. 116(1-2)**, p 69-87, dio:10.1016/0025-3227(94)90169-4

Ishibashi, J. I., Wakita, H., Nojiri, Y., Grimaud, D., Jean-Baptiste, P., Gamo, T., Auzende, J. M., and Urabe, T., 1994, Helium and carbon geochemistry of hydrothermal fluids from the North Fiji Basin spreading ridge (southwest Pacific). Earth and Planetary Science Letters, **v. 128(3-4)**, p 183-197, dio:10.1016/0012-821X(94)90144-9

Ito, G., Lin, J., and Gable, C. W., 1997, Interaction of mantle plumes and migrating mid-ocean ridges: Implications for the Galapagos plume-ridge system. Journal of Geophysical Research, v.102(B7), p 15,403-15,417, dio:0148-0227/97/97JB-01049

James, A., & Flavey, D. A., 1978, Analysis of Palaeomagnetic Data from Viti Levu, Fiji. Exploration Geophysics, **v. 9(3)**, p 115–117, dio:10.1071/EG978115

JAMSTEC, 2012, YOKOSUKA YK06-13 Leg2 Cruise Data. JAMSTEC. 10.17596/0001524

Jarvis, P. A., 1991, Tectonic deformation in the North Fiji Basin: PhD. dissertation, University of Hawai'i at Manoa

Jarvis, P. A., and Kroenke, L., 1993, Structural development of central North Fiji Basin triple junction. Geo-Marine Letters, **v. 13(3)**, p 133-138, dio:10.1007/BF01593185

Jarvis, P. A., Kroenke, L. W., Price, R. C., and Maillet, P. (1991). Structural Fabric in the Northern North Fiji Basin. South Pacific Applied Geoscience Commission: Techincal Report 130, 28 p

Johansson, L., Zahirovic, S., and Müller, R. D., 2018, The interplay between the eruption and weathering of large igneous provinces and the deep-time carbon cycle. Geophysical Research Letters, **v. 45(11)**, p 5380-5389, dio:10.1029/2017GL076691

Johnson, K.T. and Sinton, J.M., 1990, Petrology, tectonic setting, and the formation of back-arc basin basalts in the North Fiji Basin. Geologisches Jahrbuch Reihe D Heft, **v. 92**, p 517-545.

Joshima, M., Iwabuchi, Y., and Ookuma, S., 1994, Magnetic anomaly patterns around the central rift area in the North Fiji Basin: Inversion approach for detailed structure. Marine Geology**, v. 116(1-2)**, p 89-100, dio:10.1016/0025-3227(94)90170-8

Kellogg, J.N., and Kansakar, D.R., 1994, Gravity Field of the North Fiji Basin. *In* Kroenke, L.W., Eade, J.V. *(eds)* Basin Formation, Ridge Crest Processes, and Metallogenesis in the North Fiji Basin. Circum-Pacific Council for Energy and Mineral Resources Earth Science Series, Springer, Berlin, Heidelberg, **v. 15**, p 41-48, doi:10.1007/978-3-642-85043-1_5

Klischies, M., Hannington, M.D., Petersen, S., Stewart, M.S., Mensing, R., Anderson, M.O., Graber, S., Krätschell, A., and Schwarz-Schampera, U., (in prep.). Remote predictive geological

mapping of the mid-ocean ridges: Breakthroughs in classification of crustal accretion at the regional scale. Marine Geology.

Kuhn, T., Bostick, B. C., Koschinsky, A., Halbach, P., and Fendorf, S., 2003, Enrichment of Mo in hydrothermal Mn precipitates: Possible Mo sources, formation process and phase associations. Chemical Geology, **v. 199(1–2)**, p 29–43, dio:10.1016/S0009-2541(03)00054-8

LaFemina, P. C., 2015, Plate tectonics and volcanism. *In* The encyclopedia of volcanoes (second edition p 65-92, Academic Press, dio:10.1016/B978-0-12-385938-9.00003-1

Lafoy, Y., Auzende, J. M., Ruellan, E., Huchon, P., and Honza, E., 1990, The 16°40′ S triple junction in the North Fiji Basin (SW Pacific). Marine Geophysical Researches, **v. 12(4)**, p 285–296, dio:10.1007/BF02428199

Lagabrielle, Y., Goslin, J., Martin, H., Thirot, J. L., and Auzende, J. M., 1997, Multiple active spreading centres in the hot North Fiji Basin (Southwest Pacific): a possible model for Archaean seafloor dynamics? Earth and Planetary Science Letters, **v. 149(1-4)**, p 1-13, dio:10.1016/S0012-821X(97)00060-5

Lagabrielle, Y., Ruellan, E., Tanahashi, M., Bourgois, J., Buffet, G., de Alteriis, G., Dyment, J., Goslin, J., Gràcia-Mont, E., Iwabushi, Y. and Sardou, O, 1996, Active oceanic spreading in the northern North Fiji Basin: results of the NOFI cruise of R/V L'Atalante (NewSTARMER Project). Marine Geophysical Researches, **v. 18(2)**, p 225-247, dio:10.1007/BF00286079

Li, S., Suo, Y., Li, X., Liu, B., Dai, L., Wang, G., Zhou, J., Li, Y., Liu, Y., Cao, X., Somerville, I., Mu, D., Zhao, S., Liu, J., Meng, F., Zhen, L., Zhao, L., Zhu, J., Yu, S., Liu, Y., and Zhang, G., 2018, Microplate tectonics: new insights from micro-blocks in the global oceans, continental margins and deep mantle. Earth-Science Reviews, **v. 185**, p 1029–1064, dio:10.1016/j.earscirev.2018.09.005

Luyendyk, B. P., Bryan, W. B., and Jezek, P. A., 1974, Shallow structure of the New Hebrides island arc. Geological Society of America Bulletin, **v. 85(8)**, p 1287-1300, dio:10.1130/0016-7606(1974)85%3C1287:SSOTNH%3E2.0.CO;2

Macdonald, K C., 1983, Crustal processes at spreading centres. Reviews of Geophysics, **v. 21(6)**, p 1441-1454, dio:10.1029/RG021i006p01441

Macdonald, K. C., 1982, Mid-ocean ridges: Fine scale tectonic, volcanic and hydrothermal processes within the plate boundary zone. Annual Review of Earth and Planetary Sciences, **v. 10**, p 155-190

MacLeod, S. J., Williams, S. E., Matthews, K. J., Müller, R. D., and Qin, X., 2017, A global review and digital database of large-scale extinct spreading centres. Geosphere, **v. 13(3)**, p 911-949, dio:10.1130/GES01379.1

Malahoff, A., Hammond, S. R., Naughton, J. J., Keeling, D. L., and Richmond, R. N., 1982, Geophysical evidence for post-Miocene rotation of the island of Viti Levu, Fiji, and its relationship to the tectonic development of the North Fiji Basin. Earth and Planetary Science Letters, **v. 57(2)**, p 398-414, dio:10.1016/0012-821X(82)90159-5

Malahoff, A., Kroenke, L.W., Cherkis, N., and Brozena, J., 1994, Magnetic and Tectonic Fabric of the North Fiji Basin and Lau Basin. In: Kroenke, L.W., Eade, J.V. (*eds*) Basin Formation, Ridge Crest Processes, and Metallogenesis in the North Fiji Basin. Circum-Pacific Council for Energy and Mineral Resources Earth Science Series, Springer, Berlin, Heidelberg, **v. 15**, p 49-61, dio:10.1007/978-3-642-85043-1_6

Martin, A.K., 2007, Gondwana breakup via double-saloon-door rifting and seafloor spreading in a backarc basin during subduction rollback. Tectonophysics, **v. 445(3-4)**, p 245-272, dio:10.1016/j.tecto.2007.08.011

Martin, A. K., 2013, Double-saloon-door tectonics in the North Fiji Basin. Earth and Planetary Science Letters, **v. 374**, p 191-203, dio:10.1016/j.epsl.2013.05.041

Matthews, K. J., Müller, R. D., Wessel, P., and Whittaker, J. M., 2011, The tectonic fabric of the ocean basins. Journal of Geophysical Research: Solid Earth, **v. 116(B12)**, 28 p, doi:10.1029/2011JB008413

Maus, S., Barckhausen, U., Berkenbosch, H., Bournas, N., Brozena, J., Childers, V., Dostaler, F., Fairhead, J.D., Finn, C., Von Frese, R.R.B. and Gaina, C., 2009, EMAG2: A 2–arc min resolution Earth Magnetic Anomaly Grid compiled from satellite, airborne, and marine magnetic measurements. Geochemistry, Geophysics, Geosystems, **v. 10(8)**, 12 p, dio:10.1029/2009GC002471

McKenzie, D. P., and Morgan, W. J., 1969, Evolution of triple junctions. Nature, **v. 224(5215)**, p 125-133, dio:10.1038/224125a0

McKenzie, D., and Sclater, J. G., 1971, The evolution of the Indian Ocean since the Late Cretaceous. Geophysical Journal, **v. 24(5)**, p 437-528. doi:10.1111/j.1365-246X.1971.tb02190.x

Meffre, S., and Crawford, A. J, 2001, Collision tectonics in the New Hebrides arc (Vanuatu). Island Arc, **v. 10(1)**, p 33-50, dio:10.1046/j.1440-1738.2001.00292.x

Mensing, R., 2019, The Tectonic and volcanic evolution of the Mangatolu Triple Junction: M.Sc. thesis, Kiel Germany, Martin Luther University Halle-Wittenberg, 78 p

Mitchell, G. A., Montési, L. G., Zhu, W., Smith, D. K., and Schouten, H., 2011, Transient rifting north of the Galápagos Triple Junction. Earth and Planetary Science Letters, **v. 307(3-4)**, p 461-469, dio:10.1016/j.epsl.2011.05.027

Munschy, M., and Schlich, R., 1989, The Rodriguez Triple Junction (Indian Ocean): structure and evolution for the past one million years. Marine Geophysical Researches, **v. 11(1)**, p 1-14, dio:10.1007/BF00286244

Oh, J., Lee, I., Stuart, F. M., Park, M., and Kim, J., 2021, EM1-signature in the North Fiji Basin: Evidence for stagnant slab-derived mantle upwelling beneath the trench-distal back-arc basin. Journal of Geophysical Research: Solid Earth, **v.126**, 20 p, doi:10.1029/2020JB021017

Patriat, M., Collot, J., Danyushevsky, L., Fabre, M., Meffre, S., Falloon, T., Rouillard, P., Pelletier, B., Roach, M. and Fournier, M., 2015, Propagation of back-arc extension into the arc lithosphere in the southern New Hebrides volcanic arc. Geochemistry, Geophysics, Geosystems, **v. 16(9)**, p 3142-3159, dio:10.1002/2015GC005717

Patriat, P., and Courtillot, V., 1984, On the stability of triple junctions and its relation to episodicity in spreading. Tectonics, **v. 3(3)**, p 317-332, dio:10.1029/TC003i003p00317

Rey, P. F., and Müller, R. D., 2010, Fragmentation of active continental plate margins owing to the buoyancy of the mantle wedge. Nature Geoscience, **v. 3(4)**, p 257–261, dio:10.1038/ngeo825

Robertson CGG, 2017, Tellus Database of Sedimentary Basins. URL: https://services3.arcgis.com/3wBYLDMc7IlzsBlJ/arcgis/rest/services/Basin_outlines_Robertson_Basins_and_Plays/FeatureServer

Rowland, J. V., and Simmons, S. F., 2012, Hydrologic, Magmatic, and Tectonic Controls on Hydrothermal Flow, Taupo Volcanic Zone, New Zealand: Implications for the Formation of Epithermal Vein Deposits. Economic Geology, **v. 107(3)**, p 427–457, doi:/10.2113/econgeo.107.3.427

Ruellan, E., and Lagabrielle, Y., 2005, Subductions et ouvertures océaniques dans le Sud-Ouest Pacifique. Géomorphologie : Relief, Processus, Environnement, **v. 11(2)**, p 121–142, dio:10.4000/geomorphologie.307

Ryan, M., Hannington, M. D., Baxter, A. T., Stewart, M. S., Breker, K., Fassbender, M. L., Krätschell, A., and Petersen, S., 2022, Analysis of magmatic productivity at the Rochambeau Rifts, northern Lau back-arc Basin. Annual Student Minerals Colloquium at the Prospectors & Developers Association of Canada Convention, Toronto, ON, June 13-15 2022

Ryan, W.B.F., Carbotte, S.M., Coplan, J., O'Hara, S., Melkonian, A., Arko, R., Weissel, R.A., Ferrini, V., Goodwillie, A., Nitsche, F. and Bonczkowski, J., 2009, Global Multi-Resolution Topography (GMRT) synthesis data set. Geochemistry, Geophysics, Geosystems, **v. 10 (3)**, 9 p, dio:10.1029/2008GC002332

Sandwell, D. T., Müller, R. D., Smith, W. H., Garcia, E., & Francis, R., 2014, New global marine gravity model from CryoSat-2 and Jason-1 reveals buried tectonic structure. Science, **v. 346(6205)**, p 65-67, dio:10.1126/science.1258213

Schellart, W. P., Lister, G. S., & Jessell, M. W., 2002, Analogue modeling of arc and back-arc deformation in the New Hebrides arc and North Fiji Basin. Geology, **v. 30(4)**, p 311-314, doi: 10.1130/00917613(2002)030%3C0311:AMOAAB%3E2.0.CO;2

Schellart, W., Lister, G., and Toy, V., 2006, A Late Cretaceous and Cenozoic reconstruction of the Southwest Pacific region: Tectonics controlled by subduction and slab rollback processes. Earth-Science Reviews, **v. 76(3–4)**, p 191–233, dio:10.1016/j.earscirev.2006.01.002

Sclater, J. G., and Menard, H. W., 1967, Topography and heat flow of the Fiji Plateau. Nature, **v. 216(5119)**, p 991-993, doi:10.1038/216991a0

Şengör A.M.C. (2011) Continental Rifts. In Gupta H.K. (Eds) Encyclopedia of Solid Earth Geophysics. Encyclopedia of Earth Sciences Series. Springer, Dordrecht. 54 p, dio:10.1007/978-90-481-8702-7_31

Seton, M., Müller, R.D., Zahirovic, S., Williams, S., Wright, N.M., Cannon, J., Whittaker, J.M., Matthews, K.J. and McGirr, R., 2020. A global data set of present-day oceanic crustal age and seafloor spreading parameters. Geochemistry, Geophysics, Geosystems, **v. 21(10)**, dio:10.1029/2020GC009214

Seton, M., Whittaker, J.M., Wessel, P., Müller, R.D., DeMets, C., Merkouriev, S., Cande, S., Gaina, C., Eagles, G., Granot, R. and Stock, J., 2014, Community infrastructure and repository for marine magnetic identifications. Geochemistry, Geophysics, Geosystems, **v. 15(4)**, p 1629-1641, dio:10.1002/2013GC005176

Silver, E. A., 1971, Tectonics of the Mendocino triple junction. Geological Society of America Bulletin, **v. 82(11)**, p 2965-2978, dio:10.1130/0016-7606(1971)82[2965:TOTMTJ]2.0.CO;2

Sisson, V. B., Pavlis, T. L., Roeske, S. M., and Thorkelson, D. J., 2003, Introduction: An overview of ridge-trench interactions in modern and ancient settings. Geological Society of America Special Papers, v. 371, p 1-18.

Smith, D. K., Schouten, H., Zhu, W. L., Montési, L. G. J., and Cann, J. R., 2011, Distributed deformation ahead of the Cocos-Nazca Rift at the Galapagos triple junction. Geochemistry, Geophysics, Geosystems, **v. 12(11)**, 13 p, dio:10.1029/2011GC003689

Stewart, M.S., Hannington, M.D., Emberley, J., Baxter, A.T., Krätschell, A., Petersen, S., Brandl, P.A., Anderson, M.O., Mercier-Langevin, P., Mensing, R. and Breker, K., 2022, A new geological map of the Lau Basin (southwestern Pacific Ocean) reveals crustal growth processes in arc-back-arc systems. Geosphere, **v. 18(2)**, p 910-943, dio:10.1130/GES02340.1

Sinton, J. M., and Detrick, R. S., 1992, Mid-Ocean Ridge Magma Chambers. Journal of Geophysical Research, **v. 97(B1)**, p 197-216, dio:10.1029/91JB02508

Sykes, L. R., Isacks, B. L., and Oliver, J., 1969, Spatial distribution of deep and shallow earthquakes of small magnitudes in the Fiji-Tonga region. Bulletin of the Seismological Society of America, **v. 59(3)**, p 1093-1113, dio:10.1785/BSSA0590031093

Tanahashi, M., Kisimoto, K., Joshima, M., Jarvis, P., Iwabuchi, Y., Ruellan, E., and Auzende, J. M., 1994, 800-km-long NS spreading system of the North Fiji Basin. Marine Geology, **v. 116(1-2)**, p 5-24, dio: 10.1016/0025-3227(94)90165-1

Tanahashi, M., Kisimoto, K., Joshima, M., Lafoy, Y., Honza, E., and Auzende, J. M., 1991, Geological structure of the central spreading system, North Fiji Basin. Marine Geology, **v. 98(2-4)**, p 187-200, dio:10.1016/0025-3227(91)90103-B

Tarling, D. H., 1967, The paleomagnetism of some rock samples from Viti Levu, Fiji. New Zealand Journal of Geology and Geophysics, **v. 10(5)**, p 1235-1247, dio:10.1080/00288306.1967.10420215

Taylor, G. K., Gascoyne, J., and Colley, H., 2000, Rapid rotation of Fiji: paleomagnetic evidence and tectonic implications. Journal of Geophysical Research: Solid Earth, **v. 105(B3)**, p 5771-5781, dio:10.1029/1999JB900305

Thordarson, T., Miller, D. J., Larsen, G., Self, S., & Sigurdsson, H., 2001, New estimates of sulfur degassing and atmospheric mass-loading by the 934 AD Eldgjá eruption, Iceland. Journal of Volcanology and Geothermal Research, **v. 108(1-4)**, p 33-54, dio:10.1016/S0377-0273(00)00277-8

Thouret, J. C., 1999, Volcanic geomorphology - an overview. Earth-science reviews, **v. 47(1-2)**, p 95-131, dio:10.1016/S0377-0273(00)00277-8

Tian, L., Castillo, P. R., Hilton, D. R., Hawkins, J. W., Hanan. B. B., and Pietruszka, A. J., 2011, Major and trace element and Sr-Nd isotope signatures of the northern Lau Basin lavas: Implications for the composition and dynamics of the back-arc basin mantle. Journal of Geophysical Research, **v. 116(B11201)**, 18 p, doi:10.1029/2011JB008791.

Tiffin, D. L. GLORIA surveys in frontier areas of the southwest Pacific Ocean, 1993, Geo-Marine Letters, **v. 13**, p 65–70, dio: /10.1007/BF01204547

Tiffin, D. L., Clarke, J.E.H., Jarvis, P., Johnson, D., Hill, P., Huggett, Q., Parson, L. and Price, R., Scientific Party, 1993, CCOP/SOPAC GLORIA Survey, Port Vila-Apia-Port Vila on HMAS Cook, 1 August - 1 September 1989. SOPAC Cruise Report, **v. 130**, 45 p.

Van der Hilst, R. D., Widiyantoro, S., and Engdahl, E. R., 1997, Evidence for deep mantle circulation from global tomography. Nature, **v. 386(6625)**, p 578-584. dio:10.1038/386578a0

VanderBeek, B. P., and Toomey, D. R., 2019, Pn Tomography of the Juan de Fuca and Gorda Plates: implications for mantle deformation and hydration in the oceanic lithosphere. Journal of Geophysical Research: Solid Earth, v. 124(8), p 8565-8583, dio:10.1029/2019JB017707

Watanabe, T., Langseth, M. G., and Anderson, R. N., 1977, Heat flow in back-arc basins of the western Pacific. *In* Island arcs, deep sea trenches and back-arc basins, American Geophysical Union Washington, DC., **v. 1**, p 137-161

Whittaker, J. M., Afonso, J. C., Masterton, S., Müller, R. D., Wessel, P., Williams, S. E., and Seton, M., 2015, Long-term interaction between mid-ocean ridges and mantle plumes. Nature Geoscience, **v. 8(6)**, p 479-483, doi: 10.1038/ngeo2437

Wiens, D. A., Kelley, K. A., and Plank, T., 2006, Mantle temperature variations beneath back-arc spreading centres inferred from seismology, petrology, and bathymetry. Earth and Planetary Science Letters, **v. 248(1-2)**, p 30-42, dio:10.1016/j.epsl.2006.04.011

Yeo, I. A., CW, D., LeBas, T. P., Augustin, N., and Steinführer, A., 2016, Segment-scale volcanic episodicity: evidence from the North Kolbeinsey Ridge, Atlantic. Earth and Planetary Science Letters, **v. 439**, p 81-87, dio:10.1016/j.epsl.2016.01.029

York, D., 1973, Evolution of triple junctions. Nature, **v. 244(5415)**, p 341-342, dio:10.1038/244341a0

Zhang, H., Yan, Q., Li, C., Zhu, Z., Zhao, R. and Shi, X., 2019. Geochemistry of diverse lava types from the Lau Basin (South West Pacific): Implications for complex back-arc mantle dynamics. Geological Journal, **v. 54(6)**, p 1-17, doi:10.1002/gj.3354

Zhang, N., and Pysklywec, R. N., 2006, Role of mantle flow at the North Fiji Basin: insights from anomalous topography. Geochemistry, Geophysics, Geosystems, **v. 7(12),** p 1-14, dio:10.1029/2006GC001376

Appendices Contents

Appendix A – Supplementary Figures

Supplementary Figure 1 NFBTJ bottom photos taken from Bendel et al. (1993).

Supplementary Figure 2 Seismic profile 8 run across the ridges and troughs of NW limb of the NFBTJ during the KAYO88 cruise, taken from Tanahashi et al. (1991).

Supplementary Figure 3 Regional lineament map.

Supplementary Figure 4 Integrated Digital Elevation Model of the NFBTJ.

Supplementary Figure 5 Backscatter data collected during the SS2012-02 cruise.

Supplementary Figure 6 NFBTJ transect locations for cross sections presented in Figure 2.13

Supplementary Figure 7 Global distribution of Hotspots.

Appendix B - Geological Map Sheet of the North Fiji Basin Triple Junction

Appendix C – Supplementary Tables

Supplementary Table 1 Summary of abbreviations and definitions used in the attributes table for Database of Global Triple Junctions and subset Database of Oceanic Triple Junction.

Supplementary Table 2 Spreading Rate Statistics of the 41 oceanic triple junctions with averaged spreading rates

Supplementary Table 3 Summary of General Triple Junction Types and Spreading Rate Statistics of Oceanic Triple Junctions

Supplementary Table 4 Summary of the attributes of hydrothermal vent fields located at Global Triple Junctions from the InterRidge Global Vents Database.

Supplementary Table 5 Volcanism associated with Hydrothermal Systems and Global Triple Junctions.

Appendix D Global Triple Junction Database of 117 Triple Junctions

Appendix E Oceanic Triple Junction Database

Triple Junction Database References (Global and Oceanic)

Appendix A - Supplementary Figures

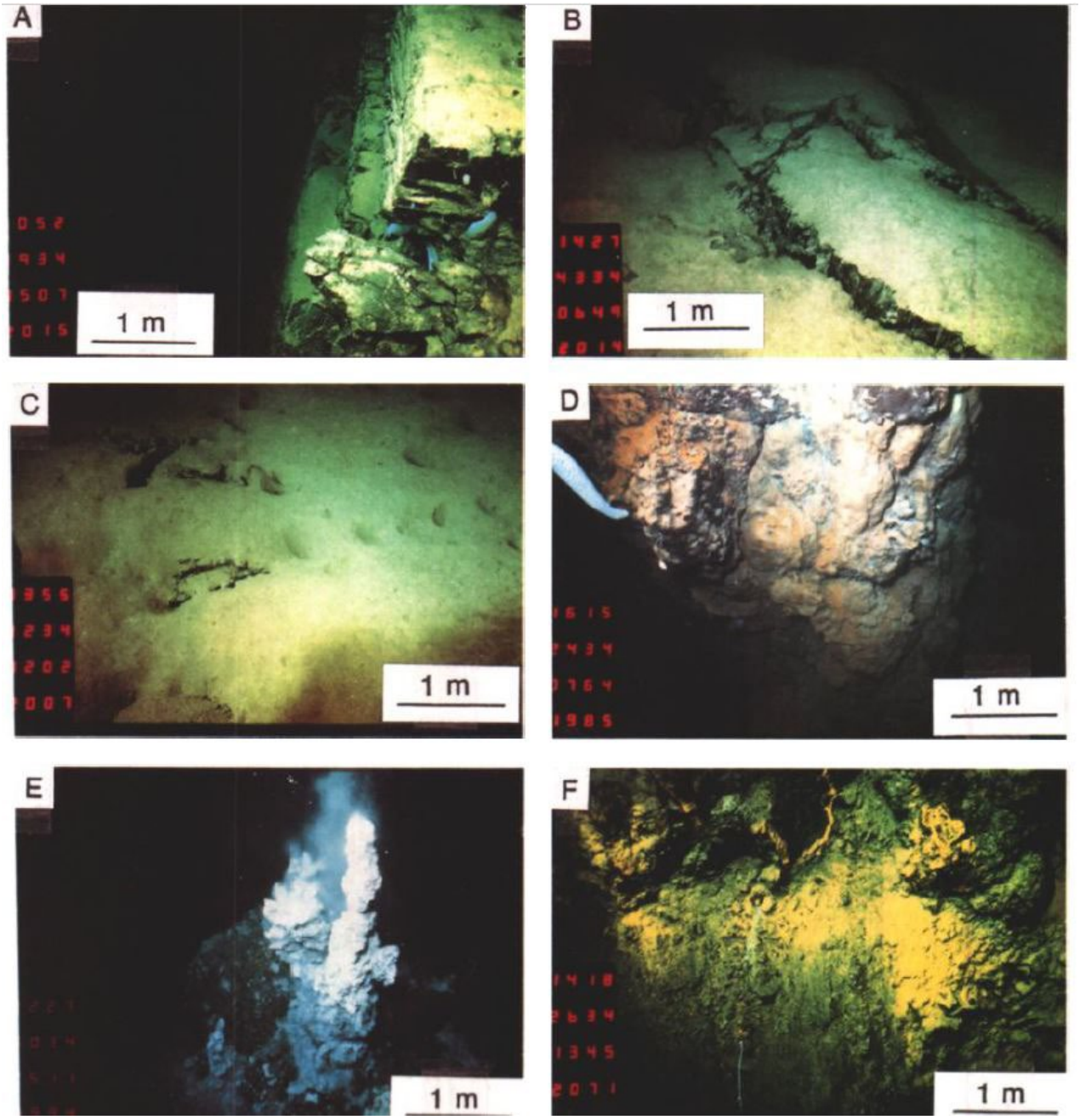

Supplementary Figure 1 NFBTJ bottom photos taken from Bendel et al. (1993). Structural features and hydrothermal deposits within SW limb neovolcanic zone of the NFBTJ. **A)** 060º fault scarp. **B)** Recently opened fissures. **C)** Alignment of funnels in unconsolidated pelagic sediments, produced by buried fissures. **D)** Inactive sulfide vent. **E)** The White Lady active chimney. **F)** Oxide staining on fault scarp. Photographs from Nautili's survey camera

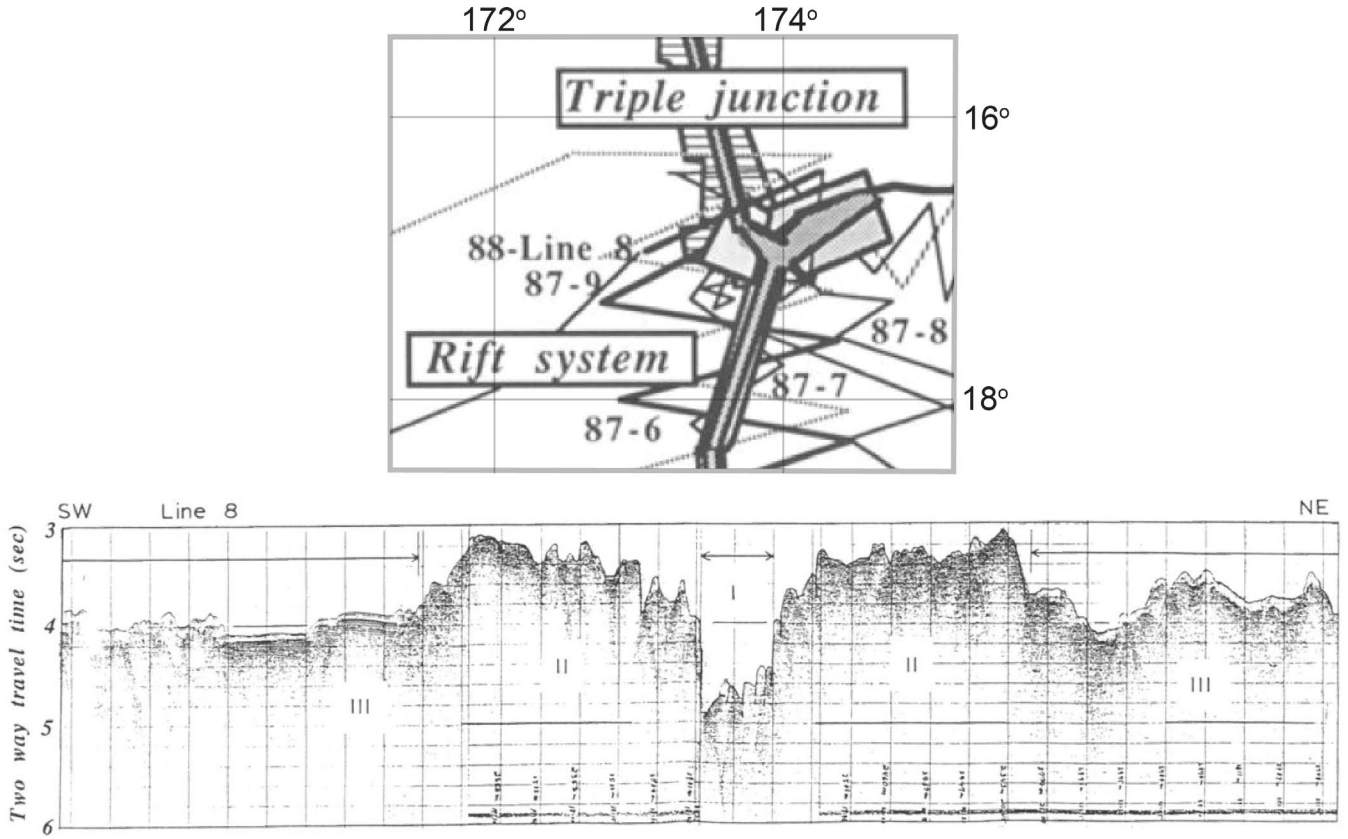

Supplementary Figure 2 Seismic profile 8 run across the ridges and troughs of NW limb of the NFBTJ during the KAYO88 cruise, taken from Tanahashi et al. (1991). Central valley (I) is interpreted as a leaky transform fault or oblique spreading system. High zone (II), about 2,400 m deep on both sides of the valley, lack sediments. Deep zones (III) surround the high zones and shows a sedimentary sequence. Vertical scale is two-way travel time in seconds. Location of profiles shown in the inset map in the top right corner as 88-Line 8.

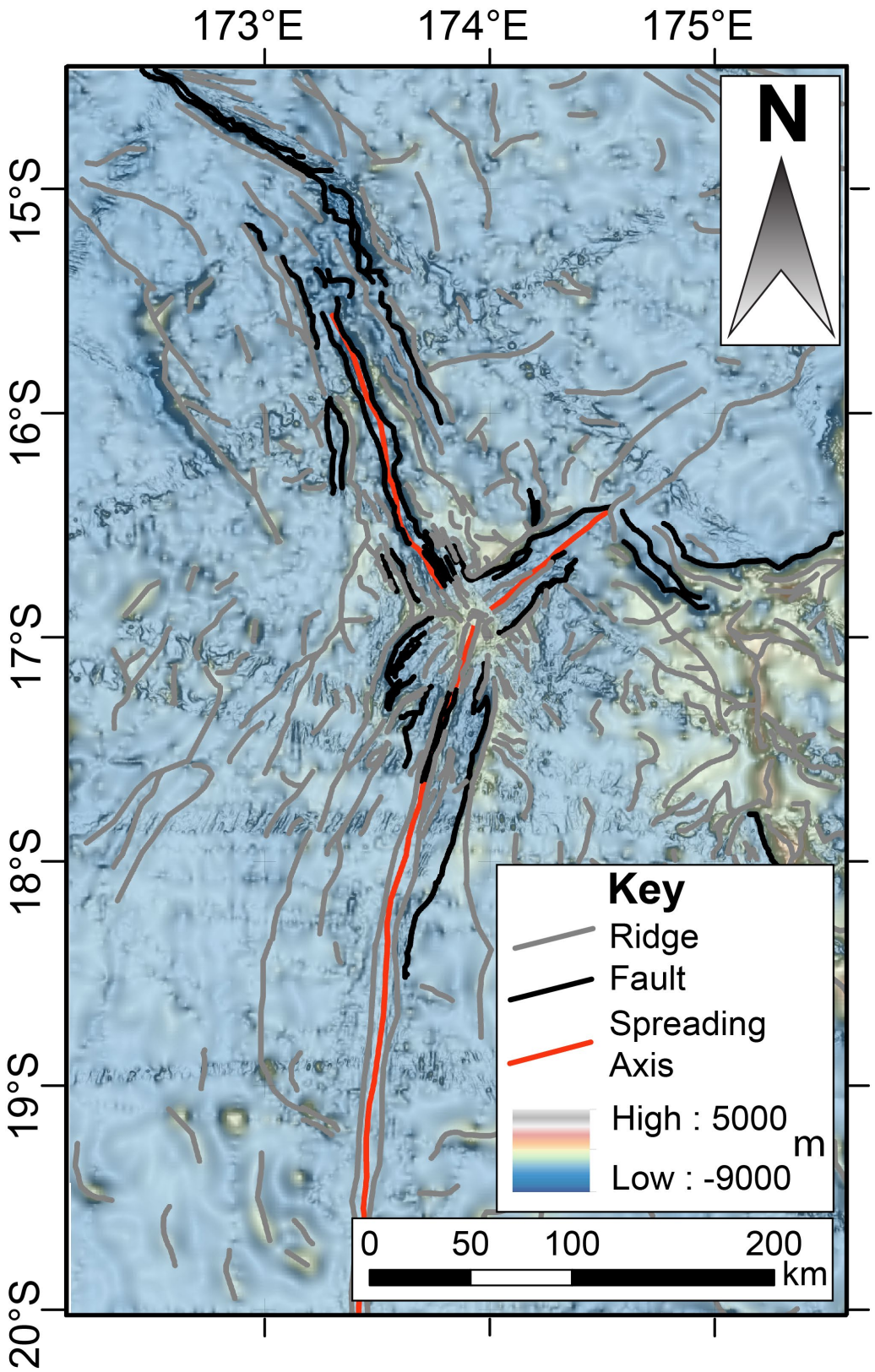

Supplementary Figure 3 A) Regional lineament map of large-scale ridges, faults and spreading axes superimposed on bathymetric data of the Global Bathymetric Chart of the Oceans (GEBCO

Compilation Group, 2021). Spreading fabrics (mostly ridge lineaments) are shown in grey, major faults with throws of >100 m are in black, and spreading axes are in red. The three longest spreading segments, corresponding to the limbs of the NFBTJ are oriented SW, NW and NE. Major NW-trending faults to the east of the triple junction are apart of the Fiji Fracture Zone (FFZ). Most of the spreading fabric mimics the three active spreading axes, except south of 19ºS and in the northeast of the map area, east of ~174.6 E. Inset black box represents this studies geological map (Figure 2.7) extent.

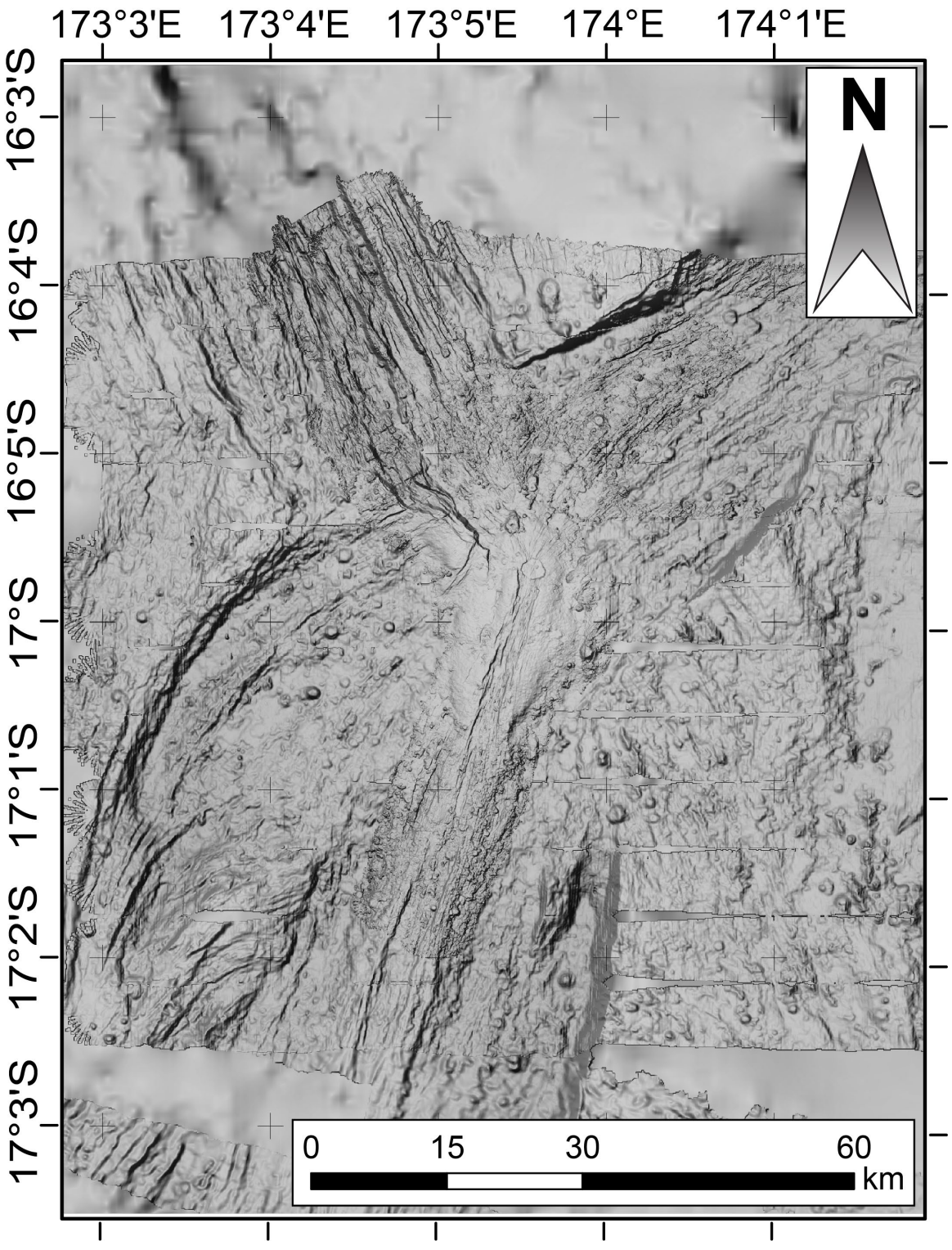

Supplementary Figure 4 Integrated DEM (gray scale) with slope-shaded enhancement (calculated slope raster and hill-shade) of Global Multi-Resolution Topography Data Synthesis

(GMRT) bathymetric grid (v3.7) (Ryan et al., 2009). MBES data were incorporated from the *RV Southern Surveyor* (SS2012-02) and *RV Yokosuka* (YK06-02) cruises and superimposed onto the GMRT. The RV Southern Surveyor data are at a resolution of 30 m; the RV Yokosuka data cover a larger area at a lower resolution of 100 m.

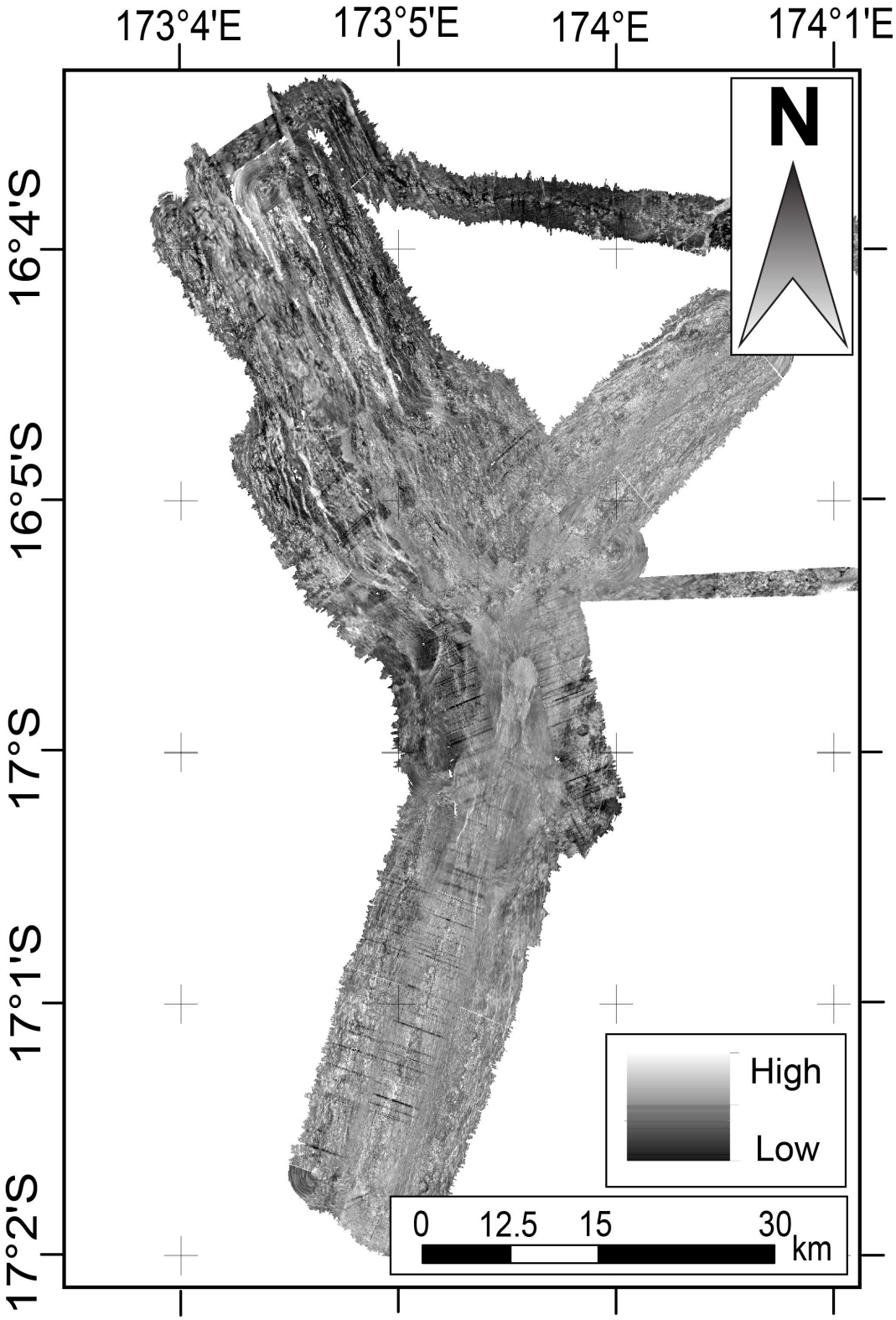

Supplementary Figure 5 Backscatter data collected during the SS2012-02 cruise. Relative backscatter strength is a proxy for the accumulation of sediment cover and provides a relative of

the underlying formations. Low sediment accumulation has a high reflectivity and appears as lighter gray. Areas of high reflectivity are associated with recent faults and fresh volcanic flows such as in the neovolcanic zones of the active rift, areas of low reflectivity (dark grey) have thicker sediment deposits and are older units.

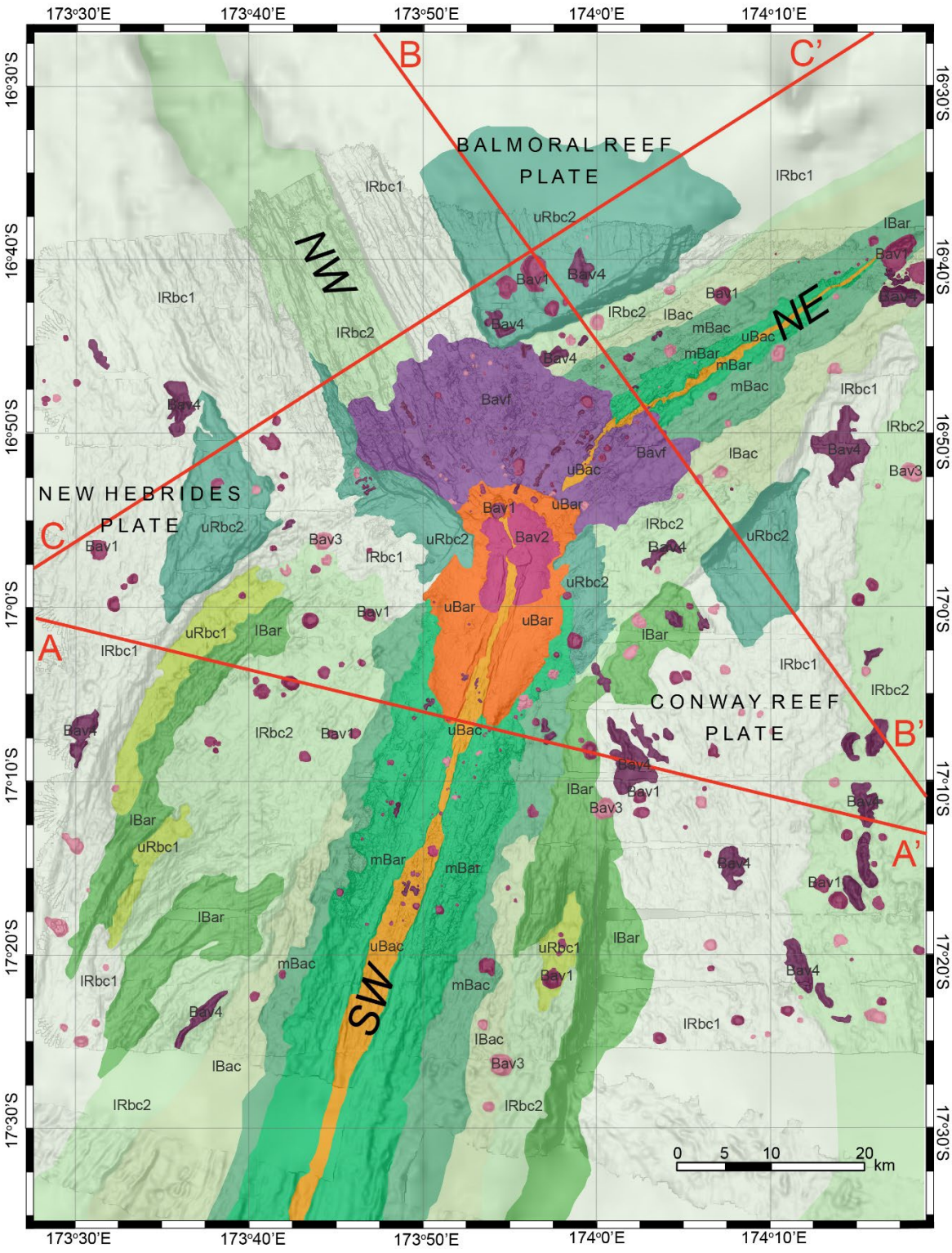

Supplementary Figure 3 NFBTJ transect locations for cross sections presented in Figure 2.13. All transects are oriented perpendicular to the principal spreading/rifting axes of each limb.

Locations shown on a reduced and simplified version of the 1:500,000 geological map of the NFBTJ. The corresponding legend is in Table 2.1. NE - Northeastern oriented limb; NW – northwestern orientated limb; SW – southwestern orientated limb.

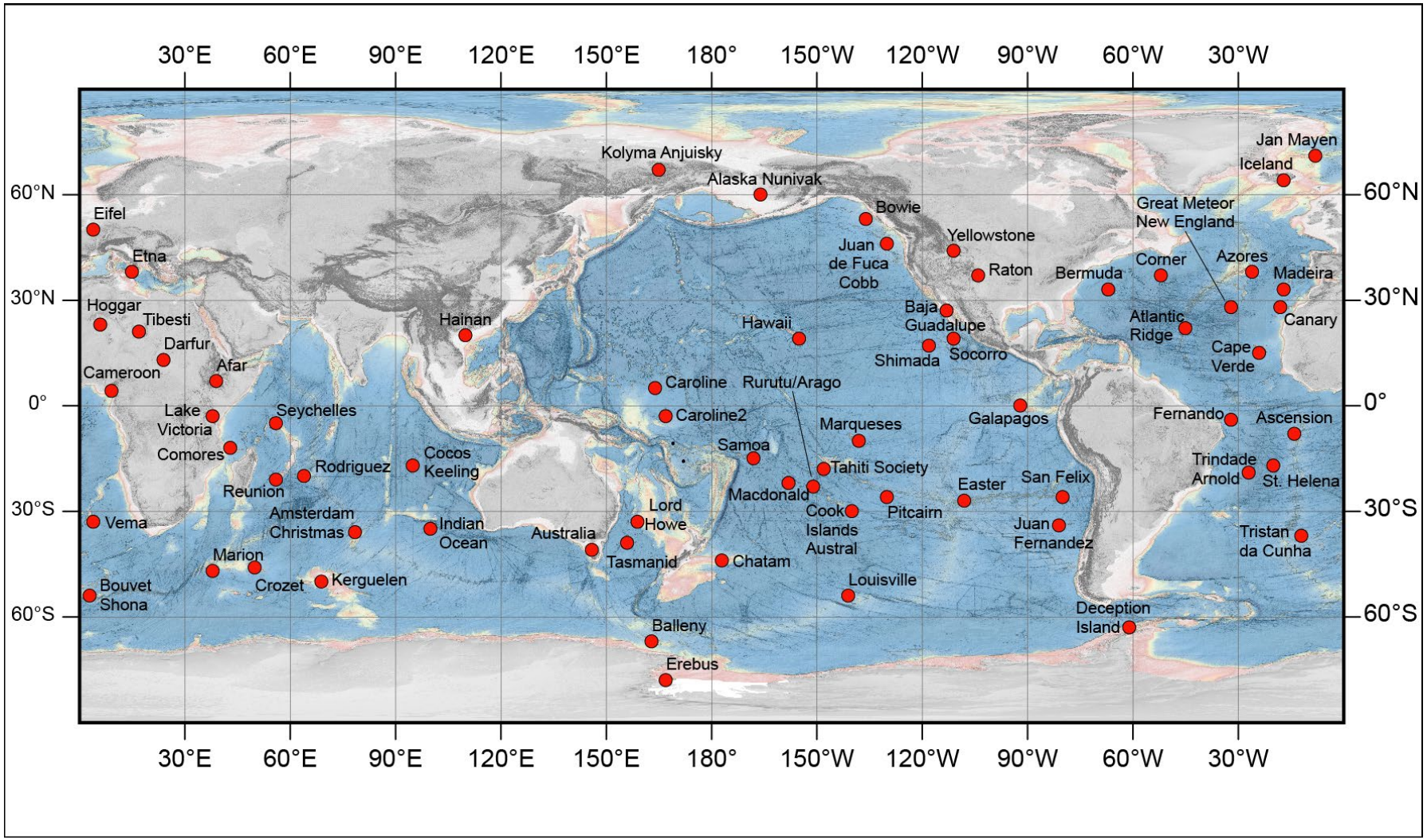

Supplementary Figure 4 Global distribution of Hotspots. Red circle icon indicates hotspot location, names are adjacent or indicated by black arrow. Hotspot information is provided by Whittaker et al. (2015).

Appendix B
Geological Map of the North Fiji Basin Triple Junction
2022

Scale 1 : 500 000

0 5 10 20 30 40 km

Author: Mary Besaw

Projection: Plate Carée - WGS 1984

BACK-ARC VOLCANOES

Bav1	**Conical volcano** Cone-shaped edifice composed of lava flows and volcaniclastic material erupted onto back-arc crust, commonly with a summit crater or caldera and/or cut by dike complexes (width:height ≤5)
Bav2	**Shield volcano** Mound-shaped edifice composed of lava flows extruded onto back-arc crust, commonly with a central caldera (width:height >5)
Bav3	**Dome volcano** Dome-shaped edifice composed of lava flows extruded onto back-arc crust or onto an axial volcanic ridge (length:width ~1)
Bav4	**Fissure volcano** Elongate volcanic edifice composed mostly of lava flows extruded onto back-arc crust, commonly with a central dike (length:width >3)
Bavf	**Volcanic field** A broad area of lava flows and volcaniclastic material surrounding a number of closely-spaced volcanoes

BACK-ARC RIFTS AND SPREADING CENTRES

Upper uBar	**Axial back-arc volcanic ridge** Volcanic ridge marking the active spreading center, commonly with discrete volcanic edifices (cones and domes), dike complexes, or calderas
uBac	**Axial back-arc crust** Undivided back-arc crust in the inner rift valley of an active spreading center
Middle mBar	**Proximal volcanic or tectonic ridge** Elongate volcanic edifice or coalesced ridges in the outer rift valley or on the flank, adjacent to an active spreading center or axial volcanic ridge
mBac	**Proximal back-arc crust** Undivided back-arc crust in the outer rift valley, adjacent to an active spreading center or axial volcanic ridge (may include products of off-axis volcanism)
Lower lBar	**Distal volcanic ridge** Elongate volcanic edifice or coalesced ridges on distal back-arc crust (may include products of off-axis volcanism or earlier seafloor spreading from a distant ridge; commonly obscured by volcaniclastic cover)
lBac	**Distal back-arc crust** Undivided back-arc crust beyond the outer rift valley and flank of an active spreading center (may include products of off-axis volcanism)

RELICT BACK-ARC

Upper uRbc1	**Upper relict back-arc crust** Undivided back-arc crust outside an identifiable area of active spreading (may be a product of intraplate volcanism, rifting of earlier back-arc crust, or an unknown spreading center)
uRbc2	**Upper tectonized relict back-arc crust** Intensely deformed back-arc crust outside an identifiable area of active spreading
Lower lRbc1	**Lower relict back-arc crust** Earliest exposed extrusive and intrusive rocks in the back-arc and outside an identifiable area of active spreading
lRbc2	**Lower tectonized relict back-arc crust** Intensely deformed earliest exposed extrusive and intrusive rocks in the back-arc and outside an identifiable area of active spreading

SYMBOLS

Crater rim	Major Fault	Flow field boundary
Caldera rim	Minor Fault	Ridge

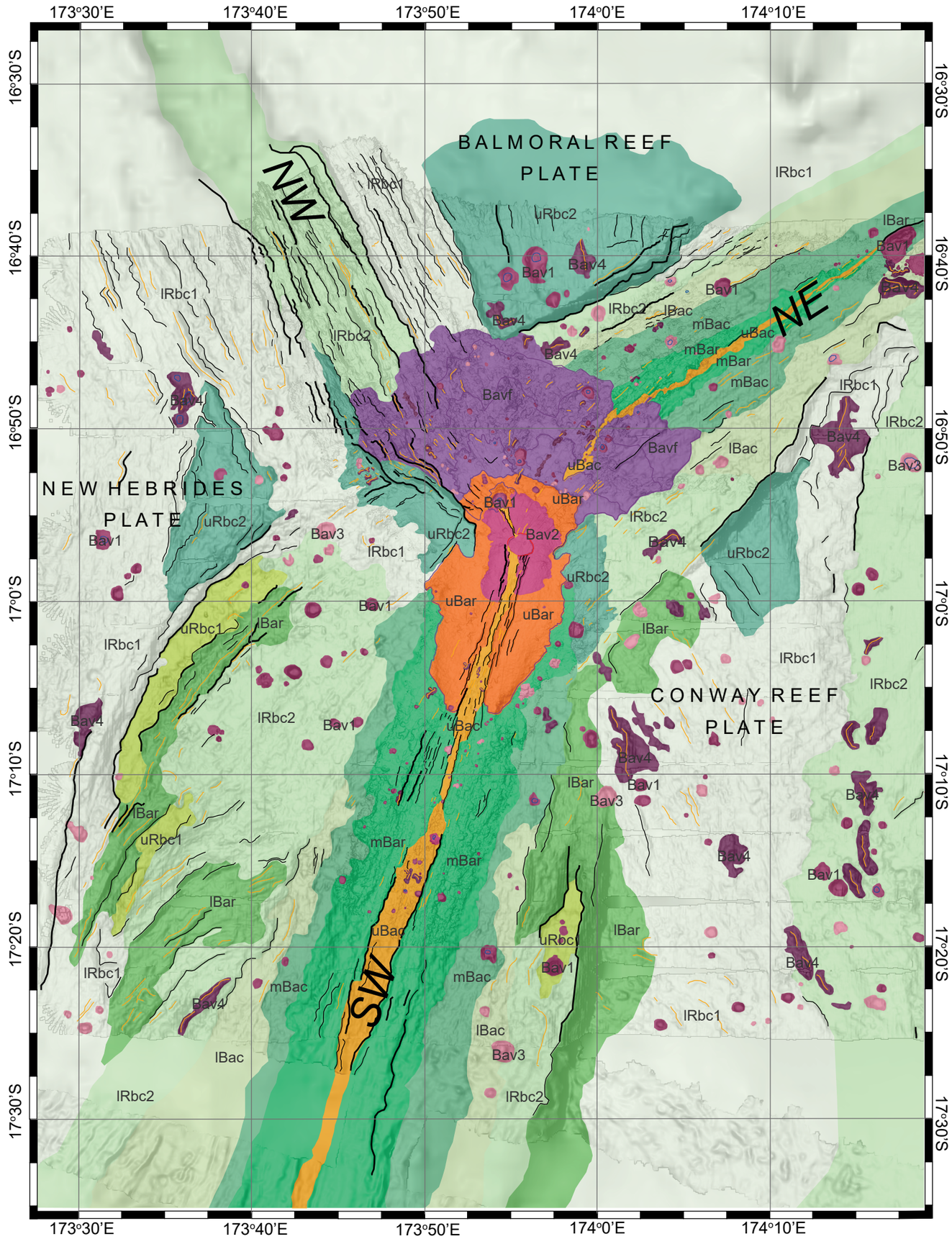

The background is the 2019 GMRT intergrated with shiptracks enhanced with slope function and multidirectional hillshade

Appendix C - Supplementary Tables

Supplementary Table 1 Summary of abbreviations and definitions used in the attributes table for Database of Global Triple Junctions (Appendix D) and subset Database of Oceanic Triple Junction (Appendix E).

Header	Abbreviation	Full Name	Description
ID	ID	Triple Junction Identification	Arbitrary numerical system for triple junction Identification.
Crustal type	O	Oceanic Crust	All plates and boundaries consist of oceanic crustal types.
	C	Continental Crust	All plates and boundaries consist of continental crustal types.
	OC	Ocean-Continent crustal boundaries	Combination of oceanic and continental crust types within a set of plates.
Geodynamic Setting	n/a	Arc	Chain of volcanoes located along the upper tectonic plate of a subduction zone, or trail of volcanoes along a moving plate across a mantle hotspot.
	n/a	Arc-Collision Zone	Active or inactive arcs interact during convergent plate tectonism.
	n/a	Arc LIP Collision	Chain of volcanoes located along the upper tectonic plate of a subduction zone with a LIP.
	ATS	Arc-Trench System	Arc-trench systems are exclusively oceanic crust and have at least one trench boundary.
	BAB	Back-Arc Basin	Basin constricted to active subduction-related back-arc basins.
	n/a	Basin	Depression of a large size, which may be structural or erosional origin.
	n/a	Continental	Defined by continental crust.
	n/a	Continental Back-Arc	Region on continental crust behind subduction-related arcs.
	n/a	Continental Collisional Zone	Tectonic plate collision of two continental crusts producing mountain ranges.
	n/a	Continental Margin	Submarine edge of the continental crust, comprising of the continental shelf, slope and rise.
	n/a	Continental Rift	Elongated fault-bound trough through continental crust, the result of extensional processes.
	n/a	Continental Strike-Slip	Lateral displacement of continental crust through regional faulting.
	MORS	Mid-Ocean Ridge Spreading	Mid-ocean spreading is always located along a mid-ocean ridge and contains at least one ridge boundary.
	n/a	Rear Arc	Adjacent to the arc, converse side of an arc relative to the trench.
TJ-Type	F	Fault	Triple junction boundary defined by a transcurrent faulting, sequence ordered by limb orientation.
	R	Ridge	Triple junction boundary defined by a spreading center, sequence ordered by limb orientation.
	T	Trench	Triple junction boundary defined by a subduction zone, sequence ordered by limb orientation.
	X	Undefined	Undefined limb boundary, sequence ordered by limb orientation.
General TJ-Type	F	Fault	Triple junction boundary defined by a transcurrent faulting, sequence is arbitrary.
	R	Ridge	Triple junction boundary defined by a spreading center, sequence is arbitrary.
	T	Trench	Triple junction boundary defined by a subduction zone, sequence is arbitrary.
	X	Undefined	Undefined limb boundary, sequence is arbitrary.
Limb Boundaries Types	CF	Continental Fault	Fault boundary within continental crust; limb indicated as 'F'.
	CFe	Continental Fault (extensional)	Extensional fault boundary within continental crust; limb indicated as 'F'.
	CFss	Continental Fault (strike-slip)	Strike-slip fault boundary within continental crust; limb indicated as 'F'.
	CFt	Continental Fault (transform)	Transform fault boundary within continental crust; limb indicated as 'F'.
	CMAF	Continental Margin Arc Fault	Fault boundary along the margin of continental arc crust, limb indicated as 'F'.
	CMAFss	Continental Margin Arc Fault (strike-slip)	Strike-slip Fault boundary along the margin of continental arc crust; limb indicated as 'F'.
	CMAFsz	Continental Margin Arc Fault (subduction zone)	Fault boundary along the margin of continental arc crust along subduction zone; limb indicated as 'F'.
	CMAFt	Continental Margin Arc Fault (transverse)	Transverse fault boundary along the margin of continental arc crust; limb indicated as 'F'.
	CMBA	Continental Margin Back-Arc	Undefined boundary along the margin of continental back-arc crust; limb indicated as 'X'.
	CMBAF	Continental Margin Back-Arc Fault	Fault boundary along the margin of continental back-arc crust; limb indicated as 'F'.
	CMF	Continental Margin Fault	Fault boundary along the margin of continental crust; limb indicated as 'F'.
	CR	Continental Rift	Rifting continental crust; limb indicated as 'X'.
	CRSCt	Continental Rift with Spreading Center (and associated transform faults)	Rifting continental crust with active spreading center and associated transform faults; limb indicated as 'X'.
	CTB	Continental Terrane Boundary	Undefined terrane boundary on continental crust; limb indicated as 'X'.
	OAF	Ocean Arc Fault	Fault boundary within oceanic arc crust; limb indicated as 'F'.
	OAFt	Ocean Arc Fault (transverse)	Fault boundary within oceanic arc crust; limb indicated as 'F'.
	OBAF	Oceanic Back-Arc Fault	Fault boundary within oceanic back-arc crust; limb indicated as 'F'.
	OBAFe	Oceanic Back-Arc Fault (extensional)	Extensional fault boundary within oceanic back-arc crust; limb indicated as 'F'.
	OBAFss	Oceanic Back-Arc Fault (strike-slip)	Strike-slip fault boundary within oceanic back-arc crust; limb indicated as 'F'.
	OBASCt	Oceanic Back-Arc Spreading Center (and associated transform faults)	Ridge boundary with associated transform faults within oceanic back-arc crust; limb indicated as 'R'.
	OCBF	Ocean-Continent Boundary Fault	Fault boundary adjacent to oceanic and continental crust; limb indicated as 'F'.
	OCBFss	Ocean-Continent Boundary Fault (strike-slip)	Strike-slip fault boundary adjacent to oceanic and continental crust; limb indicated as 'F'
	OCBu	Ocean-Continent Boundary (type uncertain)	Undefined boundary between oceanic and continental crusts; limb indicated as 'X'.
	OCLB	Ocean Continent LIP Boundary	Large igneous pluton boundary between oceanic and continental crusts; limb indicated as 'X'
	OCSZ	Ocean-Continent Subduction Zone	Trench boundary along subduction zone between oceanic and continental crusts; limb indicated as 'T'.
	OF	Oceanic Fault	Fault boundary with extinct spreading center along oceanic crusts; limb indicated as 'F'.
	OFss	Oceanic Fault (strike-slip)	Strike-slip fault boundary within oceanic crust; limb indicated as 'F'
	OFt	Oceanic Fault (transform)	Transform fault boundary with extinct spreading center along oceanic crusts; limb indicated as 'F'
	OFts	Oceanic Fault (transform with spreading centers)	Transform fault boundary with spreading center along oceanic crusts; limb indicated as 'F'.
	OLB	Ocean LIP Boundary	Large igneous pluton boundary between oceanic crusts; limb indicated as 'X'.
	OOBu	Ocean-Ocean Boundary (type uncertain)	Undefined boundary between oceanic crusts; limb indicated as 'X'.
	OOSZ	Ocean-Ocean Subduction Zone	Trench boundary along subduction zone between oceanic crusts; limb indicated as 'T'.
	OOSZt	Ocean-Ocean Subduction Zone (and associated transform faults)	Trench boundary along subduction zone between oceanic crusts with associated transform faults; limb indicated as 'T'.
	OSCt	Oceanic Spreading Center (and associated transform faults)	Ridge boundary with associated transform faults within oceanic crust; limb indicated as 'R'.
Certainty	0	Three limbs are uncertain	All three limb boundaries are uncertain and will be indicated by 'XXX' type.
	1	One limb is certain; two limbs are uncertain	One limb is certain and will be represented by 'R','F', or 'T'; two limbs are uncertain and will be indicated by two X's.
	2	Two limbs are certain; one limb is uncertain	Two limbs are certain and each will be represented by 'R','F', or 'T'; one limb is uncertain and will be indicated a 'X'.
	3	Three limbs are certain	All three limb boundaries are defined and each will be indicated by 'R','F', or 'T'.
Speed	n/a	Slow	Full spreading rate below 50 mm/yr.
	Inter.	Intermediate	Full spreading rate between 50 and 80 mm/yr.
	n/a	Fast	Full Spreading rate over 80 mm/yr.
Seabed lithology	n/a	Ash and Volcanic Sand/Gravel	Very fine to coarse grained volcanic material expelled from volcano.
	n/a	Calcareous Ooze	Calcium carbonate mud made from calcium carbonate organisms.
	n/a	Clay	Very fine grain sediment particle.
	n/a	Diatom Ooze	Siliceous oozes formed from unicellular algae.
	n/a	Fine-Grained Calcareous Sediment	Fine grained sediment with high proportion of calcium carbonate.
	n/a	Sand	Loose, fragmented, naturally-occurring material consisting of very small particles of decomposed rocks, corals, or shells.
	n/a	Siliceous Mud	Mud with enriched with Siliceous oozes formed from opal.
	n/a	Silt	Fine grain sediment particle.
Geomorphology Features	n/a	Abyssal Hills	300 to 1000 m relief in an area of seafloor located at depths below the foot of the continental slope and above the depth of the hadal zone.
	n/a	Abyssal Mountains	Over 1000 m relief in an area of seafloor located at depths below the foot of the continental slope and above the depth of the hadal zone.
	n/a	Abyssal Plains	Relief under 300 m in an area of seafloor located at depths below the foot of the continental slope and above the depth of the hadal zone.
	n/a	Basin	A depression in the seafloor, more or less equidimensional in plan and of variable extent defined by a closed bathymetric contour.
	n/a	Canyon	Steep-walled, sinuous valleys with V-shaped cross sections, axes sloping outward as continuously as river-cut land canyons and relief comparable to even the largest of the land canyons.
	n/a	Escarpment	An elongated, characteristically linear, steep slope separating horizontal or gently sloping sectors of the sea floor in non-shelf areas.
	n/a	Hadal	Seafloor occurring at depths greater than 6000 m.
	n/a	High Shelf	Over 50 m relief over a zone adjacent to a continent (or around an island) and extending from the low water line to a depth at which there is usually a marked increase of slope towards oceanic depths.
	n/a	Plateau	Flat or nearly flat elevations of considerable areal extent, dropping off abruptly on one or more sides.
	n/a	Rift Valley	Valley confined to the central axis of mid-ocean spreading ridges; they are elongate, local depressions flanked generally on both sides by ridges.
	n/a	Sill	A sea floor barrier of relatively shallow depth restricting water movement between basins.
	n/a	Spreading Ridge	The linked, major mid-oceanic mountain systems of global extent coinciding with the youngest ocean crusts mapped.
	n/a	Trench	A long narrow, characteristically very deep and asymmetrical depression of the sea floor, with relatively steep sides.
	n/a	Trough	A long depression of the seafloor characteristically flat bottomed and steep sided, generally open at one end.

Supplementary Table 2 Spreading rate statistics of the 41 oceanic triple junctions with averaged spreading rates

TJ ID	Count	MEAN Spreading Rate (mm/yr)	Min.	Max.	Range
24	141	96.1	52.0	119.3	67.3
29	127	141.7	141.4	142.1	0.6
31	129	142.4	142.2	142.5	0.3
44	132	70.8	69.7	71.9	2.2
47	115	24.1	5.5	39.2	33.8
50	157	22.9	16.3	59.6	43.3
51	255	28.6	26.7	33.2	6.5
53	169	26.7	17.9	29.6	11.7
55	134	74.8	74.7	75.0	0.2
59	64	39.4	33.1	41.2	8.1
60	141	41.3	40.9	49.0	8.1
61	3	82.5	74.9	92.3	17.4
69	253	60.3	59.8	60.7	0.9
70	251	55.2	34.3	61.7	27.4
71	254	46.3	13.4	52.0	38.6
73	252	32.8	17.1	60.7	43.6
75	243	120.4	90.2	157.9	67.7
76	256	145.7	77.6	158.1	80.4
78	256	20.0	15.2	27.0	11.8
79	254	18.8	15.4	26.6	11.2
80	233	27.3	14.9	32.4	17.5
80	7	21.5	14.9	32.1	17.2
82	250	22.8	20.4	24.5	4.1
83	124	26.4	8.7	60.8	52.0
84	253	50.8	34.3	90.1	55.8
86	255	71.4	43.7	112.7	68.9
87	6	112.7	111.1	114.6	3.5
88	67	137.3	135.6	139.5	3.9
89	254	72.9	67.5	89.1	21.5
90	205	127.4	30.1	140.5	110.4
91	253	138.5	136.7	141.4	4.7
92	252	157.9	157.6	158.1	0.5
93	251	158.6	158.6	158.7	0.1
94	254	158.4	158.3	158.5	0.3
95	254	60.1	59.1	61.1	2.0
96	248	66.0	65.1	66.9	1.8
97	210	44.1	17.8	48.2	30.4
98	254	85.6	27.6	129.9	102.3
104	146	63.3	32.0	71.2	39.3
107	130	144.8	127.2	148.6	21.4
109	126	15.8	15.4	18.7	3.4
114	31	46.8	46.7	46.9	0.3

Note: To obtain a representative spreading rate for each triple junction, we used a 100-km radius circle to average the spreading rate data published in Seton et al. (2020), Speed is categorizing the

full spreading rate in mm/yr from Seton et al., 2020 into three groups: Slow (<50 mm/yr), Inter. (50-80 mm/yr), and Fast (>80 mm/yr). Count, number of spreading rate data points from Seton et al. (2020) within a 100 km radius of each respective defined Oceanic triple junctions (Appendix E). Minimum (Min.), slowest recorded spreading rate within 100 km radius of triple junction. Maximum (Max.), fastest recorded spreading rate within 100 km radius of triple junction. Range, difference between maximum and minimum spreading rates. Abbreviations: BAB= Back-Arc Basins, MORS= Mid-Ocean Ridge Spreading, ATS= Arc-Trench Systems. General TJ type abbreviations are listed in Appendix C, Supplementary Table 1.

Supplementary Table 3 Summary of General Triple Junction Types and Spreading Rate Statistics of Oceanic Triple Junctions (Appendix C, Supplementary Table 2; Appendix E)

General TJ type	Count	Average Speed (mm/yr)	Speed Category	Max. Speed (mm/yr)	Min. Speed (mm/yr)	Range	BAB	MORS	ATS
FRR	13	53.8	Inter.	127.4	18.8	108.6	2	11	0
FTT	10	76.1	Inter.	144.8	22.9	121.9	0	0	10
RRR	9	118.0	Fast	158.6	46.3	112.3	2	7	0
RFF	5	49.6	Slow	137.3	15.8	121.5	1	4	0
RTT	1	70.8	Inter.	70.8	70.8	0	0	0	1
TFF	1	26.7	Slow	26.7	26.7	0	0	0	1
TTT	1	96.1	Fast	96.1	96.1	0	0	0	1
FFF	1	112.7	Fast	112.7	112.7	0	1	0	0

Note: To obtain a representative spreading rate for each triple junction, we used a 100-km radius circle to average the spreading rate data published in Seton et al. (2020), Speed is categorizing the full spreading rate in mm/yr from Seton et al., 2020 into three groups: slow (<50 mm/yr), inter. (50-80 mm/yr), and fast (>80 mm/yr). Count, number of spreading rate data points from Seton et al. (2020) within a 100 km radius of each respective defined Oceanic triple junctions (Appendix E). Minimum (Min.), slowest recorded spreading rate within 100 km radius of triple junction. Maximum (Max.), fastest recorded spreading rate within 100 km radius of triple junction. Range, difference between maximum and minimum spreading rates. Abbreviations: BAB= Back-Arc Basins, MORS= Mid-Ocean Ridge Spreading, ATS= Arc-Trench Systems. General TJ type abbreviations are listed in Appendix C, Supplementary Table 1.

Supplementary Table 4 Summary of the attributes of hydrothermal vent fields located at global triple junctions (Appendix D) from the InterRidge Global Vents Database (Beaulieu and Szafranski, 2020).

Crustal Type	Triple Junction ID	Geolocation	Geolocation	Geodynamic Setting	TJ Type	Age (Ma)	Latitude	Longitude	National Jurisdiction	Activity	Vent ID	Vent Name(s)	Vent Sites	Temp. Cel.	Max. Temp.	Depth (m)	Tectonic Setting	Full/Spread	Hostrock	Deposit Type	Volcano Number(s)	Dive Info
C	13	FLORES SEA	Flores Sea	REAR ARC	FAT	n/a	-8.3	119.55	Indonesia	active, confirmed	Sengeang Island	n/a	n/a	35	35	1000	arc volcano	0	n/a	n/a	262420	1991 at center, from beach
	74	RED SEA	Red Sea	CONTINENTAL	RFR	0	17.97	40.07	Saudi Arabia	active, inferred	Red Sea Rift, 18 N	n/a	n/a	n/a	n/a	1500	mid-ocean ridge	16.7	n/a	n/a	n/a	1980 submersible Alvin; 1982 dredge only
	112	ASIA	Asia	CONTINENTAL MARGIN	XXF	n/a	24.83	121.95	Taiwan	active, confirmed	Kueishan Island	Kueishantao Islet, Turtle Island, Tashi fishing grounds, Guishandao, Guishandao Island	n/a	n/a	116	30	back-arc spreading center	55.3	n/a	n/a	n/a	1999, likely by SCUBA
								122.00	Taiwan		Kueishan Island, offshore	Guishandao	n/a	n/a	1200	back-arc spreading center	53.1				2008 or earlier
							24.85	122.70	Japan		SPOT, Yonaguni Knoll IV	Dai-Yon no. 4	Lion, Crystal, Tiger, Mosquito		328	1385	back-arc spreading center	49	basalt, high-K andesite, dacite, sediment	LTH		2000 submersibles Shinkai 2000 and Shinkai 6500
	2	SUMATRA TRENCH	Sumatra Trench	ARC-TRENCH SYSTEM	FTT	n/a	-6.10	105.42	Indonesia	active, inferred	Krakatau	Sunda Strait, SSKR, Sunda Strait/Krakatau	n/a	n/a	n/a	250	arc volcano	0	n/a	n/a	262000	2002 CTD/transmissometer and dredge only
	21	TAIWAN	Taiwan	ISLAND ARC	TSF	n/a	24.83	121.95	Taiwan	active, confirmed	Kueishan Island	Kueishantao Islet, Turtle Island, Tashi fishing grounds, Guishandao, Guishandao Island	n/a	n/a	116	30	back-arc spreading center	55.3	n/a	n/a	n/a	1999, likely by SCUBA
							24.83	122.00	Taiwan		Kueishan Island, offshore	Guishandao	n/a	n/a	1200	back-arc spreading center	53.1				2008 or earlier
							24.85	122.70	Japan		SPOT, Yonaguni Knoll IV	Dai-Yon no. 4	Lion, Crystal, Tiger, Mosquito		328	1385	back-arc spreading center	49	basalt, high-K andesite, dacite, sediment	LTH		2000 submersibles Shinkai 2000 and Shinkai 6500
	35	PANAMA	Panama	CONTINENTAL MARGIN	FTT	n/a	9.12	-84.84	Costa Rica	active, confirmed	Jaco Scar	Jaco Scarp	n/a	Low	5	1790	arc volcano	0	n/a	n/a	n/a	2009 submersible Alvin
	36	MEXICO	Mexico	CONTINENTAL MARGIN	TFT	9	18.25	-108.30	Mexico	active, inferred	EPR, Marcotrio Spreading Segment	n/a	n/a	n/a	n/a	2600	mid-ocean ridge	77.7	n/a	n/a	n/a	1997 plume only
							17.68	-109.36	Mexico		EPR, Hot 17 N segment					2600	mid-ocean ridge	77.4				
							17.67	-105.01	Mexico		EPR, northern 17 N segment					2600	mid-ocean ridge	74.8				
							16.58	-105.30	Mexico		EPR, southern 17 N segment					2700	mid-ocean ridge	77.4			334020	
OC	39	JUAN DE FUCA, BRITISH COLUMBIA	Juan De Fuca, British Columbia	CONTINENTAL MARGIN	TFT	5	47.71	-127.79	Canada		Baby Bare Seamount	Baby Bare outcrop	n/a	n/a	25	2600	mid-ocean ridge	n/a	n/a	LTH		
							47.97	-129.09	Canada		High Rise Field	High Rise, Hiti, Endeavour Segment, 47.58'N, 129'	Baltic, Bambi, Blue, Moon, Boardwalk, Clam_Bed, Clam_Bed_Vents, Dante, Flying Perch_Place, Vienna	n/a	343	2200	mid-ocean ridge	56.2	N + E-MORB		319310	1995 submersible Alvin
							47.95	-129.10	Canada		Main Endeavour Field	Main Field, MEF, ME, Endeavour Segment, 47.57N, Endeavour	Bastille, Crypto, Dante, Dudley, Easter_Island, Grotto, Hulk, Lobo, MidnZ, Peanut, Puffer, Salut, Smoke & Mirrors, Sully, TP, Quebec		402		mid-ocean ridge					
							48.46	-128.71	Canada		Middle Valley, Dead Dog Vent Field	Site 858, Middle Valley	Heineken Hollow, Inspired Mounds, Chowder Hill, Puppy Dog		276	2450	mid-ocean ridge		MORB, minor E-MORB, sediment-hosted	PMS		1992 or earlier towed video
							48.43	-128.68	Canada		Middle Valley, ODP Mound	Site 858, Middle Valley	Lone Star, Shiver Brick, Spire		265	2440	mid-ocean ridge					
							47.92	-129.11	Canada		Mothra Field	MO	Bat_Tower, Boomerang, Brigid, Cauldron, Faulty_Towers (includes Comfortless_Cove, Crypto, Hot_Harold, Pinocchio, Spikes, Tower		320	2270	mid-ocean ridge		N + E-MORB			1996 ROV ROPOS; 1986 plume only
							47.96	-129.08	Canada		Sally Dawg Field	SD	Sally Dawg, Grendl, Cinjun, Tube		329	2200	mid-ocean ridge					1995 submersible Alvin, followed by ROV ROPOS
							48.00	-129.07	Canada		Sasquatch Field	n/a	Christmas Tree, Marker C-Pico		289		mid-ocean ridge					2000 submersible Alvin
							48.20	-128.93	Canada	active, inferred	ET	Split Volcano, Surveyor Seamount	n/a	n/a	n/a	2500	mid-ocean ridge	n/a	n/a	NFS, hydrothermal deposits		n/a
							47.64	-128.97	Canada		Split Seamount					2350	mid-ocean ridge			NFS, Fe & Mn crusts		1990 camera tow (need reference to check if activity confirmed)
							47.90	-129.12	Canada		Stockwerk					2300	mid-ocean ridge			n/a		2000 submersible Alvin (need publication to determine if confirmed)
							48.48	-129.04	Canada		West Valley	West Valley Segment				3000	mid-ocean ridge	56.3		NFS, hydrothermal deposits	331005	1987 and 1988 dredges only (towed camera did not confirm activity)
	101	PACIFIC	Pacific	CONTINENTAL MARGIN	FRR	3	48.45	-128.68	Canada	inactive	Middle Valley, Bent Hill Massive Sulfide	Site 858, Middle Valley		n/a	n/a	2400	mid-ocean ridge	56.2	MORB, minor E-MORB, sediment-hosted	PMS	n/a	1985 deposits only
							42.76	-126.71	United States	active, confirmed	Sea Cliff	GR-14, GR14, G14, North Gorda	n/a	n/a	308	2600	mid-ocean ridge	n/a	MORB	PMS	n/a	1986 submersible Sea Cliff; 1985 plume only; 1988 dredge and camera tow did not confirm activity
	40	JUAN DE FUCA	Juan De Fuca	ARC-TRENCH SYSTEM	TTF	n/a	42.68	-126.78	United States		Gorda Ridge, EPR94				55.7	3150	mid-ocean ridge		basalt-hosted		331031	1996 camera/temperature tow followed by ROV ROPOS dive confirm hydrothermal activity
							42.63	-126.83	United States		Gorda Ridge, EPR95					3400	mid-ocean ridge			n/a	n/a	1994 deposits only, 1996 plume only
							42.66	-126.55	United States		Gorda Ridge, GR-13					1400	mid-ocean ridge					1996 plume only
	72	GULF OF ADEN	Gulf Of Aden	CONTINENTAL MARGIN	RRR	n/a	11.95	43.67	Djibouti	active, confirmed	Aden	n/a	n/a	Low	n/a	1600	mid-ocean ridge	19.1	basalt-hosted	NFS, Fe & Mn rich crusts	n/a	1984 submersible Cyana
	77	PACIFIC	Pacific	ARC-TRENCH SYSTEM	TTR	1	-46.20	-74.90	Chile	active, inferred	Chile Triple Junction	n/a	n/a	n/a	n/a	3000	mid-ocean ridge	57.9	n/a	n/a	n/a	2010 plume only
	101	PACIFIC	Pacific	CONTINENTAL MARGIN	FRR	3	-46.20	-74.90	Chile		Chile Triple Junction, 16 km north	n/a	n/a	n/a	n/a	3000	mid-ocean ridge	n/a	n/a	n/a	n/a	2010 plume only
							23.36	-108.53	Mexico	active, confirmed	Alarcon Rise, Mejdo	n/a	Mejdo S, Mejdo N, Perico	n/a	350	2304	mid-ocean ridge	47.5	n/a	n/a	n/a	2012 ROV Doc Ricketts
							23.36	-108.54	Mexico		Alarcon Rise, Mejdo					2295	mid-ocean ridge					
							23.16	-108.56	Mexico		Alarcon Rise, Tuel- Verde				350	2445	mid-ocean ridge					
							23.56	-108.88	Mexico		Precedero Basin, Ayba				350	3073	mid-ocean ridge	46.9				
							23.54	-108.39	Mexico	active, inferred	Alarcon Rise/Pescadero intersection	n/a	n/a	n/a	n/a	2294	mid-ocean ridge	47.5	n/a	n/a	n/a	2011 ROV Doc Ricketts did not confirm activity
							23.23	-108.62	Mexico		Alarcon Rise/Tamayo intersection					2358	mid-ocean ridge					
							22.93	-108.07	Mexico		EPR/Tamayo intersection					3200	mid-ocean ridge	47.8				1979 submersible Alvin did not confirm activity
	105	PACIFIC	Pacific	CONTINENTAL MARGIN	TRF	0	49.75	-130.27	Canada	active, confirmed	Magic Mountain	southern Explorer Ridge, 49 45'N	Majestic Chimney Field (Ashtyrshe 1-4, Majestic, Obelisk, Digit Field), Merlin, Merlin Vent, Merlin 2, Tubeworm, Aberrant, Lilliget, Amphoriteji, Mystic Chimney Field (Eiselein, Eastern Island, Ridge Top), Zoo Chimney Field (Zoo Chimney, Zoo Chimney, Recordbreak	n/a	311	1650	mid-ocean ridge	56.3	N + E-MORB	PMS	n/a	1984 submersible Pisces IV
							49.73	-130.27	Canada	active, inferred	Magic Mountain, 3 km south					1600	mid-ocean ridge			n/a		2002 AUV ABE plume only
							50.58	-129.35	Canada	inactive	Defleced Segment	n/a	n/a	n/a	n/a	600	mid-ocean ridge		n/a	NFS, Fe & Mn crusts	n/a	
							50.08	-129.75	Canada		Explorer Deep					1400	mid-ocean ridge					
	117	ANTARTICA	Antarctica	ARC-TRENCH SYSTEM	FFT	n/a	-62.19	-57.27	Antarctica	active, confirmed	Hook Ridge	HR, Bransfield Strait, 62 11'S	n/a	Low	n/a	1080	back-arc spreading center	10	basalt, high-K andesite, dacite, rhyolithe, sediment-hosted	PMS	n/a	1997 hot sediment, 1995 plume only; 1999 even hotter sediment
	4	Carlsberg Ridge, Central Indian Ridge	Carlsberg Ridge, Central Indian Ridge	MID-OCEAN SPREADING	FXX	1	-8.25	68.20	high seas	active, inferred	CIR, 9-17 S, Segment 1	n/a	n/a	n/a	n/a	3600	mid-ocean ridge	33.2	n/a	n/a	n/a	2010 plume only
	27	NEW GUINEA TRENCH	New Guinea Trench	ISLAND ARC LIP COLLISION	XFF	n/a	-4.08	153.55	Papua New Guinea	active, confirmed	Tulum Bay, Ambitle Island	n/a	Waramung	n/a	38	10	arc volcano	0	n/a	LTH	254020	1998 or earlier, likely by SCUBA
	29	MARIANA	Mariana	ARC-TRENCH SYSTEM	TTF	n/a	13.10	143.68	United States	active, confirmed	Forecast	13 N Ridge Site	n/a	n/a	n/a	2900	back-arc spreading center	50.5	n/a	n/a	n/a	2000 deep-tow camera
							13.40	143.92	United States			n/a	Bart, Snail Scrum, Homer, Marge	n/a	210	1470	arc volcano	0	VAB, BABB, low-K andesite	PMS	264220	1992 submersible Shinkai 6500
							12.92	143.63	United States		Pika		Archaean (= Archaic); Pika, Uraganus		330	2990	back-arc spreading center	51.3	basalt-hosted		n/a	2003 submersible Shinkai 6500; 2003 plume only
							13.25	144.52	United States		Seamount X	Seamount "X"	n/a	n/a	n/a	1450	arc volcano	0	basaltic andesite		264230	1994 or earlier submersible Shinkai 6500
							12.95	143.62	United States		Snail	Pryer, South Backarc	Snail (= Fryer), Y (= Yamatatsu)		248	2980	back-arc spreading center	51.3	n/a	n/a	n/a	2003 ROV Jason II; 2003 plume only
							12.72	143.53	United States		TOTO Caldera	Nakayama Field, Toto Caldera	TOTO (= Tuto)	n/a	170	2960	arc volcano	0	n/a			2000 deep-tow camera (later_survey = ROV Kaiko); 1998 or earlier hydrothermal deposits analyzed, 1998 plume only
							12.76	143.48	United States	active, inferred	Mariana Trough, plume 2	n/a	n/a	n/a	n/a	2680	back-arc spreading center	51.9				2003 plume only
							-15.42	-174.25	Tonga	active, confirmed	Mata	n/a	n/a	High	n/a	1600	back-arc spreading center	107.7	n/a	n/a	243120	2008 commercial ROV; 2004 plume only; 2006 plume and chimney samples
							-15.52	-173.78	Tonga		Mata Fifo		Crowd		331	1640	arc volcano					2010 towed camera; 2009 plume and dredge only
							-15.00	-173.76	Tonga		Mata Tolu	NELS, North Mata	n/a	n/a	271	1840	arc volcano					
							-15.02	-173.78	Tonga		Mata Ua	n/a	Flashing Chimney	n/a	360	2307	arc volcano	0				2012 ROV Quest 4000; 2010 plume only (towed camera did not confirm)
							-15.07	-173.57	Tonga		Niua North	n/a	Hellow, Mussel Marsa	n/a	n/a	800	arc volcano		n/a			2012 ROV Quest 4000; 2008 plume only
							-15.17	-173.57	Tonga		Niua South	Niua, Volcano "P", Tonga Arc, Volcano P	Niua 2, Niua 3 (= Adelaide Spivey)	n/a	315	1180	arc volcano					2008 commercial ROV
							-15.38	-174.25	Tonga		Tafu	n/a	n/a	Low	n/a	1400	back-arc spreading center	109.8				2008 or 2009 commercial ROV; 2008 plume only; 2008 ROV Jason II
							-15.38	-174.02	Tonga	active, confirmed	Volcano O	Nuutafo, Niua Tahi, Caldera "O", Target O, Volcano O, Volcano O, NELS, NELCO, Northeast Caldera, Niua Tahi Arc Caldera, MTJ-1 caldera	n/a	High	n/a	1635	back-arc spreading center	107.7	n/a	n/a	243140	2009 ROV Jason II; 2003 plume only; 2004 dredging (SS11/2004 cruise); 2005 plume only; 2008 commercial ROV (report does not confirm activity)
	44	Lau Southwest Pacific	Lau Southwest Pacific	ARC-TRENCH SYSTEM	TRT	n/a	-15.10	-173.75	Tonga		West Mata submarine volcano	n/a	Axial'will, Cinnamicle, Epsilon, Fonualei, Fonualei, Mafilikeitoe, Pionnetheu, RedRockRidge, ShrimpCity, Smokefree, WhiteMat	Low	n/a	1206	arc volcano	0			243130	2009 ROV Jason II; 2006 eruption plume detected
							-15.08	-173.67	Tonga		East Mata submarine volcano	NELVI				1300	arc volcano					2008 plume only; 2009 plume only
							-14.98	-173.98	Tonga		Mata Fa					1318	arc volcano	0				
							-14.93	-173.79	Tonga		Mata Dos					1210	arc volcano					2010 plume only
							-15.04	-173.74	Tonga		Mata Tahi					1100	arc volcano					
							-15.33	-174.67	Tonga	active, inferred	MTJ, PAPATUA	Mangatolo Triple Junction, Kings Triple Junction	n/a	n/a	n/a	2100	back-arc spreading center	106.4	BABB, MORB, low-K andesite	PMS	n/a	1986 PAPATUA Expedition deposits only; 2008 plume only
							-15.96	-174.80	Tonga		MTJ, 60b01	n/a	n/a	n/a	n/a	2400	back-arc spreading center	94.2	n/a	n/a	n/a	2008 plume only
							-15.83	-174.84	Tonga		MTJ, 60b02					2600	back-arc spreading center					
							-15.83	-174.62	Tonga		MTJ, 60b03, 15.83 S					2300	back-arc spreading center	97.3				
							-15.72	-174.83	Tonga		MTJ, 60b05, 15.72 S					2400	back-arc spreading center					
							-15.78	-174.84	Tonga		MTJ, 60b05, 15.78 S					2500	back-arc spreading center	94.2				
							-15.81	-174.74	Tonga		MTJ, 60b06					2100	back-arc spreading center	100.6				
							-15.22	-174.18	Tonga		NELSC, 60b12					2000	back-arc spreading center	109.8				
							-15.33	-174.25	Tonga		Tuhi Moana 7	North East Lau 5 Target, NELS				1940	back-arc spreading center	109.8		PMS		2004 plume only; 2008 plume only; 2009 video camera tow (activity not confirmed)
							-14.96	-173.78	Tonga	inactive	Mata Nima	n/a	n/a	n/a	n/a	2072	arc volcano	0	n/a	n/a	n/a	2010 no plume detected
	47	Southwest Pacific	Southwest Pacific	ARC-TRENCH SYSTEM	TTF	n/a	-10.47	164.25	Solomon Islands	active, inferred	San Cristobal arc, Segment	n/a	n/a	n/a	n/a	2000	arc volcano	0	n/a	n/a	n/a	2002 volcano only
							-10.40	164.75	Solomon Islands		San Cristobal arc, Target M					2000	arc volcano					2002 plume and dredge only
							-10.50	164.95	Solomon Islands		San Cristobal arc, Target N					arc volcano					2002 dredge only
	51	Mid-Atlantic Ridge	Mid-Atlantic Ridge	MID-OCEAN SPREADING	RRF	1	17.15	-46.42	high seas	inactive	MAR, 17.08'N	n/a	n/a	n/a	n/a	3100	mid-ocean ridge	25.2	n/a	n/a	n/a	2014/2015 dredge only; 17/spub and corer
							16.84	-46.48	high seas		Kriarov	16.38'N, MAR	n/a	n/a	n/a	3900	mid-ocean ridge		MORB			2002 or earlier plume only; 2004 TV grab; inferred inactive; 2007 ROV Victor indicated inactive
							16.57	-46.67	high seas		MAR, 16.50'N	n/a	n/a	n/a	n/a	3000	mid-ocean ridge		n/a	VDG, and Fe oxides		
							15.92	-46.96	high seas		MAR, 15.90'N	n/a	n/a	n/a	n/a	3000	mid-ocean ridge		n/a	MnO, Mn crusts		
	52	Caribbean	Caribbean	ARC-TRENCH SYSTEM	TFT	n/a	15.25	-61.58	Dominica	active, confirmed	Champagne Hot Springs	Champagne Reef	n/a	n/a	71	5	arc volcano		n/a	n/a	600110	2001 or earlier (assume SCUBA)
							16.71	-62.23	United Kingdom		Montserrat Offshore Springs	Montserrat Seamounts, Offshore Vent Field, Northwest Volcano	n/a	Low	n/a	10	arc volcano	0	n/a	LTH	360050	1998 or earlier (assume SCUBA)
							16.46	-61.98	France	active, inferred	Montserrat-Marie Galante fault	n/a	n/a	n/a	n/a	1000	arc volcano		n/a	n/a	n/a	1987 plume and deposits
	59	soloman sea	Soloman Sea	ARC-TRENCH SYSTEM	TFT	n/a	-9.80	155.07	Papua New Guinea	active, confirmed	Woodlark Basin, Segment 3B	n/a	n/a	n/a	n/a	3300	back-arc spreading center	34.8	n/a	n/a	n/a	2009 plume only
							-9.25	156.10	Solomon Islands		Woodlark Basin, Segment 5B					3600	back-arc spreading center	39.2				1996 plume only; 2009 plume only
	63	soloman islands	Soloman Islands	ARC-TRENCH SYSTEM	XFX	n/a	-10.47	164.25	Solomon Islands	active, confirmed	Grover Seamount	n/a	n/a	n/a	n/a	600	arc volcano	0	n/a	n/a	n/a	2002 towed video
							-10.40	164.75	Solomon Islands		San Cristobal arc, Target M					2000	arc volcano					2002 plume and dredge only
							-10.50	164.00	Solomon Islands		San Cristobal arc, Target N					arc volcano					2002 dredge only
	69	INDIAN OCEAN	Indian Ocean	MID-OCEAN SPREADING	FRR	4	-37.72	77.63	France	active, inferred	Boomerang Seamount	SEIR, 75, near Amsterdam Island	n/a	n/a	n/a	850	mid-ocean ridge	64.4	n/a	n/a	234030	1998 plume and vent site only
	70	Antarctica	Antarctica	ARC-TRENCH SYSTEM	FFT	n/a	-62.10	158.80	high seas	active, inferred	AAR KR1, Maylin	Maily Harbor	n/a	n/a	n/a	2100	mid-ocean ridge	65.1	n/a	n/a	n/a	2011 plume and biological samples
	71	INDIAN OCEAN	Indian Ocean	MID-OCEAN SPREADING	RRR	0	-25.32	70.04	high seas	active, confirmed	Kairei Field	KHF	Kali chimney, F-gen chimney		360	2460	mid-ocean ridge	49.1	MORB, but see Nakamura et al. (2009)	PMS	n/a	2000 ROV Kaiko; 1993 plume only
	82	ALANTIC	Alantic	MID-OCEAN SPREADING	RFR	0	38.03	-28.60	Portugal	active, confirmed	Saldanha	S. Kurchatov	n/a	n/a	n/a	2600	mid-ocean ridge	23.1	n/a	n/a	382010	2010 or earlier SCUBA
							40.47	-29.55	Portugal	active, inferred	South Kurchatov		n/a	n/a	n/a	2600	mid-ocean ridge		n/a	n/a	n/a	1992 plume only; 1995 plume only
	83	Southwest Pacific	Southwest Pacific	BACK-ARC BASIN	RRF	4	-24.55	-179.92	Tonga	active, inferred	Tonga Arc, Volcano 19	TA25	n/a	n/a	n/a	260	arc volcano	0	basalt to basaltic andesite	n/a	n/a	2011 ROV MACKNIFE 2009 plume and dredge only
							-24.80	-177.02	Tonga		Tonga Arc, Volcano 19	TA26			265	970	arc volcano					2006 with submersibles PISCES V and PISCES V and ROV KOJ; 2004 TV grab; 2004 plume and dredge only
							-25.58	-178.71	Tonga		Tonga Arc, Volcano 14	Twin caldera, Volcano B	n/a	n/a	n/a	985	arc volcano					2003 plume and dredge only
							-23.46	-178.78	Tonga		Tonga Arc, Volcano 15	n/a				1400	arc volcano					2003 plume only
							-21.12	-178.81	Tonga		Tonga Arc, Volcano 18	n/a					arc volcano					2003 plume and dredge only
							-16.95	173.92	Fiji	active, confirmed	Sonne 99	SONNE 30, Sonne99, SO-99, SONN, SO 99, Station 4, Triple Junction	Corner Mound, Yogi Mound	Low	n/a	1580	back-arc spreading center	55.5	MORB, E-MORB, minor BABB	PMS	n/a	1995 deep low votex and TV grab
	86	North Fiji Basin	North Fiji Basin	BACK-ARC BASIN	FRR	0	-16.98		Fiji		White Lady	17 S active site, Station 4, Triple Junction	Kelvin, LH26, Mowat Hill 1-MH1, STARMER II, White Lady	n/a	n/a	291	2500	back-arc spreading center				n/a	1988 towed camera and plume; 1988 submersible Nautile
							-16.32	173.55	Fiji		Station 5B, N160 Axis	n/a	n/a	n/a	n/a	3900	back-arc spreading center	36.2	n/a	n/a	n/a	1995 plume only; 1991 temperature anomalies but submersible Shinkai 6500 did not confirm activity
							-16.97	173.93	Fiji		Station 4, Triple Junction	n/a	n/a	n/a	n/a	2000	back-arc spreading center	55.5	MORB, E-MORB, minor BABB	PMS	n/a	1999 submersible Nautile and not find activity; 1991 submersible Shinkai 6500 did not find activity
	87	FIJI	Fiji	BACK-ARC BASIN	FFF	n/a	-16.17	177.42	Fiji	active, inferred	Extensional Relay Zone A	ERZA, North Fiji Basin, 16.17S, North Fiji spreading center	Central Hill, Seahorse	n/a	n/a	2335	back-arc spreading center	68.8	n/a	VSD	n/a	1999 towed camera did not confirm activity
							-17.00	176.00	Fiji		West Fiji Ridge	n/a	n/a	n/a	n/a	3000	back-arc spreading center	50.9		n/a		1995 deep tow
	88	PACIFIC	Pacific	MID-OCEAN SPREADING	FFR	0	-1.02	-102.28	high seas	active, confirmed	Axial Field	1410, EPR	n/a	Low	n/a	2500	mid-ocean ridge	114.2	MORB	n/a	n/a	2000 towed imaging ARGO-II
							-1.02	-102.28	high seas		Pinnacles Seamount	PSMNT				2500	mid-ocean ridge	114.2				2000 deep tow camera and TV grab
							2.25	-101.50	high seas	inactive	Hess Deep	101 W, Galapagos RR	n/a	n/a	n/a	5100	mid-ocean ridge	39.5	n/a	NFS, Fe & Mn crusts	n/a	n/a
	89	PACIFIC	Pacific	MID-OCEAN SPREADING	FRR	2	18.25	-108.30	Mexico	active, inferred	EPR, Marcotrio Spreading Segment	n/a	n/a	n/a	n/a	2600	mid-ocean ridge	77.7	n/a	n/a	n/a	1997 plume only
							17.68	-109.36	Mexico		EPR, Hot 17 N segment					2600	mid-ocean ridge	77.4				
							17.67	-105.01	Mexico		EPR, northern 17 N segment					2600	mid-ocean ridge	74.8				
							16.58	-105.30	Mexico		EPR, southern 17 N segment					2700	mid-ocean ridge	77.4			334020	
	90	PACIFIC	Pacific	MID-OCEAN SPREADING	RRF	1	-1.02	-102.28	high seas	active, confirmed	Axial Field	1410, EPR	n/a	Low	n/a	2500	mid-ocean ridge	114.2	MORB	n/a	n/a	2000 towed imaging ARGO-II
							-1.02	-102.28	high seas		Pinnacles Seamount	PSMNT				2500	mid-ocean ridge	114.2				2000 deep tow camera and TV grab
							2.25	-101.50	high seas	inactive	Hess Deep	101 W, Galapagos RR	n/a	n/a	n/a	5100	mid-ocean ridge	39.5	n/a	NFS, Fe & Mn crusts	n/a	n/a
	91	PACIFIC	Pacific	MID-OCEAN SPREADING	RRR	0	-1.02	-101.49	high seas	active, confirmed	Axial Field	1410, EPR	n/a	Low	n/a	2500	mid-ocean ridge	114.2	MORB	n/a	n/a	2000 towed imaging ARGO-II
							2.25	-101.50	high seas		Hess Deep	101 W, Galapagos RR	n/a	n/a	n/a	5100	mid-ocean ridge	39.5	n/a	NFS, Fe & Mn crusts	n/a	2000 deep tow camera and TV grab
O	92	PACIFIC	Pacific	MID-OCEAN SPREADING	RRR	0	-20.10	-113.71	high seas	active, confirmed	EPR, 20 S/S	20 S, EPR	n/a	Low	n/a	3000	mid-ocean ridge	148.1	MORB	PMS	n/a	1981 Argus camera tow; 1984 submersible Alvin
							-21.43	-114.25	high seas		EPR, 21 21'S	21 S, EPR, 21.5 S, EPR, 21.35'S, EPR	Bordeaux, Grande chemines, Jasmine, Les trois diffuseurs, NahsaKuBone	n/a	n/a	354	2650	mid-ocean ridge	148.7			1994 submersible Cyana; 1983 deposits only
							-20.83	-114.17	high seas		EPR, Ridge J, 20.4'S	20 S/S, EPR	n/a	n/a	n/a	3000	mid-ocean ridge	148.5	n/a	n/a	n/a	1983 Deep Tow camera
							-21.43	-113.68	high seas		EPR, Ridge K, 20.4'S	n/a	n/a	n/a	n/a	2600	mid-ocean ridge	148.1				
							-21.56	-114.30	high seas		Rapa Nui	21 S/S, EPR	Brandon, Feathers, Kraenzo, Gronot	n/a	n/a	405	2640	mid-ocean ridge	148.7	MORB		1999 submersible Alvin; 1987-1988 deposits only
							-20.03	-113.66	high seas	active, inferred	EPR, 20 S	n/a	n/a	n/a	n/a	3000	mid-ocean ridge	148.1	n/a	n/a	n/a	1999 submersible Alvin did not confirm activity
							-21.37	-114.26	high seas		EPR, 21 20'S	n/a	n/a	n/a	n/a	2900	mid-ocean ridge	148.7				1991 plume only; 1987-1988 deposits only
							-21.63	-114.30	high seas		EPR, 21 40'S	n/a	n/a	n/a	n/a	2730	mid-ocean ridge	149				1987-1988 deposits only
							-21.90	-114.50	high seas		EPR, 21 54'S	n/a	n/a	n/a	n/a	2800	mid-ocean ridge	149	MORB			1987-1988 dredges only; 1985 Jean Francois Fouquet et al. (1993) hot sediment
							-22.50	-114.37	high seas		EPR, 22 30'S	n/a	n/a	n/a	n/a	2600	mid-ocean ridge	123.3		PMS		1995/96 or 1998 TV grab (need to check references to confirm activity)
	93	PACIFIC	Pacific	MID-OCEAN SPREADING	RRR	2	-26.21	-112.61	Chile	active, confirmed	EPR, 26 10'S	26 S, EPR, 26-10 South	n/a	n/a	n/a	2600	mid-ocean ridge	150.5	PMS, polymetallic sulfides		n/a	1997 or earlier (need to check Macling & Gundlach (1987)); 1998 submersible Alvin did not observe active vents
							-26.46	-113.63	Chile		EPR, 26.5 S	Easter Microplate, 26 S East Rift	n/a	n/a	n/a	2084	mid-ocean ridge	106.2	n/a	LTH, Fe oxide, silica Mn oxide deposits	n/a	1993 submersible Nautile (or earlier)
							-27.32	-112.32	Chile	active, inferred	EPR, 27 S, Segment W3	n/a	n/a	n/a	n/a	2126	mid-ocean ridge	150.8	n/a	n/a	n/a	1998 plume only
							-27.67	-112.01	Chile		EPR, 27.8 S, Segment W3					2130	mid-ocean ridge					
							-27.83	-112.06	Chile		EPR, 28 S, Segment W3					2120	mid-ocean ridge	

Supplementary Table 5 Volcanism associated with hydrothermal systems and global triple junctions.

TJ ID	Volcano #	Volcano Name	Volcano Type	Elevation (m)	Last Eruption	Major Rock Type
13	264050	Sangeang/Sangean Api / Bima	Complex	1912	2022	Trachybasalt / Tephrite Basanite
		Doro Api / Kalubu Crater	Cone of Sangeang Api	n/a	n/a	n/a
		Doro Mantai/Mantol				
2	262000	Krakatau / Cracatao / Krakatao	Caldera	155	2022	Andesite / Basaltic Andesite
		Anak Krakatau	Cone of Krakatau	n/a	n/a	n/a
		Perbuwatan / Perboewatan	Former cone of Krakatau			
		Rakata	Stratovolcano of Krakatau			
36	334020	Northern EPR at 17°N	Submarine	-2700	-50	Basalt / Picro-Basalt
39	331010	Endeavour Segment / Ridge	Submarine	-2050	-3490	Basalt / Picro-Basalt
		High Rise	Thermal of Endeavour Segment	n/a	n/a	n/a
		Main Endeavour				
		Mothra				
		Salty Dawg				
		Sasquatch				
	331005	West Valley Segment	Submarine	-2550		
40	331031	North Gorda Ridge Segment	Submarine	-3000	1996	Basalt / Picro-Basalt
27	254020	Ambitle / Anir	Stratovolcano	-350	450	Phono-tephrite / Tephri-phonolite
		Babase / Feni	Stratovolcano of Ambitle	n/a	n/a	n/a
		Kapkai	Thermal of Ambitle			
		Nanum River				
		Saddle				
		Waramung Plantation				
29	284220	Forcast Seamount	Submarine	-1456	n/a	n/a
	284230	Seamount X		-1230		Basalt / Picro-Basalt
44	243120	Tafu-Maka / NE Lau Speading Center	Submarine	-1400	2008	Basalt / Picro-Basalt
		Maka	Submarine crater of Tafu-Maka	n/a	n/a	n/a
		Tafu				
	243140	Niuatahi / Volcano O	Caldera	-1270		
		Motutahi	Cone of Niuatahi	n/a		
	243130	West Mata	Submarine	-1174	2009	Andesite / Basltic
		Hades	Vent of West Mata	n/a	n/a	n/a
		Prometheus				
52	360110	Plat Pays, Morne	Stratovolcano	940	1270	Dacite
		Acouma, Morne	Dome of Plat Pays, Morne	n/a	n/a	n/a
		Bois d'Inde				
		Cabrits, Morne				
		Canot, Morne				
		Champagne	Thermal of Plat Pays, Morne			
		Crabier, Morne	Dome of Plat Pays, Morne			
		Eloi, Morne				
		Falaise, La				
		Fous, Morne				
		Galion	Thermal of Plat Pays, Morne			
		Hagley	Dome of Plat Pays, Morne			
		Mountain Top				
		Patates, Morne / Potato Moutain				
		Pichelin				
		Powell				
		Rouge, Morne	Cone of Plat Pays, Morne			
			Dome of Plat Pays, Morne			
		Scotts Head				
		Socrière, La				
		Sulfur Springs / Terre Elm	Hot Spring of Plat Pays, Morne			
		Vert, Morne	Dome of Plat Pays, Morne			
		Vue/ Vigie, Morne la				
	360050	Soufriere Hills / Chance's Mountain	Stratovolcano	912	2013	Andesite / Basltic
		Castle Peak	Dome of Soufriere Hills	n/a	n/a	n/a
		Chance's Peak				
		Cow Hill Soufriere / Tar River Soufriere	n/a			
		English's Crater	Crater of Soufriere Hills			
		Gages Lower Soufriere	Fumarole of Soufriere Hills			
		Gage's Mountain	Dome of Soufriere Hills			
		Gages Upper Soufriere	Fumarole of Soufriere Hills			
		Galway's Mountain	Dome of Soufriere Hills			
		Galway's Soufriere	Fumarole of Soufriere Hills			
		Garibaldi / Caribald Hill	Stratovolcano of Soufriere Hills			
		Mulcares Soufriere	Fumarole of Soufriere Hills			
		Perche's Mountain / Roche's Mountain	Dome of Soufriere Hills			
		Rasberry Hills				
		Roche's Bluff				
		Saint/St. George's Hill	n/a			
		South Soufriere Hills	Stratovolcano of Soufriere Hills			
		Spring Ghaut Soufriere	Fumarole of Soufriere Hills			
69	234000	Boomerang Seamount	Submarine	-650	1995	Basalt / Picro-Basalt
82	382010	Fayal / Faial	Stratovolcano	1041	1958	Andesite / Basltic Andesite
		Caldeira	Caldera of Fayal	n/a	n/a	n/a
		Canto, Cabeco do	Cone of Fayal			
		Capelinhos				
		Carneiro, Monte				
		Castelo Branco	Dome of Fayal			
		Dos Trinta, Cabeco	Cone of Fayal			
		Fogo, Cabeco do				
		Funda da Caldeira				
		Guia, Monte de	Tuff cone of Fayal			
		Pacheco, Cabecos do	Cone of Fayal			
		Varadouro	Thermal of Fayal			
		Verde, Cabeco	Cone of Fayal			
83	243001	n/a	Submarine	-385	n/a	Basalt / Picro-Basalt
89	334020	Northern EPR at 17°N	Submarine	-2700	-50	Basalt / Picro-Basalt
95	331010	Endeavour Segment/Ridge	Submarine	-2550	-3490	Basalt / Picro-Basalt
		High Rise	Thermal of Endeavour Segment	n/a	n/a	n/a
		Main Endeavour				
		Mothra				
		Salty Dawg				
		Sasquatch				
	331005	West Valley Segment	Submarine	-2550		
96	331031	North Gorda Ridge Segment	Submarine	-3000	1996	Basalt / Picro-Basalt
98	243030	n/a	Submarine	-296	2017	n/a
104	243111	Dugong	Submarine	-1170	n/a	n/a
	243112	Lobster		n/a		

Note: Volcano Number(s): Some vent fields are sub-features of volcanic features identified with a permanent unique identifier in the Smithsonian Institution's Global Volcanism Program, Volcanoes of the World (2013). Triple Junction (TJ) ID, corresponding identification with this study see Appendix D. Elevation: meters (m) indicates the highest point of the volcanic edifice, positive values are above sea levels, negative are below sea level. Data provided by Smithsonian Institution's Global Volcanism Program, Volcanoes of the World (2013)

Appendix D Global Triple Junction Database of 117 Triple Junctions

ID	Crust Type	Latitude	Longitude	Geolocation	Geodynamic Setting	Known Triple Junction?	TJ Type	General TJ type	Limb 1 Boundary Type	Limb 2 Boundary Type	Limb 3 Boundary Type	Plate A	Plate B	Plate C	Limb 1 Angle	Limb 2 Angle	Limb 3 Angle	Certainty	Initiation Age (Ma)	1 km Shiptrack Spreading (yes)	Spreading (mm/yr)	Global Gravity	CrustalD	Hydrothermal Vents	Number of Vent Fields	Associated Volcano(s)	100 km Hotspot	500 km Hotspot	1000 km Hotspot	Hotspot Name	Heat Source	Hotspot References	100 km LIPs	Name Of LIPs	LIPs References	Known Sedimentary Basin	Seabed Lithology	Geomorphology Features	References
6	C	5.46	37.21	Ethiopia	CONTINENTAL RIFT	n/a	XXX	XXX	CR	CR	CR	Somalia	Victoria	Africa	31	207	266	3	n/a	n	n/a	690	n/a	n	n	n	Afar & Lake Victoria	n/a	n	y	y	Ethiopian Flood Basalts, Africa	Earthbyte dataset	North – Central Gregory Rift Eyes - Weber - South Gregory Rift	n/a	n/a	n/a	Stamps et al. (2008)
7	C	-1.66	36.25	Africa	CONTINENTAL RIFT	n/a	XXX	XXX	CR	CF	CR	Somalia	Victoria	Rovuma	10	152	198	3	n/a	n	n/a	435	n/a	n	n	n	Lake Victoria	n/a	n	n	n		Morelli et al., 2006	n	n/a	n/a	n/a	n/a	Purcell (2018)
8	C	28.11	96.28	NE India	CONTINENTAL RIFT	n/a	XXX	XXX	CTB	CTB	CTB	Burma	India	Eurasia	95	227	274	0	n/a	n	n/a	402	n/a	n	n	n	n/a	n/a	n	n	n		n/a	n	n/a	n/a	n/a	n/a	Tsutsumi and Sato (2009)
11	C	28.02	97.31	NE India	CONTINENTAL COLLISION ZONE	n/a	XXX	FFF	CTB	CTB	CTB	Burma	Sunda	Eurasia	103	135	275	0	n/a	n	n/a	3088	n/a	n	n	n	n/a	n/a	n	n	n		n/a	n	n/a	n/a	n/a	n/a	n/a
12	C	-7.89	-120.59	Flores Sea	REAR ARC	n/a	FFF	FFT	CMAF	CMAF/sz	CMAF/sz	Banda Sea	Timor	Sunda	3	96	280	3	n/a	n	n/a	410	n/a	n	y	1	264/50	n/a	n	n	n		n/a	n	n/a	n/a	n/a	Clay	Gunteni (1999)
13	C	42.77	129.98	Yamato Rise	CONTINENTAL BACK-ARC	n/a	FFF	FFT	CMBA	CMBA	CTB	Yangtze	Eurasia	Amur	108	233	324	0	n/a	n	n/a	-32	n/a	n	n	n	Emeishan Dykes, Western South China Block	n/a	n	n	n		n/a	n	n/a	n/a	n/a	Sand	Escarpment, Basin
14	C	42.77	129.98	Yamato Rise	CONTINENTAL BACK-ARC	n/a	FFF	FFT	CMBA	CTB	CTB	Yangtze	Eurasia	Amur	108	233	324	0	n/a	n	n/a	-32	n/a	n	n	n		n/a	n	n	n		Earthbyte dataset	n	n/a	n/a	n/a	Japan	Sand	Escarpment, Basin, Canyon	Schellart and Lister (2005), Xu et al. (2014)
16	C	23.30	102.64	SE China	CONTINENTAL STRIKE-SLIP	n/a	FXX	FXX	CF	CTB	CTB	Sunda	Eurasia	Yangtze	110	286	342	2	n/a	n	n/a	-1417	n/a	n	n	n	Hainan	Mid-mantle	Montelli et al., 2006	n	n	n		n/a	n	n/a	n/a	n/a	n/a	Xu et al. (2014)
17	C	41.06	138.67	Northern Japan	ARC-TRANSFORM	n/a	FFF	FFT	CMBA	CMBA	CMBA	Yangtze	Amur	Honshu	134	249	340	3	n/a	n	n/a	-123	n/a	n	n	n	n/a	n/a	n	n	n		n/a	n	n/a	n/a	n/a	Japan	n/a	Basin, Abyssal Hill,
25	C	-6.09	146.02	Papua New Guinea	ARC	n/a	FFF	FFF	CMAF	CMAFI	CMAF	Woodlark	Bird's Head	South Bismarck	119	194	305	3	n/a	n	n/a	-1020	n/a	n	n	n	n/a	n/a	n	n	n		n/a	n	n/a	n/a	n/a	n/a	Baldwin et al. (2012), Schellart and Spakman (2015)
27	C	6.90	-77.33	Colombia	CONTINENTAL COLLISION ZONE	n/a	XXX	XXX	CTB	CTB	CTB	Caribbean	Nazca	South America	64	230	312	0	n/a	n	n/a	2727	n/a	n	n	n	n/a	n/a	n	n	n		n/a	n	n/a	n/a	n/a	n/a	Baldwin et al. (2012), Schellart and Spakman (2015)
28	C	6.90	-77.33	Colombia	CONTINENTAL COLLISION ZONE	n/a	XXX	XXX	CTB	CTB	CTB	Caribbean	Cordillera Occidental	North Andean Sliver	64	230	312	0	n/a	n	n/a	2727	n/a	n	n	n	Volcanics, Eastern Panama, Nw South America (Bowland & Rosencrantz)	Earthbyte dataset, Oceanic from Ernst (2014)	n	n	n		n/a	n	n/a	n/a	n/a	n/a	Kellogg and Vega (1995), Dhont et al. (2005), Egbue and Kellogg (2010)
48	C	35.71	138.50	Japan	ARC-TRENCH SYSTEM	n/a	FFX	XFF	CMAFI	CMAFss	CMBA	Okinawa	Yangtze	Honshu	162	234	306	3	n/a	n	n/a	-743	n/a	n	n	n	n/a	n/a	n	n	n		n/a	n	n/a	n/a	n/a	n/a	Mahony et al. (2011), Xu et al. (2014)
56	C	56.06	138.09	Russia	CONTINENTAL COLLISION ZONE	n/a	XXX	XXX	CTB	CTB	CTB	Okhotsk	Eurasia	North America	71	248	312	0	n/a	n	n/a	188	n/a	n	n	n	n/a	n/a	n	n	n		n/a	n	n/a	n/a	n/a	n/a	Schellart and Spakman (2005), Pronopev et al. 2013
57	C	40.06	24.92	Mediterranean Sea	CONTINENTAL	n/a	FXF	XFF	CFss	CFss	CFss	Anatolia	Aegean Sea	Eurasia	65	139	289	3	n/a	n	n/a	-277	n/a	n	n	n	n/a	n/a	n	n	n		n/a	n	n/a	n/a	n/a	n/a	Fichtner et al. (2010)
58	C	38.89	40.59	Turkey	CONTINENTAL COLLISION ZONE	n/a	XXX	XXX	CTB	CTB	CTB	Eurasia	Anatolia	Arabia	40	98	222	0	n/a	n	n/a	-949	n/a	n	n	n	n/a	n/a	n	n	n		n/a	n	n/a	n/a	n/a	n/a	Schellart and Spakman (2005), Faccenna et al. (2017)
59	C	38.89	40.59	Turkey	CONTINENTAL COLLISION ZONE	n/a	XXX	XXX	CTB	CTB	CTB	Eurasia	Anatolia	Arabia	40	98	222	0	n/a	n	n/a	-949	n/a	n	n	n	n/a	n/a	n	n	n		n/a	n	n/a	n/a	n/a	n/a	Hergar and Ustaszewski (2010), Faccenna et al. 2013
65	C	38.84	20.61	Aegean	CONTINENTAL	n/a	FFX	XFF	CFss	CF\	CTB	Aegean Sea	Adriatic	Eurasia	123	210	324	3	n/a	n	n/a	-101	n/a	n	n	n	n/a	n/a	n	n	n		n/a	n	n/a	n/a	n/a	n/a	Taymaz et al. (2007), Fichtner et al. 2013
66	C	36.38	36.33	Aegean	CONTINENTAL	n/a	XFF	XXX	CFss	CFss	CTB	Africa	Arabia	Anatolia	25	177	227	0	n/a	n	n/a	-532	n/a	n	n	n	n/a	n/a	n	n	n		n/a	n	n/a	n/a	n/a	n/a	Fichtner et al. (2010)
74	C	18.29	39.91	Red Sea	BASIN	n/a	RFR	FRR	CRSCI	CFs	CRSCI	Danakil	Africa	Arabia	156	198	334	3	0	n	n/a	-334	n/a	y	1	n/a	n/a	n/a	n	n	n		n/a	n	n/a	n/a	n/a	Red Sea	Calcareous Ooze	Basin, Rift Valley, Abyssal Hills	Xue et al. (2006)
75	C	18.29	39.91	Red Sea	CONTINENTAL RIFT	n/a	RFR	FRR	CR	CR	CR	Danakil	Africa	Arabia	156	198	334	3	0	n	n/a	-334	n/a	y	1	n/a	n/a	n/a	n	n	n		n/a	n	n/a	n/a	n/a	n/a	Ethiopian Flood Basalts, Africa	Earthbyte dataset	n	n/a	n/a	n/a	n/a	Kier et al. (2006), Stamps et al. (2008), Pagli et al. (2014)
108	C	-8.94	33.62	Africa	CONTINENTAL RIFT	n/a	XXX	XXX	CR	CR	CR	Somalia	Victoria	Rovuma	40	178	218	0	n/a	n	n/a	516	n/a	n	n	n	Lake Victoria	n/a	n	n	n		Morelli et al., 2006	n	n/a	n/a	n/a	n/a	n/a	Roberts et al. (2012), Stamps et al. (2008)
111	C	47.37	141.85	Japan	CONTINENTAL MARGIN	n/a	XFX	FXX	CMBA	CMAFI	CMBA	Okhotsk	Honshu	Amur	70	185	245	3	n/a	n	n/a	-193	n/a	n	n	n	n/a	n/a	n	n	n		n/a	n	n/a	n/a	n/a	n/a	Vasilenko and Prytkov (2012), Xu et al. (2014)
112	C	24.41	121.35	Asia	CONTINENTAL MARGIN	n/a	FFF	FFT	CMAF	CMAFss	CMAFss	Philippine Sea	Okinawa	Yangtze	31	189	212	0	n/a	n	n/a	-714	n/a	n	n	n	n/a	n/a	n	n	n		n/a	n	n/a	n/a	n/a	n/a	Lebron et al. (2000)
113	C	-42.73	171.45	New Zealand	CONTINENTAL	n/a	FFF	FFF	CF	CF	CF	Kermadec	Pacific	Australia	60	101	244	0	n/a	n	n/a	-119	n/a	n	n	n	n/a	n/a	n	n	n		n/a	n	n/a	n/a	n/a	n/a	n/a	n/a	Lebron et al. (2000)
4	O	-6.81	66.27	Carlsberg Ridge, Central Indian Ridge	MID-OCEAN SPREADING	n/a	XXX	XXX	OSCI	OSCI	OSBU	India	Capricorn	Somalia	37	68	226	3	1	n/a	n/a	-957	n/a	n	n	n	n/a	n/a	n	n	n		n/a	n	n/a	n/a	n/a	Calcareous Ooze	Escarpment, Rift Valley, Spreading Ridge, Abyssal Mountains, Chagos Archipelago Mpa	n/a	Bird (2003)
5	C	-3.54	154.22	Bismarck Sea	ARC-LIP COLLISION	n/a	FFF	FFT	OLB	GAFI	OOSZ	Solomon	North Bismarck	Australia	158	223	330	3	n/a	n	254/20	-909	n/a	n	n	n	Ontong Plateau	Earthbyte dataset	n	n	n		n/a	n	n/a	n/a	n/a	Clay	Silicious Mud, Fine-Grained Calcareous Sediment	Basin, Trough, Abyssal Mountains, Abyss	Baldwin et al. (2012)
29	O	12.00	144.29	Mariana	ARC-TRENCH SYSTEM	n/a	TTF	FTT	OOSZ	OOSZ	OOSZ	Pacific	Philippine Sea	Mariana	63	248	299	1	n/a	n	284/20, 284/30	-900	n/a	y	7	284/20, 284/30	n/a	n	n	n		n/a	n	n/a	n/a	n/a	n/a	n/a	n/a	Kobayashi (2004), Ishizuka et al (2018)
30	O	24.62	143.39	Mariana Trench	ARC-TRENCH SYSTEM	n/a	TFT	FTT	OOSZ	OOSZ	OOSZ	Pacific	Philippine Sea	Mariana	141	225	340	1	n/a	n	n/a	-996	n/a	n	n	n	4000 Meters Mid-Pacific Seamounts, North Pacific	Earthbyte dataset, Oceanic from Ernst (2014)	n	n	n		n/a	n	n/a	n/a	n/a	n/a	n/a	n/a	Bird (2003), Schellart et al. (2006)
44	O	-14.48	-173.87	Lau Southwest Pacific	ARC-TRENCH SYSTEM	n/a	TRT	RTT	OOSZ	OBASCI	OOSZ	Tonga	Niuatoi'Ou	Pacific	111	198	287	1	n/a	n	n/a	-736	BMRG098MV	n	y	23	243/120, 243/140, 143/130	n/a	n	n	n		n/a	n	n/a	n/a	n/a	n/a	n/a	n/a	Contreras-Reyes et al. (2011)
45	O	-14.48	-173.87	Lau Southwest Pacific	ARC-TRENCH SYSTEM	n/a	TRT	RTT	OOSZ	OAFI	OOSZ	Tonga	Pacific	Australia	111	198	287	1	n/a	n	n/a	-736	n/a	n	y	3	Samoa	Deep Mantle	Montelli et al., 2006	n	n	n		n/a	n	n/a	n/a	n/a	n/a	n/a	n/a	Escarpment, Basin, Trench, Abyssal Mountains	Schellart and Spakman (2015), Anderson et al. (2016)
46	O	-14.61	166.28	Southwest Pacific-Lau Basin	ARC-TRENCH SYSTEM	n/a	TTF	FTT	OOSZ	OAFI	OOSZ	Vitiaz	New Hebrides	Australia	54	77	185	1	n/a	n	n/a	-847	n/a	n	n	n	n/a	n/a	n	n	n		n/a	n	n/a	n/a	n/a	n/a	n/a	n/a	Escarpment, Basin, Trench, Abyssal Mountains	Schellart and Spakman (2015), Anderson et al. (2016)
47	O	-11.29	162.81	Southwest Pacific	ARC-TRENCH SYSTEM	n/a	TTF	FTT	OOSZ	OAFI	OOSZ	Australia	Solomon	Vitiaz	71	251	345	1	n/a	n	n/a	-1070	n/a	n	y	3	n/a	n/a	n	n	n		n/a	n	n/a	n/a	n/a	n/a	n/a	n/a	Escarpment, Basin, Trench, Hadal	Schellart and Spakman (2015), Anderson et al. (2016)
50	O	-22.95	173.31	Hunter Ridge	ARC-TRENCH SYSTEM	n/a	TTF	FTT	OOSZ	OAFI	OOSZ	New Hebrides	Conway Reef	Australia	75	256	334	3	n/a	n	n/a	-441	n/a	n	n	n	n/a	n/a	n	n	n		n/a	n	n/a	n/a	n/a	n/a	n/a	n/a	Escarpment, Basin, Trench, Abyssal Mountains	Schellart and Spakman (2015), Anderson et al. (2016)
51	O	15.37	-46.64	Mid-Atlantic Ridge	MID-OCEAN SPREADING	n/a	RRF	FRR	OOSZ	OOSZ	OFI	Africa	South America	North America	4	96	277	2	1	y	n/a	-1084	EW97/5A, KN161/04, KN182-03,	n	y	n/a	Alarido ridge	n/a	n	n	n		Morelli et al., 2006	n	n/a	n/a	n/a	Calcareous Ooze	Escarpment, Basin, Rift Valley, Spreading Ridge, Abyssal Mountains	Pichot et al. (2012)
52	O	15.37	-46.64	Mid-Atlantic Ridge	MID-OCEAN SPREADING	n/a	RRF	FRR	OOSZ	OOSZ	OFI	Africa	South America	North America	4	96	277	2	1	y	n/a	-1084	EW97/5A, KN161/04, KN182-03,	n	y	n/a	n/a	n/a	n	n	n		Morelli et al., 2006	n	n/a	n/a	n/a	n/a	Lewis and Lundrigan	n/a	Pichot et al. (2012), Stamps et al. (2010)
53	O	-60.59	-26.03	Atlantic	ARC-TRENCH SYSTEM	n/a	TRF	TFR	OOSZ	OBASCI	OOSZ	South America	Antarctica	Sandwich	71	134	294	2	n/a	n	n/a	-1002	n/a	n	n	n	n/a	n/a	n	n	n		n/a	n	n/a	n/a	n/a	Silt	Basin, Rift Valley, Spreading Ridge, Trench, Hadal	Bruguier and Lowrie (2007), Civile et al. (2012)
54	O	-54.93	-29.00	Atlantic	ARC-TRENCH SYSTEM	n/a	TRF	TFR	OOSZ	OBASCI	OBAFss	Sandwich	Scotia	South America	91	240	268	2	62	n	n/a	-729	n/a	n	n	n	n/a	n/a	n	n	n		n/a	n	n/a	n/a	n/a	Sand	Basin, Trench, Hadal	Civile et al. 2012, Eagles et al 2005
58	O	-5.69	-175.30	Southwest Pacific	ARC-TRENCH SYSTEM	n/a	TTT	FTT	OOSZ	OOSZ	OAFI	Pacific	Kermadec	Tonga	19	191	302	1	n/a	n	n/a	-266	COOK1/MBV, MRT06/06Y	n	y	4	4000 Meters Louisville Ridge, North Pacific, Osborn Seamount	Earthbyte dataset, Koppers et al. (2004)	n	n	n		n/a	n	n/a	n/a	n/a	n/a	n/a	n/a	Escarpment, Basin, Trench, Hadal	
59	O	-7.55	155.29	Solomon Sea	ARC-TRENCH SYSTEM	n/a	TTT	FTT	OOSZ	OFss	OOSZ	Woodlark	Solomon Sea	Solomon	110	225	297	0	n/a	n	n/a	-302	MGL0906	n	y	2	n/a	n/a	n	n	n		n/a	n	n/a	n/a	n/a	n/a	n/a	n/a	Escarpment	Baldwin et al 2012, Schellart and Spakman (2015)
60	O	-7.55	155.29	Solomon Sea	ARC-TRENCH SYSTEM	n/a	TTT	FTT	OOSZ	OAFI	OOSZ	Woodlark	Solomon Sea	Australia	110	225	297	0	n/a	n	n/a	-302	MGL0906	n	y	2	n/a	n/a	n	n	n		n/a	n	n/a	n/a	n/a	Silicious Mud	n/a	Basin, Trench, Abyssal Hills	Baldwin et al 2012, Schellart and Spakman (2015)
61	O	-9.85	159.34	Solomon Islands	ARC-TRENCH SYSTEM	n/a	TTT	FTT	OOSZ	OAF	OOSZ	Woodlark	Solomon	Pacific	112	246	318	1	n/a	n	n/a	-356	Louisade Plateau, North Of Coral Sea	n	y	1	Louisade Plateau, North Of Coral Sea	n/a	n	n	n		Coffin, 2011 (PLATES project)	n/a	n/a	n/a	n/a	Mixed Calcareous, Silicious Ooze	Basin, Trench, Abyssal Hills	Schellart and Spakman (2015)
62	O	-9.77	162.34	Solomon Islands	ARC-TRENCH SYSTEM	n/a	XFX	FXX	OLB	OAFI	OLB	Vitiaz	Solomon	Pacific	3	162	342	2	n/a	n	n/a	-875	n/a	n	y	3	Caroline	n/a	n	n	n		Morelli et al., 2006	n	n/a	n/a	n/a	Clay	n/a	Basin, Trench	Anderson et al. (2016)
63	O	-36.36	79.10	Indian Ocean	MID-OCEAN SPREADING	n/a	RRR	FRR	OFss	OCSI	OSCI	Australia	Antarctica	Capricorn	51	234	317	0	n/a	n	n/a	-269	n/a	n	n	n	Amsterdam Chrismas	n/a	n	n	n		Anderson and Schramm, 2005	n	2340/20	n/a	n/a	n/a	n/a	n/a	n/a	
70	O	-61.52	160.99	Antarctica	MID-OCEAN SPREADING	n/a	RRF	FRR	OSCI	OSCI	OF	Antarctica	Australia	Pacific	118	253	338	2	0	n	n/a	-280	n/a	y	n	n	Balleny	Secondary/Tertiary	Courtillot et al., 2003	n	n	n		n/a	n	n/a	n/a	n/a	Silicious Mud	n/a	n/a	Rift Valley, Spreading Ridge, Abyssal Mountains	
71	O	-57.96	166.27	Antarctica	MID-OCEAN SPREADING	Rodriguez	RRF	FRR	OSCI	OSCI	OF	Antarctica	Australia	Pacific	118	253	338	2	0	n	n/a	-280	n/a	y	n	n	Rodriguez	n/a	n	n	n		n/a	n	n/a	n/a	n/a	Silicious Mud	Escarpment, Basin, Rift Valley, Spreading Ridge, Abyssal Mountains	
72	O	-55.95	68.27	Indian Ocean	MID-OCEAN SPREADING	Rodriguez	RRF	FRR	OSCI	OSCI	OSCI	Antarctica	Australia	Capricorn	48	183	268	0	n/a	n	n/a	-253	n/a	n	n	n	n/a	n/a	n	n	n		n/a	n	n/a	n/a	n/a	Silicious Mud	Escarpment, Basin, Rift Valley, Abyssal Mountains	Anderson et al. (2016)
73	C	-35.10	-110.81	Pacific	MID-OCEAN SPREADING	n/a	RRR	FRR	OSCI	OSCI	OSCI	Antarctica	Pacific	Juan Fernandez	82	187	268	0	n/a	n	n/a	-25	RAPA03WT	n	y	1	Easter	Deep Mantle	Montelli et al., 2006	n	n	n		n/a	n	n/a	n/a	n/a	Silicious Mud	n/a	n/a	Rift Valley, Spreading Ridge, Abyssal Mountains	Larsen et al (1992)
74	C	-34.55	-109.35	Pacific	MID-OCEAN SPREADING	n/a	RRR	FRR	OSCI	OSCI	OSCI	Antarctica	Nazca	Juan Fernandez	132	282	356	0	n/a	n	n/a	-264	PASC02WT	n	y	1	Easter	Deep Mantle	Montelli et al., 2006	n	n	n		n/a	n	n/a	n/a	n/a	Silicious Mud	n/a	n/a	Rift Valley, Spreading Ridge, Abyssal Mountains	Larsen et al (1992)
78	O	-40.93	42.91	Indian Ocean	MID-OCEAN SPREADING	n/a	FRR	FRR	OFI	OSCI	OSCI	Somalia	Antarctica	Lwandle	6	99	214	0	1	n	44	-440	n/a	n	n	n	Marion	Secondary/Tertiary	Courtillot et al., 2003	n	n	n		n/a	n	n/a	n/a	n/a	Fine-Grained Calcareous Sediment	Escarpment, Basin, Spreading Ridge, Abyssal Mountains	n/a
79	O	-47.06	32.24	Indian Ocean	MID-OCEAN SPREADING	n/a	RRR	FRR	OFss	OSCI	OSCI	Antarctica	Africa	Lwandle	25	100	221	0	4	n	34	-669	KN145-16	n	y	1	Marion	Secondary/Tertiary	Courtillot et al., 2003	n	n	n		n/a	n	n/a	n/a	n/a	Silicious Mud	n/a	n/a	Escarpment, Basin, Spreading Ridge, Abyssal Mountains	n/a
80	O	-54.69	-0.73	Atlantic	MID-OCEAN SPREADING	Bouvet	RFF	RFF	OFI	OFI	OFI	Antarctica	South America	Africa	80	166	311	0	n/a	n	65	160	n/a	n	n	n	Bouvet Shona	n/a	n	n	n		Morelli et al., 2006	n	n/a	n/a	n/a	n/a	Diatom Ooze	Escarpment, Spreading Ridge, Abyssal Mountains	n/a
81	O	-54.69	-0.73	Atlantic	MID-OCEAN SPREADING	Bouvet	RFF	RFF	OFI	OFI	OFI	Antarctica	South America	Africa	80	166	311	0	n/a	n	65	160	n/a	n	n	n	Bouvet Shona	n/a	n	n	n		Morelli et al., 2006	n	3820/130, 4001	n/a	n/a	n/a	Diatom Ooze	Escarpment, Spreading Ridge, Abyssal Mountains	Mineral Oil (2018)
83	O	-24.00	-177.17	Southwest Pacific	BACK-ARC BASIN	n/a	RRF	FRR	OBASCI	OAFI	OBAFI	Kermadec	Australia	Lau	22	144	191	1	n/a	n	n/a	-247	2A0001	n	y	5	n/a	n/a	n	n	n		n/a	n	n/a	n/a	n/a	n/a	n/a	n/a	Spreading Ridge, Pelleter, Abyssal Hills	Smith and Price (2006)
84	O	-13.53	172.80	North Fiji Basin	BACK-ARC BASIN	n/a	RRR	RRR	OBASCI	OBASCI	OBASCI	Balmoral Reef	New Hebrides	Vitiaz	57	171	265	0	1	n	0	-541	n/a	n	n	n	n/a	n/a	n	n	n		n/a	n	n/a	n/a	n/a	Calcareous Ooze	Abyssal Hills	Pelletier and Auzende (1996)
85	O	-15.52	-179.38	Southwest Pacific	BACK-ARC BASIN	n/a	RRF	FRR	OBAF	OBASCI	OAFI	Vitiaz	Australia	Balmoral Reef	20	245	298	0	n/a	n	n/a	-1	RR02/14	n	y	4	n/a	n/a	n	n	n		n/a	n	n/a	n/a	n/a	Silicious Mud	n/a	n/a	Spreading Ridge, Abyssal Mountains	Pelletier et al (1996)
86	O	-16.86	173.91	North Fiji Basin	BACK-ARC BASIN	NFBTJ	RRR	FRR	OBAF	OBASCI	OBASCI	Balmoral Reef	New Hebrides	Balmoral Reef	54	176	294	1	0	y	n/a	28	TUN06/MV	n	y	4	n/a	n/a	n	n	n		n/a	n	n/a	n/a	n/a	n/a	n/a	n/a	Spreading Ridge, Abyssal Mountains	Pelletier et al (1996)
87	O	-16.86	173.91	Fiji	BACK-ARC BASIN	NFBTJ	RRR	FRR	OF	OSCI	OSCI	Balmoral Reef	New Hebrides	Vitiaz	54	176	294	1	0	y	n/a	28	n/a	n	y	4	n/a	n/a	n	n	n		n/a	n	n/a	n/a	n/a	Silicious Mud	n/a	n/a	Spreading Ridge, Abyssal Mountains	Pelletier et al (1996)
88	O	2.27	-102.58	Pacific	MID-OCEAN SPREADING	Galapagos	RRF	FRR	OF	OSCI	OSCI	Cocos	Galapagos	Pacific	3	94	181	1	0	n	2	-95	CERES3WT, AMLR07, NBK/CGMW, PASC05WT	n	y	2	-95	n/a	n	n	n		n/a	n	n/a	n/a	n/a	Silicious Mud	n/a	n/a	Spreading Ridge, Abyssal Hills	Hammerle (1982)
89	O	18.51	-106.27	Pacific	MID-OCEAN SPREADING	Rivera	FRR	FRR	OFss	OSCI	OSCI	Cocos	Pacific	Rivera	83	180	277	0	2	y	18	117	PANR01/MV, DELV02RR	n	y	4	334/20	n/a	n	n	n		n/a	n	n/a	n/a	n/a	Silicious Mud	n/a	n/a	Spreading Ridge, Abyssal Mountains	DeMets and Traylen (2000)
91	O	2.23	-31.55	Pacific	MID-OCEAN SPREADING	n/a	RRF	FRR	OSCI	OSCI	OSCI	Nazca	Galapagos	Cocos	91	121	274	0	1	n	101	-821	CERES03WT, ENCR01WT	n	y	1	101	-821	n	n	n		n/a	n	n/a	n/a	n/a	Calcareous Ooze	Escarpment, Basin, Rift Valley, Spreading Ridge, Abyssal Mountains	Kilgord and Mammericks (1982), Schouten et al. (2008)
92	O	1.16	-102.17	Pacific	MID-OCEAN SPREADING	n/a	RRR	FRR	OSCI	OSCI	OSCI	Nazca	Pacific	Galapagos	49	188	274	0	0	y	1	148	PASC02WT, PPTJ02WT	n	y	1	PASC02WT, PPTJ02WT	n/a	n	n	n		n/a	n	n/a	n/a	n/a	Silicious Mud	n/a	n/a	Spreading Ridge, Abyssal Hills	Schouten et al. (2008)
93	O	-28.92	-113.51	Pacific	MID-OCEAN SPREADING	n/a	RRR	FRR	OSCI	OSCI	OSCI	Nazca	Pacific	Juan Fernandez	22	164	269	0	0	y	27	29	PASC02WT, PANR05MV, AT11-24	n	y	1	PASC02WT, PANR05MV, AT11-24	n/a	n	n	n		n/a	n	n/a	n/a	n/a	Silicious Mud	n/a	n/a	Spreading Ridge, Abyssal Hills	Larsen et al. (1992)
94	O	-31.52	-111.98	Pacific	MID-OCEAN SPREADING	n/a	RRR	RRR	OSCI	OSCI	OSCI	Nazca	Juan Fernandez	Pacific	8	96	191	0	1	y	31	233	PASC02WT, PANR05MV, AT11-24	n	y	1	Easter	Deep Mantle	Montelli et al., 2006	n	n	n		n/a	n	n/a	n/a	n/a	Silicious Mud	n/a	n/a	Spreading Ridge, Abyssal Hills	Larsen et al. (1992)
95	O	-48.81	-128.67	Pacific	MID-OCEAN SPREADING	n/a	RRR	FRR	OSCI	OSCI	OSCI	Pacific	Juan de Fuca	Explorer	78	207	278	0	1	n	5	93	RR10-51-BU-BD, HLY-01-01,	n	y	3	331013, 331005	n/a	n	n	n		Morelli et al., 2006	n	n/a	n/a	n/a	n/a	n/a	n/a	Escarpment, Basin, Rift Valley, Spreading Ridge, Abyssal Mountains	Chaytor et al (2004)
96	O	43.00	-126.59	Pacific	MID-OCEAN SPREADING	Mendocino	FRR	FRR	OFI	OSCI	OSCI	Juan De Fuca	Pacific	Juan De Fuca	78	211	285	0	0	y	2	-216	RP-10-BU-BD, HLY-01-01, MGL1408MV	n	y	4	331031	n/a	n	n	n		Juan de Fuca Cobb	Mid-mantle	Montelli et al., 2006	n	n/a	n/a	n/a	n/a	n/a	n/a	Escarpment, Basin, Rift Valley, Spreading Ridge, Abyssal Mountains	Bruguier and Lowrie (2007), Civile et al. (2012)
97	O	-60.10	-175.07	Atlantic	ARC-TRENCH SYSTEM	n/a	RRR	FRR	OBASCI	OBASCI	OBASCI	Antarctica	Scotia	Sandwich	13	236	332	0	n/a	n	n/a	-98	n/a	n	n	n	n/a	n/a	n	n	n		n/a	n	n/a	n/a	n/a	n/a	n/a	n/a	Escarpment, Basin, Spreading Ridge, Plateau, Abyssal Hills	Smith and Price (2006)
98	O	-14.63	-176.17	Southwest Pacific	BACK-ARC BASIN	n/a	RRR	FRR	OBASCI	OBASCI	OBASCI	Niuatoi'Ou	Tonga	Australia	91	197	279	0	n/a	n	n/a	96	KM0417, KM0804	n	y	22	240/30	n/a	n	n	n		n/a	n	n/a	n/a	n/a	n/a	n/a	n/a	Escarpment, Basin, Spreading Ridge, Plateau, Abyssal Hills	
99	O	-8.03	156.20	Southwest Pacific	BACK-ARC BASIN	n/a	RRR	FRR	OBAF	OBASCI	OAFI	Woodlark	Solomon Sea	Australia	110	225	297	0	n/a	n	n/a	-302	MGL0906	n	y	2	n/a	n/a	n	n	n		n/a	n	n/a	n/a	n/a	Silicious Mud	n/a	n/a	Escarpment, Basin, Spreading Ridge, Abyssal Hills	Baldwin et al 2012
100	O	-5.00	153.41	Solomon Sea	BACK-ARC BASIN	n/a	RRR	FRR	OBAF	OBASCI	OBAF	South Bismarck	North Bismarck	Solomon Sea	51	168	312	0	n/a	n	n/a	-814	n/a	n	n	n	n/a	n/a	n	n	n		n/a	n	n/a	n/a	n/a	n/a	n/a	n/a	Basin, Abyssal Hills	Pelletier et al. (2001)
103	O	-15.08	-179.22	Southwest Pacific	BACK-ARC BASIN	n/a	RRR	RRR	OBASCI	OBAF	OBASCI	Futuna	Australia	Vitiaz	27	126	200	0	n/a	n	1	-56	KVH10/99, KM0703	n	n	n/a	n/a	n/a	n	n	n		n/a	n	n/a	n/a	n/a	n/a	n/a	n/a	Spreading Ridge, Pelleter, Abyssal Hills	Pelletier et al. (2001)
104	O	-16.20	-177.62	Southwest Pacific	BACK-ARC BASIN	n/a	RRF	FRR	OBASCI	OBAF	OBASCI	Niuatoi'Ou	Australia	Vitiaz	7	151	220	0	n/a	n	n/a	65	WEST08MV, KM0416, KM0409	n	y	2	243/11, 243/112	n/a	n	n	n		n/a	n	n/a	n/a	n/a	n/a	n/a	n/a	Spreading Ridge, Pelleter, Abyssal Hills	Pelletier et al. (2001)
107	O	9.17	138.28	Philippine Sea	ARC-TRENCH SYSTEM	n/a	TFT	FTT	OOSZ	OF	OOSZ	Pacific	Caroline	Philippine Sea	22	113	202	0	n/a	n	n/a	-48	n/a	n	y	3	3000 Meters West Caroline Ridge, Central Pacific	n/a	n	n	n		Coffin, 2011 (PLATES project)	n/a	n/a	n/a	n/a	Calcareous Ooze	Escarpment, Basin, Trench	Kobayashi (2004)	
108	O

Appendix E Oceanic Triple Junction Database: A summary and expansion of 46 oceanic triple junction from Global Triple Junctions Database (Appendix D).

ID	Crust type	Latitude	Longitude	Geolocation	Geodynamic Setting	Known Triple Junction Names	TJ Type	General TJ Type	Limb 1 Boundary Type	Limb 2 Boundary Type	Limb 3 Boundary Type	Plate A	Plate B	Plate C
114	O	19.04	-62.36	CARIBBEAN	ATS	n/a	TFT	FTT	OOSZ	OAFt	OOSZ	Caribbean	Greater Gonave	North America
52	O	17.50	-61.04	CARIBBEAN	ATS	n/a	FTT	FTT	OFt	OOSZ	OOSZ	South America	Caribbean	North America
50	O	-22.95	173.31	HUNTER RIDGE	ATS	n/a	TTF	FTT	OOSZ	OOSZ	OAFt	Australia	New Hebrides	Conway Reef
29	O	12.00	144.29	MARIANA	ATS	n/a	TTF	FTT	OOSZ	OOSZ	OAFt	Pacific	Philippine Sea	Mariana
31	O	24.62	143.39	MARIANA	ATS	n/a	TFT	FTT	OOSZ	OAFt	OOSZ	Mariana	Philippine Sea	Pacific
107	O	9.17	138.28	PHILIPPINE SEA	ATS	n/a	TFT	FTT	OOSZ	OF	OOSZ	Pacific	Caroline	Philippine Sea
61	O	-9.85	159.24	SOLOMAN ISLANDS	ATS	n/a	TFT	FTT	OOSZ	OAF	OOSZ	Australia	Woodlark	Solomon
59	O	-7.55	155.29	SOLOMAN SEA	ATS	n/a	TFT	FTT	OOSZ	OFss	OOSZ	Woodlark	Solomon Sea	Solomon
60	O	-6.16	153.58	SOLOMAN SEA	ATS	n/a	FTT	FTT	OAFt	OOSZ	OOSZ	Solomon	Solomon Sea	South Bismark
46	O	-14.61	166.28	SOUTHWEST PACIFIC	ATS	n/a	TFT	FTT	OOSZ	OAFt	OOSZ	Vitaz	New Hebrides	Australia
47	O	-11.29	162.81	SOUTHWEST PACIFIC	ATS	n/a	TTF	FTT	OOSZ	OOSZ	OAFt	Australia	Solomon	Vitiaz
55	O	-25.69	-175.30	SOUTHWEST PACIFIC	ATS	n/a	TTF	FTT	OOSZ	OOSZ	OAFt	Pacific	Kermadec	Tonga
44	O	-14.48	-173.87	SOUTHWEST PACIFIC	ATS	n/a	TRT	RTT	OOSZ	OBASCt	OOSZ	Tonga	Niuafo'Ou	Pacific
53	O	-60.59	-26.03	ALANTIC	ATS	n/a	TFF	TFF	OOSZ	OFts	OFss	South America	Antarcticia	Sandwich
24	O	-0.63	149.33	SOUTHWEST PACIFIC	ATS	n/a	TTT	TTT	OOSZ	OOSZ	OOSZ	North Bismarck	Caroline	Pacific
87	O	-16.56	177.45	SOUTHWEST PACIFIC	BAB	n/a	FFF	FFF	OAF	OAF	OBAF	Australia	Conway Reef	Balmoral Reef
85	O	-15.52	-179.38	SOUTHWEST PACIFIC	BAB	n/a	RFR	FRR	OBASCt	OAF	OBASCt	Australia	Balmoral Reef	Vitaz
86	O	-16.86	173.91	SOUTHWEST PACIFIC	BAB	NFBTJ	FRR	FRR	OBAF	OBASCt	OBASCt	Conway Reef	New Hebirdes	Balmoral Reef
104	O	-16.20	-177.63	SOUTHWEST PACIFIC	BAB	n/a	RRF	FRR	OBASCt	OBASCt	OBAF	Niuafo'Ou	Australia	Vitiaz
83	O	-24.00	-177.17	SOUTHWEST PACIFIC	BAB	n/a	RFF	RFF	OBASCt	OAFt	OBAFe	Tonga	Kermadec	Australia
102	O	-5.00	153.41	SOUTHWEST PACIFIC	BAB	n/a	FFR	RFF	OAFt	OAFt	OBASCt	Solomon	South Bismarck	North Bismarck
84	O	-13.53	172.80	SOUTHWEST PACIFIC	BAB	n/a	RRR	RRR	OBASCt	OBASCt	OBASCt	Balmoral Reef	New Hebirdes	Vitiaz
98	O	-19.07	-176.07	SOUTHWEST PACIFIC	BAB	n/a	RRR	RRR	OBASCt	OBASCt	OBASCt	Tonga	Australia	Niuafo'Ou
103	O	-15.08	-179.22	SOUTHWEST PACIFIC	BAB	n/a	RRR	RRR	OBASCt	OBAF	OBASCt	Futuna	Australia	Vitiaz
82	O	39.40	-29.77	ALANTIC	MORS	n/a	RFR	FRR	OSCt	OFts	OSCt	Eurasia	Africa	North America
70	O	-61.52	160.99	ANTARCTICA	MORS	n/a	RRF	FRR	OSCt	OSCt	OF	Antarctica	Australia	Pacific
73	O	12.70	58.27	ARABIAN SEA	MORS	AOC	FRR	FRR	OFt	OSCt	OSCt	India	Somalia	Arabia
69	O	-36.36	79.10	INDIAN OCEAN	MORS	n/a	FRR	FRR	OFss	OCSt	OCSt	Australia	Antarctica	Capricorn
78	O	-40.93	42.91	INDIAN OCEAN	MORS	n/a	FRR	FRR	OFt	OSCt	OSCt	Somalia	Antarcticia	Lwandle
79	O	-47.06	32.24	INDIAN OCEAN	MORS	n/a	FRR	FRR	OFss	OSCt	OSCt	Lwandle	Antarctica	Africa
51	O	15.37	-46.64	MID-ALANTIC RIDGE	MORS	FTFZ	RRF	FRR	OOSZt	OOSZt	OFt	Africa	South America	North America
89	O	18.51	-106.27	PACIFIC	MORS	Rivera	FRR	FRR	OFss	OSCt	OSCt	Cocos	Pacific	Rivera
90	O	2.23	-101.55	PACIFIC	MORS	n/a	RRF	FRR	OSCt	OSCt	OF	Nazca	Galapagos	Cocos
95	O	48.81	-128.87	PACIFIC	MORS	n/a	FRR	FRR	OFss	OSCt	OSCt	Juan De Fuca	Pacific	Explorer
96	O	43.00	-126.59	PACIFIC	MORS	n/a	FRR	FRR	OFt	OSCt	OSCt	Gorda	Pacific	Juan De Fuca
80	O	-54.69	-0.73	ALANTIC	MORS	Bouvet	RFF	RFF	OSCt	OFt	OFt	Antarctica	South America	Africa
97	O	-60.10	-29.93	ALANTIC	MORS	n/a	FFR	RFF	OBAFss	OFss	OBASCt	Antarctica	Scotia	Sandwich
109	O	17.81	-81.75	CARIBBEAN	MORS	n/a	RFF	RFF	OSCt	OFt	OFt	Greater Gonave	Caribbean	North America
88	O	2.27	-102.08	PACIFIC	MORS	Galapagos	FFR	RFF	OF	OF	OSCt	Cocos	Galapagos	Pacific
71	O	-25.56	70.04	INDIAN OCEAN	MORS	Rodrigues	RRR	RRR	OSCt	OSCt	OSCt	Capricorn	Antarctica	Somalia
75	O	-35.10	-110.81	PACIFIC	MORS	n/a	RRR	RRR	OSCt	OSCt	OSCt	Antarctica	Pacific	Juan Ferandez
76	O	-34.55	-109.25	PACIFiC	MORS	n/a	RRR	RRR	OSCt	OSCt	OSCt	Antarctica	Juan Fernandez	Nazca
91	O	1.16	-102.17	PACIFIC	MORS	n/a	RRR	RRR	OSCt	OSCt	OSCt	Nazca	Pacific	Galapagos
92	O	-22.09	-114.39	PACIFIC	MORS	n/a	RRR	RRR	OSCt	OSCt	OSCt	Nazca	Easter	Pacific
93	O	-26.92	-113.01	PACIFIC	MORS	n/a	RRR	RRR	OSCt	OCSt	OSCt	Nazca	Pacific	Easter
94	O	-31.52	-111.98	PACIFIC	MORS	n/a	RRR	RRR	OSCt	OSCt	OSCt	Nazca	Juan Fernandez	Pacific

Note: Detail of abbreviations and attributes definition and classification schemes can be found in appendix C- Supplementary Table 1. Known Triple Junction abbreviations: NFBTJ= North Fiji Basin Triple Junction, AOC= Aden-Owen-Carlsb
into three groups: slow (<50 mm/yr), inter. (50-80 mm/yr), and fast (>80 mm/yr). Crustal growth and inflation associated with the individual triple junctions were estimated by measuring the volume of crust in a 100 km radius surrounding the
permanent unique identifier in the Smithsonian Institution's Global Volcanism Program, Volcanoes of the World (2013), summarized in Appendix C, Supplementary Table 5.100-, 500-, and 1,000-km Hotspot: Yes (y)/ No (n) indication if a ho

Limb 1 Angle	Limb 2 Angle	Limb 3 Angle	Angle 1-2	Angle 2-3	Angle 3-1	Certainty	Initation Age (Ma)	Spreading (mm/yr)	Average Spreading rate (mm/yr)	Speed	Global Gravity	1 km Shiptrack	CrusieID	Volume Addition (km3)	100 km Hydrothermal Vents	Number of vent fields	Associated Volcano(s)
127	249	301	122	52	186	0	n/a	n/a	141.7	Fast	n/a	y	EW9803, RB0305, AT21-05	60568	n	n/a	n/a
104	148	329	44	181	135	0	n/a	n/a	142.4	Fast	-350	y	EW9304, RC2907	71134	y	3	360110, 360050
75	256	324	181	68	111	1	35	n/a	70.8	Inter.	-441	n	n/a	135445	n	n/a	n/a
63	248	299	185	51	124	1	n/a	n/a	n/a	n/a	-900	n	n/a	23052	y	7	284220, 284230
141	226	340	85	114	161	2	139	n/a	24.1	Slow	-996	n	n/a	101866	n	n/a	n/a
22	115	202	93	87	180	0	n/a	n/a	22.9	Slow	-46	n	n/a	142582	n	n/a	n/a
112	246	318	134	72	154	0	n/a	n/a	n/a	n/a	-385	n	n/a	126037	n	n/a	n/a
110	225	297	115	72	173	0	n/a	n/a	26.7	n/a	-302	n	n/a	284056	y	2	n/a
11	130	303	119	173	68	0	37	n/a	74.8	Inter.	-1064	y	MGLN06MV	260228	n	n/a	n/a
1	77	180	76	103	181	1	n/a	n/a	39.4	Slow	-447	n	n/a	110447	n	n/a	n/a
71	251	345	180	94	86	1	n/a	n/a	41.3	Slow	-1070	n	n/a	127563	y	3	n/a
19	191	302	172	111	77	1	97	n/a	82.5	Fast	-266	y	COOK14MV, MRTN06WT	84547	n	n/a	n/a
111	198	287	87	89	184	1	n/a	n/a	144.8	Fast	-736	y	BMRG08MV	95527	y	32	243120, 243140,243130
71	134	254	63	120	177	1	20	n/a	96.1	Fast	-1002	n	n/a	1720	n	n/a	n/a
116	297	345	181	48	131	3	37	n/a	46.8	Slow	-427	n	n/a	141394	n	n/a	n/a
65	241	280	176	39	145	3	n/a	n/a	26.4	Slow	-684	n	n/a	204051	y	2	n/a
20	245	298	225	53	82	0	n/a	0	50.8	Inter.	n/a	y	RR0914	32622	n	n/a	n/a
54	176	294	122	118	120	1	0	n/a	n/a	n/a	28	y	TUIM06MV	62958	y	4	n/a
7	131	298	124	167	69	0	3	n/a	71.4	Inter.	65	y	WEST06MV, KM0416, KM0409	40461	y	5	243111, 243112
20	144	197	124	53	183	1	4	n/a	112.7	Fast	-97	n	n/a	44459	y	5	243001
5	168	314	163	146	51	0	n/a	n/a	85.6	Fast	-814	n	n/a	208318	n	n/a	n/a
57	171	265	114	94	152	0	1	0	n/a	n/a	-541	n	n/a	55904	n	n/a	n/a
91	197	279	106	82	172	0	1	1	n/a	n/a	96	y	KM0417, KM0804	33103	y	22	243030
27	126	200	99	74	187	0	n/a	1	63.3	Inter.	-56	y	KIWI10RR, KM0703	20245	n	n/a	n/a
13	101	264	88	163	109	0	0	52	28.6	Slow	-72	n	n/a	6196	y	2	382010
118	253	338	135	85	140	2	0	62	46.3	Slow	-280	n	n/a	25363	y	1	n/a
44	188	302	144	114	102	0	6	58	32.8	Slow	-673	n	n/a	56729	n	n/a	n/a
51	234	317	183	83	94	3	4	n/a	145.7	Fast	-289	n	n/a	24650	y	1	234000
6	99	214	93	115	152	0	1	44	20.0	Slow	-440	n	n/a	46634	n	n/a	n/a
26	100	221	74	121	165	0	4	n/a	18.8	Slow	-669	y	KN145-16	35869	n	n/a	n/a
4	96	277	92	181	87	2	1	n/a	22.8	Slow	-1084	y	EW9704, KN161-04, KN182-03,	53933	y	4	n/a
83	180	277	97	97	166	0	2	18	137.3	Fast	117	y	PANR01MV, DELV02RR	48530	y	4	334020
91	121	274	30	153	177	0	1	101	72.9	Inter.	-821	y	CERE03WT, ENCR01WT	64957	y	3	n/a
78	207	278	129	71	160	0	0	5	127.4	Fast	93	y	RP-15-SU-83, AT03-56	52877	y	13	331010, 331005
78	211	285	133	74	153	0	0	2	138.5	Fast	-216	y	RP-10-SU-80, HLY-01-01, MGLN46MV	7994	y	4	331031
80	166	311	86	145	129	0	0	65	60.3	Inter.	160	n	n/a	33688	n	n/a	n/a
139	236	322	97	86	177	0	0	9	55.2	Inter.	187	n	n/a	9232	y	1	n/a
3	84	261	81	177	102	0	n/a	n/a	120.4	Fast	-1326	y	FK008	188297	y	4	n/a
0	94	181	94	87	179	0	0	2	157.9	Fast	-88	y	ERE03WT, AMLR90T, NEMO02MV, PASC05W	65426	y	3	n/a
186	241	334	55	93	212	3	0	n/a	24.4	Slow	-561	n	n/a	49714	y	1	n/a
82	187	288	105	101	154	0	0	n/a	158.6	Fast	-25	y	RAPA03WT	29443	n	n/a	n/a
132	262	356	130	94	136	0	3	34	158.4	Fast	-394	y	PASC03WT	49588	n	n/a	n/a
49	188	274	139	86	135	0	0	1	60.1	Inter.	148	y	PASC05WT, PPTJ02WT	35686	y	3	n/a
11	89	253	78	164	118	0	0	22	66.0	Inter.	71	y	PASC05WT, GEOMETEP-4	23533	y	10	n/a
22	184	265	162	81	117	0	2	27	44.1	Slow	39	y	GLOR05MV, PASC04WT	16637	y	8	n/a
8	98	191	90	93	177	0	0	31	15.8	Slow	233	y	PASC03WT, PANR05MV, AT11-24	54620	y	8	n/a

erg, FTFZ= Fifteen Twenty Fracture Zone. Additional abbreviations and descriptions of entries are found in Appendix C, Supplementary Table 1.See Figure 3.3 (this study; Chapter 3) for illustration of plate and limb identification within a triple junction. Spreading (mm/yr) point data value at the ce
triple junction. Volumes were calculated using an ArcGIS polygon volume function, which calculates the volume and surface area between a polygon and a surface. The surface, and terrain in this cases is defined by a triangular irregular network (TIN). The crustal inflation is determined between the
tspot is within the designated radius surrounding each triple junction. Hotspot location, name, heat source and associated references are sourced from Whittaker et al. (2015). LIPs: Large Igneous Provinces (LIPs) location, name and individual LIPs references data from Johansson et al. (2018). 100-km

100 km Hotspot	500 km Hotspot	1000 km Hotspot	Hotspot Name	Heat Source	LIPs 100km	LIP Name/Location	LIPs age	Sedimentary Basin	Seabed Lithology	Geomorphology Features
n	n	n	n/a	n/a	n	n/a	n/a	n/a	Clay	Basin, Trench, Hadal
n	n	n	n/a	n/a	n	n/a	n/a	Leeward Ultradeep	Clay	Escarpment, Abyssal Mountains,
n	n	n	n/a	n/a	n	n/a	n/a	n/a	Fine-Grained Calcareous Sediment	Escarpment, Basin, Trench, Abbysal Mountains
n	n	n	n/a	n/a	n	n/a	n/a	n/a	N/A	n/a
n	n	n	n/a	n/a	y	4000 Meters Mid-Pacific Seamounts, North Pacific	110	n/a	Sand	Escarpment, Basin, Trench, Hadal
n	n	n	n/a	n/a	y	3000 Meters West Caroline Ridge, Central Pacific	25	n/a	Calcareous Ooze	Escarpment, Basin, Trench
n	n	n	n/a	n/a	y	Louisade Plateau, North Of Coral Sea	100	n/a	Mixed Calcareous-Siliceous Ooze	Basin, Trench, Abyssal Mountains
n	n	n	n/a	n/a	n	n/a	n/a	n/a	Siliceous Mud	Escarpment
n	n	n	n/a	n/a	n	n/a	n/a	n/a	Clay	Basin, Trench, Hadal
n	n	n	n/a	n/a	n	n/a	n/a	n/a	Ash And Volcanic Sand/Gravel	Basin, Sill, Trench, Abyssal Mountains
n	n	n	n/a	n/a	n	n/a	n/a	n/a	Clay	Escarpment, Basin, Trench, Hadal
n	n	n	n/a	n/a	y	4000 Meters Louisville Ridge, South Pacific, Osbourn Seamount	78.8	n/a	Clay	Escarpment, Basin, Trench, Hadal
n	n	y	Samoa	deep mantle	n	n/a	n/a	n/a	Fine-Grained Calcareous Sediment	Basin, Trench, Hadal
n	n	n	n/a	n/a	n	n/a	n/a	n/a	Silt	Basin, Rift Valley, Spreading Ridge, Trench, Hadal
n	n	n	n/a	n/a	n	n/a	n/a	Manus	Clay	Basin, Trough, Abyssal Mountains
n	n	n	n/a	n/a	n	n/a	n/a	FIJI	Fined-Grained Calcareous Sediment	Escarpment, Plateau, Abyssal Hills
n	n	n	n/a	n/a	n	n/a	n/a	n/a	Siliceous Mud	Escarpment, Basin, Plateau, Abyssal Mountains
n	n	n	n/a	n/a	n	n/a	n/a	FIJI	Clay	Spreading Ridge, Abyssal Mountains
n	n	n	n/a	n/a	n	n/a	n/a	n/a	Ash And Volcanic Sand/Gravel	Escarpment, Ridge, Spreading Ridge, Plateau, Abyssal Moun
n	n	n	n/a	n/a	n	n/a	n/a	n/a	Clay	Spreading Ridge, Plateau, Abyssal Mountains
n	n	n	n/a	n/a	n	n/a	n/a	Bougainville	Clay	Basin, Abyssal Mountians
n	n	n	n/a	n/a	n	n/a	n/a	FIJI	Calcreous Ooze	Abyssal Hills
n	n	n	n/a	n/a	n	n/a	n/a	n/a	Fine-Grained Calcareous Sediment	Escarpment, Basin, Spreading Ridge, Plateau, Abyssal Hil
n	n	n	n/a	n/a	n	n/a	n/a	n/a	Ash And Volcanic Sand/Gravel	Plateau, Abyssal Mountains
n	y	y	Azores	deep mantle	n	n/a	n/a	n/a	Calcareous Ooze	Escarpment, Spreading Ridge, Abyssal Mountains
n	n	y	Balleny	secondary/tertiary	n	n/a	n/a	n/a	Siliceous Mud	Rift Valley, Spreading Ridge, Abyssal Mountians
n	n	n	n/a	n/a	n	n/a	n/a	n/a	Calcareous Ooze	Basin, Rift Valley, Abyssal Mountian
y	y	y	Amsterdam Christmas	n/a	n	n/a	n/a	n/a	N/A	n/a
n	n	y	Marion	secondary/tertiary	n	n/a	n/a	n/a	Fined-Grained Calcareous Sediment	Escarpment, Basin, Spreading Ridge, Abyssal Mountians
n	n	y	Marion	secondary/tertiary	n	n/a	n/a	n/a	Clay	Basin, Abyssal Mountains
n	n	y	Altantic Ridge	n/a	n	n/a	n/a	n/a	Calcareous Ooze	Escarpment, Basin, Rift Valley, Spreading Ridge, Abyssal Mou
n	n	y	Socorro	secondary/tertiary	n	n/a	n/a	n/a	Siliceous Mud	Spreading Ridge, Abyssal Mountains
n	n	n	n/a	n/a	n	n/a	n/a	n/a	Calcareous Ooze	Escarpment, Basin, Rift Valley, Spreading Ridge, Abyssal Mou
n	y	y	Juan de Fuca Cobb	mid-mantle	n	n/a	n/a	n/a	Clay	Spreading Ridge, Abyssal Hills
n	n	y	Juan de Fuca Cobb	mid-mantle	n	n/a	n/a	n/a	Clay	Escrapment, Basin, Rift Valley, Spreading Ridge, Abyssal Mou
n	y	y	Bouvet Shona	n/a	n	n/a	n/a	n/a	Datom Ooze	Escarpment, Spreading Ridge, Abyssal Mountains
n	n	n	n/a	n/a	n	n/a	n/a	n/a	Silt	Escarpment, Abyssal Mountians
n	n	n	n/a	n/a	n	n/a	n/a	n/a	Fine-Grained Calcareous Sediment	Escarpment, Basin, Rift Valley, Spreading Ridge, Abyssal Mou
n	n	n	n/a	n/a	n	n/a	n/a	n/a	Calcareous Ooze	Spreading Ridge, Abyssal Hills
n	n	y	Rodriguez	n/a	n	n/a	n/a	n/a	Calcareous Ooze	Escarpment, Basin, Spreading Ridge, Abyssal Mountian
n	n	y	Easter	deep mantle	n	n/a	n/a	n/a	Siliceous Mud	Spreading Ridge, Abyssal Hills
n	n	y	Easter	deep mantle	n	n/a	n/a	n/a	Siliceous Mud	Rift Valley, Spreading Ridge, Abyssal Mountains
n	n	n	n/a	n/a	n	n/a	n/a	n/a	Calcareous Ooze	Spreading Ridge, Abyssal Hills
n	n	y	Easter	deep mantle	n	n/a	n/a	n/a	Fined-Grained Calcareous Sediment	Sreading Ridge, Abyssal Hills
n	n	y	Easter	deep mantle	n	n/a	n/a	n/a	Calcareous Ooze	Spreading Ridge, Abyssal Hills
n	n	y	Easter	deep mantle	n	n/a	n/a	n/a	Calcareous Ooze	Spreading Ridge, Abyssal Hills

nter of the triple junction from MORVEL: DeMets, et al. (2010). Average spreading Rate (mm/yr): to obtain a representative spreading rate for each triple junction, we used a 100-km radius circle to average the spreading rate data published in Seton et al. (2020), for further detail see Appendix C, Supplementary T
ninimum elevation value (Zmin) of the TIN and the overlying polygon. Hydrothermal vents: Yes (y)/ No (no) indication if a identified hydrothermal vent is within 100-km radius a triple junction center, data sourced from Vents InterRidge Global Vents Database; Beaulieu and Szafranski, (2020). Associated volca
LIPs: Yes (y)/ No (n) indication if an identified LIPs within 100-km radius of a triple junction. Known Sedimentary Basin: data sourced from Tellus Database of Sedimentary Basins (Robertson CGG, 2017). Seabed Lithology: data sourced form Dutkiewicz et al. (2015). Geomorphology Features: data sources fro

	References
	Civile et al. 2012, Bruguier and Livermore 2001
	Anderson et al. 2016
	Pelletier and Auzende 1996, Montelli et al. 2006
	n/a
	Earthbyte dataset, Kopper et al. (2004), Ishizuka et al. (2018)
	ishizuka et al. 2018, Kobayashi 2004, Coffin 2011 (PLATES project)
	Moreno et al. 2011, Benford et al. 2012 ,Coffin 2011 (PLATES project)
	n/a
	Smith and Price 2006
	n/a
	Pelletier et al. 2001
	Contreras-Reyes et al. 2011, Earthbyte dataset, Koppers et al. 2004
	Pelletier and Auzende 1996, Montelli et al. 2006
	Anderson et al 2016, Schellart and Spakman 2015
	Smith and Price 2006
	n/a
	Larsen et al. 1992
	Neves et al. 2003
	Schouten et al. 2008
tains	Anderson et al. 2016
	Klitgord and Mammerickx 1982, Schouten et al. 2008
	Pichot et al. 2012, Calais et al. 2010
	Neves et al. 2003
ls	Mann et al. 1995, Calais et al. 2010, Benford et al. 2012
	n/a
	n/a
	Miranda et al. 2018, Montelli et al. 2006
	Bruguier and Livermore 2001, Civile et al. 2012, Courtillot et al. 2003
	Fournier et al. 2008
	Anderson and Schramm 2005
s	Audet et al. 2008, Courtillot et al. 2003
	Courtillot et al. 2003
ntians	Pelletier et al. 2001 ,Montelli et al. 2006
	Larsen et al. 1992, Courtillot et al. 2003
ntains	n/a
	Schelllart and Spakman 2015 ,Montelli et al. 2006
ntians	Baldwin et al. 2012, Schellart and Spakman 2015, Montelli et al. 2006
	DeMets and Traylen 2000, Montelli et al. 2006
	Kobayashi 2004
ntains	Baldwin et al. 2012
	Larsen et al. 1992
	Klitgord and Mammerickx 1982, Anderson and Schramm 2005
	Koeing and Jokat 2010, Montelli et al. 2006
	Chaytor et al. 2004, Montelli et al. 2006
	Pichot et al. 2012
	Montelli et al. 2006
	Dhawaskar et al. 2018, Montelli et al. 2006
	Schellart and Spakman 2015, Montelli et al. 2006

able 2. Speed is categorizing the full spreading rate in mm/yr from Seton et al., 2020
no(s): Some vent fields are sub-features of volcanic features identified with a
om Harris et al. (2014).

Triple Junction Database References (Global and Oceanic)

A.V. Lukhnev, V.A. San'kov, A.I. Miroshnichenko, S.V. Ashurkov, E. Calais, GPS rotation and strain rates in the Baikal–Mongolia region. 2010, Russian Geology and Geophysics, **v. 51(7)**, p 785-793, dio:10.1016/j.rgg.2010.06.006

Anderson, D.L., Schramm, K.A., Foulger, G.R., Natland, J.H. and Presnall, D.C., 2005, Global hotspot maps. Special Papers-Geological Society of America, **v. 388**, p.19

Anderson, M. O., Hannington, M. D., Haase, K., Schwarz-Schampera, U., Augustin, N., McConachy, T. F., and Allen, K., 2016, Tectonic focusing of voluminous basaltic eruptions in magma-deficient back-arc rifts. Earth and Planetary Science Letters, **v. 440**, p. 43–55

Argus, D.F., Gordon, R.G. and DeMets, C., 2011, Geologically current motion of 56 plates relative to the no-net-rotation reference frame. Geochemistry Geophysics Geosystems, **v. 12(11)**, 13 p, dio:10.1029/2011GC003751

Arnulf, A.F., Harding, A.J., Kent, G.M., Carbotte S.M., Canales J.P., and Nedimović, M.R., 2014, Anatomy of an active submarine volcano, Geology, **v. 42(8)**, p 655–658, doi:10.1130/G35629.1

Audet, P., Bostock, M. G., Mercier, J. P., and Cassidy, J. F., 2008, Morphology of the Explorer–Juan de Fuca slab edge in northern Cascadia: Imaging plate capture at a ridge-trench-transform triple junction. Geology, **v. 36(11)**, p 895–898, doi:10.1130/G25356A.1

Baldwin, S.L., Fitzgerald, P.G. and Webb, L.E., 2012, Tectonics of the New Guinea region. Annual Review of Earth and Planetary Sciences, **v. 40(495)**, 29 p

Beaulieu, S. E., & Szafranski, K., 2020, InterRidge Global database of active submarine hydrothermal vent fields, Version 3.4, URL:http://vents-data. interridge.org

Benford, B., Tikoff, B. and DeMets, C., 2012, Character of the Caribbean–Gônave–North America plate boundaries in the upper mantle based on shear-wave splitting. Geophysical research letters, **v. 39(24)**, 6 p, dio:10.1029/2012GL053766

Bird, P., 2003, An updated digital model of plate boundaries. Geochemistry, Geophysics, Geosystems, **v. 4(3)**, p 25-28, doi:10.1029/2001GC000252

Bonvalot, S., Balmino, G., Briais, A., M. Kuhn, Peyrefitte, A., Vales N., Biancale, R., Gabalda, G., Reinquin, F., and Sarrailh, M., 2012, World Gravity Map. Commission for the Geological Map of the World. Eds. BGI-CGMW-CNES-IRD, Paris

Bouysse, P., 2014, Geological Map of the World (third edition, revised): Paris, France, Commission for the Geological Map of the World, 2 sheets, scale 1:35,000,000, doi:F10.14682/2014CGM3R.

Bruguier, N.J. and Livermore, R.A., 2001, Enhanced magma supply at the southern East Scotia Ridge: evidence for mantle flow around the subducting slab? Earth and Planetary Science Letters, **v. 191(1-2)**, p 129-144, doi:10.1016/S0012-821X(01)00408-3

Burke, K., and Dewey, J. F., 1973, Plume-generated triple junctions: key indicators in applying plate tectonics to old rocks. The Journal of Geology, **v. 81(4)**, p 406-433

Calais, E., Freed, A., Mattioli, G., Amelung, F., Jónsson, S. Jansma, P., Hong, S-H., Dixon, T., Prépetit. C., and Momplaisir, R., 2010, Transpressional rupture of an unmapped fault during the 2010 Haiti earthquake. Nature Geoscience, **v. 3**, p 794–799, dio:10.1038/ngeo992

Carbotte, S. M., Smith, D. K., Cannat M. and E. M Klein, 2016, Tectonic and magmatic segmentation of the Global Ocean Ridge System: a synthesis of observations. Geological Society of London, **v. 420**, p 249-295, doi:10.1144/SP420.5

Chaytor, J. D., Goldfinger, C., Dziak, R. P., and Fox, C. G., 2004, Active deformation of the Gorda plate: Constraining deformation models with new geophysical data. Geology, **v. 32(4)**, p 353-356, doi:10.1130/G20178.1

Civile, D., Lodolo, E., Vuan, A. and Loreto, M.F., 2012. Tectonics of the Scotia–Antarctica plate boundary constrained from seismic and seismological data. Tectonophysics, **v. 550**, p 17-34, dio:10.1029/2011JB008434

Contreras-Reyes, E., Grevemeyer, I., Watts, A.B., Flueh, E.R., Peirce, C., Moeller, S. and Papenberg, C., 2011, Deep seismic structure of the Tonga subduction zone: Implications for mantle hydration, tectonic erosion, and arc magmatism. Journal of Geophysical Research: Solid Earth, **v. 116(B10)**, 18 p, dio:10.1029/2011JB008434

Courtillot, V., Davaille, A., Besse, J. and Stock, J., 2003, Three distinct types of hotspots in the Earth's mantle. Earth and Planetary Science Letters, **v. 205(3-4)**, p 295-308, dio:10.1016/S0012-821X(02)01048-8

DeMets, C. and Traylen, S., 2000, Motion of the Rivera plate since 10 Ma relative to the Pacific and North American plates and the mantle. Tectonophysics, **v. 318(1-4)**, p 119-159, dio:10.1016/S0040-1951(99)00309-1

DeMets, C., Gordon, R. G., and Argus, D. F., 2010, Geologically current plate motions. Geophysical journal international, **v. 181(1)**, p 1-80, dio:10.1111/j.1365-246X

Déprez, A., Doubre, C., Masson, F. and Ulrich, P., 2013. Seismic and aseismic deformation along the East African Rift System from a reanalysis of the GPS velocity field of Africa. Geophysical Journal International, **v. 193(3)**, p 1353-1369, dio:10.1093/gji/ggt085

Dhont, D., Luxey, P. and Chorowicz, J., 2005, 3-D modeling of geologic maps from surface data. AAPG bulletin, **v. 89(11)**, p 1465-1474, dio:10.1306/06270504108

Duffy, B., Quigley, M., Harris, R. and Ring, U., 2013. Arc-parallel extrusion of the Timor sector of the Banda arc-continent collision. Tectonics, **v. 32(3)**, p 641-660, dio:10.1002/tect.20048

Dziewonski, A. M., Chou, T. A., and Woodhouse, J. H., 1981, Determination of earthquake source parameters from waveform data for studies of global and regional seismicity. Journal of Geophysical Research: Solid Earth, **v. 86(B4)**, p 2825-2852, dio:10.1029/JB086iB04p02825

Eagles, G., Livermore, R.A., Fairhead, J.D. and Morris, P., 2005, Tectonic evolution of the west Scotia Sea. Journal of Geophysical Research: Solid Earth, **v. 110(B2)**, 19 p, dio:10.1029/2004JB003154

Egbue, O. and Kellogg, J., 2010, Pleistocene to present North Andean "escape". Tectonophysics, **v. 489(1-4)**, p 248-257, dio:10.1016/j.tecto.2010.04.021

Ekström, G., Nettles, M., and Dziewoński, A. M., 2012, The global CMT project 2004–2010: Centroid-moment tensors for 13,017 earthquakes. Physics of the Earth and Planetary Interiors, **v. 200**, p 1-9, dio:10.1016/j.pepi.2012.04.002 002

Ernst, R. E., and Buchan, K. L., 2003, Recognizing mantle plumes in the geological record. Annual Review Earth Planetary Science, **v. 31**, p 463-523, doi:10.1146/annurev.earth.31.100901.145500

Fichtner, A., Trampert, J., Cupillard, P., Saygin, E., Taymaz, T., Capdeville, Y. and Villasenor, A., 2013, Multiscale full waveform inversion. Geophysical Journal International, **v. 194(1)**, p 534-556, dio:10.1093/gji/ggt118

Fletcher, M., and Wyman, D. A., 2015, Mantle plume–subduction zone interactions over the past 60 Ma. Lithos, **v. 233**, p 162-173, dio:10.1016/j.lithos.2015.06.026

Fournier, M., Agard, P. and Petit, C., 2008, Micro-tectonic constraints on the evolution of the Barles half-window (Digne nappe, southern Alps). Implications for the timing of folding in the

Valensole foreland basin. Bulletin de la Société géologique de France, **v. 179(6)**, p 551-568, dio:10.2113/gssgfbull.179.6.551

Franke, D., Jokat, W., Ladage, S., Stollhofen, H., Klimke, J., Lutz, R., Mahanjane, E.S., Ehrhardt, A. and Schreckenberger, B., 2015, The offshore East African Rift System: structural framework at the toe of a juvenile rift, Tectonics, **v. 34(10)**, p 2086-2104, dio:10.1002/2015TC003922

GEBCO Compilation Group, 2021, GEBCO 2021 Grid, doi:10.5285/c6612cbe-50b3-0cff-e053-6c86abc09f8f

Global Volcanism Program, 2013, Volcanoes of the World. **v.** 4.11.0. (2020), *In* Venzke, E (*Eds*). Smithsonian Institution, dio:10.5479/si.GVP.VOTW4-2013

Guntoro, A., 1999, The effect of collision of the Banggai-Sula microcontinent to the tectonic development in Central Indonesian region. Bulletin of the Geological Society of Malaysia, **v. 43**, p 103-111.

Guzman-speziale, M., 2012, Seismological constraints on the motion of the Central America Forearc Silver. Geological Society of America, **v. 44(3)**, 25 p

Harris, P. T., Macmillan-Lawler, M., Rupp, J., and Baker, E. K., 2014, Geomorphology of the oceans. Marine Geology, **v. 352**, p 4-24, dio:10.1016/j.margeo.2014.01.011

Heidbach, O., Rajabi, M., Cui, X., Fuchs, K., Müller, B., Reinecker, J. Reiter, K., Tingay, M., Wenzel, F., Xie, F. and Zoback, M., 2018, The World Stress Map database release 2016: Crustal stress pattern across scales. Tectonophysics, **v. 744**, p 484-498, dio:10.1016/j.tecto.2018.07.007

Hinschberger, F., Malod, J-A., Réhault, J-P., Villeneuve, M., Royer, J-Y., and Burhanuddin, S., 2005, Late Cenozoic geodynamic evolution of eastern Indonesia. Tectonophysics, **v. 404(1-2),** p 91-118, dio:10.1016/j.tecto.2005.05.005

Imaeva, L.P., Gusev, G.S., Imaev, V.S., Ashurkov, S.V., Melnikova, V.I. and Seredkina, A.I., 2017, Geodynamic activity of modern structures and tectonic stress fields in northeast Asia. Geodynamics & Tectonophysics, **v. 8(4)**, p. 737-768, dio:10.5800/GT-2017-8-4-0315

Ishizuka, O., Hickey-Vargas, R., Arculus, R.J., Yogodzinski, G.M., Savov, I.P., Kusano, Y., McCarthy, A., Brandl, P.A. and Sudo, M., 2018, Age of Izu–Bonin–Mariana arc basement. Earth and Planetary Science Letters, **v. 481**, p 80-90, doi: 10.1016/j.epsl.2017.10.023

Isozaki, Y., Aoki, K., Nakama, T. and Yanai, S., 2010, New insight into a subduction-related orogen: A reappraisal of the geotectonic framework and evolution of the Japanese Islands. Gondwana Research, **v. 18(1)**, p 82-105, dio:10.1016/j.gr.2010.02.015

Johansson, L., Zahirovic, S., and Müller, R. D., 2018, The interplay between the eruption and weathering of large igneous provinces and the deep-time carbon cycle. Geophysical Research Letters, **v. 45(11)**, p 5380-5389, dio:10.1029/2017GL076691

Keir, D., Ebinger, C.J., Stuart, G.W., Daly, E. and Ayele, A., 2006, Strain accommodation by magmatism and faulting as rifting proceeds to breakup: Seismicity of the northern Ethiopian rift. Journal of Geophysical Research: Solid Earth**, v. 111(B5)**, p 291-294, dio:10.1038/nature04978

Kellogg, J.N., and Vega, V., 1995, Tectonic development of Panama, Costa Rica, and the Colombian Andes: constraints from global positioning system geodetic studies and gravity. Special Papers-Geological Society of America, p 75-75.

Klitgord, K.D. and Mammerickx, J., 1982, Northern East Pacific Rise: magnetic anomaly and bathymetric framework. Journal of Geophysical Research: Solid Earth, **v. 87(B8)**, p 6725-6750, dio:10.1029/JB087iB08p06725

Kobayashi, K., 2004, Origin of the Palau and Yap trench-arc systems. Geophysical Journal International, **v. 157(3)**, p 1303-1315, dio:10.1111/j.1365-246X.2003.02244.x

Kogan, M.G., Frolov, D.I., Vasilenko, N.F., Freymueller, J.T., Steblov, G.M., Ekström, G., Titkov, N.N. and Prytkov, A.S., 2017, Plate coupling and strain in the far western Aleutian arc modeled from GPS data. Geophysical Research Letters, 44(7), pp.3176-3183.

Koppers, A.A., Duncan, R.A. and Steinberger, B., 2004, Implications of a nonlinear 40Ar/39Ar age progression along the Louisville seamount trail for models of fixed and moving hot spots. Geochemistry, Geophysics, Geosystems, **v. 5(6)**, 22 p, dio:10.1029/2003GC000671

LaFemina, P. C., 2015, Plate tectonics and volcanism. *In* The encyclopedia of volcanoes (second edition p 65-92, Academic Press, dio:10.1016/B978-0-12-385938-9.00003-1

Larsen, R.M., Larsen, B.T., Brekke, H. and Talleraas, E., 1992, Structural and tectonic modelling and its application to petroleum geology. Norwegian Petroleum Society, **v. 1**, 570 p, dio:10.1016/B978-0-444-88607-1.50005-X

Lebrun, J.F., Lamarche, G., Collot, J.Y. and Delteil, J., 2000, Abrupt strike-slip fault to subduction transition: The Alpine fault-Puysegur trench connection, New Zealand. Tectonics, **v. 19(4)**, p 688-706, dio:10.1029/2000TC900008

Li, S., Suo, Y., Li, X., Liu, B., Dai, L., Wang, G., Zhou, J., Li, Y., Liu, Y., Cao, X., Somerville, I., Mu, D., Zhao, S., Liu, J., Meng, F., Zhen, L., Zhao, L., Zhu, J., Yu, S., Liu, Y., and Zhang, G., 2018, Microplate tectonics: new insights from micro-blocks in the global oceans, continental margins and deep mantle. Earth-Science Reviews, **v. 185**, p 1029–1064, dio:10.1016/j.earscirev.2018.09.005

Livermore, R., Balanyá, J.C., Maldonado, A., Martínez, J.M., Rodríguez-Fernández, J., de Galdeano, C.S., Zaldívar, J.G., Jabaloy, A., Barnolas, A., Somoza, L. and Hernández-Molina, J., 2000, Autopsy on a dead spreading centre: the Phoenix Ridge, Drake Passage, Antarctica. Geology, **v. 28(7)**, p 607-610, dio:10.1130/0091-7613(2000)28%3C607:AOADSC%3E2.0.CO;2

Macdonald, K. C., 1982, Mid-ocean ridges: Fine scale tectonic, volcanic and hydrothermal processes within the plate boundary zone. Annual Review of Earth and Planetary Sciences, **v. 10**, p 155-190

Macdonald, K. C., 1983, Crustal processes at spreading centres. Reviews of Geophysics, **v. 21(6)**, p 1441-1454, dio:10.1029/RG021i006p01441

Macdonald, K. C., 1991, Mid-Ocean Ridge Tectonics, Volcanism, and Geomorphology. *In* Encyclopedia of Ocean Sciences (third edition), **v.4**, p 405-419, Academic Press, dio:10.1016/B978-0-12-409548-9.11065-6

MacLeod, S. J., Williams, S. E., Matthews, K. J., Müller, R. D., and Qin, X., 2017, A global review and digital database of large-scale extinct spreading centres. Geosphere, **v. 13(3)**, p 911-949, dio:10.1130/GES01379.1

Mahony, S.H., Wallace, L.M., Miyoshi, M., Villamor, P., Sparks, R.S.J. and Hasenaka, T., 2011, Volcano-tectonic interactions during rapid plate-boundary evolution in the Kyushu region, SW Japan. Geological Society of America, **v. 123(11-12)**, p 2201-2223, dio:10.1130/B30408.1

Manea, V. C., Manea, M., & Ferrari, L., 2013, A geodynamical perspective on the subduction of Cocos and Rivera plates beneath Mexico and Central America. Tectonophysics, **v. 609**, p 56-81, dio:10.1016/j.tecto.2012.12.039

Mann, P., 1995, Geologic and tectonic development of the Caribbean plate boundary in southern Central America. Geological Society of America, **v. 295**, 350 p.

Marshall, J.S., Fisher, D.M. and Gardner, T.W., 2000, Central Costa Rica deformed belt: Kinematics of diffuse faulting across the western Panama block. Tectonics, **v. 19(3)**, p 468-492, dio:10.1029/1999TC001136

Matthews, K. J., Müller, R. D., Wessel, P., and Whittaker, J. M., 2011, The tectonic fabric of the ocean basins. Journal of Geophysical Research: Solid Earth, **v. 116(B12)**, 28 p, dio:10.1029/2011JB008413

Mendoza, C., Castro Torres, S. and Gomez Gonzalez, J.M., 2011. Moment-constrained finite-fault analysis using teleseismic P waves: Mexico subduction zone. Bulletin of the Seismological Society of America, **v. 101(6)**, p 2675-2684, dio:10.1785/0120100126

Miranda, T.S., Santos, R.F., Barbosa, J.A., Gomes, I.F., Alencar, M.L., Correia, O.J., Falcão, T.C., Gale, J.F.W. and Neumann, V.H., 2018, Quantifying aperture, spacing and fracture intensity in a carbonate reservoir analogue: Crato Formation, NE Brazil. Marine and Petroleum Geology, **v. 97**, p 556-567, dio:10.1016/j.marpetgeo.2018.07.019

Montelli, R., Nolet, G., Dahlen, F.A. and Masters, G., 2006, A catalogue of deep mantle plumes: New results from finite-frequency tomography. Geochemistry, Geophysics, Geosystems, **v. 7(11)**, 69 p, dio:10.1029/2006GC001248

Moreno, C.J., Horton, B.K., Caballero, V., Mora, A., Parra, M. and Sierra, J., 2011, Depositional and provenance record of the Paleogene transition from foreland to hinterland basin evolution during Andean orogenesis, northern Middle Magdalena Valley Basin, Colombia. Journal of South American Earth Sciences, **v. 32(3)**, p 246-263, dio:10.1016/j.jsames.2011.03.018

Neves, S.P., Araújo, A.M., Correia, P.B. and Mariano, G., 2003, Magnetic fabrics in the Cabanas Granite (NE Brazil): interplay between emplacement and regional fabrics in a dextral transpressive regime. Journal of Structural Geology, **v. 25(3)**, p 441-453, dio:10.1016/S0191-8141(02)00003-2

Pagli, C., Wang, H., Wright, T.J., Calais, E. and Lewi, E., 2014, Current plate boundary deformation of the Afar rift from a 3-D velocity field inversion of InSAR and GPS. Journal of Geophysical Research: Solid Earth, **v. 119(11)**, p 8562-8575, dio:10.1002/2014JB011391

Pelletier, B. and Auzende, J.M., 1996. Geometry and structure of the Vitiaz trench lineament (SW Pacific). Marine Geophysical Researches, **v. 18(2)**, p 305-335, dio:10.1007/BF00286083

Pelletier, B., Lagabrielle, Y., Benoit, M., Cabioch, G., Calmant, S., Garel, E. and Guivel, C., 2001, Newly identified segments of the Pacific–Australia plate boundary along the North Fiji transform zone. Earth and Planetary Science Letters, **v. 193(3-4)**, pp.347-358, dio:10.1016/S0012-821X(01)00522-2

Pichot, T., Patriat, M., Westbrook, G.K., Nalpas, T., Gutscher, M.A., Roest, W.R., Deville, E., Moulin, M., Aslanian, D. and Rabineau, M., 2012, The Cenozoic tectonostratigraphic evolution of the Barracuda Ridge and Tiburon Rise, at the western end of the North America–South America plate boundary zone. Marine Geology, v. 303, p 154-171, dio:10.1016/j.margeo.2012.02.001

Polonia, A., Torelli, L., Mussoni, P., Gasperini, L., Artoni, A. and Klaeschen, D., 2011, The Calabrian Arc subduction complex in the Ionian Sea: Regional architecture, active deformation, and seismic hazard. Tectonics, **v. 30(5)**, 28 p, dio:10.1029/2010TC002821

Prokopiev, A.V., Borisenko, A.S., Gamyanin, G.N., Pavlova, G.G., Fridovsky, V.Y., Kondrat'eva, L.A., Anisimova, G.S., Trunilina, V.A., Ivanov, A.I., Travin, A.V. and Koroleva, O.V., 2018, Age constraints and tectonic settings of metallogenic and magmatic events in the Verkhoyansk-Kolyma folded area. Russian Geology and Geophysics, **v. 59(10)**, p 1237-1253, dio:10.1016/j.rgg.2018.09.004

Purcell, P.G., 2018, Re-imagining and re-imaging the development of the East African Rift. Petroleum Geoscience, **v. 24(1)**, p 21-40, dio:10.1144/petgeo2017-036

Dhawaskar, P., Ganguly, S., Mukhopadhyay, R., Manikyamba, C., Iyer, S.D., Karisiddaiah, S.M. and Mahender, K., 2020. Geochemical heterogeneity along the Vema Fracture Zone, Indian Ocean: Mixing of melts from the Reunion plume and the Central Indian Ridge. Geological Journal, **v. 55(1)**, p 330-343, dio:10.1002/gj.3395

Roberts, D.G. and Bally, A.W. eds., 2012, Regional geology and tectonics: Principles of geologic analysis. Elsevier, **v. 1**, 846 p.

Robertson CGG, 2017, Tellus Database of Sedimentary Basins. URL:https://services3.arcgis.com/3wBYLDMc7IlzsBlJ/arcgis/rest/services/Basin_outlines_Robertson_Basins_and_Plays/FeatureServer

Ryan, W.B.F., Carbotte, S.M., Coplan, J., O'Hara, S., Melkonian, A., Arko, R., Weissel, R.A., Ferrini, V., Goodwillie, A., Nitsche, F. and Bonczkowski, J., 2009, Global Multi-Resolution Topography (GMRT) synthesis data set. Geochemistry, Geophysics, Geosystems, **v. 10 (3)**, 9 p, dio:10.1029/2008GC002332

Sandwell, D. T., Müller, R. D., Smith, W. H., Garcia, E., & Francis, R., 2014, New global marine gravity model from CryoSat-2 and Jason-1 reveals buried tectonic structure. Science, **v. 346(6205)**, p 65-67 dio:10.1126/science.1258213

Sandwell, D. T., Müller, R. D., Smith, W. H., Garcia, E., & Francis, R., 2014, New global marine gravity model from CryoSat-2 and Jason-1 reveals buried tectonic structure. Science, **v. 346(6205)**, p 65-67 dio:10.1126/science.1258213

Schellart, W.P. and Lister, G.S., 2005, The role of the East Asian active margin in widespread extensional and strike-slip deformation in East Asia. Journal of the Geological Society, v. 162(6), p 959-972, dio:10.1144/0016-764904-112

Schellart, W.P. and Spakman, W., 2015, Australian plate motion and topography linked to fossil New Guinea slab below Lake Eyre. Earth and Planetary Science Letters, **v. 421**, p 107-116, dio:10.1016/j.epsl.2015.03.036

Schouten, H., Smith, D.K., Montési, L.G., Zhu, W. and Klein, E.M., 2008, Cracking of lithosphere north of the Galapagos triple junction. Geology, **v. 36(5)**, p 339-342, dio:10.1130/G24431A.1

Şengör A.M.C. (2011) Continental Rifts. In Gupta H.K. (Eds) Encyclopedia of Solid Earth Geophysics. Encyclopedia of Earth Sciences Series. Springer, Dordrecht. 54 p, dio:10.1007/978-90-481-8702-7_31

Seton, M., Müller, R.D., Zahirovic, S., Williams, S., Wright, N.M., Cannon, J., Whittaker, J.M., Matthews, K.J. and McGirr, R., 2020. A global data set of present-day oceanic crustal age and seafloor spreading parameters. Geochemistry, Geophysics, Geosystems, **v. 21(10)**, dio:10.1029/2020GC009214

Seton, M., Whittaker, J.M., Wessel, P., Müller, R.D., DeMets, C., Merkouriev, S., Cande, S., Gaina, C., Eagles, G., Granot, R. and Stock, J., 2014, Community infrastructure and repository for marine magnetic identifications. Geochemistry, Geophysics, Geosystems, **v. 15(4)**, p 1629-1641, dio:10.1002/2013GC005176

Sinton, J. M., and Detrick, R. S., 1992, Mid-Ocean Ridge Magma Chambers. Journal of Geophysical Research, **v. 97(B1)**, p 197-216, dio:10.1029/91JB02508

Smalley Jr, R., Dalziel, I.W.D., Bevis, M.G., Kendrick, E., Stamps, D.S., King, E.C., Taylor, F.W., Lauría, E., Zakrajsek, A. and Parra, H., 2007, Scotia arc kinematics from GPS geodesy. Geophysical Research Letters, **v. 34(21)**, 6 p, doi:10.1029/2007GL031699

Smith, I.E. and Price, R.C., 2006, The Tonga–Kermadec arc and Havre–Lau back-arc system: their role in the development of tectonic and magmatic models for the western Pacific. Journal of volcanology and geothermal research, **v. 156(3-4)**, p 315-331, dio:10.1016/j.jvolgeores.2006.03.006

Socquet, A., Vigny, C., Chamot-Rooke, N., Simons, W., Rangin, C. and Ambrosius, B., 2006, India and Sunda plates motion and deformation along their boundary in Myanmar determined by GPS. Journal of Geophysical Research: Solid Earth, **v. 111(B5)**, 11 p, dio:10.1029/2005JB003877

Stamps, D.S., Calais, E., Saria, E., Hartnady, C., Nocquet, J.M., Ebinger, C.J. and Fernandes, R.M., 2008, A kinematic model for the East African Rift. Geophysical Research Letters, **v. 35(5)**, 6 p, dio:10.1029/2007GL032781

Stamps, D.S., Flesch, L.M. and Calais, E., 2009, Large-scale dynamics of the East African Rift. In AGU Fall Meeting Abstracts.

Steblov, G.M., Vasilenko, N.F., Prytkov, A.S., Frolov, D.I. and Grekova, T.A., 2010. Dynamics of the Kuril-Kamchatka subduction zone from GPS data. Izvestiya, Physics of the Solid Earth, **v. 46(5)**, p 440-445, dio:10.1134/S1069351310050095

Taymaz, T., Yilmaz, Y. and Dilek, Y., 2007, The geodynamics of the Aegean and Anatolia: introduction. Geological Society, London, Special Publications, **v. 291(1)**, p 1-16, dio:10.1144/SP291.1

Thomas, C., Livermore, R. and Pollitz, F., 2003, Motion of the Scotia Sea plates. Geophysical Journal International, **v. 155(3)**, p 789-804, dio:10.1111/j.1365-246X.2003.02069.x

Thouret, J. C., 1999, Volcanic geomorphology - an overview. Earth-science reviews, **v. 47(1-2)**, p 95-131, dio:10.1016/S0377-0273(00)00277-8

Tiesheng, Wu. (2016, November 30). *ArcBeachball (v.2.2)*. ArcGIS. URL: https://www.arcgis.com/home/item.html?id=380b8f93cd684dbea56083218a3b2f43#!

Tsutsumi, H. and Sato, T., 2009, Tectonic Geomorphology of the Southernmost Sagaing Fault and Surface Rupture Associated with the May 1930 Pegu (Bago) Earthquake, MyanmarTectonic

Geomorphology of the Sagaing Fault and Surface Rupture with the May 1930 Pegu Earthquake. Bulletin of the Seismological Society of America, **v. 99(4)**, p 2155-2168, dio:10.1785/0120080113

Van der Hilst, R. D., Widiyantoro, S., and Engdahl, E. R., 1997, Evidence for deep mantle circulation from global tomography. Nature, **v. 386(6625)**, p 578-584, dio:10.1038/386578a0

Vasilenko, N.F. and Prytkov, A.S., 2012, GPS-based modeling of the interaction between the lithospheric plates in Sakhalin. Russian Journal of Pacific Geology, **v. 6(1)**, p 35-41, dio:10.1134/S1819714012010137

Vergés, J., Saura, E., Casciello, E., Fernandez, M., Villaseñor, A., Jimenez-Munt, I. and García-Castellanos, D., 2011, Crustal-scale cross-sections across the NW Zagros belt: implications for the Arabian margin reconstruction. Geological Magazine, **v. 148(5-6)**, p 739-761, dio:10.1017/S0016756811000331

Whittaker, J. M., Afonso, J. C., Masterton, S., Müller, R. D., Wessel, P., Williams, S. E., and Seton, M., 2015, Long-term interaction between mid-ocean ridges and mantle plumes. Nature Geoscience, **v. 8(6)**, p 479-483, doi:10.1038/ngeo2437

Wiens, D. A., Kelley, K. A., and Plank, T., 2006, Mantle temperature variations beneath back-arc spreading centres inferred from seismology, petrology, and bathymetry. Earth and Planetary Science Letters, **v. 248(1-2)**, p 30-42, dio:10.1016/j.epsl.2006.04.011

Xu, J., Ben-Avraham, Z., Kelty, T. and Yu, H.S., 2014. Origin of marginal basins of the NW Pacific and their plate tectonic reconstructions. Earth-Science Reviews, v. 130, p 154-196, dio:10.1016/j.earscirev.2013.10.002